Vortex lattices under stress

Visualizing the superconducting vortex lattice in presence of disorder and magnetism

José Benito Llorens

Dissertation submitted in partial satisfaction
of the requirements for the degree of
Doctor of Philosophy in Physics

Vortex lattices under stress:

Visualizing the superconducting vortex lattice in presence of disorder and magnetism

José Benito Llorens

November, 2019

Thesis advisers
Hermann Suderow and Isabel Guillamón
Universidad Autónoma de Madrid

Acknowledgments

Aunque esta tesis resuma el trabajo de los últimos 5 años, de forma implícita finaliza un periodo de 11 años desde el comienzo de la universidad. Por tanto, es inevitable pensar como he llegado hasta aquí y sobre todo a hombros de quién.

Primero, querría agradecer profundamente a mis directores Hermann e Isabel. Gracias a Hermann por tu positivismo (a pesar de los twisters) y la pasión con la que vives la ciencia. A Isabel, porque es un todoterreno capaz de arreglar cualquier cosa. También, querría agradecer a Sebastián Vieira los buenos consejos cuando se los he pedido. I would also like to thank the members of the jury for doing the effort of reading this thesis and coming to Madrid to listen to my defense.

Por supuesto a mis compañeros durante la tesis. A mis predecesores Ed y Antón, os debo casi la tesis entera. Ed, gracias por estar dispuesto a TODO por ayudarme. Tus clases de salsa, tus sanduches de pizza y por traer la fiesta al laboratorio (y fuera de él). Antón, gracias por saber siempre que decir en el momento adecuado y por nuestros duelos con espadas de corcho pan. Por supuesto, gracias a Augusto, Ché, Manuel, Thomas, Manolo, Lolo y demás amigos que han ido pasando por el laboratorio. A los que dejo continuando la tesis. Gracias a Fran porque empezó siendo mudo y acabó cantando las canciones más casposas que te puedas imaginar. Dale duro. Gracias a Victor (aunque seas del old lab) porque, aunque no hayas ganado el premio Edwin, te lo mereces. Gracias a Raquel, porque eres capaz de hablar de cualquier cosa con una sonrisa. También muchas gracias a las últimas incorporaciones, Beilun, Marta y David. Ánimo con lo que os queda. Muchísimas gracias también a los tres mosqueteros Rafa, Sara y Chema. Os encargáis de arreglar cualquier destrozo que hacemos, y no hay palabras suficientes para agradecer todo lo que hacéis.

Fuera de nuestro grupo, también quería dar las gracias a Laura, porque hemos tenido carreras muy paralelas y siempre me he sentido muy respaldado. Muchas gracias a David, el de la UAM, no el desconocido del mail. También a Cesar, Mariano, Alexandros, Charalambos, Siya, Juanpe, Isidoro, Antonio y Jon. No me quiero olvidar de quienes siempre me han ayudado con los papeleos, Elsa, Luisa, Ángeles, Ana Isabel e Irene. Además, me gustaría agradecer a Javier, Mariano, Juan Antonio y Nacho su paciencia y dedicación con la electrónica. Además, querría agradecer. También a Macarena y Reyes y las demás trabajadoras de limpieza. Por último, querría dar las gracias a Andrés por su apoyo durante mi primera parte de esta tesis.

Por supuesto tengo infinito que agradecer a toda la gente de la carrera. Muchísimas gracias a Javs, desde los minijuegos en primero hasta nuestro futuro

como creadores; a JM, desde nuestras charlas siendo compañeros de mesa hasta tus futuras visitas sorpresas; a Jorg, desde nuestra historia en los labos de química hasta que al fin lo petemos como music stars; a Kiks, desde nuestras charlas en Chamartín hasta tus próximas quejas donde quiera que vivas (alguna montaña). Muchas gracias al silencioso Quereda por transmitir paz haya donde va. También agradezco a Acero, Sara, Colin, Clau, Rocio, Jezú, Adrian, Carmen, Xabi, Mar, Luis y demás personas que me han acompañado en este periodo Tengo que seguir echando la vista atrás, y agradecer a la gente del instituto. Gracias a Miguel, Pou y Jorge por haber estado SIEMPRE ahí. Tenemos pendiente la subida a la Morra de Lechugales, no me olvido.De verdad, siempre sentiré gran orgullo de haber compartido con vosotros más de 20 años. Tampoco me olvido de Clara, Marina, Teresa, María, Eloy o los cocodrilos.

Muchas gracias a mi familia. Gracias a mis abuelos, mis tios y mis primos porque siempre me he sentido tremendamente apoyado por ellos. Gracias a los amigos de mis padres, que son como de mi familia. Por supuesto, gracias a los Monzuitos y Cubanitos por hacerme sentir uno más. Muchísimas gracias en especial a Maribel y David.

Muchísimas gracias a mis padres porque me han enseñado a poner ilusión y trabajo duro a todo lo que hago. Muchísimas gracias a mi hermano, que en general tiene que aguantar mis tonterías. Mis próximos retos incluyen hacer una paella cómo las de mi madre, estar tan en forma como mi padre y ser la mitad de estiloso que mi hermano.

Finalmente quiero darle las gracias a la Helen. Esto está finalizado gracias a ti. Gracias por siempre estar dispuesta a absolutamente TODO y con un plan perfecto para cada nueva situación. Eres simplemente mi persona favorita.

Contents

Abstract

While I was an undergraduate student, my future thesis co-director showed us a video where dolphins create and play with vortices in water. Some years later, I realised I have done the same, using magnetic vortices in superconductors.

Vortices were first proposed by Abrikosov in 1957. Still today, vortex physics is a very active and fruitful research field. Individual vortices can be considered the fingerprint of any superconductor because the way superconductivity is suppressed inside them, directly depends on characteristic parameters such as the coherence length and the London penetration depth. At the same time, the electrodynamic properties of superconductors, important for applications, are governed by the collective behaviour of the vortex lattice. The vortex lattice was first observed by magnetic decoration in 1967 and, since then, a great number of microscopic tools have been developed to probe its properties at local scale. In this thesis, I have analysed vortex images with three different techniques: squid-on-tip (SOT), magnetic force microscopy (MFM) and scanning tunnelling microscope (STM). I have made an effort to improve our understanding of the behaviour of the vortex lattice in different materials, with different pinning landscapes and in a large range of temperatures and magnetic fields.

In chapter 3, I report measurements in $CaK(Fe_{0.95}Ni_{0.05})_4As_4$. This material belongs to the 1144 family of iron based superconductors. The absence of glide symmetry in the crystalline structure, makes this family of compounds unique among the iron-based superconductors. The stoichiometric compound, $CaKFe_4As_4$, has been previously characterized by different techniques such as STM, ARPES or penetration depths measurements. It shows isotropic two band superconductivity, a disordered vortex lattice and a Fermi surface consistent with the paramagnetic state of iron-based superconductors. Electron doping of the parent compound, introduced for instance by substituting Fe by Ni, induces antiferromagnetic order which is non-collinear. Because the spin orientation in the Fe layer, this non-collinear antiferromagnetic order has been named Hedgehog spin vortex crystal. In this chapter, I describe the first microscopic characterization of the superconducting properties of $CaK(Fe_{0.95}Ni_{0.05})_4As_4$ where superconductivity eventually coexist with the Hedgehog antiferromagnetic order. In particular, we study how this coexistence modifies the normal and superconducting state electronic properties.

In chapter 4, I have analysed the properties of a new vortex phase that appears at very low magnetic fields in the superconductor β-Bi_2Pd. SOT measurements at magnetic fields of a few Gauss have shown very inhomogeneous vortex distribution, with vortices closed packed along lines separated by vortex-free regions. I have

characterized in detailed the structural and fractal properties of this arrangement and followed its dependence with the magnetic field.

In chapter 5, I have discussed the concept of disordered hyperuniformity in the vortex lattice. The term hyperuniformity was coined by Torquato to describe an arrangement of particles with suppressed density fluctuations that results in the same physical properties in all directions at shorter distances. To draw a conclusion about the hyperuniformity in vortex lattice, I have analysed images of the disordered vortex lattice taken in a number of materials with different pinning properties.

In chapter 6, I have studied vortex creep in the anisotropic superconductor 2H-$NbSe_2$ under tilted magnetic fields. Contrary to what has been reported so far, we observed that vortex creep can be initiated by decreasing the temperature. I have quantified vortex motion during creep. This allowed to compare with theory and obtain an understanding of the cooling induced motion through the anisotropic properties of 2H-$NbSe_2$.

Resumen

Cuando estaba todavía en la carrera, el que iba a ser uno de mis directores de tesis, nos enseñó un vídeo de unos delfines jugando con vórtices que ellos mismos formaban en el agua. Años más tarde me di cuenta de que eso es lo que he hecho, pero con vórtices en superconductores.

Los vórtices superconductores fueron predichos por Abrikosov en 1957. En la actualidad, la física de vórtices sigue siendo un campo muy activo y fructífero. El núcleo de un vórtice aislado puede considerarse la huella dactilar de un superconductor, debido a que, en su interior, la manera en que se suprime la superconductividad depende directamente de sus parámetros característicos, como son la longitud de coherencia y la penetración de London. Al mismo tiempo, las propiedades electrodinámicas de los superconductores, importantes para las aplicaciones, vienen determinadas por el comportamiento colectivo de la red de vórtices.

La primera imagen de la red de vórtices se obtuvo en 1967 usando decoración magnética y, desde entonces, se han inventado multitud de técnicas microscópicas que permiten estudiar sus propiedades a escala local. En esta tesis, he analizado imágenes de vórtices obtenidas usando tres técnicas diferentes: squid-on-tip (SOT), microscopía de fuerza magnética (MFM) y microscopía de efecto túnel (STM). Durante este periodo, he tratado de mejorar nuestra comprensión del comportamiento de la red de vórtices en diferentes materiales, con diferente distribución de centros de anclaje y en un amplio rango de temperaturas y campos magnéticos.

En el capítulo 3, mostramos las medidas en $CaK(Fe_{0.95}Ni_{0.05})_4As_4$. Este material, pertenece a la familia 1144 de superconductores basados en hierro. La ausencia de simetría de espejo en la estructura cristalina, hace que esta familia de compuestos sea única entre los superconductores basados en hierro. El compuesto estequiométrico, $CaKFe_4As_4$, se caracterizó previamente mediante diferentes técnicas, como STM, ARPES o medidas de longitud de penetración. Este material presenta superconductividad isótropa de dos bandas, una red de vórtices desordenada y una superficie de Fermi consistente con el estado paramagnético de los superconductores basados en hierro. El dopaje con electrones en el compuesto estequiométrico, como por ejemplo, sustituyendo el Fe por Ni, induce un orden antiferromagnético no colineal. Debido a la distribución de espines en la capa del Fe, este orden antiferromagnético no colineal es conocido como orden antiferromagnético tipo erizo. En este capítulo, presento la primera caracterización microscópica de las propiedades superconductoras de $CaK(Fe_{0.95}Ni_{0.05})_4As_4$, composición en la

cual la superconductividad coexiste con el orden antiferromagnético de tipo erizo. Concretamente, estudiamos cómo se modifican las propiedades electrónicas del estado normal y superconductor debido a esta coexistencia.

En el capítulo 4, he analizado las propiedades de una fase de vórtices nueva que aparece a campos magnéticos muy bajos en el superconductor β-Bi_2Pd. En presencia de campos magnéticos de unos pocos Gauss, las medidas con SOT muestran una distribución de vórtices muy inhomogénea, con vórtices anclados a lo largo de líneas que quedan separadas por regiones vacías. He caracterizado en detalle las propiedades estructurales y multifractales de esta distribución y estudiado su dependencia con el campo magnético.

En el capítulo 5, he discutido el concepto del desorden hiperuniforme en la red de vórtices. El término hiperuniforme fue acuñado por Torquato para describir una distribución de partículas sin fluctuaciones de densidad, dando lugar a propiedades físicas similares en todas las direcciones para distancias pequeñas. Para extraer una conclusión sobre la hiperuniformidad en la red de vórtices, he analizado imágenes de redes de vórtices desordenadas tomadas en varios materiales con diferentes propiedades de anclaje.

En el capítulo 6, he estudiado el movimiento de arrastre de los vórtices en el superconductor anisótropo 2H-$NbSe_2$ bajo un campo magnético inclinado. A diferencia de lo que se había visto hasta ahora, se ha observado que el movimiento de arrastre de los vórtices se puede activar al disminuir la temperatura. He cuantificado el movimiento de los vórtices y reproducido los datos experimentales con un modelo teórico.

1 | Introduction

1.1 Superconductivity

The discovery of superconductivity is linked to the physics of low temperatures. In 1908, Kamerling Onnes achieved the liquefaction of Helium at 4.2 K. Three years later, in 1911, Onnes measured the temperature dependence of the electrical resistance in Hg [1]. As we show in Fig. 1.1, Onnes observed a drop of several orders of magnitude around 4.15 K. The term "superconductivity" was coined and many other materials with the same behaviour were discovered in the following years.

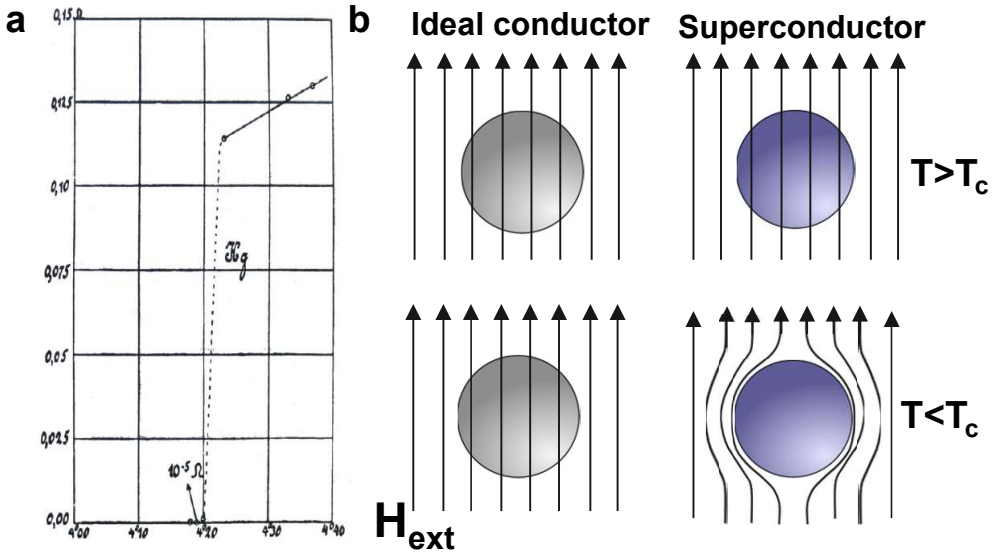

Figure 1.1: (a) Historic plot of the resistance as a function of temperature in mercury [1]. Resistance goes abruptly to zero around 4.15 K .(b) Comparison of the behaviour between an ideal conductor and a superconductor. The superconductor acts as a perfect diamagnet in the Meissner state.

The transition temperature was called the critical temperature, T_c. It was soon discovered that not only superconductivity is destroyed by temperature. Depending on the material, magnetic field and electrical current at specific values (H_c, J_c) also destroy the superconductivity state. The dependence of the critical magnetic field

with temperature was characterized by an empirical formula:

$$H_c(T) = H_c(0)\left(1 - \left(\frac{T}{T_c}\right)^2\right) \tag{1.1}$$

The thermodynamic critical magnetic field is proportional to the free energy difference between the normal and the superconducting state, f_n and f_s respectively, as:

$$f_n - f_s = \frac{1}{2}\mu_0 H_c^2 \tag{1.2}$$

Superconductivity was thought as a perfect electrical conductivity until in 1933, when, W. Meissner and R. Ochsenfeld [2] discovered that in the superconducting state, magnetic field does not penetrate in the interior of the material similarly to what happens in a perfect diamagnet (Fig. 1.1b). In a perfect conductor, the state inside the sample will remain the same as in the normal state, so that if the perfect conductor is cooled down below its T_c at zero field, and then the field is applied, the magnetic field in its interior will be zero. However, if the perfect conductor is cooled down below the transition temperature in presence of a magnetic field, the field will be "frozen" in its interior. This is fundamentally different from the Meissner state in a superconductor, in which the magnetic field is expelled when the material goes through the superconducting transition.

1.1.1 London theory

A phenomenological theory was proposed by the London siblings. It describes electrodynamics of superconductors using only two equations [3]. According to this theory, perfect diamagnetism is due to supercurrents flowing around the sample boundaries, screening the external magnetic field. The external magnetic field and screening currents penetrate into the superconductor at a characteristic distance, which is called the London penetration depth, λ.

1.1.2 Ginzburg-Landau theory

Ginzburg and Landau provided a theory for superconductors based on an expansion of the free energy in terms of a small parameter that is zero in the normal phase and finite in the superconducting phase [4, 5].

The parameter is called "order parameter" and was subsequently connected to the square of the Cooper pair wavefunction $|\Psi|^2$, which is also proportional to the density of Cooper pairs.

In 1950, Landau and Ginzburg (GL) described the thermodynamic properties of superconducting transition [5]. Using Landau's theory of phase transitions [4]. This theory described a second order phase transition as a sudden change of a symmetry at the transition temperature. The system goes to a more ordered state at lower temperatures. Landau showed that we can expand the free energy in terms of an

order parameter which is zero at high temperatures and increases continuously when entering the ordered phase upon cooling.

GL theory uses as the order parameter a wave function $\Psi(\boldsymbol{r})$ that describes macroscopic properties of the superconducting state. The square modulus of the wave function, $|\Psi|^2$, is the density of superconducting electrons, n_s. The free energy density of a superconductor, f_s, is:

$$f_s = f_n + \alpha|\Psi|^2 + \frac{\beta}{2}|\Psi|^4 + \frac{1}{2m^*}|(i\hbar \bigtriangledown + e^*\boldsymbol{A})\Psi|^2 + \frac{h}{8\pi} \tag{1.3}$$

Being f_n the free energy of normal state, α and β, parameters characteristic of the material, h the magnetic field per unit volume, $\boldsymbol{A}$ the vector potential and m^* and e^* are the mass and charge of superconducting electrons. Ginzburg and Landau then found the equations that carry their name. These are very useful to describe spatial variations of the Cooper pair wavefunction and can be written as:

$$\alpha\Psi + \beta|\Psi|^2\Psi + \frac{1}{2m^*}(i\hbar \bigtriangledown + e^*\boldsymbol{A})^2\Psi = 0 \tag{1.4}$$

$$J = -\frac{i\hbar e^*}{2m^*}(\Psi^* \bigtriangledown \Psi - \Psi \bigtriangledown \Psi^*) - \frac{e^{*2}}{m^* c}\Psi^*\Psi\boldsymbol{A} \tag{1.5}$$

These two equations describe the spatial distribution of the magnetic field and the superconducting order parameter. By solving these equations, different responses of the superconductor under magnetic field can be considered. The magnetic field can penetrate the superconductor producing an inhomogeneous distribution of normal and superconducting regions. In this context, the magnetic field penetrates into the normal regions and is expelled from the superconducting regions.

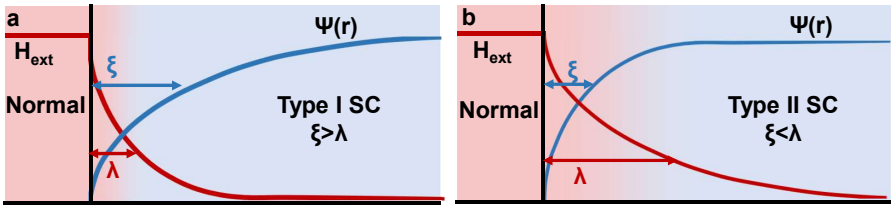

Figure 1.2: Schematic diagram of the behaviour of Ψ, ξ and λ in an interface between the normal and superconducting state along the direction perpendicular to the interface. In type I superconductors (a), the decay of the wavefunction is slower than the penetration of the magnetic field inside the superconductor, and the contrary happens in type II superconductors (b).

The responses to magnetic field can be described using two characteristics length scales: the coherence length, ξ, showing the spatial decay of the order parameter, and the penetration depth, λ, characterizing the decay distance of penetrating magnetic

field. Both lengths have the same dependence with temperature near T_c,

$$\lambda, \xi \propto \frac{1}{\sqrt{(T_c - T)}} \tag{1.6}$$

The ratio of both parameters is the so called Ginzburg-Landau parameter, κ. Using this parameter we can distinguish two regimes. When $\kappa < 1/\sqrt{2}$ ($\xi > \lambda$), the penetration of a magnetic field is not energetically favorable. On the contrary, when $\kappa > 1/\sqrt{2}$ ($\xi < \lambda$) the magnetic field can penetrate into small regions of the superconductor through flux tubes known as vortices.

Therefore, we can classify superconductors taking into account their response under magnetic field as type I, where magnetic field is fully ejected (Meissner effect) and type II, where magnetic field penetrates as vortices. Each vortex carries a quantum flux given by

$$\Phi_0 = \frac{h}{2e} = 2.07 \times 10^{-15} Wb \tag{1.7}$$

In Fig. 1.2 we show an sketch of the difference between the behaviour of ξ and λ in type I (a) and type II (b) superconductors.

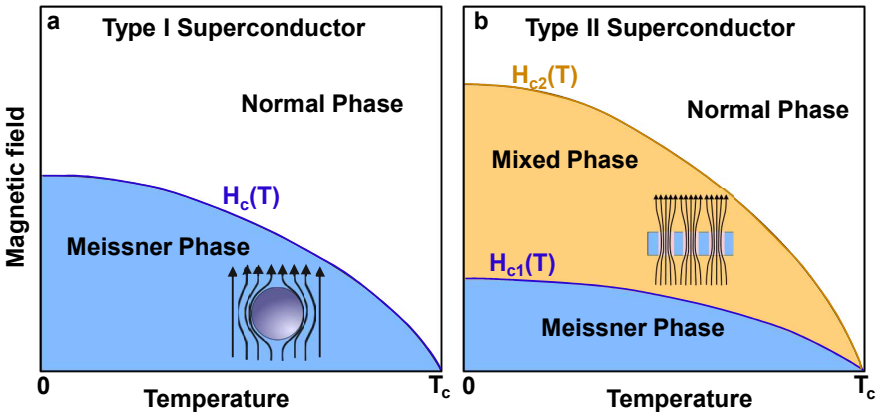

Figure 1.3: Magnetic field vs temperature phase diagrams of a type I (a) and type II (b) superconductors. In a type I superconductor, Meissner phase is found until H_c where the superconductor transits to the normal phase. In Type II superconductors, however, an intermediate region between H_{c1} and H_{c2} is found, where the magnetic field partially penetrates in form of vortices.

In Fig. 1.3 we compare the phase diagrams of type I (a) and type II (b) superconductors. Type I superconductors maintain superconductivity in the Meissner phase up to a critical value of magnetic field that depends on λ and ξ

$$H_c = \frac{\Phi_0}{4\sqrt{2}\pi\lambda\xi} \tag{1.8}$$

When magnetic field exceeds Equation 1.8, the superconductor turns completely normal. Type II superconductors are characterized by two critical magnetic fields, H_{c1} and H_{c2}. When external magnetic field is below H_{c1}, type II superconductors

expel the magnetic field as type I superconductors do. At magnetic fields above H_{c1} and below H_{c2} the magnetic field penetrates into the superconductor in form of vortices in the so called mixed state. Finally, when the magnetic field is higher than H_{c2} superconductivity is destroyed. Due to the partial flux penetration of type II superconductors, the energy cost to drive out the magnetic field from superconducting regions is much less than in type I superconductors, increasing the magnetic field H_{c2} with respect to the critical magnetic field H_c.

1.1.3 Microscopic theory

In 1957, Bardeen, Cooper and Schrieffer published the so called BCS theory [6, 7]. Some experimental observations helped to the development of this theory. One of the most important ones was the isotope effect [8]. The same material with different isotopes has a different critical temperature. The expected dependence is given by $T_c \propto M^{-\alpha}$, being $\alpha \approx 1/2$ and M the mass of the isotope. This pointed to a very fundamental role of the atomic lattice in the superconducting state.

In 1950, Fröhlich proposed that a weak attractive interaction mediated by phonons could be the key to understand the microscopic origin of the superconducting state [9]. In Fig. 1.4 we show an electron moving through the lattice that has an attractive interaction with the positive ions of the lattice. This increases locally the positive charge, exciting a phonon. A second surrounding electron, can be attracted to the positive charge created by the first electron, absorbing the phonon associated with the lattice vibration.

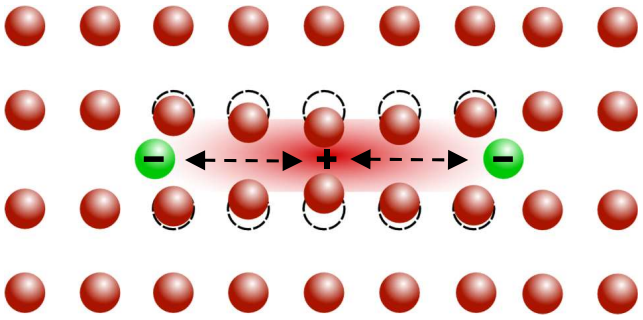

Figure 1.4: An electron moving through the lattice is attracted to the ions of the lattice. As a consequence, lattice slightly disorders creating a positive charge concentration or phonon. Another electron feels the accumulation of charge and absorbs the phonon.

Cooper showed in [10], that when a weak attractive interaction between electrons exists, a bound state with opposite momentum and spin is created close to the Fermi energy. The electron pair is called Cooper pair. BCS theory generalizes the problem for multiple electrons. According to BCS theory, the conduction band electrons are unstable when an effective attractive interaction is present and the system energy is reduced due to the formation of Cooper pairs.

BCS description of the superconducting ground state finds that energy E_k of excited states is given by:

$$E_k = \sqrt{\Delta^2 + \epsilon_k^2} \tag{1.9}$$

where ϵ_k is the kinetic energy with respect to the Fermi level and Δ is a constant named as superconducting gap. Equation 1.9 is showing that a finite energy of Δ is always necessary to create an excited state. Therefore, a gap of size Δ is opened where no states are allowed in this energy range. Note that, to break a Cooper pair, we require an energy of 2Δ. For energies $\epsilon_k >> \Delta$ the metallic behaviour is recovered.

As the number of states is the same in the normal and the superconducting states ($N_n(\epsilon_k)$ and $N_s(E)$), and assuming a constant density of states in the normal phase $N_n(\epsilon_k) \approx N_n(0)$, $N_s(E)$ can be written as:

$$\frac{N_s(E)}{N_n(0)} = \frac{d\epsilon_k}{dE} = \begin{cases} 0 & E < \Delta \\ \frac{E}{\sqrt{E^2-\Delta^2}} & E > \Delta \end{cases} \tag{1.10}$$

BCS theory also describes a relation between the superconducting gap, Δ, and the critical temperature

$$\Delta = 1.76 k_B T_c \tag{1.11}$$

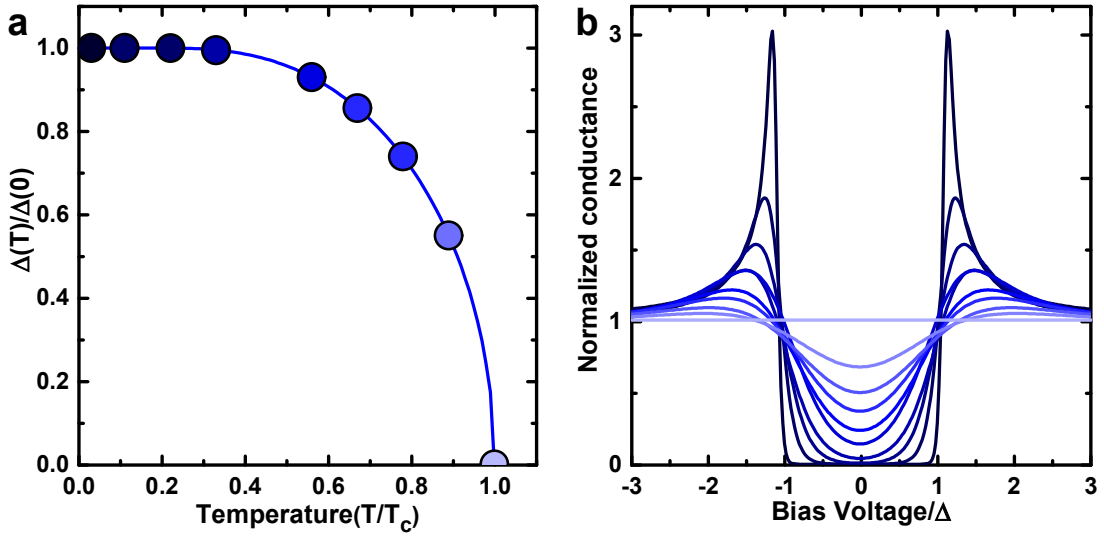

Figure 1.5: (a) Temperature dependence of the superconducting gap in BCS theory. (b) Superconducting density of states as a function of temperature. The colors of the curve match with the color of the points in (a).

Fig. 1.5a shows $\Delta(T)$ as a function of temperature. At low temperature Δ is almost constant and near T_c, $\Delta(T) \propto (T\text{-}T_c)^{1/2}$. In Fig. 1.5b we show the temperature dependence of the superconducting density of states. Above T_c, we observe the flat density of states of a normal metal close to the Fermi energy.

1.2 Superconducting vortices

As we mentioned before, in type II superconductors, the magnetic field penetrates in form of vortices. Each vortex has a normal state core with supercurrents around the core and a quantised flux of Φ_0. In Fig. 1.6b we show that the magnetic field profile decays from the center of the vortex to the exterior within a length scale of the order of λ. Furthermore, Cooper pair density, $|\Psi(r)|^2$, decays as approaching the core center within a length scale of the order of ξ.

The energy per unit length of each vortex is given by

$$\epsilon_L = \frac{\Phi_0^2}{4\pi\mu_0\lambda^2} ln\left(\frac{\lambda}{\xi}\right) \tag{1.12}$$

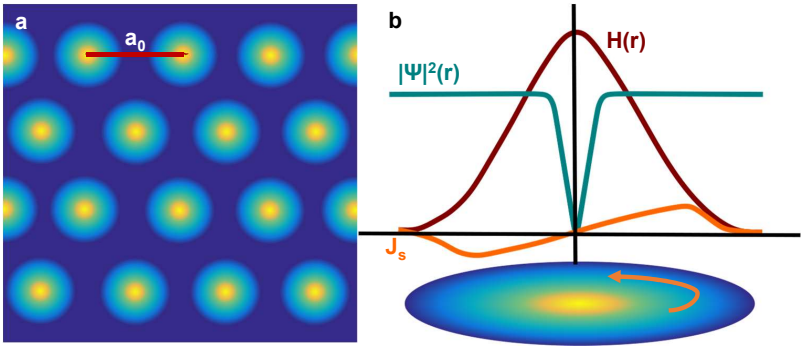

Figure 1.6: In (a), an schematic view of vortices arranged in a triangular Abrikosov lattice with an intervortex distance of a_0. In (b), a cartoon of the magnetic field (red), order parameter (turquoise) and supercurrents (orange) variation around a vortex.

The interaction among pairs of vortices is usually repulsive, with a force that can be written as

$$F_{12} = \frac{\Phi_0^2}{8\pi^2\lambda^2} K_0\left(\frac{r_{12}}{\lambda}\right) \tag{1.13}$$

Where K_0 is the zero-th order Hankel function. Therefore, the characteristic length for the intervortex interaction is of the order of λ. Abrikosov showed that vortices arrange in an ordered lattice, the so called Abrikosov lattice. This lattice is typically hexagonal but some examples of square lattices have been found. The distance between vortices is given by the expression:

$$\text{Triangular lattice:} \qquad a_0 = \sqrt[4]{\frac{4}{3}}\left(\frac{\Phi_0}{B}\right)^{1/2} \tag{1.14}$$

$$\text{Square lattice:} \qquad a_0 = \left(\frac{\Phi_0}{B}\right)^{1/2} \tag{1.15}$$

We observe that the distance between neighbouring vortices only depends on the external magnetic field.

There are different techniques that allow the observation of the vortex lattice in real space with single vortex resolution. Some techniques are sensitive to the magnetic field and other to the superconducting density of states. Bitter decoration, [11], Squid-on-tip (SOT), [12], or magnetic force microscopy (MFM), [13], are examples of techniques sensitive to the magnetic field distribution. Usually, large areas can be measured, although only at low magnetic fields, when the intervortex distance is of order or below λ. At higher fields, vortices overlap producing a homogeneous magnetic field in the surface and too small contrast to be observed by magnetic field sensing techniques. On the contrary, STM directly measures the spatial variation of the density of states. As the density of states varies at the scale of the coherence length and intervortex distance becomes of the order of ξ only at H_{c2}, using STM we can observe the vortex lattice in a large region of the mixed state. STM at low temperatures usually allows to make images with a size of a few microns, and is thus not suited for the range of small magnetic fields. Using a STM we can get detailed information on the internal electronic structure of individual vortex core, as well as visualize the structural and dynamic properties of the lattice. More details on vortex visualization with STM are given in refs. [14, 15].

The following subsections use concepts explained in greater detail in the books of Tinkham [16] and Schmidt, [17] and the reviews of Brandt [18] and Blatter [19].

1.2.1 Vortex core

First we start by discussing a model developed by Kogan to describe the evolution of vortex core size with the magnetic field [20]. Vortex core C is defined as the slope of the order parameter at the vortex core center (see inset of Fig. 1.7b). Therefore, the coherence length is related with C and the order parameter as

$$\frac{d\Delta}{dr}|_{r\longrightarrow 0} \propto \frac{1}{\xi} \propto \frac{1}{C} \tag{1.16}$$

The model proposed by Kogan is based on the De Gennes equation for the density of states (DOS)

$$\frac{N(r)}{N_n} = 1 - \frac{|\Delta(r)|^2}{\Delta_0^2} \tag{1.17}$$

Being N(r) the zero bias density of states (DOS) and N_n the DOS in normal phase. In order to simplify the spatial dependence, Wigner-Seitz approximation is used considering the unit cell as circle of radius a where $\pi a^2 = \phi_o/H$ and hence $2a \approx 1.05a_0$.

The model proposes a variation of the normalized conductance σ as:

$$\sigma = 1 - \frac{\rho^2(1+\eta^2)}{\rho^2+\eta^2)} exp[\frac{\eta^2(1-\rho^2)}{1+\eta^2}], \qquad \rho = r/a, \qquad \eta = C/a \tag{1.18}$$

Here in Equation 1.18 all distances have been normalized to the radius a. ν is similar to the width of a Gaussian. The bigger ν, the bigger the profile.

The model has been tested in different materials [21] as S-doped 2H-$NbSe_2$, β-Bi_2Pd and $CaKFe_4As_4$ [22]. When sample is in the dirty limit (mean free path $l < \xi$) we observe that vortex core is approximately constant with magnetic field (Fig. 1.7a-b), but if superconductor is in the clean limit ($l > \xi$), the vortex core size decreases when increasing the magnetic field as $\propto 1/\sqrt{H}$ (Fig. 1.7c-d).

The model has been also used for superconductors with multiple gaps over the Fermi surface [23, 20].

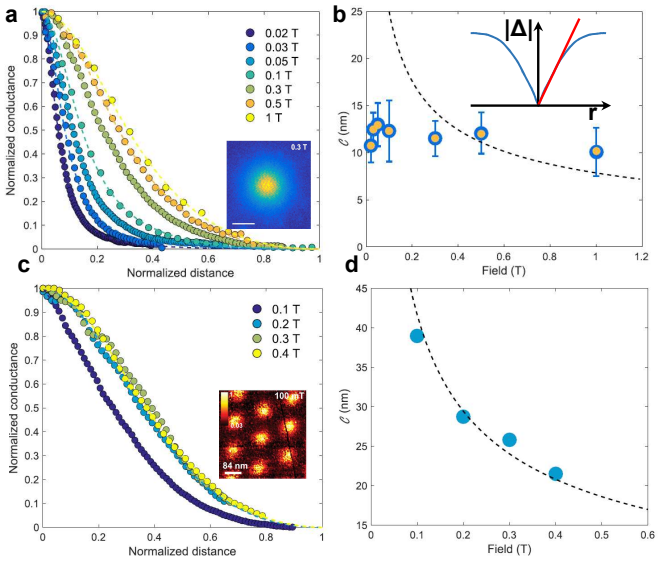

Figure 1.7: In (a) we show the normalized profiles of the core in 2H-$NbSe_{1.8}S_{0.2}$ with the vortex image at H=0.3 T. (b), we plot the different sizes of the vortex core with magnetic field as points and the dashed line shows the behaviour for a superconductor in clean limit. In the inset we show how vortex core C is defined as the slope of the order parameter at the vortex core center. In (c) we show the results of the normalized profiles in β-Bi_2Pd with an image of vortex lattice at H=0.1 T. In (d), the sizes of the vortex core of (c), with magnetic field as points and the dashed line represents behaviour for a superconductor in clean limit. Data taken from [21].

1.2.2 Vortex phases

We have discussed in previous sections that vortices interact among each other with a repulsive interaction. In order to minimise the free energy, vortices are organised in a triangular or square lattice with a lattice parameter only dependent on the magnetic field. In real superconductors, defects are present. Defects in the atomic

structure can locally deplete the superconducting properties in a region around the defect with size of the order of ξ. As a consequence, the energy cost to create a vortex in a defect is less than in a defect-free region. Thus, defects pin vortices creating a pinning potential landscape in the sample. Pinning centres distribute over the sample and can influence the whole vortex lattice creating disorder. As we show in Equation 1.13 the interaction among vortices depends on the distance among them and λ, being weaker at the lowest and the highest magnetic fields (where vortices are, respectively, too far apart to feel the repulsive interaction or too close producing a homogeneous field distribution). At intermediate fields, however, the repulsive interaction is stronger (where vortices are close enough to feel repulsive interaction but far enough to avoid overlapping). The pinning potential is, in principle, acting over a region of the order of ξ and thus does not change much when modifying the magnetic field. Therefore, the influence of pinning strongly depends on the magnetic field, mainly due to the elastic properties of the vortex lattice, or the changes in the vortex-vortex interaction when changing the intervortex distance by the magnetic field.

Another important magnitude is the temperature. When thermal energy is of the order of the vortex interaction energy or pinning potential, vortex lattice is influenced by temperature as well. Therefore, the combination of vortex-vortex interaction, pinning potential and thermal energy offers a playground where different phases can exist. In Fig. 1.8 we show a simplified magnetic field vs temperature phase diagram of the vortex lattice.

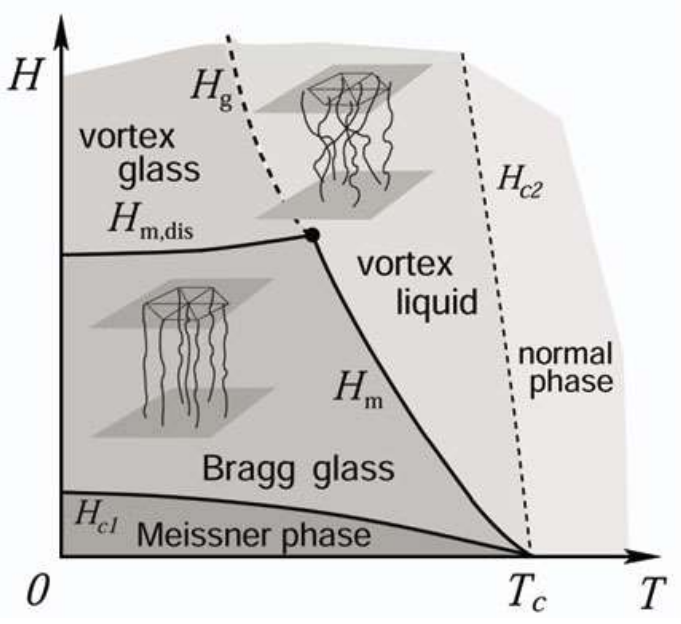

Figure 1.8: A schematic phase diagram of the vortex lattice. The vortex solid is, in most of the phase diagram, a Bragg glass, but disordered vortex phases can also occur in some compounds. In light gray the vortex liquid phase. Image taken from [19].

An important parameter to quantify the relevance of temperature is

Ginzburg-Levanyuk number, G_i:

$$G_i = \frac{1}{2}\left(\frac{k_b T_c}{4\pi\mu_o H_c^2 \xi^3}\right)^2 \approx 10^{-7}\frac{\kappa^4 T_c^2}{H_{c2}} \tag{1.19}$$

This number compares the thermal energy with the superconducting condensation energy. The larger G_i, the larger the thermally induced effects. We can observe that high T_c superconductors will have a larger G_i, typically of the order of 10^{-1}-10^{-3}. G_i is also highly dependent on the Ginzburg-Landau parameter, κ. In most conventional superconductors, G_i is very small, of the order of 10^{-8}-10^{-11}, and therefore thermal effects are restricted to a region of a few milikelvin below the transition to the normal state.

Hence, superconductors with a large value of G_i as high T_c or extreme type II superconductors have an extended region of the phase diagram close to the transition lines $H_{c1}(T)$ and $H_{c2}(T)$ where vortices are in liquid phase.

This has been seen in several macroscopic measurements, but also in neutron scattering, Hall probe and nuclear magnetic resonance [24, 25, 26, 27]. Furthermore, melting has been observed in STM measurements in amorphous W-based thin films [28]. STM experiments are very useful, because vortices can be observed individually.

At low temperatures, the vortex lattice is solid. The vortex solid can be an ordered solid at intermediate fields when vortex-vortex interactions are strong, or a disordered solid at high fields where vortex-vortex interactions are weak (Fig. 1.8). Depending on the pinning landscape, the magnetic field range of an ordered or disordered lattice can change. The ordered solid can appear when the vortex-vortex interactions are strong and pinning is weak. The ordered vortex solid is usually ordered as a triangular (see Fig. 1.9a) or less commonly as a square lattice. The ordered vortex solid is called a Bragg glass because it is not perfectly ordered as a consequence of the interaction of the whole lattice with pinning centres. Pinning disorder induces small vortex displacements producing quasi-long range positional order but leaving long range orientational order.

When vortex-vortex interaction is much lower than pinning, the vortex lattice can fully disorder in a vortex glass (Fig. 1.9b). When magnetic field is increased from the Bragg glass, vortex lattice starts to disorder through the appearance of topological defects in the lattice. These topological defects are called dislocations and disclinations. Disclinations are vortices characterized by a number of first neighbours larger or smaller than 6 (in the triangular lattice) as shown in Fig. 1.9(c,d). The energy cost of a disclination is very high because it produces large vortex displacements, breaking translational and orientational order. 5 and 7 first nearest neighbours disclinations tend to pair, decreasing notably the energy cost of the defect (see Fig. 1.9e). These defects are called dislocations. Dislocations do not break orientational order of the lattice. Typically, the vortex lattice tends to disorder forming first dislocations, and then disclinations appear when vortex lattice is a disordered glass (Fig. 1.9b) [29].

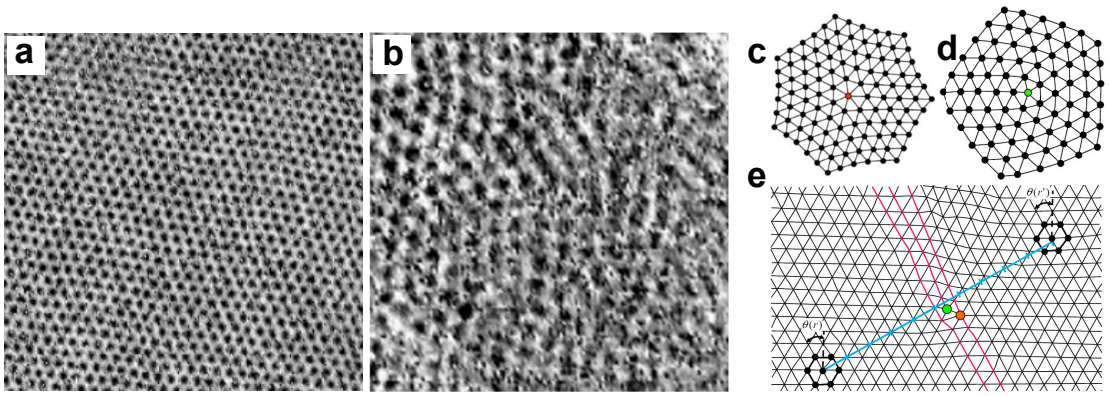

Figure 1.9: In (a) and (b), we show images of the vortex lattice taken at 100 mK in the Bragg glass phase (a, at 2.5 T) and the vortex glass phase (b, at 5 T) in an amorphous thin film based on W [29]. (c) and (d) are disclinations of 5 and 7 first nearest neighbours respectively and e shows a dislocation. We observe that orientational order is maintained in (e) and lost in (c) and (d). (c), (d) and (e) are taken from [30].

The size of region in the phase diagram where the glass phase appears is very material dependent. In clean systems such as 2H-$NbSe_2$, the vortex lattice remains ordered until it reaches a field very close to H_{c2}. However, in other superconductors with larger intrinsic pinning, such as iron based superconductors, the glass vortex phase may be found in a large region of the phase diagram.

Magnetization of the superconductor can be very dependent on the applied magnetic field history. We can distinguish two different procedures, zero field cooling (ZFC) or field cooled (FC). In a ZFC, first the temperature is decreased below T_c and then the magnetic field is applied. With this method, the magnetic field inside the superconductor, B, is similar to the applied magnetic field, H.

However, the opposite is found in a FC experiment. In a FC procedure, the magnetic field is applied in the normal phase, and then the temperature is decreased below T_c under applied magnetic field. In a FC experiment at high fields, the vortex lattice first goes through the vortex liquid phase before becoming solid at low enough temperatures. This may introduce quenched disorder in the vortex lattice.

At lower fields, in a FC experiment, we first enter in the vortex liquid phase and then we enter the Meissner state. This may lead to a situation where vortices get trapped below H_{c1}, producing a frozen disordered lattice in the Meissner phase [31].

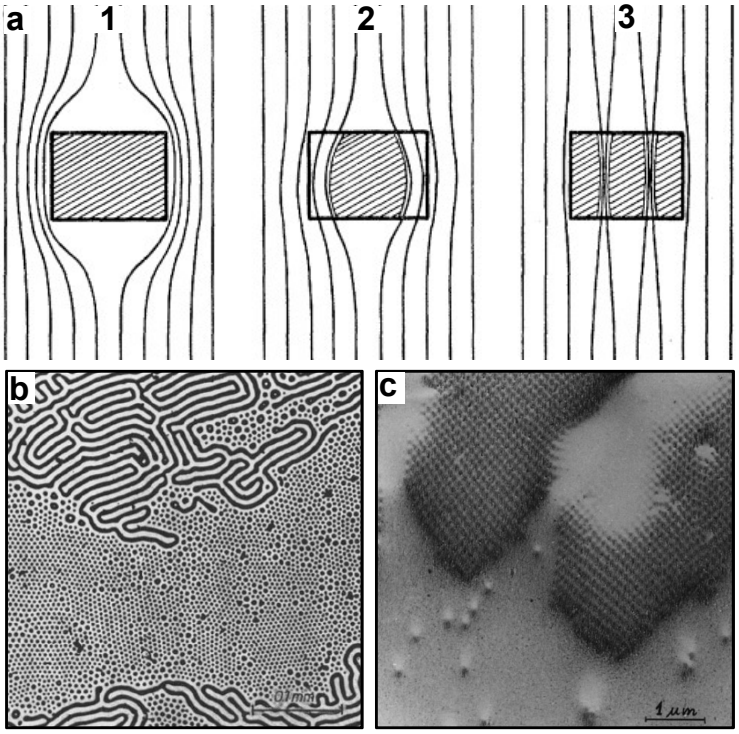

Figure 1.10: In (a) we show a flux distribution around a short cylinder. When magnetic field is not strong it does not penetrate (1), then, if it is increased, magnetic field penetrates at edges (2), and finally we found an intermediate state where magnetic field passes through normal regions (3). Image taken from [32]. In (b) the intermediate state we observed in a disk of Ta at H = 34 mT. In (c) the intermediate mixed state observed in Nb at H = 110 mT. Both images are taken by Bitter decoration from [33].

1.2.3 Intermediate and intermediate mixed state

Intermediate state

Let us consider a superconducting sphere of a type I superconductor in the presence of an external magnetic field, H_a. As magnetic field lines are always tangential to the surface, depending on the place, the density of flux lines will change. In the top of the sphere, the magnetic field is zero, however, in the equator the magnetic field is maximum. The equation of the tangential component of the magnetic field in the sphere is

$$H_{surface} = \frac{3}{2} H_a sin\theta \tag{1.20}$$

When the field reaches $\frac{2}{3}H_c$, the magnetic field at the surface of the sphere will be larger than H_c, forcing the transition of a surface region to the normal state. This, however, will modify the flux distribution, because the flux needs no longer to be expelled up to the surface. Further increasing the magnetic field leads to the establishment of normal regions, in which the local magnetic field is exactly H_c, and

superconducting regions in which the magnetic field is expelled.

When the magnetic field is below $\frac{2}{3}H_c$ all the sphere will be in Meissner state and if the magnetic field is stronger than H_c the sample will be normal. Therefore, in the region of $\frac{2}{3}H_c<H_a<H_c$ the magnetic field enters the sample. In the normal regions inside the sample, the magnetic field is H_c and in the superconducting regions, the magnetic field is zero.

The shape of the normal and superconducting regions in the intermediate state depends on the geometry of the superconducting specimen. For a superconductor of arbitrary shape, we can write

$$H_{surface} = \frac{H_a}{1-n} \tag{1.21}$$

Being n, a shape dependant demagnetization factor. For example, for a sphere $n=\frac{2}{3}$, for cylinder in a parallel field, n=0, and for a thin plate in perpendicular field, n=1. This means, that the intermediate state in a thin plate will exist starting from a small magnetic field (Fig. 1.10a). In Fig. 1.10b we show an intermediate state in tantalum type I superconductor where black regions are in the superconducting state [33]. The distribution of normal and superconducting regions is very complex to predict and depends on the actual value of H_c at each position of the sample. Small variations of the sample properties can strongly influence the field distribution. Generally, however, one observes rather large normal and superconducting regions interspersed.

Intermediate Mixed state

A similar effect happens in the type II superconductors below H_{c1}. In this case instead of macroscopic regions of superconducting and normal material, vortex lattice domains are created. There are experiments showing that the inter-vortex distance in the intermediate mixed state (IMS) domains is equivalent to a distance corresponding to H_{c1} [34]. Furthermore, the area occupied by the zero induction regions decreases linearly with the magnetic field, until the applied magnetic field is equal to H_{c1} where the mixed state is found. Fig. 1.10c shows superconducting grey regions, and vortex lattice domains as two fingers at the top right of the figure. The sample is Nb and the image is taken from [33].

1.2.4 Vortex dynamics

One of the main characteristics of the superconducting state, is the null electrical resistance. In the mixed state, with the appearance of vortices, this may change. When a current $\boldsymbol{J}$ is applied along the surface, vortices will experience a Lorentz force as:

$$\boldsymbol{F}_L = \boldsymbol{J} \times \boldsymbol{B} \tag{1.22}$$

The pinning force, F_p, acts against the Lorentz force. When vortices depin, the

Lorentz force is compensated by a dissipative viscous force, providing a constant velocity for vortex motion in between pinning centres.

Critical state

We have discussed the dynamics of vortices as a consequence of an electrical current. The Lorentz force is not only produced by an external current but, also, a current can appear in the the superconductor when the magnetic field is changed [35].

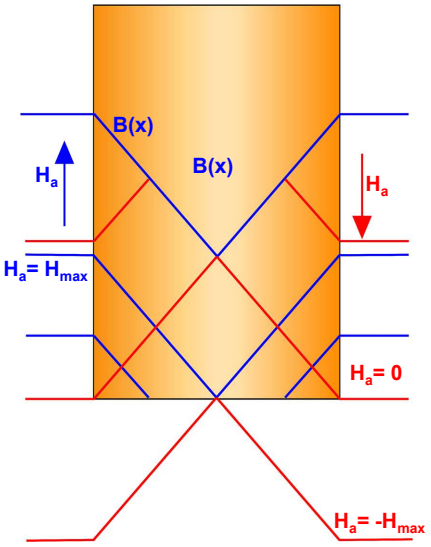

Figure 1.11: Magnetization curves when the field is increased (blue) and decreased (red). H_{max} is the maximum applied field that can be screened at the midplane.

Let us assume an infinite superconducting slab with thickness d, immersed in a magnetic field smaller than H_{c1}. When magnetic field increases above H_{c1}, vortices will enter the sample from the borders. Due to surface barriers (Bean-Livinston barrier) and pinning, there will be a magnetic field gradient from the borders to the center of the slab that induces a perpendicular current as

$$J_\theta = \frac{c}{4\pi}\frac{dH}{dr} \tag{1.23}$$

This current will create a Lorentz force towards the center of the sample. Therefore, vortices will move to the center to reduce the magnetic field gradient until

$$F = \frac{J_\theta H}{c} < F_p \tag{1.24}$$

creating the critical state. C.P. Bean assumed that in a random isotropic pinning potential, $\frac{dB}{dr}$ = constant (Fig. 1.11). In this case we can observe how the magnetic field changes with r.

1.3 Iron based superconductors

In conventional superconductors the pairing mechanism is due to attractive electron interaction mediated by phonons. However, the discovery of cuprate superconductors by Bernorz and Muller in 1986 completely changed this paradigm [36]. Soon after the discovery, it was clear that the paring mechanism leading to the high critical temperature (HT_c) in the cuprates was different from the BCS mechanism found in conventional superconductors.

Another breakthrough in superconductivity was the discovery of iron based superconductors (FeBSCs). LaFePO was the first compound discovered by Kamihara [37] in 2006 with T_c=4 K, but it was in 2008 from the discovery of $LaFeAsO_{1-x}F_x$ by Kamihara [38] with T_c=26 K where research in FeBSCs was boosted. It was very surprising to observe superconductivity in materials that contain iron. Iron is a magnetic material and the idea of magnetism and superconductivity as competing phenomena was very accepted.

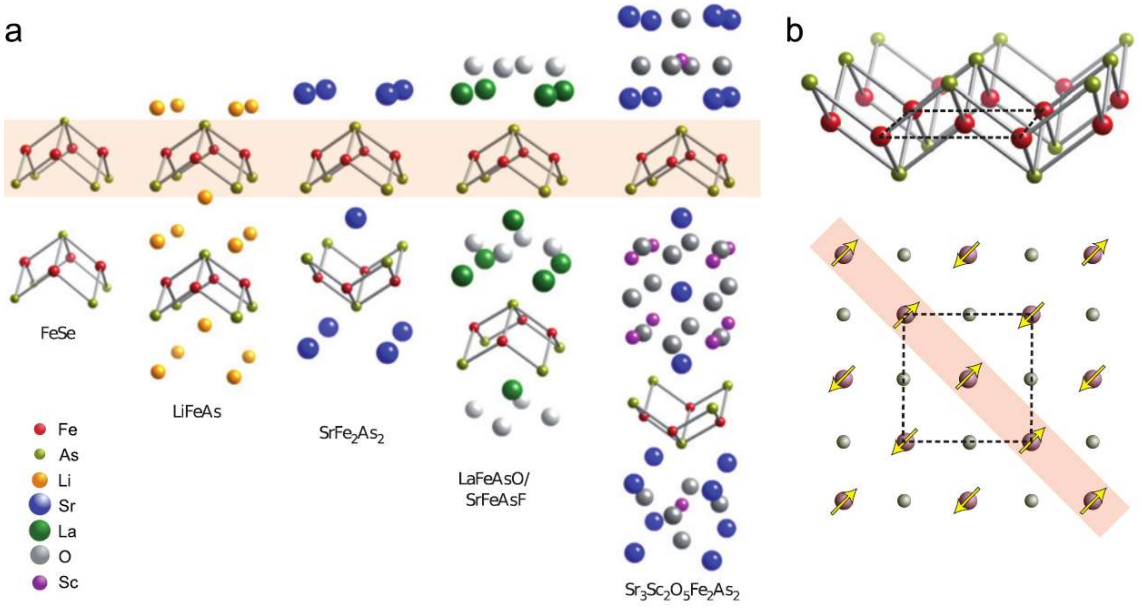

Figure 1.12: (a) Crystal structures of the different families of iron pnictides. Fe-As planes are highlighted in red, taken from [39]. In top (b), a detailed view of the Fe-As layer. In bottom (b) we show the unit cell of Fe-As layer with the spin of Fe atoms represented with yellow arrows.

1.3.1 Crystal structures

There are a large and increasing number of FeBSCs with different crystals structures. The crystal structure includes layers formed by iron atoms with chalcogens (Ch) and pnictogens (Pn) in group 15 and 16 of the periodic table [40]. Examples of iron pnictides are the so called 111 systems as LiFeAs, 122 systems as XFe_2As_2 (where X is an alkaline earth metal), 1111 systems as RFeAsO (where R is a rare earth

metal) and 1144 as $YXFe_4As_4$ where X is an alkaline earth metal (Ca, Ba..) and Y an alakali metal (K,Rb...). Iron chalcogenides are found as 11 systems in FeSe or FeTe and 122 systems. In Fig. 1.12a we show some examples of these different crystal structures taken from [39].

1.3.2 Generic phase diagram

Fig. 1.13 shows the generic phase diagram of iron based superconductors. The parent compounds at low temperatures are usually antiferromagnetic (AFM), showing most often stripe-like spin density wave (SSDW) AFM order. In the SSDW state, the spins of Fe atoms are parallel along one crystalline direction and antiparallel to the other (Fig. 1.12b). The crystalline structure of the parent compounds at low temperatures is orthorhombic, and they present an electronic order that also breaks the C4 symmetry, called nematic order. When introducing doping or pressure, these orders disappear and superconductivity emerges with maximum T_c close to the point where these orders go to zero at zero temperature. In some materials, the magnetic, structural and nematic transition remained coupled with same T_c across the phase diagram, but in others they split given rise to different T_{cs}. Most often, there is a coexistence region between the superconducting and AFM/nematic states although it is not yet clear whether this occurs through phase separation or microscopic coexistence [40].

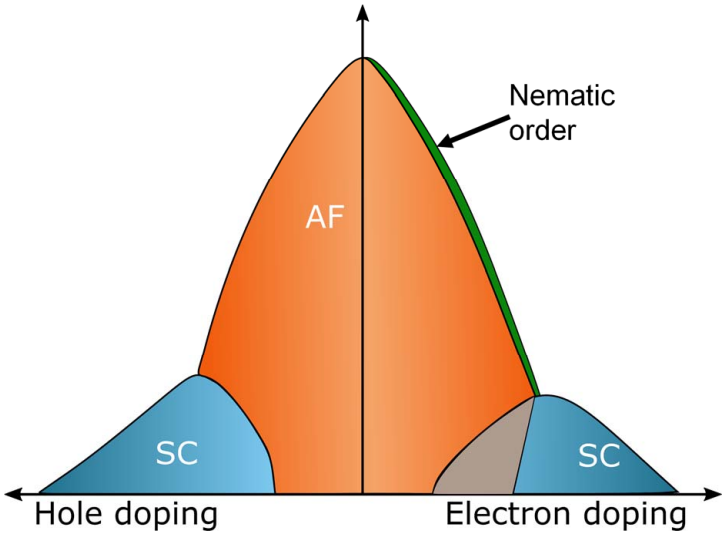

Figure 1.13: Generic temperature vs doping phase diagram for FeBSC. Parent compound usually presents an antiferromagnetic order (orange). When introducing electron or hole doping, superconductivity emerges as a dome where both superconductivity and magnetism can coexist. Green region shows the presence of nematic order.

The 1111 family was the first discovered FeBSC crystals, with very high critical temperatures. Some materials are $LaO_{1-x}F_xFeAs$ [38] or $NdFeAsO_{1-y}$ with a T_c =

54 K. These materials are very hard to study as samples are small and surfaces show different properties from the bulk, making it difficult to use surface sensitive techniques such as STM or angle resolved photoemission (ARPES).

The 111 family has very interesting compounds as LiFeAs. LiFeAs is a stoichiometric compound with a T_c=18 K [41]. This material does not show AFM order. The superconducting gap and vortex lattice have been characterized in detail using STM [42].

The 11 family includes only chalcogenides as FeAs does not crystalize. FeSe presents vortex nemacity and monolayer of this material has the highest T_c among FeBSC with a T_c=100 K [43].

The 122 family has been widely studied, in particular, the series with parent compound $BaFe_2As_2$ [44]. The phase diagram presents a competition and coexistence of magnetism and superconductivity. For instance, $Ba_xK_{1-x}Fe_2As_2$ when x=1 is antiferromagnetic and non superconducting, but with x=0, it is an stoichiometric superconductor with T_c=4 K, a critical temperature much lower than this found in the optimally doped composition with x=0.5 (T_c=38 K).

There are a lot of possible combinations of compounds, offering a big playground to study the iron based superconductivity. As we will discuss in Chapter 3, 122 family is highly linked to the new 1144 family.

1.3.3 Fermi surface

FeBSCs are multiband systems. Several bands cross the Fermi level producing at least three hole pockets at the center of the Brillouin zone (Γ point) and two electron pockets at the edge of the Brillouin zone (M-point). The Fermi surface is quasi-two dimensional with the c-axis warping increasing in the 122 compounds with respect to this in the 1111 compounds.

Furthermore, the contribution of the electronic states near the Fermi surface mainly comes by the three orbitals d_{xy}, d_{yz}, d_{xz} and charges carriers hop between Fe atoms through a Pn or Ch site [45, 38].

In the AFM state the Fermi surface reconstructs due to the doubling of the unit cell and the corresponding reduction of the Brillouin zone in the magnetic state. This doubling produces a band folding along the direction of the AFM vector in reciprocal space (Fig. 1.14 a). The electron bands at M are translated (folded) to the Γ point. This produces a crossing between hole-like and electron-like bands (Fig. 1.14b). In the simplest case, where the shape and size of electron and hole bands are the same, the crossing is produced exactly at the Fermi level (Fig. 1.14c). The bands will then hybridize and a gap will appear at the Fermi level. This would make the FS to disappear and the material would become insulating. However, electron and hole pockets are not usually identical, and folding produces a reduced FS formed by small pockets [46].

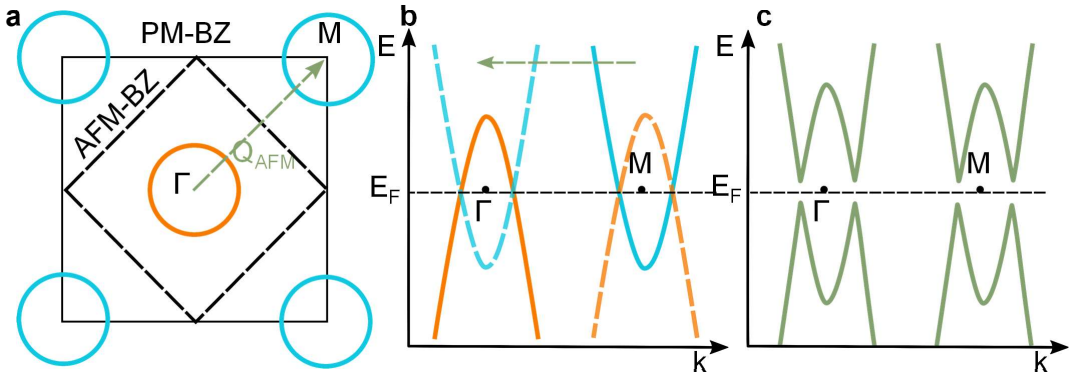

Figure 1.14: In (a), 2D-Fermi surface of paramagnetic state. Continuous line is the Brillouin zone (BZ) in the paramagnetic state and dashed line is the BZ in the AFM state. (b), Bandstructure energy-momentum curves of the paramagnetic state (continuous lines) and in dashed line, we show the folding of the band at M to the Γ point. (c), final result of the folded band structure in the antiferromagnetic state [46].

1.3.4 Order parameter

The symmetry of the order parameter and the pairing interaction is still unknown for FeBSC (Fig. 1.15). There are different proposals, and the most common ones are s± pairing, s_{++} symmetry or d-wave [40]. The s±, is favoured by interband spin fluctuations. s_{++}, could be mediated by an attractive interband interaction, because of nematic fluctuations. d -wave symmetry, could be related for intraband repulsive interactions [47].

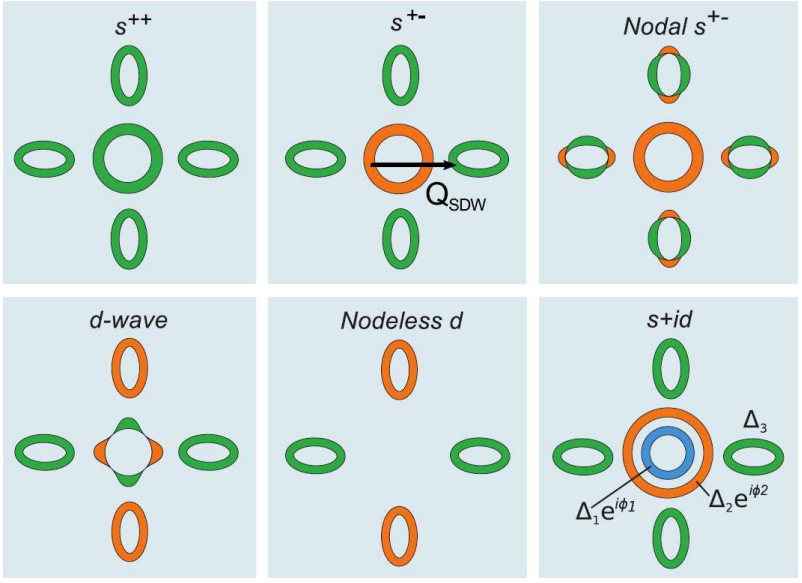

Figure 1.15: Sketch of different proposed possibilities for the pairing symmetry. The sign associated to the phase of the order parameter is represented by the color. Taken from [40].

Now, s± symmetry is the more likely candidate. In this context, spin fluctuations with the AFM SSDW vector joining hole and electron pockets will favor the interpocket interaction.

1.4 Scope

During the following chapters I am going to review the work I have done during my PhD thesis. In chapter 2, I am going to address the experimental and computational methods we have used to obtained the results that will be presented in the following chapters. I have used low temperature STM under applied magnetic fields. STM allows to directly measured the spatial changes of the density of states, giving access to the visualization of the vortex lattice or the determination of the electronic band structure. Low temperatures provide the needed energy resolution and magnetic field is used as a tuning parameter to get access to the different vortex phases. In particular, I have designed and constructed an STM for high magnetic fields from scratch. Furthermore, I will review the techniques we have developed to handle and to treat spectroscopic data to get information on the superconducting gap, bandstructure and vortex lattice of the studied materials.

In chapter 3, I will discuss the results I have obtained in a FeBSC compound that belong to the recently discovered family of 1144 FeBSCs. This family was discovered in 2016 [48] and in particular, an intense work has been done in $CaKFe_4As_4$. $CaKFe_4As_4$ is an optimally doped stoichiometric superconductor with T_c=38 K being this the largest T_c for an stoichiometric FeBSCs. Previous studies have reported two band superconductivity consistent with s± paring and a Fermi surface in agreement with its paramagnetic state. In this thesis, I have investigated the properties of this material when Fe is substituted by Ni. Macroscopic measurements have reported the appearance of a unique Hedgehog antiferromagnetic order. Here, I will provide the first microscopic characterization of superconductivity in the presence of Hedgehog AFM order.

In chapter 4, I will describe and characterize a new arrangement of the vortex lattice at very low fields that has not been previously reported. Measurements of the vortex lattice at low fields have been done in the material β-Bi_2Pd using magnetic scanning probes by groups at ICMM-CSIC in Madrid and Weizmann Institute of Science in Israel. We have characterized the structural properties and found new features never observed before in vortex physics but so in other interacting systems in the regime of low interactions such as gels.

In chapter 5, I focus on the behaviour of the vortex lattice at high magnetic fields. Recently a new ordering named hyperuniformity has been theoretically proposed. Here, I will study vortex lattices from different systems such as W-based thin film, Co-$NbSe_2$, or stoichiometric and Ni-doped $CaKFe_4As_4$ at different magnetic fields. We will show how we can distinguish a random disorder from a hyperuniform disorder in reciprocal and real space. Finally, I will discuss if vortex lattice is compatible with hyperuniformity.

Lastly, in chapter 6, I will study vortex creep at low temperatures using data taken from previous STM works in 2H-$NbSe_2$ with tilted fields. Here, I will report a different creep motion that can only appears in anisotropic superconductors under tilted magnetic fields. I will discuss the tools I have developed in order to being able to follow individual vortices from consecutive images, and different parameters we can obtain with them. Finally, we will compare the experimental results with a theoretical model made by R. Willa.

2 | Experimental Methods

The STM is a very powerful tool to study superconductors and other materials, enabling precise measurements of the electronic bandstructure and visualization of vortex lattices and other electronic patterns. There are few STM experiments working at cryogenic temperatures and high magnetic fields. Improvements in their design are making these devices more versatile and handy. In this thesis, I have contributed to this effort by building an STM whose lateral size has been reduced. Furthermore, STM produces huge amounts of data in the form of tunnelling conductance curves as a function of the position. These data provide images of the vortex lattice and images that can be used to obtain the electronic bandstructure. Extracting this information is not always straightforward. I have developed software, now used by other people in the laboratory, to handle the data and obtain vortex lattice positions, correlation functions and the energy dependence of the electronic bandstructure.

During this PhD thesis, I have been working in setting up a new STM for magnetic fields as high as 17 T with a helium 4 cryostat capable of reaching 4 K. I designed the microscope, achieving improvements over previous designs, and used it to collect results. I have also participated in explaining a number of experiments and developing the related software, mostly in the superconducting density of states and vortex lattice. To make measurements in superconducting materials, I use a STM that cools to lower temperatures for which I used a dilution refrigerator. In this chapter, I will first describe the microscope I set up. Then, I will describe the dilution refrigerator and the three axis coil. Furthermore, I will explain a few elements of the methods and programs I developed to work with the results obtained in STM.

2.1 Cooling and high magnetic fields: liquid helium, dilution refrigerator and superconducting coils

2.1.1 Superconducting magnets

A superconducting magnet consists of a wound coil of superconducting wire inserted in a superinsulated vacuum vessel, called cryostat. In Fig. 2.1a we can see a drawing of the cryostat used in this PhD. The liquid helium part of the cryostat consists of a container with a small diameter at the bottom, just with enough space for the superconducting coil to be inserted in, and a large belly. This design eliminates dead

volumes of liquid helium surrounding the coil. The coil should be always immersed in liquid Helium. The measurement device in inserted from the top inside the hole of the superconducting magnet. The measurement device hangs from the top, as well as the superconducting magnet.

One problem we encountered is that the suspension system needed strong reinforcement, because it produced vibrations in the measurement device. We thus designed a system to clamp the superconducting coil to the inner side of the helium container. The latter consists of tubes, which considerably improved the rigidity of the whole system and reduced the vibrations. The support is shown in Fig. 2.1b.

Let us mention that our 17 T superconducting coil consists of two concentric coils separated by an Aluminum tube (Fig. 2.1c). The outer coil is made with a superconductor with smaller critical field and current (NbTi) and the inner one with a superconducting material with very large critical field and current ($NbSn_3$). The coil is protected from overvoltage by a set of diodes that are located at ambient temperature and connected through copper rods to the coil. In case of a quench, there are a series of low value high power resistors designed to absorb partially the heat due to the normal current.

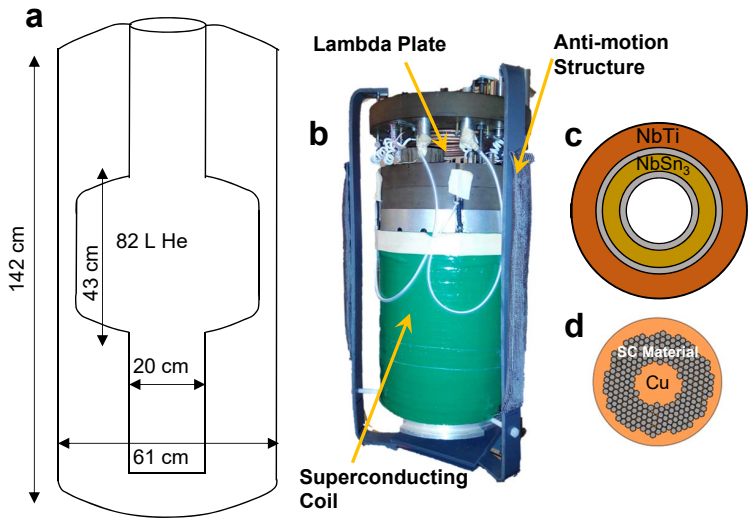

Figure 2.1: (a), Scheme of the cryostat. (b), Photograph of the superconducting magnet with the structure built to reduce vibrations. (c), Top view of the superconducting coil with two different superconducting cables and (d), scheme of a section of the superconducting cable.

Our superconducting coil can provide magnetic fields up to 15 T at 4.2 K and up to 17 T at 2 K (Fig. 2.1b). In order to be able to have a persistent field, the coil is shunted by a superconducting wire located far from the high field region. The shunt has a heater. When we want to charge the coil, we heat the shunt so that it becomes normal. The applied current flows through the coil and remains trapped in there when the heater is switched off.

On the top of the coil, we have a serpentine of copper with a needle valve. We can pump helium through the needle valve and the serpentine. The temperature of

the bath decreases then to 2 K and, above the serpentine, the temperature increases to 4.2 K, or the temperature at the pressure of the liquid-gas interface. That way, we can cool to 2 K and refill the helium bath without stopping the pump.

2.1.2 Dilution refrigerator

A dilution refrigerator has enormous advantages for an experiment as STM. It can cool down to temperatures of around tens of milikelvins. The thermal noise in these conditions is minimum, of the order of k_BT, and allow us to have a perfect cryogenic vacuum that maintains a clean surface and tunnelling barrier. Furthermore, a dilution fridge is very stable and the experiment can be running for months while a He refill is required only once or twice a week.

The principle of operation of a dilution refrigerator has been previously explained in many references [49, 50] and it is based on the quantum properties of ^{3}He and ^{4}He. In Fig. 2.2 we show a scheme of the dilution refrigerator. It consists of different stages. First, the mixture is injected through a tube with a pressure of few hundred millibar to the 1K-pot at T=1.2 K. The 1K-pot is a small container that is connected to the outer helium bath and where we can pump ^{4}He to reach temperatures of about 1 K. As the liquefaction temperature of the mixture is below 4.2 K, the temperature of liquid helium, the 1K-pot is a needed requisite to be able to condense the mixture. The liquefied mixture, is continuously cooled with heat exchangers. Heat exchangers play an important role in the cooling power of the dilution refrigerator, using the enthalpy of the outgoing mixture. Finally the mixture reaches the mixing chamber, the coldest part of the dilution fridge. Here, phase separation occurs where a concentrated ^{3}He phase is floating over a dilute ^{3}He phase. The mixing chamber is connected to the still (going through the heat exchangers). In the still, the liquid-gas interface forms. The difference of temperature between the mixing chamber and the still generates a difference of equilibrium concentrations of ^{3}He. Furthermore, a pump is connected to the still. Due to the vapour pressure differences at the still, of ^{4}He and ^{3}He, most of the gas that goes out is pure ^{3}He. This perturbs the equilibrium ^{3}He concentration in the still and generates an osmotic pressure difference between the mixing chamber and the still. This pressure gradient drives the ^{3}He atoms from the mixing chamber to the still. Thus, ^{3}He atoms are forced to cross the boundary between the concentrated and the dilute phase in the mixing chamber. The process of passing atoms of ^{3}He from the concentrated phase to the dilute phase is an endothermic process that provides to the dilution fridge its cooling power. Pumped ^{3}He atoms from the still are injected again, in order to repeat the process.

In our case, we use a standard dilution refrigerator Oxford-Kelvinox MX100, with base temperature of 25 mK and 100μW cooling power at 100 mK. The dilution refrigerator is closed inside an inner vacuum chamber made of Al. The inner vacuum chamber (IVC) is closed by a conventional indium seal and immersed in a He liquid bath cryostat. The liquid helium volume in the cryostat is between 15 L and 80 L. The lower limit is imposed by the 1K-pot. The capillary must be immersed always in the He bath and when He level is around 1 K-pot capillary height a liquid Helium

transfer is done. In our cryostat, the transfer is carried out every 4-5 days.

The temperature was controlled by a LakeShore370 [51]. Ruthenium Oxide RX-202A sensors [52] were used in the 1K-Pot, the still and the mixing chamber stages. Furthermore, an additional sensor is located on the STM holder. As a heater a wire wound is used in the mixing chamber in order to control temperature.

Thermometry and STM signal cables are soldered from the electrical vacuum feed to a connector. A crucial point in low temperature experiments is the correct thermalisation of the wiring. The cables start at room temperature outside of the experiment and they are thermalised at 4 stages inside the dilution fridge. Each stage consists on two gold plated copper plates that clamp the wires.

Also for STM it is crucial to reduce mechanic noise, so pumps are in a different room. Furthermore, the tubes connecting the pumps with the experiment go through a sandbox, reducing the vibrations coming from the pumps.

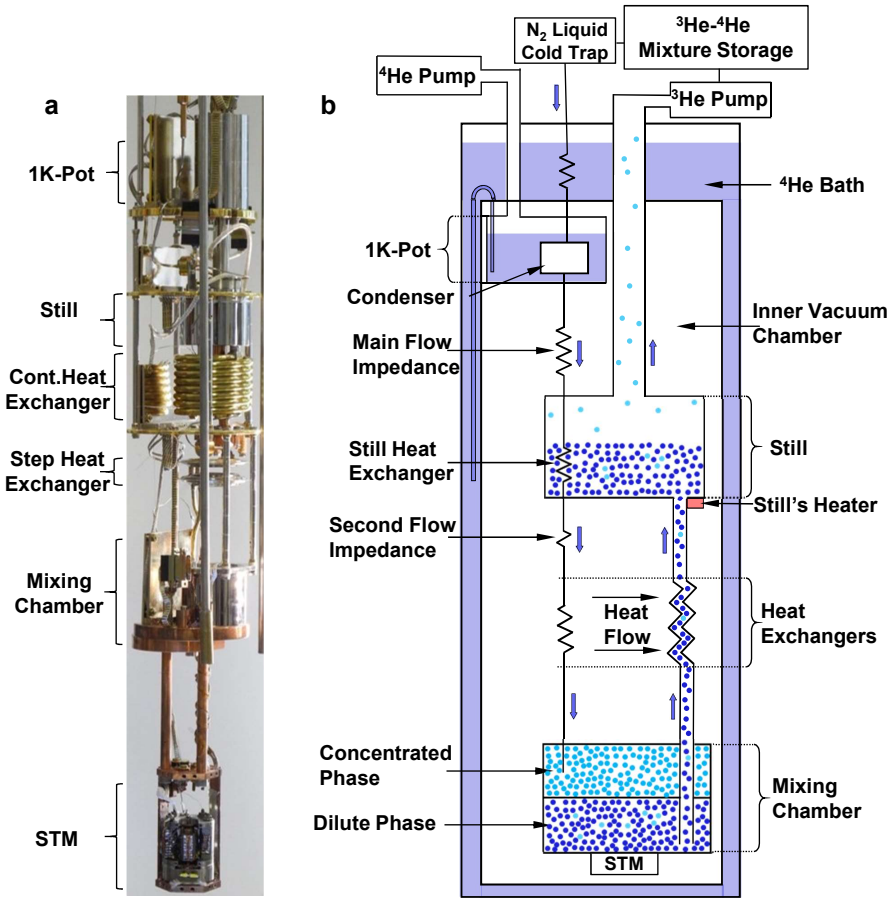

Figure 2.2: Photograph (a) and scheme (b) of a dilution refrigerator.

2.1.3 3-Axis Superconducting Magnet

The dilution refrigerator set-up has a home-made three axis magnet consisting on five coils mounted in an Al cage [53]. One solenoid is for the z-axis and the others are for the x-y plane as split coils. A maximum of 5 T in the z direction is obtained and 1.2 T for the x-y plane. Therefore, full three dimensional capabilities are achieved for magnetic fields below 1.2 T. The magnetic field has been measured along all the coils finding an homogeneous field of 0.2% and 1% within a sphere of 0.5 cm along the z-axis and in-plane axis respectively.

The three coils have each their own persistent mode switch. This allows us to work independently in the three directions. The magnet is energised with a power supply with three current sources. A commuted internal commercial stage of 5 V and 100 A is followed by a voltage to current converter. The power supply was designed and built by SEGAINVEX [54].

In order to reduce unused liquid helium volume around the magnet, the remaining free space has been filled using Polyvinyl Chloride (PVC).

During the last year of the thesis we moved this whole system into a new location with anti-vibrational floor. We had to relocate and adapt all the different parts that this experiment contains such as pumps, pipes, the cryostat, the dilution fridge refrigerator, the dilution control panel with the ^{3}He-^{4}He mixture storage and the control electronics.

2.2 STM at high magnetic fields

Scanning tunnelling microscope was invented by Binnig and Rohrer at IBM in Zurich [55]. In a STM, we use the precise positioning capabilities of piezoelectrics and the properties of electron tunneling through vacuum between a flat electrode and an atomically sharp tip. It allows the study of both surface and electronic properties near the Fermi level with great resolution. Additionally, the STM is a very adaptable tool depending on the experimental conditions. For this thesis we have developed a STM for high magnetic fields up to 17 T.

The STM has a piezotube that allows making scans at atomic sizes. To be able to operate the piezotube, we need a series of devices. First, a device allowing to move macroscopic (mm) distances and bring a tip on top of a sample. A device allowing to change macroscopically the position (mm scale) of the tip over the sample should be also there. Furthermore, one should be able to clean and sharpen the tip in-situ and to prepare the sample, so as to get clean surfaces without debris or oxides. Our approach has been to include all these devices in a single set-up, which is cooled and inserted in the magnet. This permits eliminating long manipulators and other ancillary apparatus that are often used in other systems.

2.2.1 Construction of an STM at high magnetic fields

In order to get a more intense magnetic field, the cross-sectional diameter of the coil is usually reduced. Previous designs of the STM were too large to fit inside the superconducting coil of 17 T. Having so many devices into a single setup is quite difficult, which usually increases the size of the microscope to dimensions that are not compatible with superconducting coils. Therefore, during this thesis we designed and constructed an STM for working at high magnetic fields. First, we reduce the size of the STM from 50 mm to 30 mm (Fig. 2.3a). Second, the whole STM is constructed with non-magnetic materials. The STM uses Ti pieces constructed by SEGAINVEX [54]. Screws, nuts and washers are made from brass; springs are made from CuBe and the sample holder from Cu. We hereby distinguish between three parts in a STM, (Fig. 2.3): Body (b), Head (c) and Base (d).

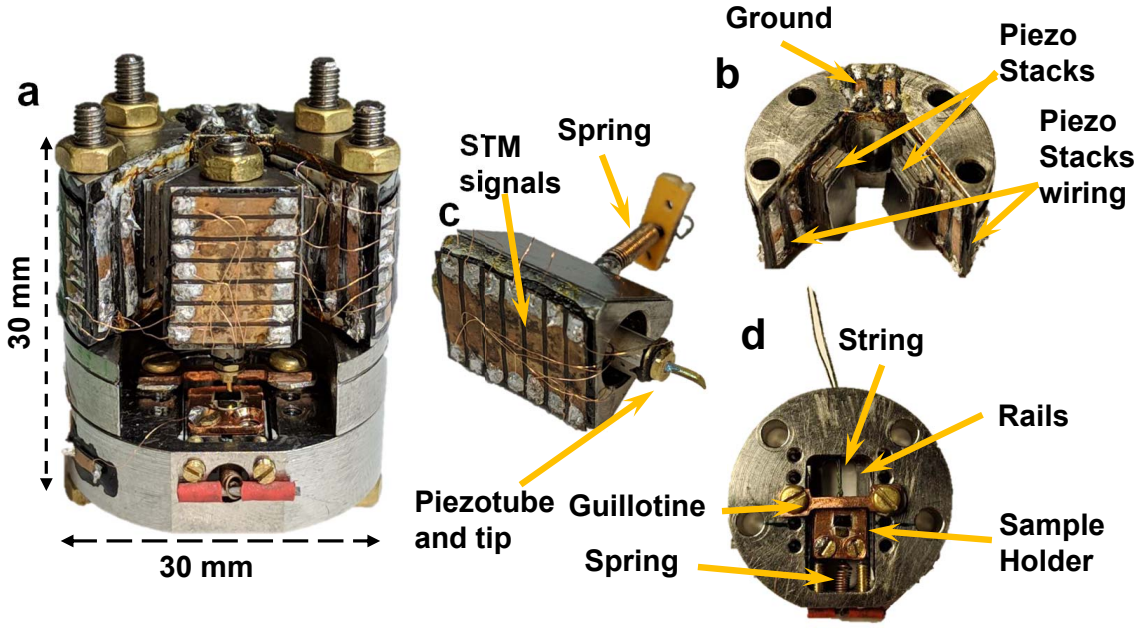

Figure 2.3: (a), Image of the assembled STM. In (b) a photography of the Body. In (c), a photo of the Head and in (d) the Base.

Base

The bottom part of the STM is the base (Fig. 2.3d). The sample holder is screwed on a piece (slider) that can slide in a plane perpendicular to the tip along the rails of the base. Two samples are glued to the sample holder, the sample we want to measure for the experiment and a sample of the same material of the tip, typically gold. This way, we can clean the tip *in situ*. Furthemore, in the sample holder we solder a copper cable that serves to apply the bias voltage to the sample.

The sample holder is screwed on a piece that can slide in a plane perpendicular to the tip.

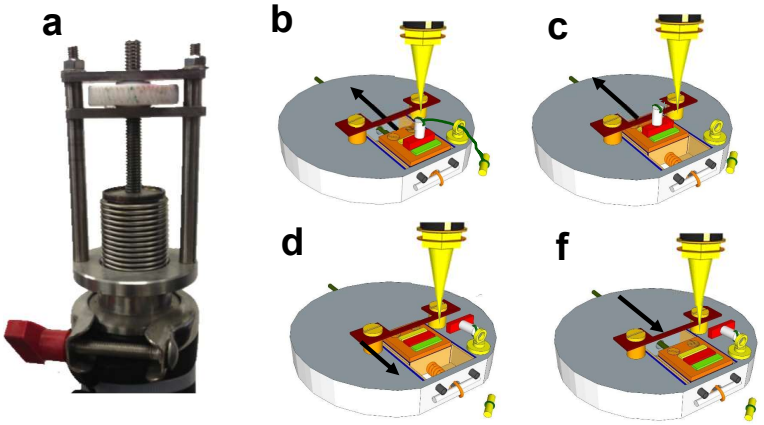

Figure 2.4: In (a) we show the top screw outside the cryostat. In (b-f) we show the process to exfoliate a sample. In (b), an alumina is glued to the sample. The sampleholder is pulled with the top screw (b-c) until the alumina touches the guillotine and the sample cleaves. A counterweight is additionally used to remove the alumina with the top part of the sample from the tip's way [56].

To move the slider along its rails, we use a thread tied to the slider in one side. At the other end, the thread is knotted to a piano string that is soldered to a fixed screwed in the upper part of the dewar (Fig. 2.4a). By screwing the top screw at the top of the dewar, the piano wire tenses pulling the slider backwards. In order to move in the reverse direction a spring is attached to the front of the slider. When the slider is in the front part, the spring is in its equilibrium position. When the top screw is unscrewed, tension in the piano wire is liberated and the spring pulls the slider forward. Besides, a spring is attached connecting the slider with the bottom part of the base. This spring gives stability to the slider and maintains the slider completely flat to the surface of the rail when is being pulled with the string. It is not easy to move a sample holder *in-situ* at low temperatures. The motion should not create heat, for which the slider should be lubricated. Furthermore, there should be enough space to move, but the slider should be firmly attached to the rest of the microscope. To solve these issues, the sample holder is surrounded by alumina sheets that are polished and covered with graphite as a lubricant. The sample holder is attached to the bottom and to one side using helicoidal springs, and it is built in such a way as to minimise the space between the holder and the rail. Both springs are made of a non magnetic material (CuBe).

This technique is very useful for a low temperature STM. First, we are able to change from one sample to another for cleaning the tip. Second, we can change macroscopically to other areas in the same sample with nanometric accuracy. Surfaces of the samples are not always perfect, and with this technique we maximized our chances to be able to find appropriate fields of view, where we obtain clean tunnelling conditions. Third, we can cleave our samples *in situ* having pristine surfaces uncontaminated at cryogenic vacuum at liquid helium temperature.

Depending on the sample, the cleavage process can be by exfoliation or breaking [56]. The exfoliation method is used for layered samples. We glue a piece of alumina

on top of the sample. The piece of alumina is large enough so that it will collide with another piece that acts as a guillotine when we slide the sample holder along the rail. (Fig. 2.4b). When the experiment is running, the slider is moved backwards with the screw and the alumina crashes with the guillotine (Fig. 2.4c). As the glue between alumina and surface is stronger than interlayer forces, the sample is exfoliated (Fig. 2.4d). Furthermore, in order to remove the remaining part out of the sample holder, a counterweight is glued to the alumina, to remove the exfoliated part at the bottom of the inner vacuum chamber (Fig. 2.4f). We used this method in the cleaving process of Ni-doped $CaKFe_4As_4$. In samples that are too hard, so that the glue breaks instead of the sample, we can use a slightly modified method. Then, we need however a long sample that breaks when touching the guillotine. This is somewhat trickier, but works in samples that can be conditioned into long needle like pieces.

Head

The head of the STM contains the piezotube and the tip (Fig. 2.3c). The head is attached to the body with a CuBe spring. The tension must be strong enough to maintain the head fixed, but flexible enough to be able to move the head vertically with the piezostacks.

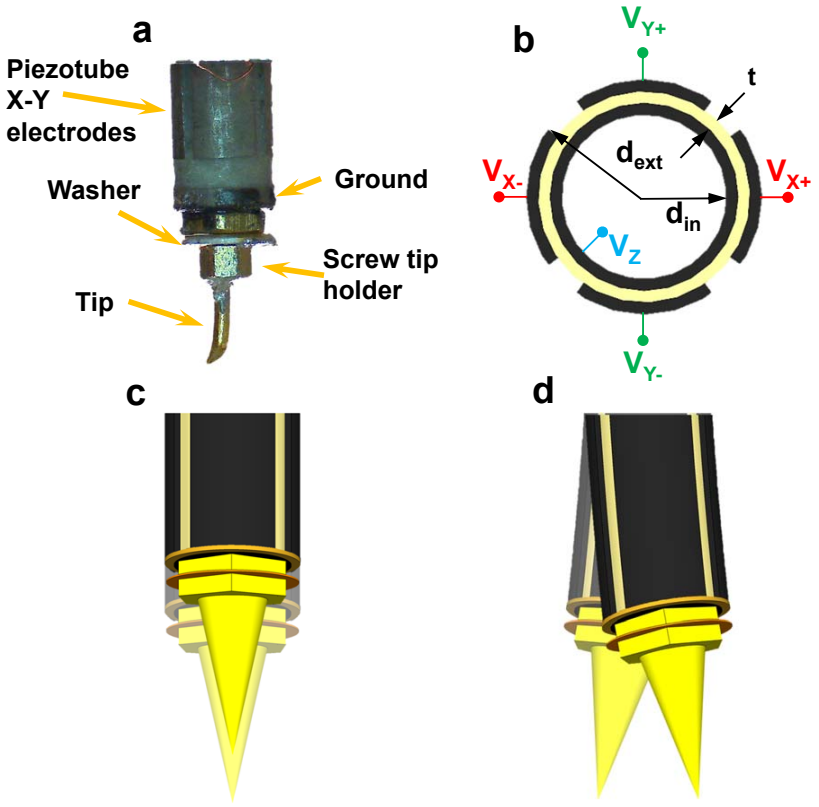

Figure 2.5: (a), Picture of the piezotube and the tip. In (b) we show a section of the piezotube. (c) shows the vertical motion of the piezotube and (d) the in plane X-Y motion of the piezotube.

The piezotube is a piezoelectric tube that goes from the interior of the head until the exterior as shown in Fig. 2.3c. The piezotube has 6 separated electrodes. In the exterior, along its length the X-Y electrodes are found (Fig. 2.5a). When a voltage difference is applied between two opposite electrodes, the piezotube will bend along that direction, depending on the sign of the voltage difference. This property provides the X-Y motion (Fig. 2.5d). In the interior, an electrode is found along all the inner piezotube. When a voltage is applied to this electrode, the piezotube stretches or shrinks to control Z motion of the tip (Fig. 2.5c). Furthermore, another electrode exists at the bottom of the piezotube used as ground. The dependence of the motion is determined by:

$$\Delta x[\text{Å}] = y[\text{Å}] = \frac{0.9 d_{31} L^2 V_{x,y}}{d_m t} \qquad \Delta z[\text{Å}] = \frac{d_{31} L V_z}{t} \tag{2.1}$$

For our system we have a range of X and Y of 2 μm and of about 0.3 μm in Z.

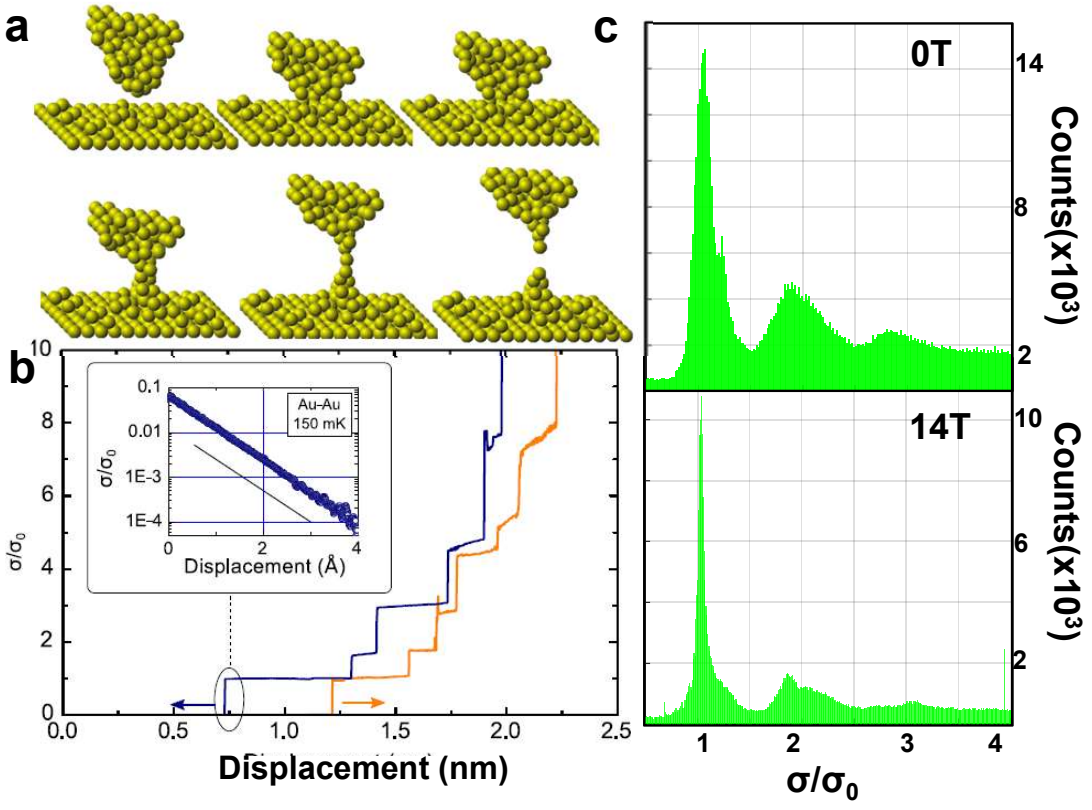

Figure 2.6: (a) and (b) are taken from Guillamon [30]. (a) shows a drawing of the nanoindentation process and (b) the current as a function of distance between tip and sample. The inset shows an exponential fit of the gold workfunction. (c) shows an histogram of conductance values vs distance in gold in the designed STM at 0 T and 14 T. Both of them show almost three peaks at multiples values of σ_0.

The tip is placed at the bottom of the piezotube but it is prepared independently. A gold wire is glued to an screw tip holder of ϕ=1 mm and is then screwed in a nut

glued at the bottom of the piezotube. In between the nut and the screw a washer is collocated to minimise the movements of the tip. A wire is additionally soldered in the washer in order to obtain the tunnelling current signal coming from the tip. The tip is sharpened at the end of the process cutting diagonally with clean scissors.

sharpen the tip. We use a sample made of the same material as the tip and a controlled nanoindentation process (described in [57], see also Fig. 2.6 a and b).

As we discussed before, the motion of the sample holder has many advantages. One of them is the possibility to clean and atomically sharpen the tip. We use a sample made of the same material as the tip and a controlled nanoindentation process (described in [57], see also Fig. 2.6(a-b)). When the displacement is large, the tip is completely crashed into the sample. When we start separating the tip out of the sample, conductance is decreased. The conductance is quantized because the size of the contact between tip and sample is reduced when separating both parts. When only one atom is in between tip and sample we have only one transport channel with the minimum possible conductance of σ_0. Finally, when the junction is completely broken, we are in the tunnelling regime. At this point, it is possible to measure the work function (inset of Fig. 2.6b). At the end of the process, we obtain a clean, atomically sharpened tip. In Fig. 2.6c we show a histogram of several thousands of normalized conductance values by repeating the nanoindentation process thousands of times at 0 T and 14 T. In both magnetic fields, we obtain a clear peak at the last atomic contact, with conductance $\sigma = \sigma_0$.

Body

The body of the STM is the part of the STM that assembles the head and the base (Fig. 2.3b). All connections coming from the base (bias voltage) and the head (tip, X,Y and Z) are centralised in the STM hody. We also find two piezostacks glued to the hody that hold the head steady while allowing a macroscopic control of vertical movement.

The piezostacks consists on 5 piezoelectric plates of size 10 mm x 5 mm x 0.5 mm. Each piezoelectric plate has a shear movement when a voltage difference is applied in both faces of the plate. The shear direction depends on the sign of the voltage difference and in order to have a reference, the plates includes a cut corner (Fig. 2.7a). For our purpose we need that all plates forming a stack move along the same direction. In order to obtain this, we glued the plates as shown in Fig. 2.7a. Every plate is glued to the consecutive plate, with a copper cable in the center of both in order to apply voltage. The motion is controlled with a sawtooth signal (see Fig. 2.7b). At first piezostacks are flat, but as the applied voltage is increased they move synchronously and slowly enough to move also the head due to the friction. To achieve macroscopic motion, we use a stip-slick approach. We apply a sawtooth signal to the piezostack, so that it moves slowly along one direction and very rapidly goes back to the opposite direction. The prism holding the piezotube (Fig. 2.7b-1) moves when motion is slow, sticking to the piezostack, but it slips when motion is fast (Fig. 2.7b-2). The mechanics behind this effect are rather complex and depends on the properties of the surfaces, which must be conditioned in such a way as to

obtain slip within the timescale of the fast motion of the piezostack. The spring that holds the moving part is an important element to achieve this. The contact between the piezostacks and the head is with alumina painted with graphite. We call this motion as Z'.

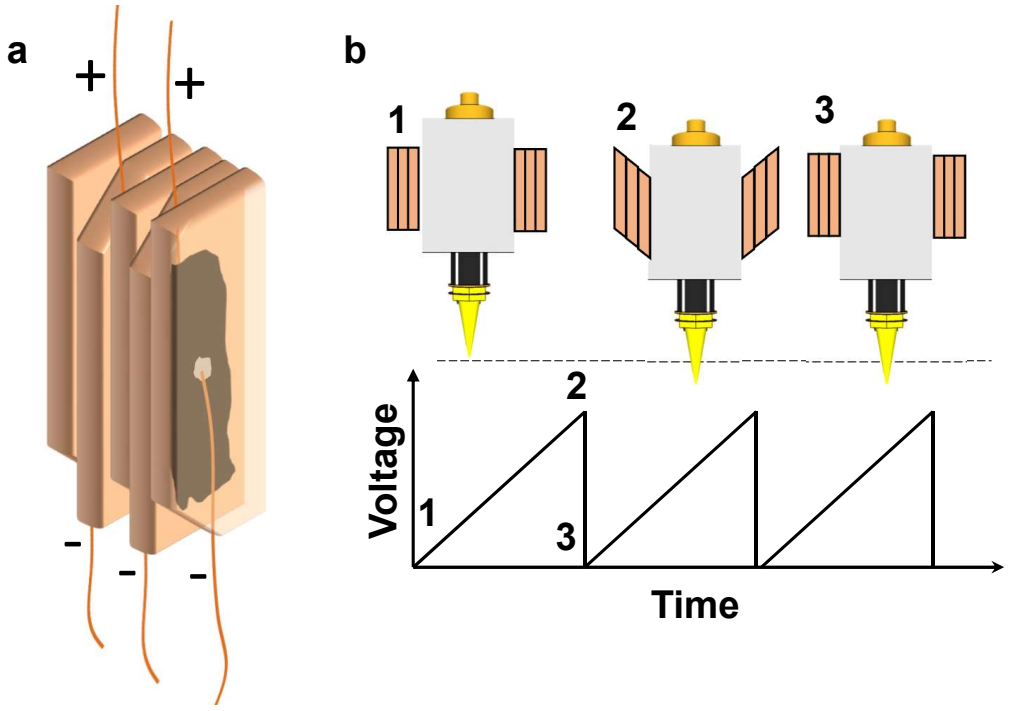

Figure 2.7: In (a) we show how each plate is glued to the consecutive one. They are ordered alternating the cut corner up and down. In between both plates a cable is set to apply a voltage difference and move the head up or down. In (b), we show an schematic picture of the Z' movement of the STM. The saw tooth signal of bottom, is sent to the piezostacks moving up or down the head following the three steps marked in the picture.

Z' motion is very useful to approach the tip macroscopically to the sample faster and to be able to separate it in order to cleave the sample or move it from one to another sample.

Insert

We have also designed an insert to work at helium temperature. The total length is of 120 cm. It has radiation shields to avoid heating of the He bath from room temperature top parts. In the top plate of the insert there are two connectors of the STM and thermometry wiring. The support system for the STM is attached at the bottom of the insert, so that the sample is placed at the center of the superconducting coil. The support is made of copper to keep an homogeneous temperature in the STM.

The wiring goes from room temperature at the top soldered to an electric vacuum feed to connectors at the STM stage. The wiring is made of twisted pairs inserted

inside a conducting shield. Wires are thermalized by winding them over different copper rods on top the 4.2 K copper plate. We use 0.1 mm thick wires of copper and manganin. Manganin has a lower thermal conductivity and the thermal contact with the top part at room temperature is reduced. Furthermore, manganin cables have a higher resistance filtering the high frequency component of the signal. Therefore, we use manganin cables for the thermometer, and the X, Y and Z signals of the piezotube. For the piezostacks (Z'), voltage and current signals we use copper cables. As the capacity of the piezostack is of a few nF, the use of copper wires minimises the resistance of the circuit and allows for fast motion and ultimately allows the prism to slip from the piezostack. For the bottom part of the insert we use copper twisted pairs wounded along thermalization blocks.

Furthermore, we attached a carbon glass thermometer and a heater to the supporting system. Thermometer is measured with the 4-point contact method. These provide us a full control of the STM temperature.

Control of STM

The STM also needs an electronic and computer control to operate correctly as schematically shown in Fig. 2.8. We create a signal using the computer and send it through an input-output port card (PIO) to a digital to analog converter (DAC). We use a 16 bit DAC. This converts the signal to analogical, and goes through a high-frequency filter and depending on the signal, is divided (bias voltage) or amplified (X,Y,Z and Z'). From the amplifier/divider, the signal is again filtered and goes to the connectors of the cryostat. The input signals (current) does the opposite path. The current comes from the cryostat, then to an analogue to digital converter (ADC), and it is read in the computer. Tunnelling current is of the order of nA. We use an IV converter that converts a nA signal to a voltage of the order of volts. Notice that we do not use here the usual digital signal processing (DSP) of FPGA units that many other STM set-ups use. We prefer to have a full control over the signals we send to our microscope and use direct write ports (PIO) of the computer. There are many industrial computers with these ports nowadays and these can be used Windows operating system. Instead of real time experiments, we thus always send a signal and wait until we receive the answer. In practice, even with the interruptions of Windows, this works extremely fast. Our bandwidth is always limited by the cabling of the cryostat and is not larger than several tens of kHz.

A proportional-integral (PI) feedback control maintains the tunnelling current constant. The tunnelling current is read by the PI and compared with a reference current. Depending on the comparison the PI sends a signal to the Z piezotube in order to stretch or shrink to keep current constant.

The usual way to measure is the following. Starting from the tip macroscopically separated we apply a bias voltage between tip and sample. In order to approach we send a saw-tooth signal to the Z' from the computer that goes to the piezostacks. The tip approaches while the current is read in the computer and the PI controller. As soon as a finite current is detected Z' signal is cut and the feedback control is on.

To move in-plane over the sample we have two different possibilities: positioning and scanning. For positioning the tip in any coordinate of the window, we apply a constant signal to the piezotube, in order to bend it and place it in the chosen point. For the scanning, we send a triangular signal to the piezo in X/Y and a ramp in Y/X. The triangular or the ramp voltage signals are centred around the tip position with an amplitude depending on the chosen scanning window. During the scan the feedback control is always on.

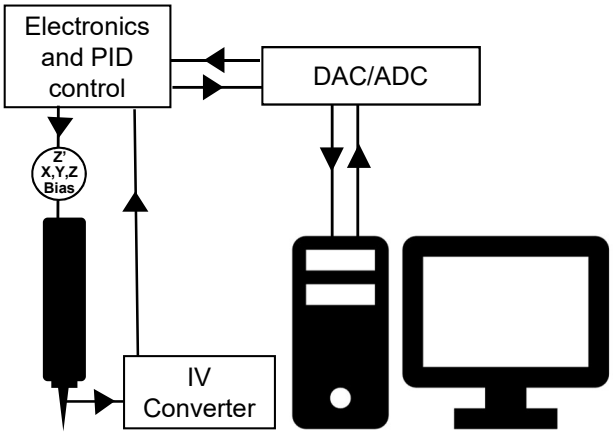

Figure 2.8: Schematic representation of the STM control.

In order to obtain an I-V curve the feedback is switched off and we send a voltage ramp and read the resulting current. Once the ramp is finished the feedback control is switched on automatically. I-Z curves are also taken in the same manner as I-V but ramping the Z signal instead of the bias voltage V.

2.2.2 Principle of operation

Precursor experiments of STM are planar tunnelling junctions. Bardeen applied time dependent perturbation theory to evaluate tunnelling matrix elements to understand tunnelling junction experiments [58]. The overlap of the wavefunctions of both electrodes governs the amplitude of electron transfer between both electrodes. Two years after the invention of the STM, Tersoff and Hamann applied a modified Bardeen's theory to STM. They make calculations for typical distances and sizes in the experiments [59, 60]. The tunnelling current is obtained using Fermi golden rule:

$$I(V) = \frac{4\pi e}{\hbar}\int_{\infty}^{\infty}[f(\epsilon+eV)-f(\epsilon)]N_s(\epsilon+eV)N_t(\epsilon)|M|^2 d\epsilon \tag{2.2}$$

where $f(E)$ is the Fermi distribution function, N_s and N_t are the density of states of the sample and the tip, respectively, and |M| is the transmission probability expressed as:

$$M = \frac{\hbar^2}{2m}\int_{\Omega}[\Psi_t * \bigtriangledown\Psi_s - \Psi_s * \bigtriangledown\Psi_t]dS \tag{2.3}$$

We can simplify Equation 2.2 by using the Fermi energy as reference, thus E_F=0 and if we assume, as we have performed measurement with a gold tip, that the density of states N_t can be considered independent of the energy in a small energy range around the Fermi level. Furthermore, Bardeen showed in [58] that |M| can be treated as a constant. Using these approximations we have:

$$I(V) = \frac{4\pi e}{\hbar}|M|^2 \int_{\infty}^{\infty} N_s(\epsilon) f(\epsilon - eV) d\epsilon \tag{2.4}$$

If we differentiate with V, in order to obtain the conductance $\sigma(V)$:

$$\sigma = \frac{dI}{dV} \propto \int_{\infty}^{\infty} N_s(\epsilon) \frac{\partial f(\epsilon - eV)}{\partial V} d\epsilon \tag{2.5}$$

Equation 2.5 shows that conductance is proportional to the convolution of the sample density of states and the Fermi distribution. As our experiments are typically performed at low temperatures, we can approximate the Fermi distribution with a delta function $\delta(\epsilon - eV)$ and Equation 2.5 can written as

$$\sigma = \frac{dI}{dV}|_{T \longrightarrow 0} \propto N_s(eV) \tag{2.6}$$

Therefore, the tunnelling conductance is proportional to the density of states close to the Fermi energy in the limit of low temperatures. STM provides the local measurement of the density of states (DOS) as a function of the energy in the sample. Measuring the DOS as a function of the position and energy is called scanning tunnelling spectroscopy (STS).

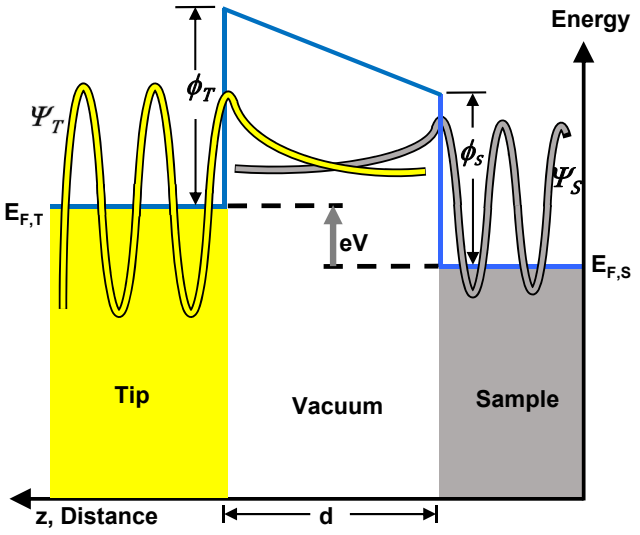

Figure 2.9: Image adapted from [50]. Tunnelling process between tip and sample separated by a vacuum barrier of width d. The wave function of tip and sample decays exponentially over the vacuum barrier.

Another important property comes from the fact that the wavefunction of tip and sample decay exponentially with distance inside the barrier (vacuum). A schematic picture is shown in Fig. 2.9. We can write the wavefunction in 1-D as:

$$\Psi_s \propto= e^{-\kappa z}; \qquad \Psi_t \propto= e^{-\kappa(d-z)}; \qquad \kappa = \sqrt{\frac{2m\phi}{\hbar}} \approx 0.5\sqrt{\phi}\text{Å}^{-1}; \tag{2.7}$$

where m is the electron mass and ϕ is the mean value of the work function of tip and sample in eV. By substituting the wavefunctions of Equation 2.7 we obtain

$$|M|^2 \propto e^{2\kappa d} \tag{2.8}$$

If we introduce the value of $|M|^2$ in Equation 2.4 we obtain that

$$I \propto e^{2\kappa d} \tag{2.9}$$

thus, the tunnelling current depends exponentially on the distance between tip and sample and this gives a huge resolution in z direction. Usually, we can assume that when current changes one order of magnitude, the distance between tip and sample is changed by an Å.

2.3 Measurements with STM

2.3.1 Topography

As Equation 2.9 shows, the tunnelling current is very sensitive to the distance between tip and sample. This provides a high resolution measurement of the changes in the electron density over the surface of the sample. Therefore, a topography image can be done by scanning the surface recording the changes in Z in the piezotube in order to maintain a constant current.

2.3.2 Spectroscopy

Equation 2.6 also gives an important result. The tunnelling conductance is proportional to the density of states at low temperatures. In spectroscopic images, we can obtain much more information than just with a topographic scan. This generates however a lot of data, which have to be appropriately treated, as we show below. Taking for each point the normalized conductance through a numerical derivative gives the normalized DOS at each point of the scanning window as a function of energy, for filled and empty states.

The duration of spectroscopy images can be very long depending on parameters such as the number of points, the number averages for each point, and the scanning velocity. In order to be effective, it is important to choose the duration considering the goal of the measurements. Usually, we first test a fast spectroscopy (30 min) to

make sure that the final result will be what we expect to observe in a given field of view. High quality measurements of vortices take around 8h-12h, or quasiparticle interference measurements take around 20-40h.

Vortex Lattice

The opening of the gap in the DOS of a superconductor is a very clear fingerprint that can be measured as a function of the position [61]. For example, superconducting vortices in type II superconductors, have clear DOS variation in the surface (Fig. 2.10). If we map the DOS as a function of the energy we will obtain DOS maps at constant energy. At an energy larger than the gap, we will have flat maps, as DOS does not vary over space. However, DOS maps at energies smaller than the gap will provide the contrast needed to observe the vortex lattice. The maximum contrast is obtained at zero bias.

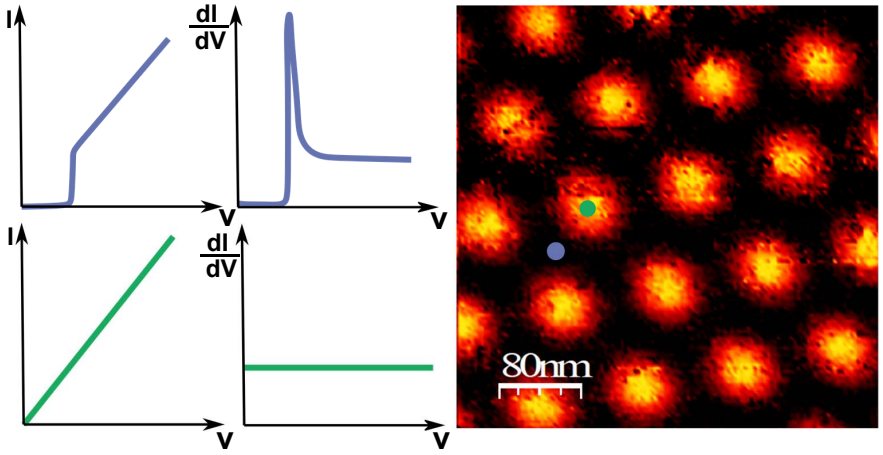

Figure 2.10: Current vs voltage and conductance vs voltage curves over a vortex and among them. Colours of each curve correspond with the point marked in the vortex image. Vortex image has been taken in of β-Bi_2Pd at 0.5T [62].

Quasi-particle interference

STM measurements of the local density of states (LDOS) are related to the dispersion relation, $\epsilon(\boldsymbol{k})$ through:

$$LDOS(E, \boldsymbol{r}) \propto \sum_{\boldsymbol{k}} |\Psi(\boldsymbol{r}_k)|^2 \delta(E - \epsilon(\boldsymbol{k})) \tag{2.10}$$

In an ideal metal, the momentum eigenstates $\Psi(\boldsymbol{r}_k)$ are the Bloch functions and the LDOS would be spatially homogeneous. In presence of impurities that break crystal lattice periodicity, electrons will be scattered producing oscillating patterns on the surface (see Fig. 2.11a).

Scattering of electrons by defects and impurities is most often elastic, so that the energy is conserved and momentum is modified. For instance, if the scattering mixes

two states of $\boldsymbol{k_1}$ and $\boldsymbol{k_2}$ the result is a standing wave with wave vector $\boldsymbol{q}$=($\boldsymbol{k_2}$-$\boldsymbol{k_1}$). This wavevector will produce a modulation in the LDOS, observable in the tunnelling conductance. In a metal the amplitude of the scattering obeys Fermi's golden rule:

$$w(i \to f) \propto \frac{2\pi}{\hbar}|V(\boldsymbol{q})|^2 N_i(E_i, \boldsymbol{k_i}) N_f(E_f, \boldsymbol{k_f}) \tag{2.11}$$

where $\boldsymbol{q}$=$\boldsymbol{k_f}$-$\boldsymbol{k_i}$ is the scattering vector, V($\boldsymbol{q}$) is the scattering potential and N_i and N_f are the initial and final density of states. In particular for a superconductor Bogoliubov quasi-particles have a dispersion relation:

$$E_{\pm}(\boldsymbol{k}) = \pm\sqrt{\epsilon(\boldsymbol{k})^2 + \Delta_{\boldsymbol{k}}^2} \tag{2.12}$$

where Δ is the superconducting gap. We can apply the same Fermi golden rule as Equation 2.11, introducing the effect of coherence factors

$$w(i \to f) \propto \frac{2\pi}{\hbar}|u_{k_i}u^*_{k_i} \pm v_{k_f}v^*_{k_f}|^2|V(\boldsymbol{q})|^2 N_i(E_i, \boldsymbol{k_i}) N_f(E_f, \boldsymbol{k_f}) \tag{2.13}$$

where plus and minus signs are for magnetic and non-magnetic scatters respectively and $|u_k|^2$ and $|v_k|^2$ are the probabilities that a pair of states with wavevector $\pm\boldsymbol{k}$ is empty or filled [63].

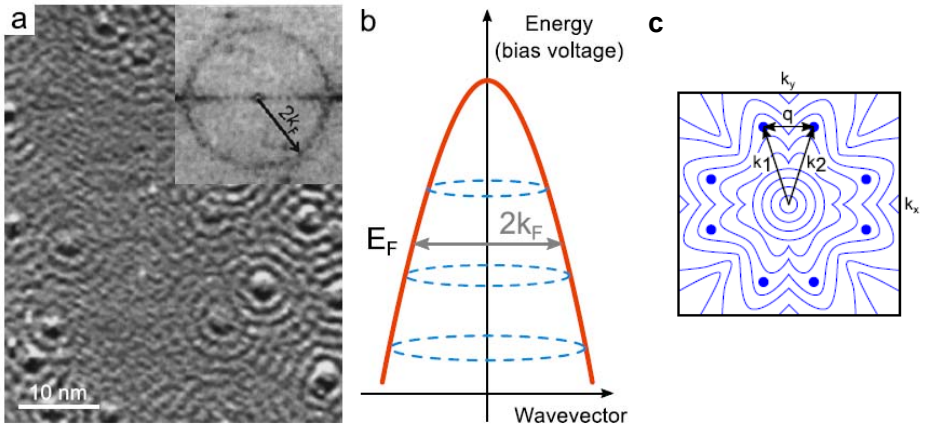

Figure 2.11: Image taken from [49]. (a) STM image taken in Cu(1,1,1) at 150mK. A modulation is observed from the point defects [64] . In the inset, the 2D-FFT indicating the main scattering vector. (b), Scheme of the dispersion relation of Cu(1,1,1) that can be reconstructed from the scattering vectors at different bias voltages. (c), Schematic Brillouin zone indicating the scattering between parts of Fermi surface with large JDOS (hotspots) adapted from Hoffman [65].

Therefore, with Equation 2.11 and Equation 2.13 we observe that the scattering signal will be higher for scattering vectors connecting states with large joint DOS (JDOS). These points of large JDOS are the so-called hotspots (Fig. 2.11c). As DOS $\propto \frac{1}{|\nabla_k(E)|}$ large JDOS will be found for $\boldsymbol{q}$ connecting parallel regions of band structure or from large flat regions in the k-space that have large DOS. Furthermore,

V(q) would account for any contribution from the scattering process such as spatial anisotropies [66].

If a certain number of scattering centres exist in our material modulation in the DOS in the real space (Fig. 2.11a) will result in an enhancement of the spectral weight for the corresponding vector $\boldsymbol{q}$. Therefore, a set of conductance maps at different energies allows to track the scattering vectors as a function of the energy. Looking at the geometry of the bandstructure at each energy, we can thus obtain the dispersion relation for each band from which we observe scattering (Fig. 2.11b).

2.4 Data analysis

As the STM measurements are improving over time, longer measurements can be taken and also new techniques can be used, as for example quasiparticle interference measurements (qpi). These demand to design software in order to access and analyse all possible information from the data.

First we have designed a program that opens the specific file of an spectroscopy. These files contain the information of the current at different energies. This program offers a quick visualization and a possibility to do a general preanalysis for both conductance map and FFT at different energies.

First we obtain the DOS curves by differentiating the current vs voltage data. We are able to plot the conductance map and its FFT for every chosen energy. Images can then be treated by changing the contrast in order to better observe their main features.

We have focused on the analysis of superconducting vortices and qpi. We have designed specific functions to analyse separately both of them [67].

2.4.1 Vortices

Vortex identification

We have implemented a set of functions in order to be able to analyse vortex lattices in detail. First we identify the vortex centres. We first determine the coordinates of each vortex in the images. To locate the vortex positions, the cores are first identified as regions where the normalized conductance is above a given threshold. Depending on certain features of the image, such as amount of defects or shape of vortices, we chose an appropriate threshold that allows us to identify the vortex positions as precisely as possible. We also imposed a tunable area for vortex candidates. This allowed to filter out possible contributions due to experimental noise. In this way, the vortex lattice images (Fig. 2.12a) were transformed into a binary map with value 1 (white) inside vortex cores and 0 (black) outside (Fig. 2.12b). We identified each white region in the image and calculated the center of mass (Fig. 2.12c). This gives us the coordinates center of each vortex. This method works robustly but produces false negatives and positives for noisier images. We implemented a method to correct

by clicking in order to erase or add bad or missing points respectively. The output result is a vector of the X-Y centres of vortex positions called centroids.

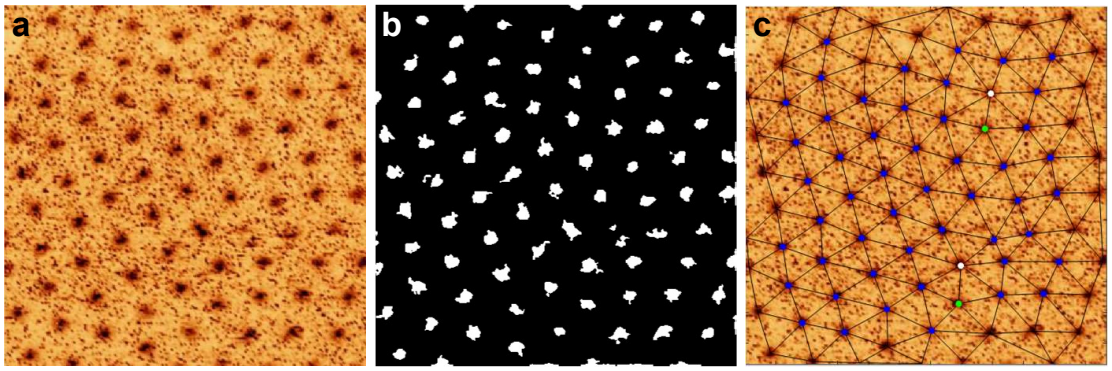

Figure 2.12: (a), Vortex image of W-film at H=0.03T. In (b), a binary image is associated to a is shown, for a certain threshold in conductance. The white regions are identified and the center of mass is calculated in order to have the centroids in (c) (blue points). We also plot the triangulation and the vortices with 6 neighbours and more or less than 6 (white and green respectively). Two dislocations are observed as white-green vortex pairs.

Triangulation

Another important feature to analyse vortex image is the Delaunay triangulation. Delaunay triangulation is an algorithm consisting on, given a set of points (vortex centers), three points are found that are circumscribed in the smallest possible circumference which, in addition, does not contain any other point inside. This gives a vector of size 3x(Number of triangles). Each row represents the three vortices that forms the triangle. Furthermore, if some triangles are not correct, we are able to remove them by clicking inside.

First neighbours map

With the triangulation output we can count the number of first nearest neighbours of each vortex and plot them in the image. Using this map we can observe how many defects the vortex lattice has. In an ordered vortex lattice each vortex has 6 first neighbours (in a triangular lattice). If the lattice is distorted due to the pinning or temperature, topological defects appear as vortices with more or less than 6 first nearest neighbours. These defects can be dislocations or disclinations (see subsection 1.2.2).

Using the first neighbour map we also can compute a histogram of first neighbours that can quantify the structural defect density. An example of dislocations is shown in Fig. 2.12c with a vortex pair of 5 neighbours (green) and 7 neighbours (white).

Combining information obtained from the centroids and triangulation, we can compute a histogram of the distance between the first nearest neighbours. We can

follow the mean distance with magnetic field. We then can obtain, for instance, the Abrikosov dependence for the intervortex distance in a hexagonal vortex lattice. Additionally, the standard deviation of the first neighbours distance provides an estimation of the distortion of the image. In chapter 4, we will discuss the behaviour of the standard deviation with magnetic field.

Translational and orientational order

Translational (G_K) and orientational (G_6) correlation functions quantify the positional and orientational disorder in the lattice as a function of distance [29]. We define them as:

$$G_K(r) = \frac{1}{6}\sum_{l}^{6}\frac{1}{N(r)}\sum_{i,j}^{N(r)}\Psi_{K_l}(r_i)\Psi^*_{K_l}(r_j) \qquad \Psi_{K_l}(r_i) = e^{iK_l r_l} \tag{2.14}$$

$$G_6(r) = \frac{1}{N(r)}\sum_{i,j}^{N(r)}\Psi_6(r_i)\Psi^*_6(r_j) \qquad \Psi_6(r_i) = \frac{1}{N^i_N}\sum_{k}^{N^i_N} e^{i6\theta(r_{ik})} \tag{2.15}$$

where r is the distance of any lattice site in the origin, N(r) is the number of vortex pairs separated by a distance r, K_l represents the 6 main reciprocal lattice vectors, N^i_N is the number of the nearest neighbours of vortex i and $\theta(r_{ik})$ is the angle of nearest neighbours bond between vortices i and j with respect to the reference axis.

Furthermore, we have implemented functions for analyse multifractality (see subsection 4.3.5), calculation of the structure factor and number variance (see section 5.2) and to follow individual vortices along different consecutive images (see section 6.2).

All this methods are centralised in a program that is constructed as master of the different functions. This facilitates the changes and the addition of new methods for vortex analysis [67].

2.4.2 QPI analysis

Symmetrization

For qpi measurements, noise reduction is crucial (Fig. 2.13a). In order to increment our scattering signal we symmetrize the FFT signals. The basic hypothesis is that Bloch functions follow the symmetry of the crystal, so that we can reduce the information to the corresponding symmetry component. For instance, in a square lattice, a square is simply repeated 4 times making the appropriate rotation and mirroring operations. First we rotate the FFT maps (Fig. 2.13b), in order to have crystallographic direction in the vertical and horizontal axes and make a zoom to observe the first Brillouin zone. Then, the symmetrization process can be different given the symmetry of the sample. For a 4-fold symmetry sample we average four quadrants of the FFT along the vertical and horizontal axes (crystallographic

directions). This increments notably the scattering signal over the background noise (see Fig. 2.13c).

After this process we follow the scattering vectors as a function of energy by making profiles at constant energy and tracking the changes in the size of the qpi vectors. We can perform vertical, diagonal or radial profiles. These profiles give 2D maps of the scattering signal as a function of energy and momentum in the direction used. These profile maps are usually Gaussian filtered.

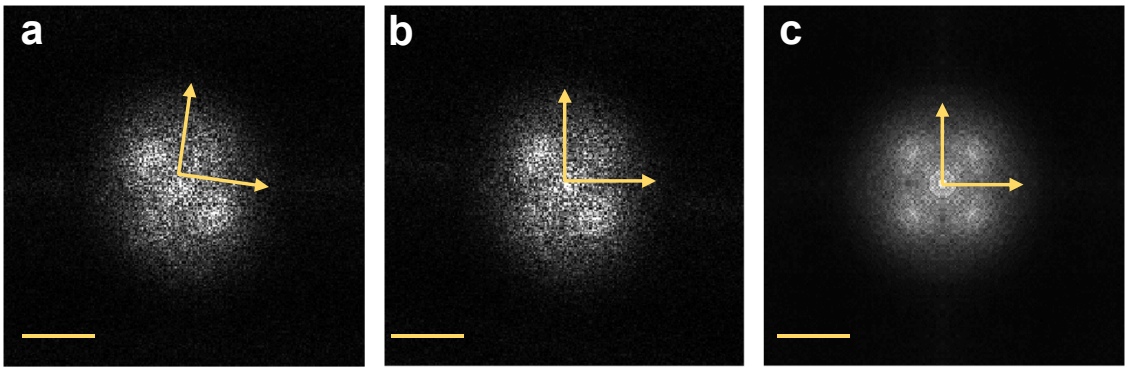

Figure 2.13: (a), 2D FFT of a 7mV bias conductance map measured with STM in $CaK(Ni_{0.05}Fe_{0.95})_4As_4$. Yellow arrows indicate the crystallographic directions. (b), Rotation of the image a with an angle of 8° in order to have the crystallographic axes in vertical and horizontal directions. In (c), we symmetrized (b), with a 4 fold symmetry in order to enhance the scattering signal. The size of the yellow bar is $0.3\pi/a$, being a the lattice constant.

Determination of dispersion relationship

From the profile maps we are able to follow the peaks with energy. Using the energy vs momentum map is already a method to observe the scattering vectors. However, in order to have more accuracy we can identify qpi vectors as peaks in profiles of FFT as a function of q at a given direction and fixed energy. Then, we can study the energy dependence of the qpi vectors and relate them with the bandstructure.

Gap anisotropy

In superconductors, the scattering signal disappears at energies below the superconducting gap. Then, we can determine the reciprocal space structure of the superconducting gap by following the amplitude of qpi vectors as a function of energy from above to below the superconducting gap energy.

2.5 Conclusions

We have built and designed from scratch a high magnetic field STM. We have prepared the different parts of the STM, like the piezostack, the piezotube or the

springs. We also have made the connections from the STM to the top of the cryostat with twisted pairs cables to reduce the noise level and designed different stages to thermalise the cables. Furthermore, we have tested the high magnetic field coil and designed an anti-vibrations structure to improve the noise level of the microscope.

We also have designed a set of functions to treat STM data efficiently. We are able to analyse vortex images, by detecting vortex centres, and triangulate them to calculate the number first nearest neighbours and their distances, hyperuniform and multifractal properties or translational and orientational correlation functions. We also have implemented functions to analyse qpi measurements, in order to filter, symmetrise or identify the scattering vectors to obtain the dispersion relationship.

Furthermore, we have moved and prepared a dilution fridge refrigerator STM system into a new location with anti-vibration floor including moving and reinstalling all the pumps, pipes, the cryostat and the dilution refrigerator into the new laboratory.

3 | Coexistence of non-collinear magnetic order with superconductivity

3.1 The 1144 family

As we have shown in the introduction, the generic phase diagram of the FeBSC consists of magnetic phases and a maximum critical temperature often occurring in the vicinity to a quantum critical point where magnetism vanishes. Although there are several stoichiometric superconductors, such as KFe_2As_2 [68], FeSe, [69], LiFeP [70], LiFePO [71], or LiFeAs [41], the maximum critical temperature in the phase diagram of each system occurs most often in non-stoichiometric compositions. We say that optimally doped FeBSC are most often non-stoichiometric. A notable exception is the $CaKFe_4As_4$ compound, where doping induces a decrease in T_c and the appearance of magnetism. This occurs with a maximum T_c of 35 K and a huge critical field, well in excess of 60 T, making $CaKFe_4As_4$ also interesting for applications [72].

Superconductivity in the 1144 family of compounds was first discovered by Iyo et al [48], who synthesized polycrystals and found a T_c of around 30 K. In a tour-de-force, the group of Ames [73], managed to synthesize single crystals of the new family [73]. Soon it was shown that the $CaKFe_4As_4$ compound is optimally doped and that its properties are similar to the properties of the optimally K-doped $(Ba_{1-x}K_x)Fe_2As_2$, as we will discuss below. Contrasting the well studied family of 122 compounds, as $(Ba_{1-x}K_x)Fe_2As_2$, the structure is somewhat different and it is important to dwell on the similarities and differences.

First, the structure is tetragonal and there are two planes built by the FeAs blocks, separated by the alkali or alkaline earth planes. The alkali and alkaline earth planes are located respectively on top and on the bottom of the FeAs groups. Thus, the planes formed by FeAs blocks have a different environment in their top and in their bottom. This does not occur in the 122 family, where the planes above and below the FeAs blocks always have the same kind of atoms. The consequence is that the distance between FeAs layers and alkali layers is different than the distance between FeAs layers and alkaline earth layers. This lowers the symmetry of the unit cell and

the glide plane along the FeAs layers, present in the 122 compounds, is absent in the 1144 compounds. In Fig. 3.1 we show the structure of 122 and 1144 families marking the different distances in the $CaKFe_4As_4$. We see that the As atoms in the FeAs are not equivalent in the 1144 structure. This makes a fundamental change with respect to what occurs usually in 122 pnictide superconductors.

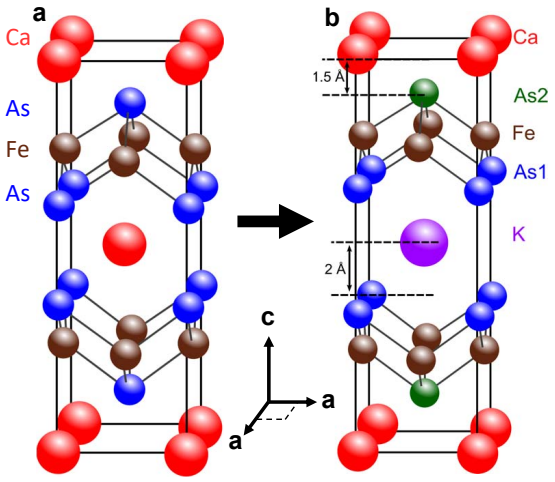

Figure 3.1: In (a) we show the unit cell of the $CaFe_2As_2$ representing the 122 family having glide symmetry in the plane defined by the iron layers. In (b) we show the unit cell of the 1144 family. Alkaline earth atoms are shown in red (here Ca) and alkali atoms in violet (here K). Fe atoms are shown in brown and As atoms in blue (site 1) and in green (site 2). The distance between the As2 sites and Ca is of 1.5 Å, whereas the distance between As1 and K is of 2 Å.

In spite of being a compound discovered relatively recently, we now know a great deal about $CaKFe_4As_4$, and there are even first tries to make wires out of it [74]. It was soon shown by a combined study of STM and penetration depth that this system is a $s_\pm$ superconductor, without any nodes in the order parameter [22, 75]. Nuclear magnetic resonance is also compatible with $s_\pm$ superconductivity [76]. Furthermore, it is a multigap system as shown by measurements of STM (Fig. 3.2a), penetration depth and ARPES. Penetration depth and STM, measures two gaps, $\Delta_1 \approx 3$ meV and $\Delta_2 \approx 8$ meV [22]. The Fermi surface is similar to this in the 122 FeBSC. There are three hole pockets around the Γ-points and two electron pockets at the M-point (Fig. 3.2b). The superconducting gap has largest values in middle hole pockets and in one electron pocket. These pockets have similar size suggesting that superconductivity is enhanced by nesting. These results were obtained from ARPES and confirmed with quasiparticle interference [77, 22]. In quasiparticle interference, mostly scattering between Γ centred bands is observed, with quasiparticle peaks and gap opening clearly visible in the interference pattern.

The vortex lattice was observed in Ref. [22]. The lattice is hexagonal up to 8 T, with vortices being clearly visible over large areas. Vortices are pinned at defects and surface structures where pair breaking is identified at the same time using STM. This determines the orientation of the vortex lattice. An example of a vortex lattice is shown in Fig. 3.2c. Vortex lattice structure was characterized

by calculating the positional correlation length $G_K(r)$, finding that $G_K(r)$ decays at about 3.5 intervortex distances. The vortex cores have the expected magnetic field dependence for superconductors in the clean limit, with a shrinking size that can be extrapolated to the coherence length at H_{c2}.

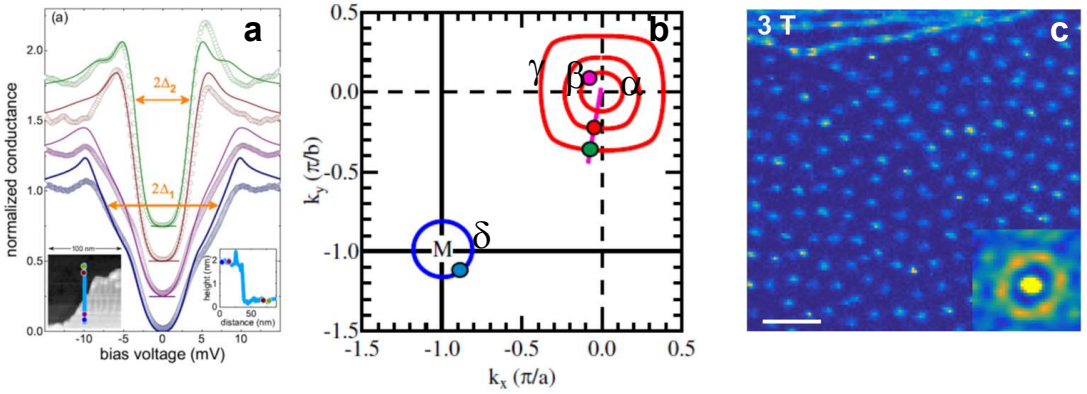

Figure 3.2: In (a) we show tunnelling conductance curves along the surface observed in the inset [75]. Gap is completely open in both regions, and in the white area, 2 gaps are found. In (b), Fermi surface of $CaKFe_4As_4$ determined by ARPES [77]. Three hole pockets in red and one electron pocket in blue. Dots indicate gap measurements finding $\Delta_\alpha = 10.5$ meV, $\Delta_\beta = 13$ meV, $\Delta_\gamma = 8$ meV, $\Delta_\delta = 12$ meV. In (c), a vortex lattice at 3T in the stoichiometric compound. We observe a disorder lattice with linear defect that pin vortices. In the inset autocorrelation function shows a very disorder lattice but with peaks as in a triangular lattice [22].

Finally, let us note that the $CaKFe_4As_4$ system is an excellent compound for STM, because the surfaces obtained with low temperature cleaving are flat and allow measurements over very large areas. Sometimes, a surface reconstruction is observed. But most often, the surface consists of flat areas without clearly defined features. The cleaving plane is almost certainly the bonding plane between FeAs and the alkali atom layer or the alkaline earth atom layer. Thus, the surface likely consists of Ca or K [22].

3.2 Non-collinear hedgehog order

Electron count and other physical properties show a clear similarity between K-doped $BaFe_2As_2$ and the stoichiometric $CaKFe_4As_4$. We show in Fig. 3.3a that penetration depth curve of $CaKFe_4As_4$ (yellow curve) is very close to K-doped $BaFe_2As_2$ at x=0.54 (black) [75] indicating a nodeless full gap. In this system, stripe-type spin density wave (SSDW) antiferromagnetic order is suppressed by hole doping as shown in the phase diagram of Fig. 3.3b [68]. Following this analogy, it was suggested that magnetic order could be also induced in $CaKFe_4As_4$ by electron doping.

Soon later, Canfield's group reported the emergence of non-collinear

antiferromagnetic order by adding electrons via substitution of Fe by Co or Ni in $CaKFe_4As_4$ [78]. The antiferromagnetic order in this material is different from the usual stripe-type spin density wave (SSDW) (Fig. 3.4a) that breaks the C4 rotational symmetry and has been reported in most 122-compounds. Instead, electron-doped $CaKFe_4As_4$ shows non-collinear antiferromagnetic order consistent with a hedgehog spin vortex crystal (SVC) (Fig. 3.4c) which preserves the C4 rotational symmetry. In the so-called hedgehog SVC phase, there are two inequivalent magnetic order parameters, M_1 and M_2, associated to the antiferromagnetic vectors $Q_1=(\pi,0)$ and $Q_2=(0,\pi)$, with $|M_1|=|M_2|$ and $|M_1|\perp|M_2|$. In the SSDW phase, there is only one nonzero M_i.

The realization of the hedgehog antiferromagnetic order in electron-doped $CaKFe_4As_4$ is a direct consequence of the glide symmetry absence and the two inequivalent As sites, and was confirmed by NMR measurements [78].

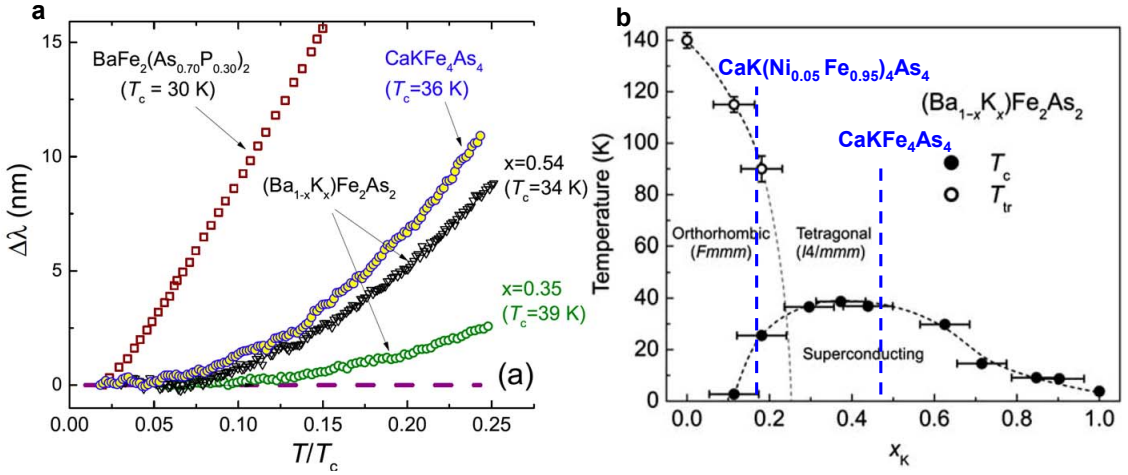

Figure 3.3: (a), Penetration length measurements of $Ba_{1-x}Fe_2(As_{0.7}P_{0.3})_2$ (maroon), $CaKFe_4As_4$ (yellow) and $(Ba_{1-x}K_x)Fe_2As_2$ at x=0.54 (black) and x=0.35 (green) obtained from [75]. The curve of $(Ba_{0.45}K_{0.55})Fe_2As_2$ is similar to the one obtained in $CaKFe_4As_4$. (b), phase diagram of $(Ba_{1-x}K_x)Fe_2As_2$. Dashed lines indicate where we can locate, for comparison, Ni doped and pure $CaKFe_4As_4$ studied here. Phase diagram is obtained from [68]

Fig. 3.5b shows the phase diagram obtained for Ni and Co doped $CaKFe_4As_4$. Electron doping by either Ni or Co suppresses the superconducting critical temperature and induces the hedgehog SVC order. As Ni has two times more electrons than Co, the doping level needed to achieve the same results is half of it [78]. Experimentally, larger and cleaner crystals have been obtained for Ni-doping because it implies less substitution.

^{57}Fe Mossbauer spectroscopy experiments have shown evidence for the microscopic coexistence between superconductivity and hedgehog SVC order [79]. However, it has been also reported that, similar to what is found in 122 compounds, the ordered magnetic moment is gradually suppressed when entering in the superconducting phase, suggesting that superconductivity and magnetism (both collinear and

noncollinear) are competing for the same electrons in the FeBSC [80].

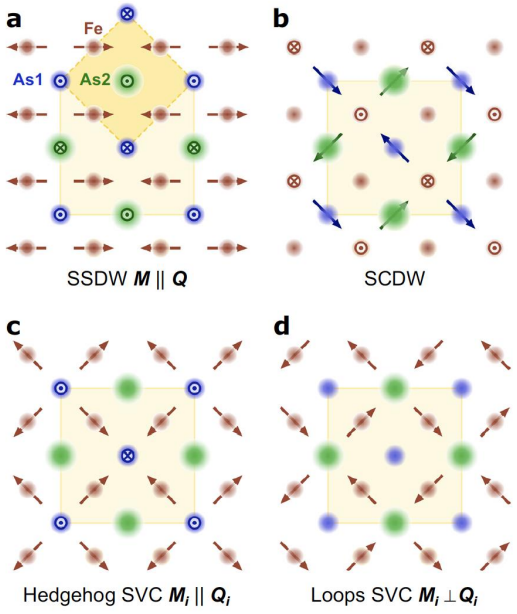

Figure 3.4: In (a) and (b) are the magnetic orders that have been previously observed in FeBSC. In (c) and (d) are two examples of the SVC, hedgehog SVC in (c) and loop SVC in (d). Image taken from [78].

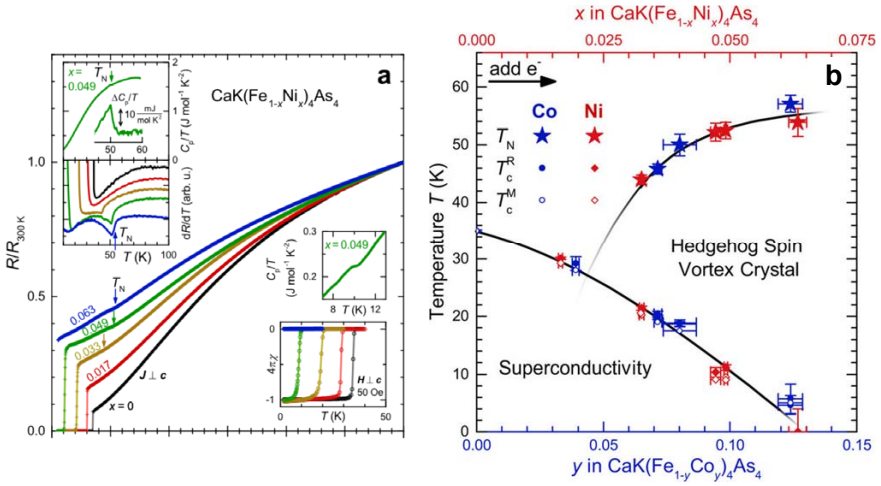

Figure 3.5: In (a), we show the resistivity measurements in $CaK(Ni_xFe_{1-x})_4As_4$ at different doping level. The inset shows the jump in heat capacity (top) and in the derivative of the resistance with temperature at the magnetic transition. (b) shows the critical temperatures for superconductivity and hedgehog SVC order vs Ni and Co doping.

Here, we have studied in detail Ni-doped $CaKFe_4As_4$ with 5% of Ni. At this composition, superconductivity coexists with the hedgehog SVC order at

low temperatures. We have measured the superconducting gap, performed qpi measurements and imaged the vortex lattice to show how superconducting properties are modified by the coexistence with the hedgehog SVC order.

3.3 Results

3.3.1 Topography

We have measured single crystals 1 mm long, 0.5 mm wide and 0.5 mm thick with c-axis perpendicular to the surface. We always cleaved the crystals *in situ* at 4K. As in $CaKFe_4As_4$, the cleaving plane is in between the FeAs and Ca or K planes, and therefore the surface likely consists of Ca or K atoms.

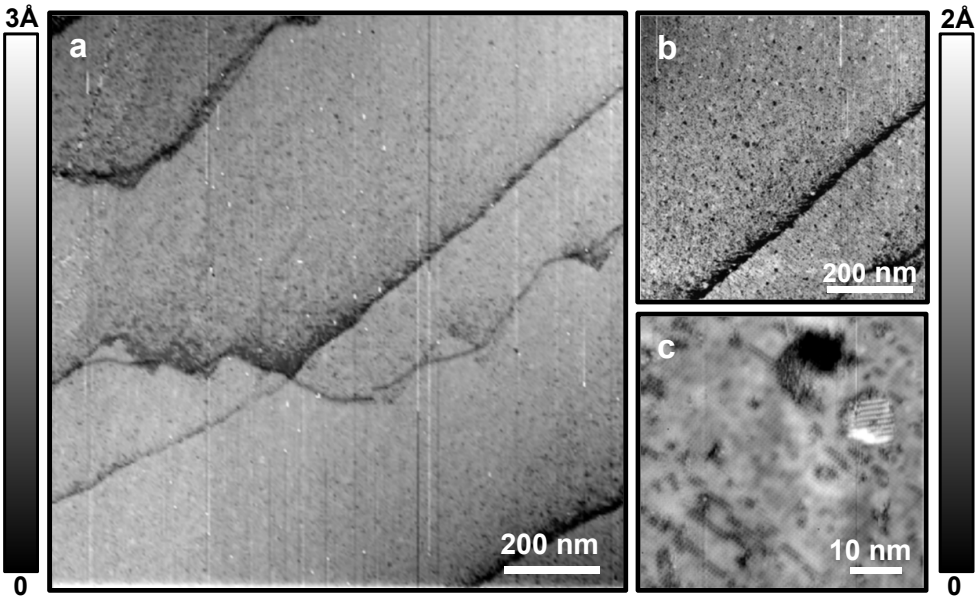

Figure 3.6: In (a) we observe a very flat area of about 1 μm. We find line defects which often appear in the surface of this material. In (b), a zoom of (a). Flat areas of the sample are corrugated with random defects in white and black. (c) is a zoom of (b). $\sqrt{2} \times \sqrt{2}$ reconstruction appears but also circular region at the same height of 1×2 reconstruction.

Fig. 3.6a shows a typical topographic image obtained in this sample. It shows very large atomically flat areas, allowing us to make images with the maximum size of our scanning window (2 μm). Quite often we observed small lines producing an small corrugation of 10% of c-axis parameter. These were also observed in the stoichiometric compound $CaKFe_4As_4$ and are likely produced during the cleaving process. Image in Fig. 3.6b is a zoom taken in a region of Fig. 3.6a. At smaller scale, we find the presence of hole-like defects but most often, we do not observe clear atomic features. A similar result was also found in $CaKFe_4As_4$. In a few places, however, we have observed atomic size features in the images. We show

an example in Fig. 3.6c. Here, we have found surface reconstructions of the Ca or K atoms with periodicity $\sqrt{2}a \times \sqrt{2}a$ a and 1a×2a. The surface reconstructions $\sqrt{2}\times\sqrt{2}$ and 1×2 often appear in the 122 superconductors [81, 49] and they were also found in small areas of $CaKFe_4As_4$ [49]. Surface reconstructions are a result of the energy minimization during the cleaving process. We use the surface reconstruction to identify the direction of the crystalline axes.

Fig 3.7 shows a scanning electron microscopy (SEM) image of the sample taken once the experiment is finished. This allows us to verify the surface quality after the cleaving and compare topographic features at different scales. Image in Fig 3.7 shows that the surface is indeed very flat, with a few steps produced by the breaking of layers during the cleaving.

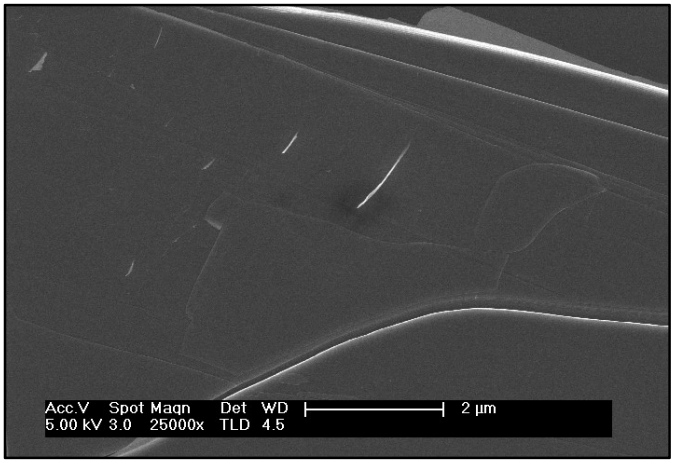

Figure 3.7: A SEM image of the sample. We observe flat areas in the micrometer scale and lines similar to those found in STM images.

3.3.2 Superconducting density of states

In Fig 3.8, we present a typical tunnelling conductance curve measured in this material at 300 mK. It is characterised by reduced quasiparticle peaks and a V-shape with finite conductance at zero bias. Close to defects, we have observed an increased zero bias conductance due to pair breaking as in the stoichiometric compound $CaKFe_4As_4$.

In order to get more information on the gap structure we have calculated the superconducting local density of states (LDOS) using a distribution of gaps as follows:

$$LDOS \propto \sum_{\Delta_i} \gamma_i Re\left(\frac{E}{\sqrt{E^2 - \Delta_i^2}}\right) \tag{3.1}$$

where γ_i is the weight of the different gap values Δ_i. This approach has been used before in MgB_2, [82] and the parent compound of this material $CaKFe_4As_4$ [22]. By using this calculation we are taking into account the contribution of the different gaps that open in the Fermi surface to the tunnelling conductance.

Inset in Fig. 3.8 shows γ_i values associated to each Δ_i. The gap distribution is very broad and centred at 1.5 meV. Note also that there is a considerable proportion of superconducting gap which is practically zero. This is related to the very large density of states at zero bias, absent in the non-doped compound [22, 75]. The origin of this effect is unclear, and might be due to the influence of magnetism and the large amount of disorder present in this sample.

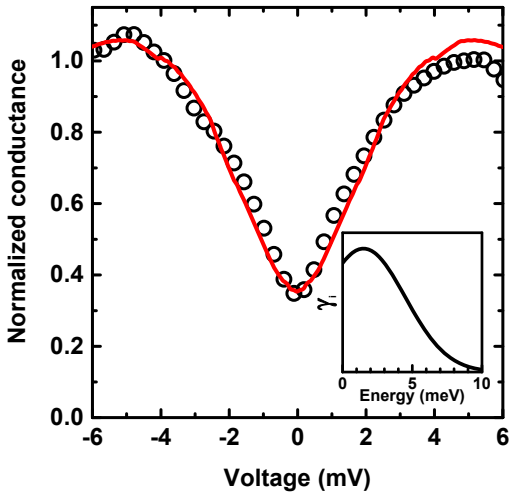

Figure 3.8: Tunnelling conductance measured in $CaK(Ni_{0.05}Fe_{0.95})_4As_4$ at 300 mK. Red line is the convolution between the LDOS and the Fermi function. Inset shows the gap distribution used to calculate the superconducting LDOS.

Red line in Fig. 3.8 shows the convolution of the superconducting LDOS calculated using Equation 3.1 with the Fermi function following Equation 2.5. We find a good agreement between the experimental data and the fit.

Fig. 3.9a shows the temperature dependence of the tunnelling conductance up to 8K. Experimental data are shown by circles and red lines are the fit obtained following the procedure described above. Namely, we obtain the LDOS using Equation 3.1 and then convolute it with the Fermi function at each temperature. Fig. 3.9b shows the derivative of the superconducting LDOS at different temperatures. The energy associated to the maximum at each curve corresponds to the average value of the distribution of the superconducting gap. In Fig. 3.9c we plot the temperature dependence of such an average gap value. Red line in Fig. 3.9c is the temperature dependence of the superconducting gap expected by BCS theory (subsection 1.1.3) using a $\Delta(0\ \mathrm{K})$=1.5 meV and $T_c = 9.5$ K.

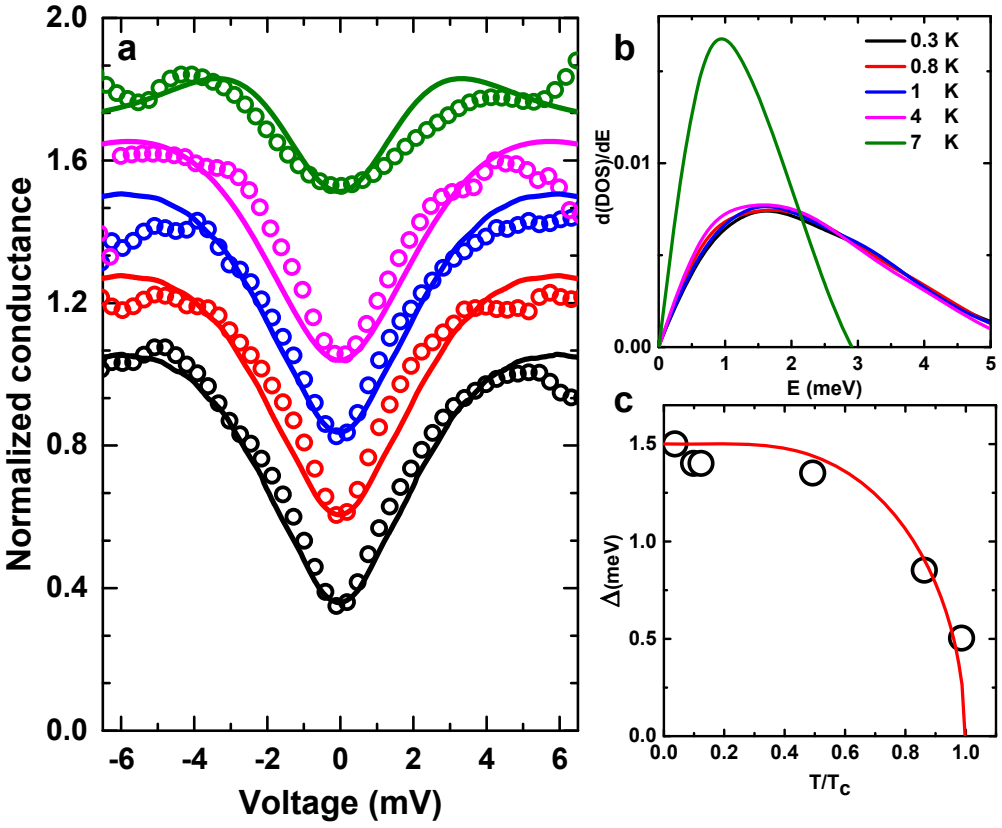

Figure 3.9: (a) Tunnelling conductance as a function of temperature for 0.3 K (black), 0.8 K (red), 1 K (blue), 4 K (magenta), 7 K (green). Lines are the result from the convolution between the DOS and the derivative of the Fermi function at each temperature. (b) Derivative of the DOS. The maxima in the curves correspond to the gap values at each temperature. (c) Superconducting gap as a function of temperature with T_c = 9.5 K. Red line shows temperature dependence of the superconducting gap obtained from BCS theory.

3.3.3 Electronic and superconducting gap structure from qpi measurements.

As I described in subsubsection 2.3.2, STM provides a method to measure the band structure of the material through quasi-particle interference (qpi). We have performed qpi measurements at 300 mK and zero magnetic field in a flat area.

Fig. 3.10 shows the topography of the area where we made the qpi measurements. This area is atomically flat and shows the presence of defects such as holes or small atomic chains in the surface. The image has a size of 75.3 nm leading to a resolution in the reciprocal space of 1/75.3 nm^{-1}=0.013 nm^{-1}. The limits of the first Brillouin zone are at 1/0.38 nm^{-1}=1.32 nm^{-1}. In order to obtain the qpi signal, we performed spectroscopic measurements in this area by taking tunnelling conductance curves from -30 mV to 30 mV in each point of the image. We then build conductance maps of 256 x 256 pixels for different bias voltages, obtaining one image each 0.3 mV.

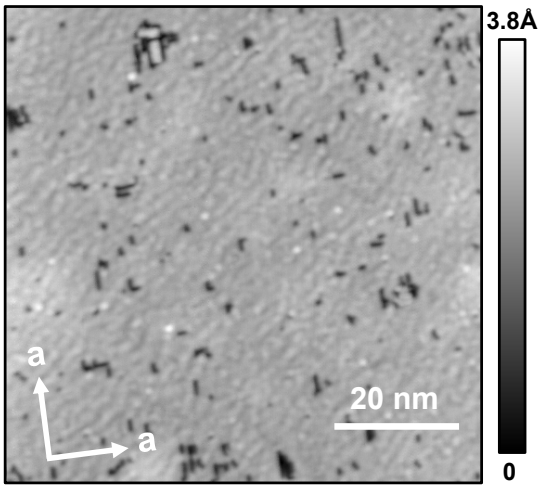

Figure 3.10: Topographic image taken simultaneously in the region where qpi measurements were made at 300 mK and 0T.

Several conductance maps are shown in the top panels of Fig. 3.11(a-e). They show interference patterns due to impurity scattering that change with energy. The corresponding Fourier transforms (FFT) within the first Brillouin zone are shown in the bottom panels of Fig. 3.11(a-e) (using symmetrization as explained in subsection 2.4.2). We plot the crystalline axes as arrows. Note that the FFT is rotated with respect to the real space images, to more clearly discuss the behaviour as a function of the crystalline axis. We find that the amplitude of the qpi signal also changes with the bias voltage, being larger at high bias voltage (with the strongest signal at negative bias voltages) and almost disappearing at energies below the superconducting gap.

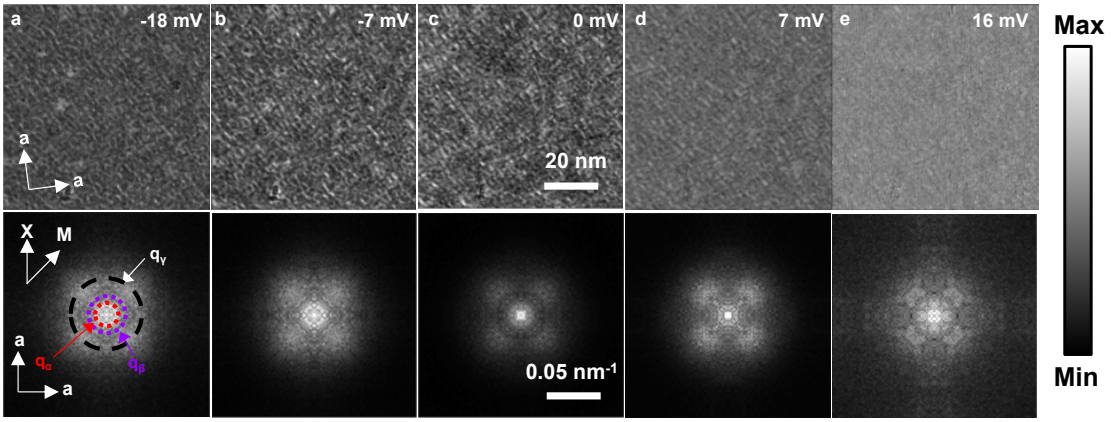

Figure 3.11: (a-e) Top panels shows conductance maps at -18 mV, -7 mV, 0 mV, 7 mV and 16 mV. Bottom panels show the symmetrized FFT in the first Brillouin zone where Ca/K atoms are found at [0, $\pm 2\pi/a$] and [$\pm 2\pi/a$, 0]. Dashed circles represent the observed scattering vector that we called q_α (red), q_β (purple) and q_γ (black) pockets.

We have identified three qpi vectors that we call q_α, q_β and q_γ. To determine the qpi vectors and follow their energy dependence we search for maxima in the FFT profiles as a function of energy along the two main high symmetry directions, Γ-X and Γ-M. In Fig. 3.12 we show FFT profiles vs energy along Γ-M (a) and Γ-X (b) in the q-range from 0.2π/a to 0.4π/a. For clarity we highlight in this figure the maxima corresponding to q_γ as black circles.

In Fig. 3.13 we show a 2D-map of the bias voltage vs q with the intensity of the scattering signal in qpi providing the color scale. In (a) we represent the Γ-M direction and in (b) Γ-X direction. The color scale corresponds in both images to similar changes in the intensity of scattering. In both of them we identify three scattering vectors, q_α (red), q_β (purple) and q_γ (black) shown by circles in Fig. 3.13. The size of the three qpi vectors decrease with energy being this dependence more strongly for q_α and q_β. The size of the vectors reflect the in-plane shape of the corresponding scattering circles (Fig. 3.13). In particular, q_α and q_β are approximately isotropic, although q_β is slightly larger along the Γ-M direction. However, in q_γ we find a clear in plane anisotropy. In particular, q_γ is larger along the Γ-M direction than in Γ-X direction. At voltages of order or smaller than the superconducting gap, we observe a clear decrease in the scattering intensity. In order to quantify this, we represent in the inset of Fig. 3.13b the FFT amplitude at q_α, q_β and q_γ as a function of energy. We find that the scattering signal decreases at bias voltages below the gap for the three qpi vectors, indicating that the superconducting gap opens in Fermi surface sheets associated with these vectors.

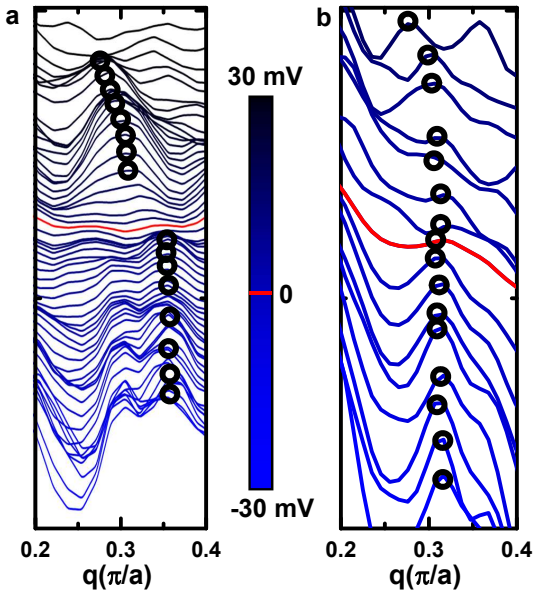

Figure 3.12: FFT profiles as a function of q in the range [0.2-0.4]π/a in Γ-M (a) and Γ-X (b) direction. The curves are shifted vertically for clarity. We identify the peaks of the FFT signal corresponding to q_γ (black circles) and follow them with energy.

We can clearly see that the decrease in intensity inside the superconducting

gap region is band and direction dependent. In particular the latter points towards a sizeable anisotropy of the superconducting gap. Fig. 3.14a shows the energy dependence of the FFT amplitude in q_γ as a function of the angle. Here 0° corresponds to the Γ-X direction and 45° to the Γ-M direction. We find that the scattering intensity has a clear four-fold symmetry, indicating that the superconducting gap is also four-fold. From the observed in-plane dependence of the scattering amplitude, we can see that the superconducting gap anisotropy is of about a factor of three, being largest along Γ-X. We observe in Fig. 3.14b the correspondence of the θ angle with the atomic directions.

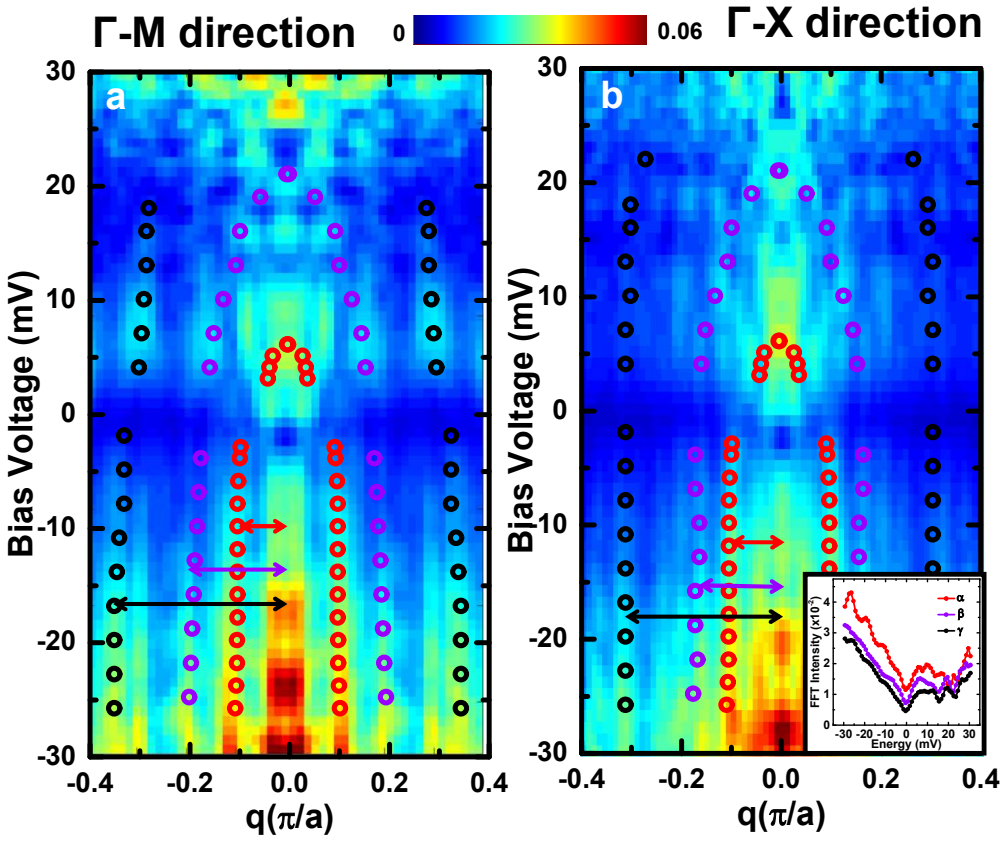

Figure 3.13: We show the amplitude of FFT (color plot) and qpi vectors (q_α in red, q_β in purple and q_γ in black) as a function of the bias voltage along the Γ-M direction (a) and Γ-X (b). Inset in (b) shows the energy dependence of the FFT amplitude at q_α, q_β and q_γ.

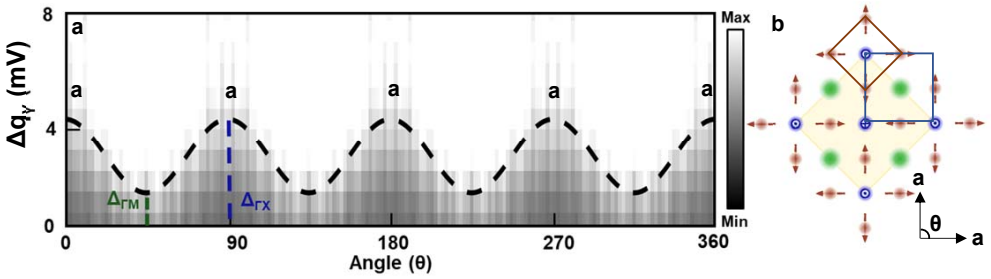

Figure 3.14: (a), FFT amplitude of q_γ as a function of energy. Black color indicates that the superconducting gap is open suppressing the qpi signal. The dashed line is a simple sinusoidal dependence and serves as a guide to the eye. (b) Representation of the FeAs layer of $CaKFe_4As_4$ with the magnetic moments of Fe atoms (brown) in the hedgehog phase. Hyperfine field generated by Fe magnetic moments in As1 atoms are shown as blue arrows. The hyperfine field is zero in the As2 sites. The larger gap $\delta_{\Gamma X}$ is found along the direction of the main crystalline axis (blue square) while the smaller gap $\delta_{\Gamma M}$ is observed at 45°, along the main axis of the Fe lattice (brown square).

3.3.4 Vortex lattice in Ni-doped $CaKFe_4As_4$

We have observed the vortex lattice under magnetic field. Fig. 3.15b shows a large scale image of the vortex lattice showing hundreds of vortices. This image is built from the spatial changes of the zero bias conductance in the region shown in Fig. 3.15a. This region is as large as our maximal scanning window at cryogenic temperatures. Notice that the height changes in the image (of 2 μm × 2 μm size) amount to merely 0.5 nm. Topographic features observed in Fig. 3.15a are also seen in the vortex map of Fig. 3.15b because defects produce enhanced zero bias conductance through pair breaking. Pair breaking in topographic defects produces similar contrast in the image than the vortex lattice, making it sometimes difficult to resolve isolated vortices. In the following, we will discuss smaller sized images, where we can clearly identify the positions of isolated vortices.

In order to understand the behaviour with field, we took images at four different magnetic fields, 0.5 T, 2 T, 3 T, and 4 T. These are shown in Fig. 3.16. The vortex lattice is very disordered at all magnetic fields.

We quantified the disorder in the vortex lattice, by identifying vortex positions in the images shown in Fig. 3.16 and calculated the Delaunay triangulation following subsection 2.4.1. Using the vortex positions, we can calculate the average distance between first neighbours. The result is plotted in the inset of Fig. 3.16d as a function of the magnetic field. We find that the intervortex distance follows the behaviour expected for an Abrikosov vortex lattice.

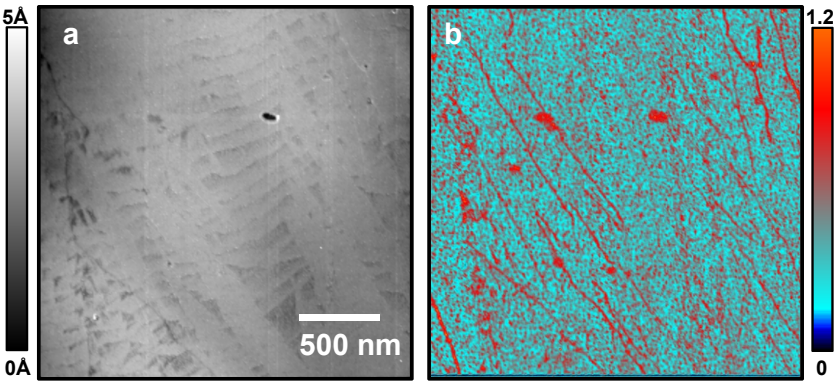

Figure 3.15: In (a) we show the topographic image of the region where the vortex lattice shown in (b) has been observed. (b) Conductance map taken at 0 mV, T = 300 mK and H=2 T, showing a vortex lattice (vortices are the tiny red dots distributed over all of the image) with more than 1000 vortices. Red lines and larger size dots in (b) are due to pair breaking in topographic defects.

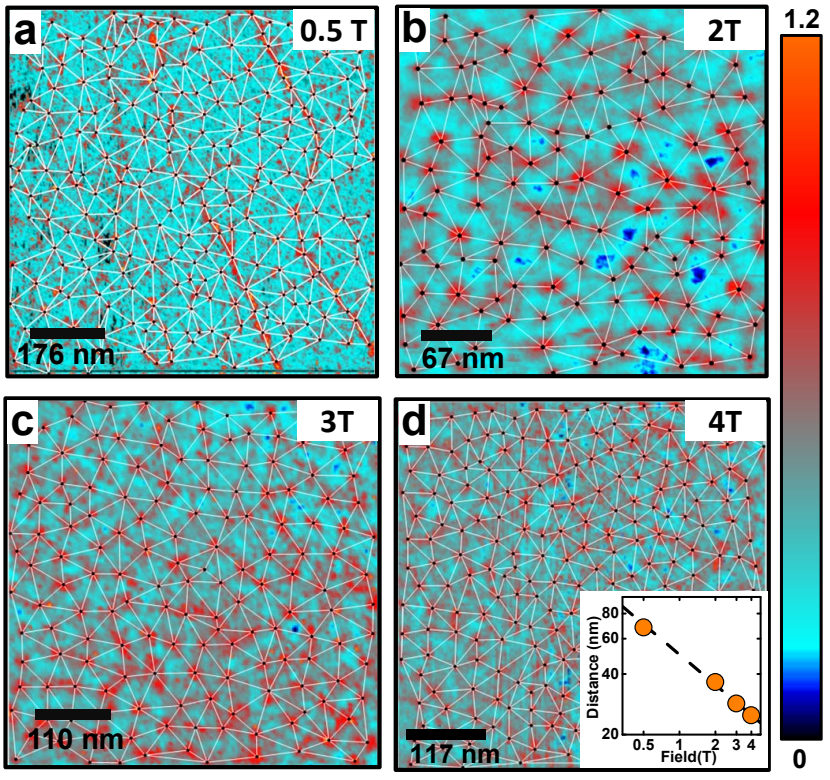

Figure 3.16: Vortex lattice images at different values of the magnetic field. The lattice is very disordered with a lot of defects. White lines are the Delaunay triangulation of the lattice. In the inset of (d), we show first nearest neighbour distance versus magnetic field. Dashed line is the intervortex distance as a function of magnetic field for a triangular Abrikosov vortex lattice.

We also have calculated the number of first neighbours for each vortex. In

Fig. 3.17a we show the vortex image at 4 T. Vortices with less than 6 neighbours are marked by green dot, with more than 6 neighbours with black dots and with 6 neighbours with white dots. Some vortices are at the borders of the image and we cannot determine their nearest neighbours. We thus do not consider these vortices in our calculations. We observe dislocations and disclinations. A histogram of the number of neighbours is shown in Fig. 3.17c. The percentage vortices without 6 neighbours is 56%.

In Fig. 3.17c we show the positional correlation function $G_k(r)$ for the 4 T image, calculated following subsection 2.4.1. There is a very fast decay of $G_k(r)$ in a very short distance of around $\backsim 2a_0$. The vortex lattice has clearly no long range order. Furthermore, the size of ordered vortex bundles is merely a couple of intervortex distances. There is also, of course, no orientational order. All this is seen in the Fourier transform of the vortex lattice (inset of Fig. 3.17a), which shows a thick circle around the average intervortex distance.

We also examined the evolution of the tunnelling conductance from the vortex core to the superconducting area in between vortices (Fig. 3.18a). In between vortices we find a similar tunnelling spectroscopy as in zero field (Fig. 3.8). As we approach the vortex core, the gap closes. Contrary to what was observed in the parent compound, we did not find a zero bias peak in the center of the vortex. This is consistent with the reduced mean free path found in this system.

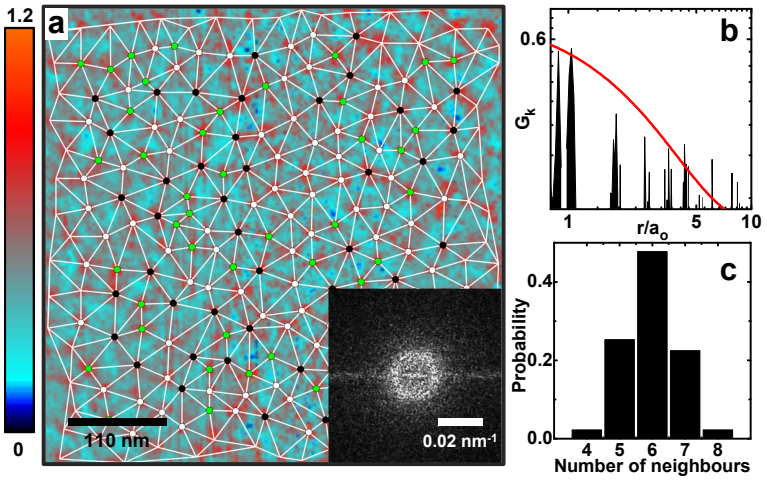

Figure 3.17: (a) Zero bias normalized conductance map at 4 T. White lines indicate the Delaunay triangulation and vortices coloured in white have 6 nearest neighbours, in green less than 6 and in black more than 6 nearest neighbours. In the inset, the 2D-FFT map of the image. In (b), the translational correlation function $G_k(r)$, [29]. It decays very fast with distance. Red line is the fit to exponential decay with a length scale of about $\backsim 2a_0$. A histogram of first nearest neighbours for the image in a is shown in (c).

When we take a look on individual vortices, we see that their shape is often not really round. Probably this is due to the mixture between the features in the density of states due to pair breaking in defects and the presence of vortices. Nevertheless,

there is clearly no tendency to form square vortices, as for instance in LiFeAs [42].

As discussed in subsection 1.2.1, it is interesting to extract the vortex core size from the spatial dependence of the tunnelling spectroscopy and plot this as a function of the magnetic field. In the clean limit, vortex cores are observed to increase their size with decreasing magnetic field. Furthermore, in multigap superconductors, complex vortex core shapes could eventually appear. In the dirty limit [20], the core size is expected to be magnetic field independent. Finally, as shown in [83], determining the vortex core size is an independent and neat way of obtaining the superconducting coherence length and compare the result with the one obtained from the upper critical field.

To use the analysis of [83], we faced here however significant problems. All vortices are a little different from each other, so that we did not manage to choose a representative vortex at each magnetic field. To overcome this difficulty, we have designed a new method, which we describe in the next section.

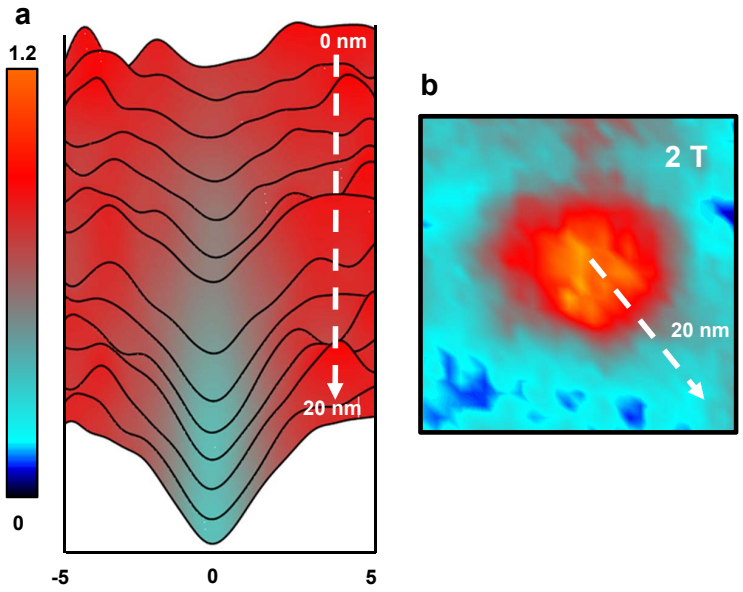

Figure 3.18: (a), Normalized tunnelling conductance along the path showed in (b). As we move inside the vortex core, gap completely closes without a zero bias peak. (b), Conductance image at 0 mV, 2 T and 300 mK showing a single vortex. Dashed white arrows indicate the path along which the conductance curves shown in a have been taken.

Determining vortex core

We can understand images of the vortex lattice obtained by STM as containing information about both structure of the lattice and shape and size of the vortex core. Let us try to separate these two contributions in the images. To this end, we introduce a structure and a form factor. The structure factor of the lattice, $I_{structure}(\boldsymbol{r})$, is defined by the vortex positions. The form factor of the vortex, $I_{form}(\boldsymbol{r})$ describes the shape in real space of a single vortex. The vortex lattice images

obtained by STM, I($\boldsymbol{r}$), are the result of the convolution between the structure and the form factors. This can be expressed as:

$$I(\boldsymbol{r}) = I_{structure}(\boldsymbol{r}) * I_{form}(\boldsymbol{r}) = \int_{-\infty}^{\infty} I_{structure}(\boldsymbol{r}) I_{form}(\boldsymbol{r} - \boldsymbol{r}') d\boldsymbol{r}'. \tag{3.2}$$

We can obtain $I_{structure}(\boldsymbol{r})$ by identifying vortex positions and setting up a matrix containing the position of each vortex. To obtain the form factor, we go to reciprocal space and write:

$$I(\boldsymbol{q}) = FFT[I_{structure}(\boldsymbol{r}) * I_{form}(\boldsymbol{r})] = I_{structure}(\boldsymbol{q}) I_{form}(\boldsymbol{q}). \tag{3.3}$$

As the Fourier transform of a convolution is the product between the Fourier transform of both components of the convolution. Now we take the Fourier transform of the structure factor and obtain from it, using Equation 3.3, the Fourier transform of the form factor. Once we have done this, we can go back to real space and write the form factor:

$$I_{form}(\boldsymbol{r}) = \int_{-\infty}^{\infty} \frac{I(\boldsymbol{q})}{I_{structure}(\boldsymbol{q})} e^{2\pi i \boldsymbol{r}\boldsymbol{q}} d\boldsymbol{q}. \tag{3.4}$$

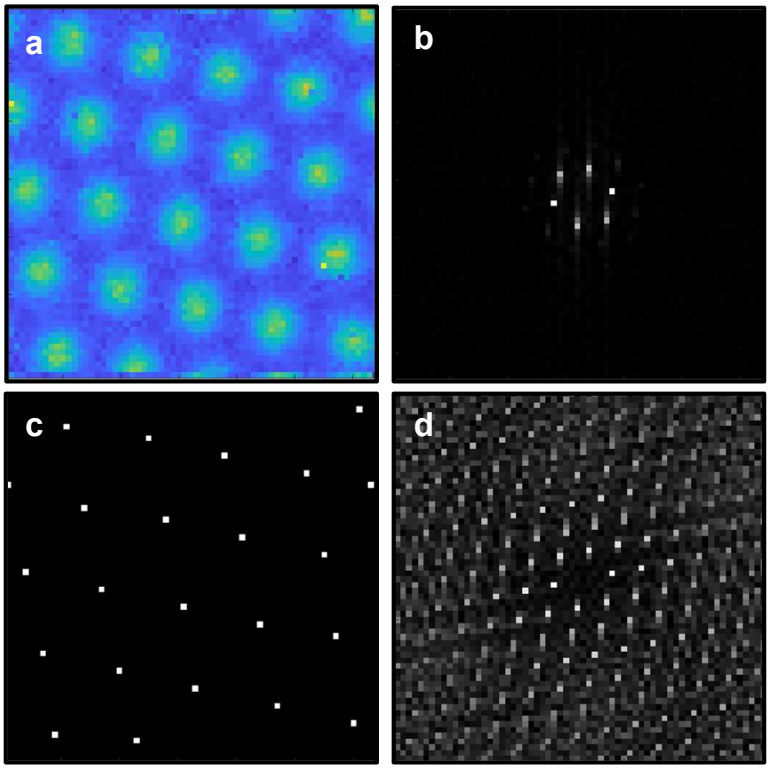

Figure 3.19: In (a) we show a vortex image of β-Bi_2Pd at 0.2 T (I($\boldsymbol{r}$)). In (b), we show the the FFT of (a), I($\boldsymbol{q}$). In (c) $I_{structure}(\boldsymbol{r})$ is calculated by determining the vortex centres creating a binary matrix of zeros where the vortex centres have a value of 1. (d) shows the FFT of $I_{structure}(\boldsymbol{r})$.

We can now test this method using β-Bi_2Pd, where the vortex core size has been already obtained previously [21]. Fig. 3.19(a-b) we show a vortex lattice image in β-Bi_2Pd ($I(\boldsymbol{r})$) and its FFT ($I(\boldsymbol{q})$). We first determine vortex positions to obtain the structure factor ($I_{structure}(\boldsymbol{r})$, panel c) and its FFT ($I_{structure}(\boldsymbol{q})$, panel d). Using Equation 3.3 and Equation 3.4 we can calculate the form factor $I_{form}(\boldsymbol{r})$. The results are shown in Fig. 3.20.

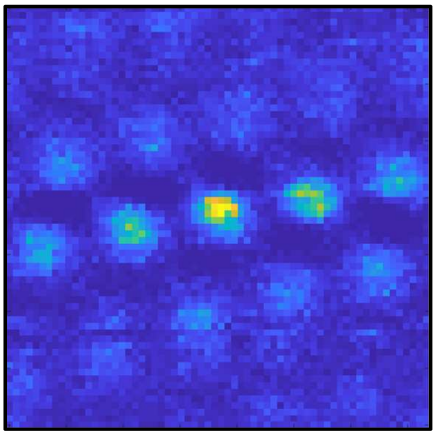

Figure 3.20: $I_{form}(\boldsymbol{r})$ of Fig. 3.19a obtained by deconvoluting the $I_{structure}(\boldsymbol{r})$ of $I(\boldsymbol{r})$. The image has the same scale and units as $I(\boldsymbol{r})$ (see previous figure).

In Fig. 3.21a we show the vortex profiles obtained from $I_{form}(\boldsymbol{r})$ for different magnetic fields. Lines are the fits to Kogan's model that allows to determine the vortex core size[83] (see also subsection 1.2.1). The resulting core sizes are shown in Fig. 3.21b (black points) and compared with the vortex core sizes obtained previously using a different method to determine the vortex profile. We find a very good agreement between both methods.

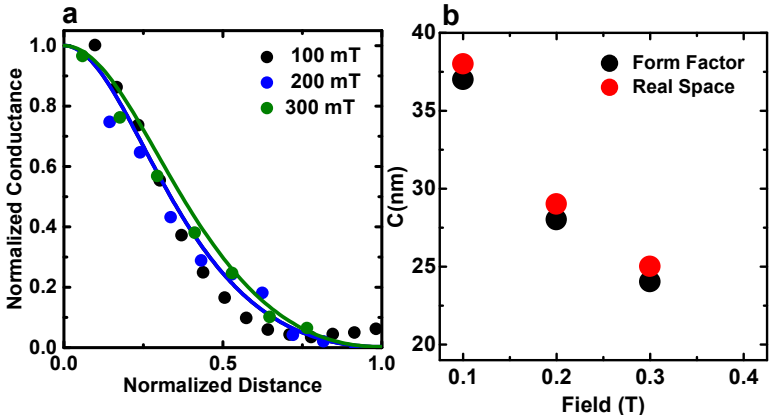

Figure 3.21: In (a), we show vortex core profiles obtained from the form factor (points) and the fitting to Kogan's model lines. (b) shows the vortex core size vs field obtained using the two different methods to get the vortex profiles.

We also want to test the method with a more exotic example. We applied the convolution to the star-shape vortices in 2H-$NbSe_2$, [84]. In Fig. 3.22 we show the

result of applying the procedure described above to obtain the form factor of vortices in 2H-$NbSe_2$. Vortex cores in 2H-$NbSe_2$ have a sixfold star shape (Fig. 3.22a). Using the image shown in Fig. 3.22a, Equation 3.3 and Equation 3.4, we can obtain the form factor. The result is shown in Fig. 3.22b. As the vortex is six-fold, it is rather difficult to understand a radial average and see study its variation with the magnetic field. However, this example helps us understanding the meaning of the form factor. By making the procedures described here, we make an average over the shape of all vortices. Thus, the form factor presents a vortex shape averaged over many vortices.

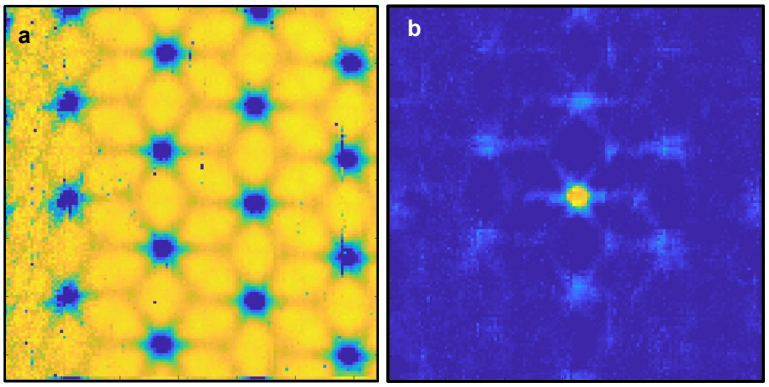

Figure 3.22: (a), Vortex lattice image in 2H-$NbSe_2$ taken at 0.1 K and 0.1 T [84]. (b), Form factor of the vortex cores in this material using the procedure described in the text.

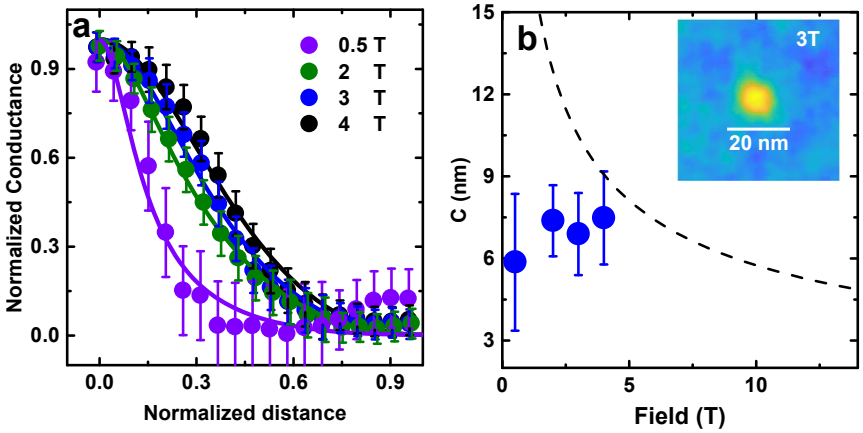

Figure 3.23: In (a), vortex profile taken from the normalized zero bias map vs normalized distance ($r/2a_0$) for different fields. Point are experimental data and lines are the fit to Kogan's model [21]. In (b), we plot the size of the core as a function of field. The vortex core size does not change with magnetic field. Dashed line is the behaviour expected for a superconductor in the clean limit with coherence length of ≈ 4-5 nm. The inset shows an example of the form factor image at 3T.

Now that we first tested the method for obtaining vortex core profiles, we apply this method to the vortex lattice of Ni doped $CaKFe_4As_4$. Fig. 3.23a shows profiles of

the vortex cores taken from the normalized zero bias conductance maps at different magnetic fields. Lines show the fit to the model described in subsection 1.2.1 [21]. The resulting vortex core size is plotted in Fig. 3.23b as a function of the magnetic field. We find that the vortex core has a size of about 7 nm that remains constant with the magnetic field. As we have discussed earlier, this is expected, as $CaKFe_4As_4$ doped with Ni is in the dirty limit. This behaviour is different than the $1/\sqrt{H}$ dependence observed in the clean limit, which is also roughly obtained in pure $CaKFe_4As_4$.

3.4 Discussion

As we showed in Fig. 3.8, $CaK(Ni_{0.05}Fe_{0.95})_4As_4$ has an open V-shape superconducting gap with almost non-existent quasiparticle peaks and a large zero bias conductance. In the stoichiometric compound, however, the gap is completely opened with zero bias conductance and has multigap features consistent with $s_\pm$ superconductivity [22, 76].

Still, in some areas of the parent compound $CaKFe_4As_4$, tunnelling conductance disappears and a finite contribution at zero bias appears near defects areas as a consequence of pair breaking. The doped system has much more scattering and pair breaking probably occurs all over the sample. Often, we observe lines where the superconducting gap is fully closed. This occurs along lines that are seen in the topography (Fig. 3.15b and Fig. 3.6a) as well as in optical and SEM images of the surface (Fig. 3.7). Similar lines are observed in pure $CaKFe_4As_4$ and it has been shown that they produce vortex pinning and determine the direction of the vortex lattice. Here, there seems to be additional disorder in between those lines, producing a more disordered vortex lattice and strong pair breaking effects everywhere (Fig. 3.16) [22, 49].

Now the question arises if the zero bias conductance is related to the hedgehog magnetism or due to extended defects. Probably, the presence of magnetism has a certain influence, increasing the strength of pair breaking by defects.

In the pure compound, the role of disorder is not as dramatic as in the Ni doped compound. It has been shown that highly disordered samples of $CaKFe_4As_4$ maintain a similar critical temperature [85]. We can thus speculate that, in absence of hedgehog order, the Ni doping induced disorder should not lead to such a large influence on the superconducting properties as we observe here. Thus, part of the pair breaking might be due to the magnetic properties of the Ni doped compound.

Recently, penetration depth measurements have been done in this compound for Ni concentrations of x = 0.17 and x = 0.34 [86]. They find a nodeless two gap superconductivity compatible with $s_\pm$ pairing (see table 3.1). Assuming a linear dependence of the gap values with x, we find that for x=0.049, the superconducting gap values would be $\Delta_1 \approx 0.4$ meV and $\Delta_2 \approx 1.5$ meV . Δ_2 corresponds to the maximum in the gap distribution we have obtained from our data (see in Fig. 3.8). Δ_1 has also an important weight in the gap distribution although we do not

distinguish a local maximum around this gap value.

Ni doping %	Δ_1 (meV)	Δ_2 (meV)
0	-2.76	8.66
1.5	-2.11	6.82
3.4	-1.14	4.14
4.9	-0.4	1.5

Table 3.1: Gap measured in Ref. [86] for Ni doping (x) of 0, 1.5% and 3.4%. The gap values for 4.9 % Ni-doping are calculated by fitting the gaps measured in [86] vs x to a linear dependence and extrapolating the gap value.

The vortex lattice may also be affected by the magnetic order. We can compare our results with those obtained in the parent compound. Translational order in the Ni-doped system decays much faster. While in the parent compound, it decays in $3.5a_0$ in our system, it is suppressed in about $2a_0$. Also, if we compute the defect density of the lattice we obtain a 53% of vortices with more or less than 6 first neighbours, while in the parent system the defect density is 46% of total number of vortices. Furthermore, pair breaking effect is more important in Ni-doped compound as it does not happen only in line defects, but we observe it in form of a finite zero bias conductance over the whole surface. Thus, the doped sample has more defects than the undoped sample, and this probably influences vortex pinning.

The influence of the doping is also observed by looking to individual vortices. In the Ni-doped compound, vortex core size does not change with magnetic field and we did not observe a zero bias peak in the center of the vortex. In the parent compound there is a dependence of the vortex core size with field, and zero bias peak is observed. Thus, the Ni doping has decreased drastically the mean free path going from a clean limit superconductor in $CaKFe_4As_4$ to dirty limit superconductor in $CaK(Ni_{0.05}Fe_{0.95})_4As_4$.

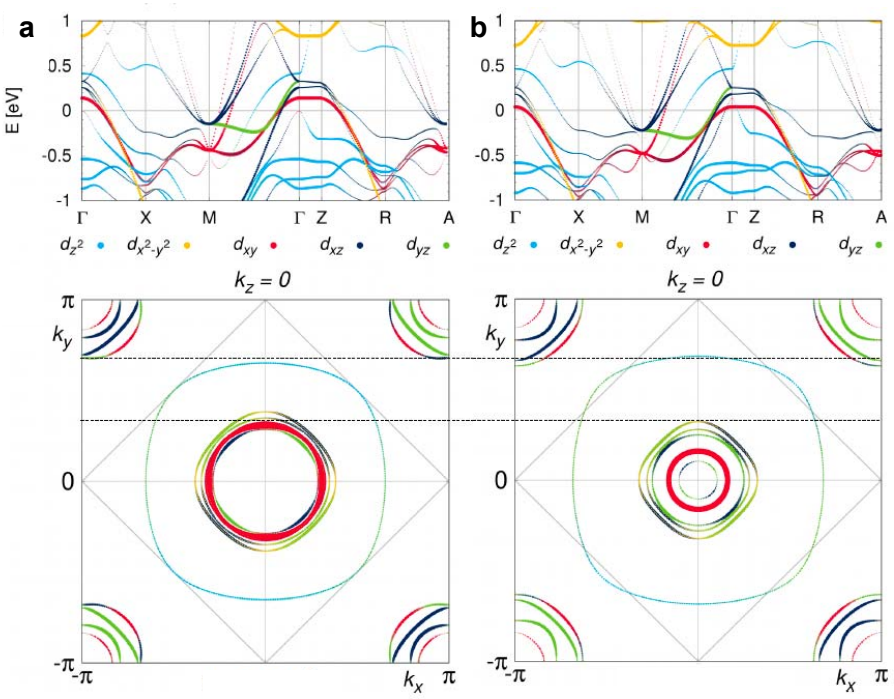

Figure 3.24: We show a comparison between the bandstructure (top) and the Fermi surface (bottom) of the stoichiometric compound in (a), and the 5 % Ni-doped system in (b) in the paramagnetic state.

A related important point is how the doping level or hedgehog magnetic order affects the Fermi surface. First, let us compare scattering pattern of both stoichiometric and doped sample. The scattering pattern of $CaK(Fe_{0.95}Ni_{0.05})_4As_4$ is very different than the pattern found in $CaKFe_4As_4$ [22]. The first remarkable point is the enhanced scattering, pointing out the presence of much more disorder in $CaK(Fe_{0.95}Ni_{0.05})_4As_4$.

R. Valentí and V. Borisov have calculated the bandstructure of the pure and 5% Ni-doped compounds with DFT in Fig. 3.24(a-b) respectively. When comparing the electronic bandstructure in both compounds, we find a slightly increase of electron pockets and a significant shrink of most hole pockets in the Ni-doped compound. This is in agreement with the fact that the substitution of Fe by Ni introduces electron doping in the system. We have compared the qpi vectors obtained in Fig. 3.13 with the Fermi surface of Fig. 3.24b. We find that these vectors do not match with any possible scattering vector in this FS. Indeed, our result is not surprising because the Fermi surface of Fig. 3.24b corresponds to the paramagnetic state and the qpi measurements are made in the hedgehog AFM state.

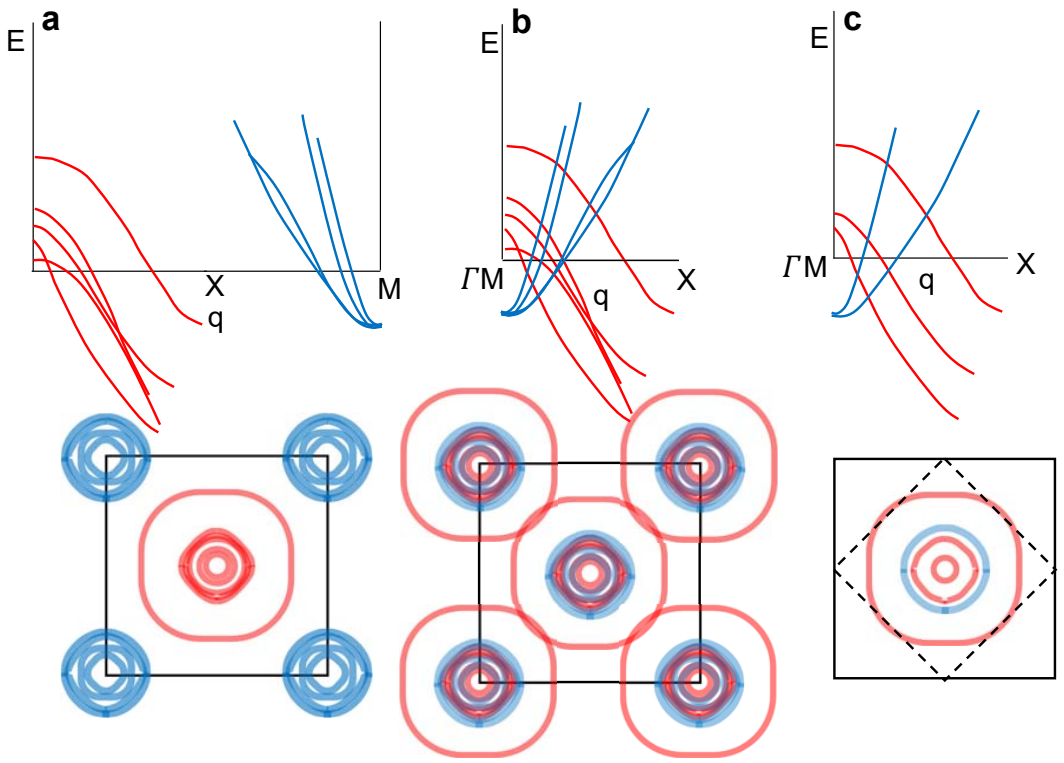

Figure 3.25: In (a) we show schematically the band structure (top) and Fermi surface (bottom) in the paramagnetic state of the $CaK(Fe_{0.95}Ni_{0.05})_4As_4$. In (b), bandstructure folded by the hedgehog antiferromagnetic vectors. (c), Bandstructure in the hedgehog antiferromagnetic state. We have removed the gapped bands in the Fermi level due to hybridization of electron and hole bands. Squares with continuous and dashed lines represent the first Brillouin zone in, respectively, the paramagnetic and Hedgehog antiferromagnetic states.

If instead we assume the existence of the hedgehog antiferromagnetic order, the magnetic unit cell is doubled. This results in a folding of the band structure along the AFM vectors as shown in Fig. 3.25 (see subsection 1.3.3). Fig. 3.25a shows schematically, the paramagnetic Fermi surface of Fig. 3.24b. Fig. 3.25b shows the result of folding the band structure along the hedgehog antiferromagnetic vectors. We find that some hole-like and electron-like band cross exactly at the Fermi level. As we discussed in subsection 1.3.3 these bands hybridize and a gap appears at the Fermi level. Therefore, these bands will not contribute to the electronic band structure close to the Fermi level in the hedgehog antiferromagnetic state, and we could remove these from the discussion. The reconstructed bandstructure resulting from the folding in the hedgehog antiferromagnetic state is shown in Fig. 3.25c.

Fig. 3.26 shows in detail the FS and bandstructure in the hedgehog antiferromagnetic state. When we compare this bandstructure with the results from qpi measurements we observe a good matching between the qpi vectors and scattering vectors in the FS. In particular, we find that q_β (purple) corresponds to an intraband scattering vector in the inner hole pocket, and q_α (red) and q_γ (black)

are interband scattering vector between electron and hole pockets. In addition, we find that the dispersion of these scattering vectors given by the reconstructed band structure of Fig. 3.26b is hole-like. This is in agreement with results from qpi, where we observed that the three qpi vectors, q_α , q_β and q_γ, decrease its size with increasing energy (Fig. 3.13). Our qpi measurements reproduce the in-plane anisotropy in q_γ also observed in band structure calculations (Fig. 3.26a and Fig. 3.13). As we find in the experiments, q_γ is larger along Γ-M direction than along Γ-X direction. This simple analysis of the consequences of band-folding calls for a more detailed account of the bandstructure in the magnetic phases, a recurring problem which is difficult to address theoretically.

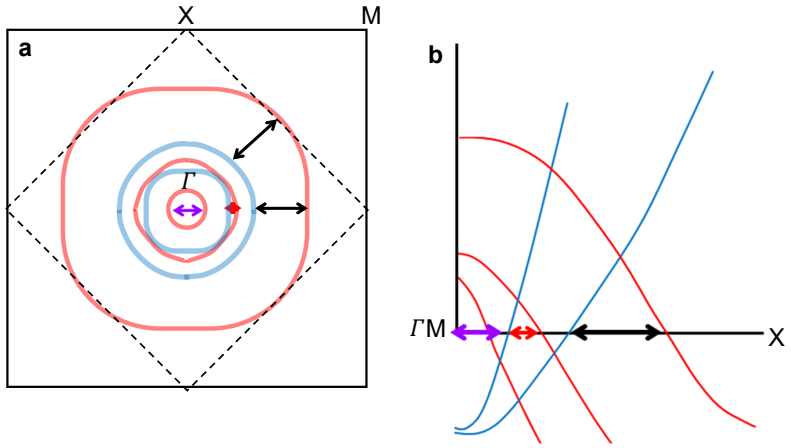

Figure 3.26: We show the final Fermi surface (a) and bandstructure (b) of $CaK(Fe_{0.95}Ni_{0.05})_4As_4$, in the hedgehog antiferromagnetic state. We compare the scattering vectors obtained in our qpi measurements shown in Fig. 3.13 (coloured arrows, purple for q_β, red for q_α, black for q_γ) with the band structure observing a good agreement.

We should also note that we find a four-fold symmetry of the superconducting gap in a small part of the bandstructure (Fig. 3.14a). The gap is smallest along the Γ-M and largest along the Γ-X direction. We compare Γ-X (parallel to a) and Γ-M (45° to a) directions with the magnetic moment orientation in the hedgehog phase (Fig. 3.14b). We observe that along the direction of a, the hyperfine field in the As1 sites (blue) cancel with each other, while, along Γ-M, the hyperfine field in the As1 sites (blue) have the same orientation. This strongly suggests that the anisotropy of the superconducting gap is caused by the hedgehog magnetic order, and confirms the mutual influence of disorder and magnetism in producing in-plane isotropic properties in many properties of this compound, such as gap anisotropy, the vortex core shape or vortex lattice symmetry.

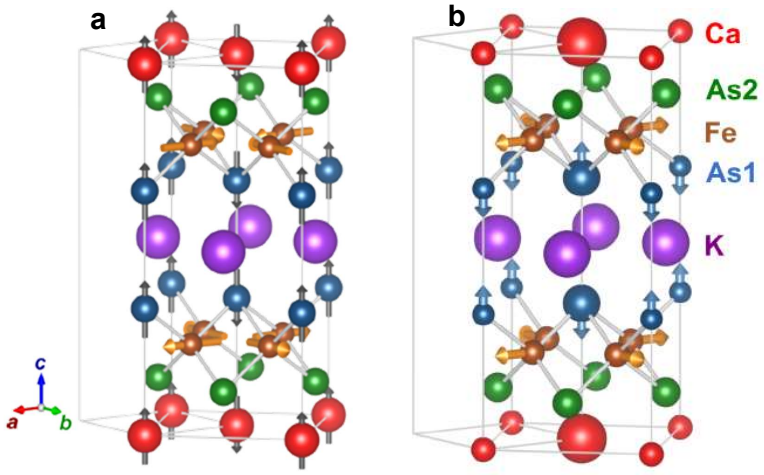

Figure 3.27: In (a) we show the crystal structure of $CaKFe_4As_4$. (Ca in red, K in violet, Fe in orange and the two inequivalent As in green (As2) and blue (As1)). Grey arrows represent the hyperfine field on Ca and on one of the As sites. Orange arrows represent the magnetic moments leading to the hedgehog order. In (b) we represent the same structure. The size of the Ca atoms provide possible local variations of the charge density. The blue and orange arrows represent the atomic displacements observed in the Fe and As1 sites, respectively. The atomic displacements and the associated charge density variations have been proposed in [73] as a consequence of the symmetry properties of the hedgehog charge order. These variations are only expected in the presence of a finite magnetic field. The crystalline axis (of the paramagnetic structure) are shown in the bottom left of (a). Image taken from [73].

Let us further investigate the consequences of the hedgehog order. As was shown by Meier, [73], there is a symmetry imposed modification of the crystalline structure, resulting in a slight periodic modulation of atomic positions. Using our real space imaging capabilities, and the fact that we sometimes obtain atomic resolution, we have explored this possibility in the locations with atomic resolution.

In Fig. 3.27 we show a sketch of the magnetic moments of the different atoms in hedgehog phase taken from his thesis [73]. The magnetic moments of the hedgehog phase are at the iron atomic sites. Furthermore, there are hyperfine fields at Ca and As1 sites. In presence of a magnetic field, the hyperfine field leads to displacements on the Ca atoms along the diagonals of the unit cell. In Fig. 3.28 we show an atomic resolution image taken at 3 T.

We identify two clear peaks in the Fourier transform. One corresponds to the interatomic spacing between Ca atoms (yellow arrow). The other one, to $\sqrt{2} \times \sqrt{2}$ of the interatomic spacing. Now we can consider two different situations to explain such a pattern.

First, the Ca lattice might be reconstructed at the surface in a $\sqrt{2} \times \sqrt{2}$ lattice, in which case, the Bragg peak marked by a white circle in Fig. 3.28b might be due to such a reconstruction. Then, the peak marked by a yellow arrow could only be due to the As lattice which should pop up below the Ca lattice. The corresponding

pattern in real space is shown in Fig. 3.28c. Second, the Ca lattice might show the charge modulations discussed above, in which case the corresponding real space patterns is shown in Fig. 3.28d.

The Fourier transforms of both lattices (their modulus, more exactly) are the same. Both images consist of two interpenetrating square lattices, and the origin of one of these lattices is just shifted by the black arrow marked in Fig. 3.28d. The image of Fig. 3.28a is highly disordered. There are missing rows and the intensities vary as a function of the position, probably due to charge variations produced by these missing rows. Nevertheless, we can try to see which one of the two configurations is more likely, by looking at the part of the image which is more ordered.

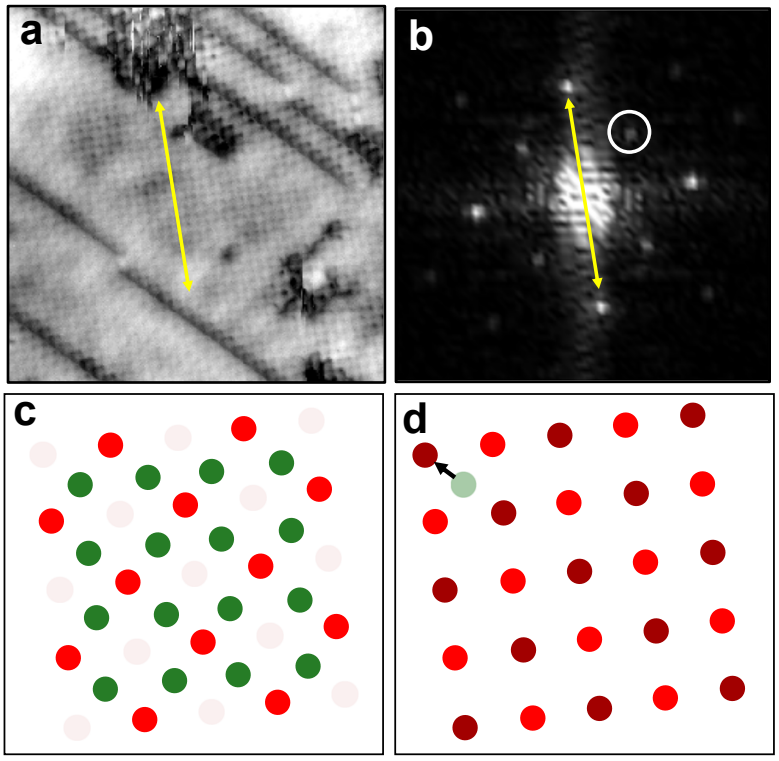

Figure 3.28: In (a), a topographic image at H=3 T with atomic resolution. Yellow arrow indicates the orientation of the lattice. FFT of (a) is shown in (b). we clearly observe two peaks. One, highlighted by the yellow arrow, coincides with the interatomic distance of the Ca atoms. Another one is at $\sqrt{2} \times \sqrt{2}$ of this distance. In (c) and (d) we show two possible scenarios that can produce the same FFT. In (c), the modulation of the Ca atoms as a consequence of the hedgehog [73]. In (d) we observe the reconstruction of Ca atoms in red and beneath the atoms of As in green. Black arrow marks the displacement from (c) to obtain (d).

In order to be able to distinguish between both scenarios we first crop the topographic image in a free of defects area (see Fig. 3.29a). In b and c, we filter out all the signals except the atomic and the reconstructed lattices respectively.

As we see, the pattern shown in Fig. 3.29d is more consistent with the lattice

as shown in Fig. 3.28d. In an STM image, the real difference between patterns Fig. 3.28c and Fig. 3.28d correspond to different heights. In Fig. 3.28c, there are two atomic species, Ca and As, with the As atoms located below the Ca atoms. This should result in dips at the positions of the As atoms. In the image Fig. 3.28d, there is however a charge density difference, which should also result in a height difference. Thus, the observable difference between both images is a differing distribution of peaks and troughs in real space. Notice that this does not occur in the amplitude of the FFT, which is the same for both cases.

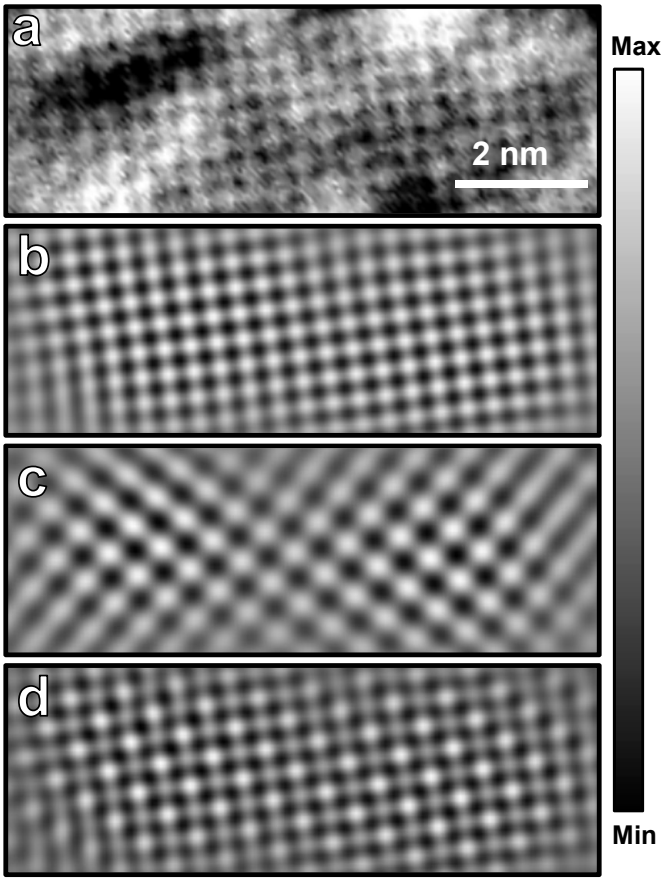

Figure 3.29: In (a) we show a crop of the image in Fig 3.28a in an area free of defects. (b) and (c) are filtered images to only have the contribution of the atomic and reconstructed lattices respectively. In (d), we sum both of them and we observe a very good agreement with the picture of a modulation in Ca atoms.

3.5 Conclusions

$CaK(Fe_{0.95}Ni_{0.05})_4As_4$ has a magnetic hedgehog order coexisting with superconductivity. We have performed the first measurements with STM in this material. We obtained a gap curve pointing to a $s_{\pm}$ superconductivity and with a finite signal at zero bias. We were able to follow the gap with temperature obtaining T_c of 9.5 K.

We have also observed vortex lattice showing a very disordered Abrikosov triangular lattice with pair breaking effects. The vortex core does not change with magnetic field and we do not observe any zero bias peak in the core of the vortex. These results indicate that Ni-doped $CaKFe_4As_4$ is a dirty limit superconductor.

QPI measurements show three scattering vectors q_α, q_β and q_γ. q_α, q_β are nearly isotropic but q_γ has a four-fold in-plane anisotropy. We have found that these qpi vectors correspond to scattering vectors in the reconstructed Fermi surface due the hedgehog antiferromagnetic state. Our qpi data also shows the opening of the superconducting gap in the reciprocal space. In particular, we have observed that the gap open in the Fermi pockets associated to q_γ has a fourfold in-plane anisotropy, being maximum along Γ-M direction and minimum along Γ-X direction. Our qpi results provide microscopic evidence for the coexistence of superconductivity and hedgehog antiferromagnetic order, and suggest that this coexistence produces the strong anisotropy observed in the superconducting properties of this material.

We also have identified a modulation of $\sqrt{2} \times \sqrt{2}$ in Ca atoms possibly produced by a charge order associated to the hedgehog magnetic order.

4 | The vortex gel

4.1 Spatial inhomogeneities in the superconducting phase

Vortices are quantized flux lines that repeal each other, and in order to minimize the energy, they usually fill all available space. The behaviour of vortices has some parallels to the behaviour of large arrangements of particles or molecules, and impacts other fields, such as soft matter. One main consequence of the repulsive interaction between vortices, is that the vortex density is spatially homogeneous with small fluctuations due to thermal or quenched disorder [18, 19]. Different vortex phases have been observed as a result of the balance between vortex interaction, thermal energy and pinning energy. Among them, we find free-defect vortex lattices such as the so-called Bragg glass, and disordered arrangements due to point-like disorder (disordered glass), columnar defects (Bose glass) or thermal fluctuations (vortex liquid) [87, 29] (see subsection 1.2.2).

Despite of their different arrangements, these vortex phases have in common a homogeneus distribution along the space. However, a few exceptions have been found at very low magnetic fields where vortices are far apart and, thus, the intervortex repulsion is negligible.

For instance, in MgB_2 at very low fields (~ 1 Oe)[88, 89, 90], a highly inhomogeneous lattice with unequally distributed vortices has been found using Bitter decoration (Fig. 4.1b). MgB_2 is a two-gap superconductor. Authors suggested a combination of type I and type II superconductivity leading to a peculiar vortex-vortex interaction. At short distances vortices strongly repeal each other, but there are also long range weakly attractive vortex interactions. With this particular interaction, vortex distribution presents a highly inhomogeneous arrangement in form of clusters of vortices. Authors find a histogram of first nearest neighbour distances with two peaks, suggesting two different length scales. These length scales have been connected to the two-band characteristics of superconductivity in this compound, and a new term, 1.5 superconductivity, was coined to describe the observed behaviour [91, 23].

Spatially inhomogeneous vortex patterns have been found using neutron scattering in ultra-pure single crystals of Nb [34, 92], as we show in Fig. 4.1c. Here, the spatial inhomogeneities are due to the properties of Nb, which is a low κ superconductor with a relatively large first critical field H_{c1}. The magnetic field enters well below H_{c1} because of demagnetizing effects (see subsection 1.2.2). Instead of having interspersed normal and superconducting areas, as in type I superconductors, Nb

presents areas with and without vortices that form the intermediate mixed state (IMS) briefly mentioned in subsection 1.2.3. The vortex lattice in the droplets is highly ordered in a hexagonal symmetry whose principal axes lock to the crystal lattice [34].

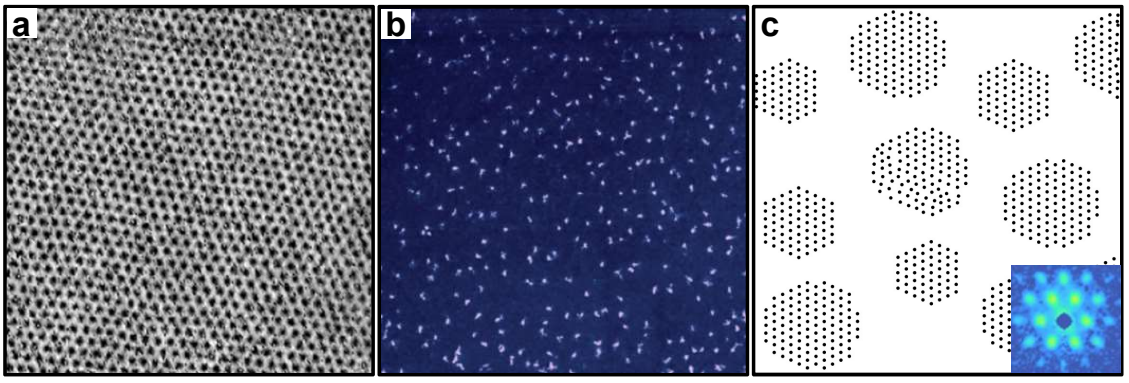

Figure 4.1: (a) Most common vortex distribution is a triangular lattice filling all available space. Image taken with STM in W-based films at 2.5 T [29]. (b) Vortex arrangement in MgB_2 [88], there are some voids and the lattice is very disordered. (c) Simulation of vortex arrangement in ultra-pure single crystals of Nb measured with small angle neutron scattering (SANS) [34]. Vortices are ordered in hexagonal droplets of different size. Inset shows the diffraction pattern obtained by SANS.

In type I superconductors, the arrangement of normal and superconducting areas has also been under debate. In Ref. [93], an interesting parallel is drawn with the physics of froths. Froths are found in many different systems in nature, in metallurgy, biological cells, or foams [94, 95]. In such systems, the shape of the foam is determined by the shape of cells, which change their arrangement and size with temperature or other parameters. Usually, these changes are due to diffusion of vapour molecules between cells or drainage of liquid from cell walls. We show an example in Fig. 4.2a. Other examples are ferrofluids or magnetic domain structures [96]. In all these processes, cells are modified through mass transport.

Fig. 4.2b shows the superconductor froth-like system. This consists on a froth-like distribution where the interior of the cells are in the normal state and the cell boundaries are superconducting. This was named *suprafroth* as it is a superconducting froth [93]. This new phase is tuned by magnetic field and temperature. Authors of this work verified Euler tiling theorem, stating that 6-side polygon is the most likely to form. They also studied von Neumann law (Fig. 4.2c) predicting linear dependence between the rate of change of the average area with the number of sides of a n-fold polygon A_n. The variation of the area was obtained with magnetic field and temperature.

In this chapter, we report the observation and characterization of vortex arrangements at very small magnetic fields showing spatially inhomogeneous patterns in the type II superconductor β-Bi_2Pd. As we will see, the results provide distinctive features with respect to previous observations. We suggest that these features might be generic to type-II superconductors at very low magnetic fields and

have not been detected in previous work.

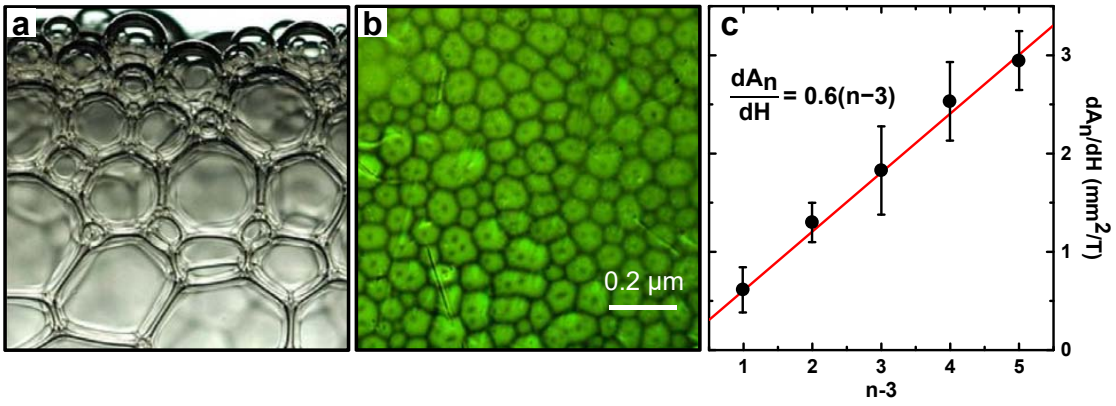

Figure 4.2: (a) Classical foam system of bubbles, when the number of bubbles is increased they touch each other forming polygon of different sizes and faces. (b) Suprafroth state in the intermediate state of a type I superconductor in [93]. Superconducting regions are shown in black and green regions are in normal state. In (a) superconductor, the cell size increases and decreases just by modifying the magnetic field. Increasing and decreasing the magnetic field leads to qualitatively similar patterns. (c) von Neumann law, describing the cell size in the intermediate state of Pb. The plot shows the area of the polygon as a function of the number of polygon sides [93].

4.2 Characterization of β-Bi_2Pd

β-Bi_2Pd is a binary alloy superconductor first reported by Zhuravlev [97]. This material is very interesting for local probe experiments, because it has an excellent and stable surface that can be easily exfoliated [98, 62].

The crystal structure is tetragonal, in the space group *I4/mmm* with constants a=3.362(1)Å and c=12.983(1)Å. Schematically, it can be described as a stacking of square bilayers of ...Pd/Bi/Bi/Pd/Bi/Bi/Pd... along z-axis as Fig. 4.3a shows.

The Fermi surface (FS) of this material has been studied theoretically and experimentally [98, 99]. The main contribution to the Fermi surface comes from Pd 4d and Bi 6p orbitals. The FS has four main structures (Fig. 4.3b): a 2D hole-like deformed cylinder; a small hole-like pocket centred in Γ-point; electron-like 3D pockets overlapping the cylinder and with an extension until the corners of the Brillouin zone, and lastly a small pocket embedded inside the electron-like 3D pocket. It was measured with angle resolve photoemission spectroscopy (ARPES), finding two hole and two electron like pockets named as α, β and γ and δ respectively (Fig. 4.3c) [99].

Band structure calculations show some anisotropies in the chemical bondings which produce that Bi/Bi layers are less coupled than the adjacent Bi/Pd sheets. Therefore, when the sample is cleaved, Bi is the most likely surface [62].

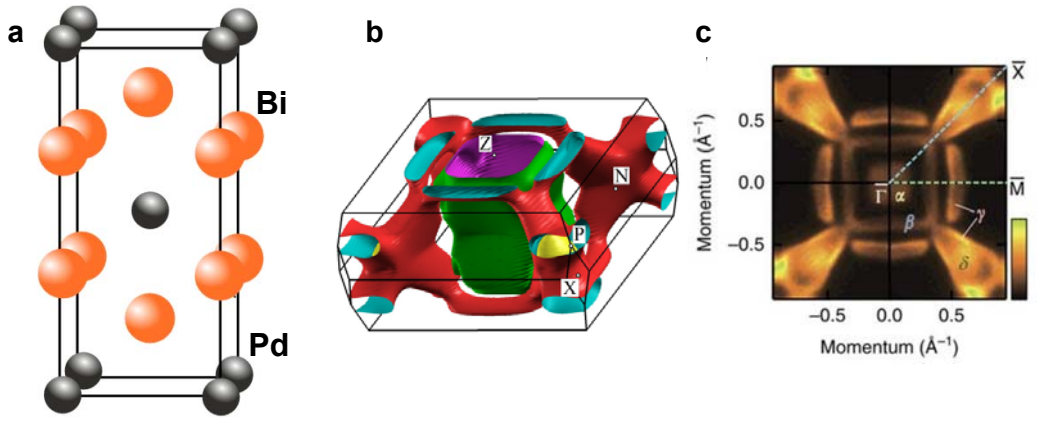

Figure 4.3: In (a) we show a scheme of the crystal structure of β-Bi_2Pd. It has a tetragonal structure in the space group of *I4/mmm*. In gray, the atoms of Pd and in orange the atoms of Bi. In (b) we show the Fermi surface of β-Bi_2Pd from bandstructure calculations [98]. In (c) we show angle resolve photoemission spectroscopy (ARPES) measurements. The Fermi surface consists on two hole and two electron like pockets named as α, β and γ and δ respectively [99].

Resistivity measurements [62] in our samples show a critical temperature of T_c= 5 K. Magnetometry measurements indicate a H_{c1}=0.0225 T [100]. Upper critical field has also been studied by susceptibility, resistivity and specific heat measurements detecting a H_{c2}=0.6 T, λ = 172 nm and ξ = 23 nm [62].

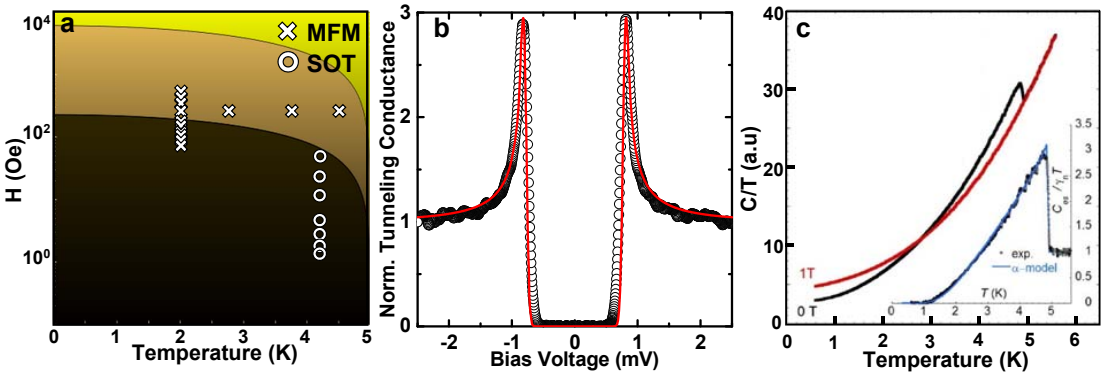

Figure 4.4: (a) Phase diagram of β-Bi_2Pd. Dark brown is used for Meissner state, light brown for mixed state and yellow for normal state. SQUID-on-tip (SOT) and magnetic force microscopy (MFM) measurements have been taken at the temperature/magnetic field values highlighted by crosses and circles. (b) Superconducting gap of β-Bi_2Pd measured at 150 mK with STM. Red curve is a fit to single gap BCS superconductivity [62]. (c) Specific heat vs temperature at zero magnetic field (black curve) and under magnetic fields (red curve), from Ref. [100]. In the inset, we show the subtracted electronic specific heat together with a fit to single gap BCS superconductivity [100].

β-Bi_2Pd is a single gap superconductor, as shown by the tunnelling spectroscopic data measured using STM experiments at very low temperatures (Fig. 4.4b, from

Ref. [62]) and by the temperature dependence of the specific heat (Fig. 4.4c, from Ref. [100]).

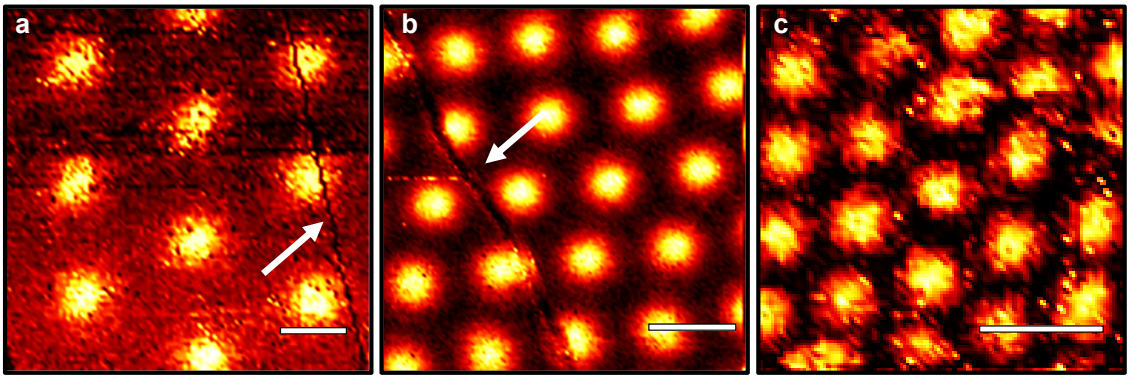

Figure 4.5: Superconducting vortex lattice measured by STM ([62]) at 150 mK and 50 mT (a), 200 mT (b) and 450 mT (c). The panels show vortices as bright spots with normal or near to normal superconducting density of states. White lines indicate the scale of the images and each are 100 nm in size. The vortex lattice is well ordered and vortices are generally round. The orientation of the lattice locks to the square crystalline axis, giving two main orientations (see Ref. [62]). White arrows show linear features in the images. These features are due to linear defects in the topography. We discuss this in length further on.

STM measurements also show the topography of the surface, which is atomically flat and where the Bi atomic lattice can be easily observed [62]. The images show clear steps, whose size is of an integer multiple of the size of the Bi-Pd groups. The vortex lattice is clearly observed (Fig. 4.5). Vortices orient along the crystalline axis of the square atomic lattice [62]. No pinning is observed, with a vortex lattice being largely hexagonal. The linear features in the topography do not influence the vortex positions, at least in the field range shown in Fig. 4.5.

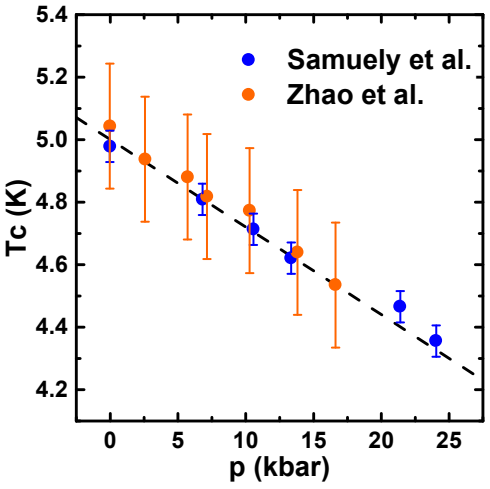

Figure 4.6: T_c as a function of pressure shown as orange points [101] and blue points [102]. The dashed line corresponds to dT_c/dp = -0.025 K/kbar.

There are also two studies on β-Bi_2Pd (Fig. 4.6) with applied pressure [102, 101]. Both of them agree on a linear decrease of T_c when pressure is increased with a slope of dT_c/dp = -0.025 K/kbar. The suppression of T_c with pressure has been proposed to be due to weakening of electron-phonon interactions induced by the increase in the phonon frequencies with pressure. The opposite has been recently proposed to occur if negative pressure could be applied using a gate [103].

4.3 Results

4.3.1 Vortices at low magnetic fields. Imaging.

Here we focus on data measured at low fields in a range of ~ 100 to 600 Oe with a magnetic force microscope, MFM [104], and at very low fields in a range of ~ 10 to 50 Oe with a squid on tip, SOT [12]. All data in this chapter have been taken previously by Alex Correa and Yonathan Anahory. It is also important to note that my work starts to be described from subsection 4.3.4 onwards, with the calculation of the standard deviation and of the fractal properties of the vortex lattice. I also participated strongly in understanding the features created by the cleaving process due to fracture. However, my main contribution is from subsection 4.3.4 on, also including the comparison to other systems such as the cuprate Bi2212 superconductor.

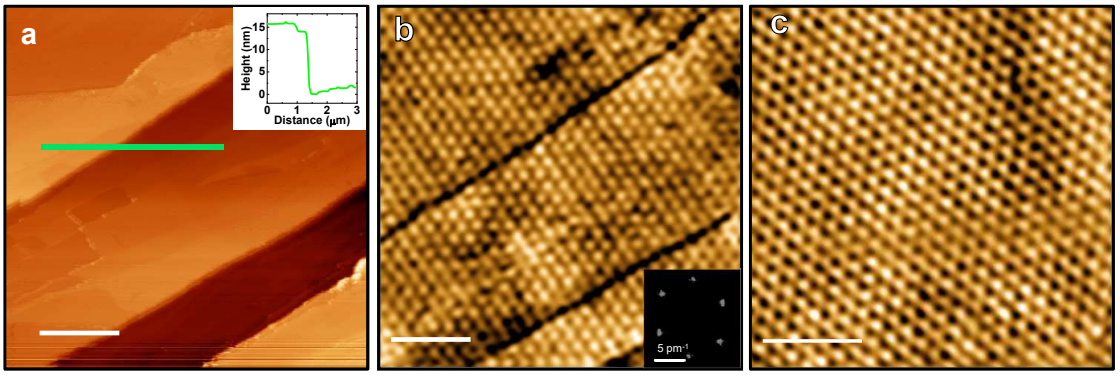

Figure 4.7: (a) Typical topographic AFM image, with a line profile that show a 15 nm step in the inset (green line). (b) MFM image showing the vortex lattice at 2 K and 300 Oe and its Fourier transform (inset). The vortex lattice is clearly hexagonal over the whole area. White color denotes the normal phase and black the superconducting phase. Dark lines and other darker regions in the MFM image are the result of the non-magnetic tip-sample interaction. The scale bar in both images is of 1.4 μm. (c) Vortex lattice at 600 Oe and 2 K with a scale bar of size 1 μm.

MFM measurements were acquired using a commercial Low-Temperature SPM equipment from Nanomagnetics in a 300 K - 1.8 K temperature range. Both topographic and magnetic information were simultaneously taken (Fig. 4.7(a-b)), by doing the so-called *two pass mode* with the cantilever oscillating at its resonance

frequency. First, topography is measured with a tip-sample distance of less than 10 nm, where Van der Waals (VdW) forces dominate. Resonance frequency is kept constant and the shift in the amplitude oscillation, due to the VdW interaction between cantilever and sample, is measured. In order to measure magnetic field, the tip is lifted up to 100 nm where VdW forces are very small compared with magnetic forces, and the same scan is repeated. In this case, tip-sample distance is kept constant using the previous topographic information and the phase shift of frequency is measured. The tip is previously magnetized by applying a magnetic field of 1500 Oe at 10 K [53].

Atomic force microscopy images provide flat topographic images with steps of about 10 nm in size. In Fig. 4.7(b-c) we show some examples of the vortex lattice at 300 Oe and 600 Oe at a constant temperature of 2 K measured in field cooled conditions. All of them present a very well ordered triangular lattice indicating a very similar result to that obtained in the STM measurements (Fig. 4.5). Notice, however, that here we can scan much larger areas and observe many more vortices.

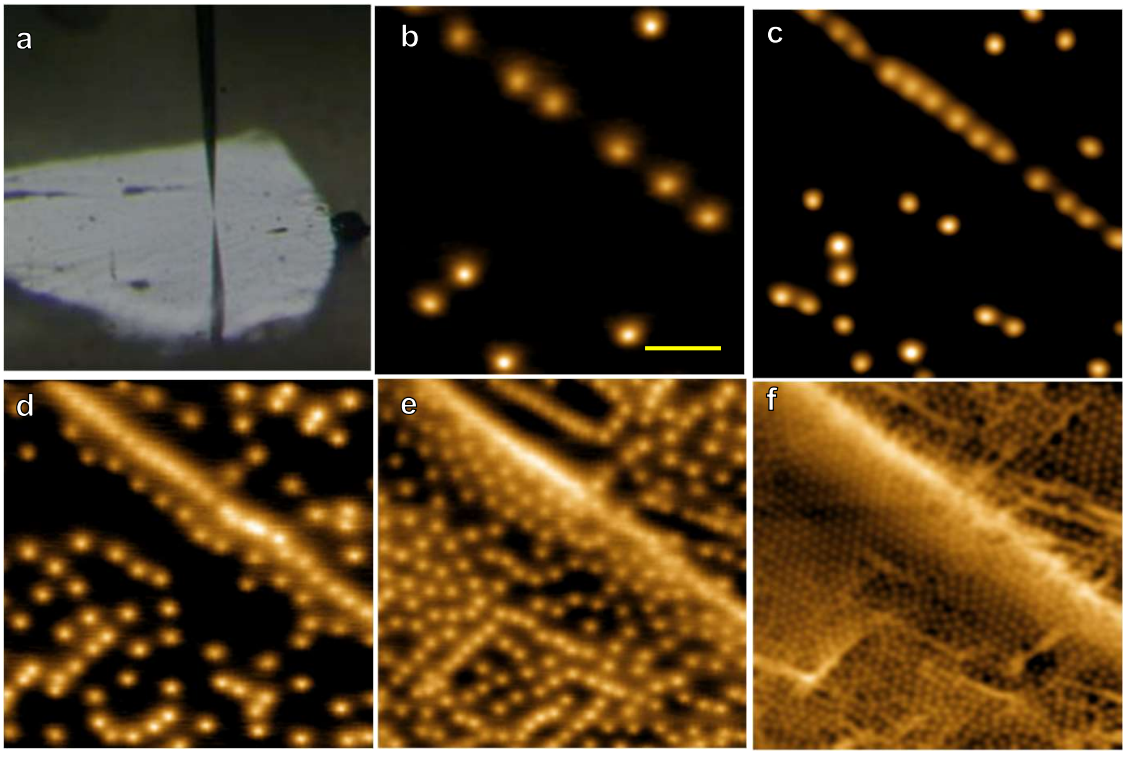

Figure 4.8: a, Optical image of the SOT at a few tens of μm from the β-Bi_2Pd surface. The SOT reflection on the surface is visible on the bottom part. b-f, 20 $\times$ 20 μm^2 SOT images that represent the out-of-plane field B(x, y) obtained after field cooling the sample in magnetic fields of 2 (b), 3 (c), 25 (d), 35 (e) and 50 (f) Oe. The color scale represents a span of 13 Oe in b-d, 32 Oe in e and 27 Oe in f. Yellow line is 4 μm long.

At very low magnetic fields, vortex lattice was measured using Squid On a Tip (SOT). SOT provides high spatial resolution imaging reaching single-spin sensitivity.

A hollow quartz tube is shaped as a very sharp pipette. Nb or Pb is evaporated in order to fabricate the superconducting loop of the nano SQUID, and then connected to Au electrodes [12]. A picture of the tip over the sample of β-Bi_2Pd is shown in Fig. 4.8a. The distance between tip and sample was typically 300 nm. The SOT used here had an effective diameter of 260 nm, a critical current of 160 μA and white flux noise of around 800 $n\Phi_0 Hz^{-1}$. All measurements were performed field cooled at 4.2 K in a magnetic field range of 2-50 Oe, well below H_{c1}.

The results obtained at low magnetic fields with SOT are very different than the ordered hexagonal lattices obtained at higher magnetic fields with MFM (Fig. 4.8(b-f)). Vortices arrange in two different ways. They either are pinned at linear defects of the sample as the ones showed in Fig. 4.7a, or they arrange filling the space between those lines. At low fields, from 2 Oe to 25 Oe, vortices filling the space are not overlapping and they are very disordered creating large vortex free areas. By increasing the magnetic field, they finally arrange in a triangular lattice filling most of the space. Vortex density is maximum along the linear defects for all magnetic fields.

4.3.2 Single vortex profile. Strain and T_c variation

From the different vortex arrangements, there is another striking feature of Fig. 4.8b. Vortices located along linear defects are less bright than those elsewhere. This effect is better visible at low magnetic fields, because at high fields, vortices overlap and the contrast is much more homogeneous. At low fields there is a clear magnetic contrast. SOT measures directly the magnetic field on the surface. Thus, the change in brightness means that the magnetic field at the vortex core is smaller along linear defects than elsewhere.

We can trace a profile along both a defect and a bulk vortex, shown as blue and black points respectively in Fig. 4.9. In order to fit the magnetic profile, first we need two parameters: distance between the tip and the sample d_{SOT} and the transfer function that converts the measured current flowing in the SOT into magnetic field (dI_{SOT}/dB). Transfer function can be calculated by measuring the current created by a known magnetic field source. We can assume that vortices far from defects, appearing brighter in the images, have a flux of Φ_0 and a $\lambda = 186$ nm. We can model the field $B(x, y)$ as a monopole located at λ below the surface and, therefore, at a distance of $\lambda + d_{SOT}$ from the sample. By fitting bright vortex in Fig. 4.8b with the fitting parameters d_{SOT} and dI_{SOT}/dB and averaging the results, we obtain a d_{SOT} = 270 nm.

Now, we can discuss two representative vortices in β-Bi_2Pd, a brighter vortex far from defects and less brighter close to a defect. We have two fitting parameters, penetration length, λ, and the vortex flux, Φ. In ref [100] a $\lambda \simeq 186$ nm is measured so, we fix first this value of λ and make the fit varying Φ, obtaining the turquoise curves in Fig. 4.9. For the vortex far from the defect we obtain a nice fit with $1.06\Phi_0$. Nevertheless, for the vortex in linear defects a poorer fit is achieved with a value of $0.62\Phi_0$.

On the other hand, if the magnetic flux is constant and λ is fitted instead, a better approximation is obtained for both cases as shown by the orange curves in Fig. 4.9. For vortices far from the linear defects, we obtain λ= 172 nm, a value very similar to this found in the macroscopic measurements. However, for vortices in the defects we calculate a value of λ =360 nm.

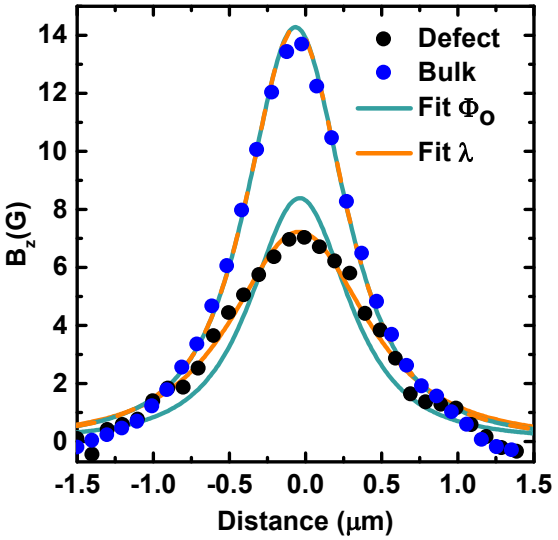

Figure 4.9: Vortex field profiles $B_z(r)$ along vortices far from a defect (blue points) and close to a defect (black points). In turquoise, the fit of the vortex profile with free parameter the magnetic flux Φ. Vortices far from defects provide an excellent fit with $1.06\Phi_0$ where Φ_0 is the flux quantum. However, to fit the vortices at defects, we need to considerably reduce Φ down to $0.62\Phi_0$. In orange, the fit of the same vortex profiles, but using the penetration depth λ as a free parameter. The quality of the orange fit is significantly better than the turquoise. We find λ = 172 nm (which is of order of λ measured using Hall probes [100]) for vortices far from a defect and λ = 360 nm for vortices at a defect.

Thus, the magnetic flux is the flux quantum, as expected for a simple s-wave superconductor, and the fit is much more accurate.

Notice that a recent work [105] suggests that circular β-Bi_2Pd structures show flux quantization at half a flux quantum. They discuss, on this basis, the possibility of p-wave superconductivity. It is unclear, at present, how this anomalous flux quantization would affect vortices. Therefore, we can conclude that λ is not constant in the β-Bi_2Pd and can increase up to its double around defects areas.

We can associate this change in λ to the stress in the sample. Generally, if dT_c/dp >0 vortices are repelled from areas with internal stress, while when dT_c/dp <0 the opposite occurs. For this sample we have a dT_c/dp = -0.025 K/kbar [102]. This can explain the higher vortex density in the areas with defects. This sample has a $T_{c,bulk}$ = 5 K and the experiments are performed at T = 4.2 K. We can calculate the

change in T_c necessary to double λ with

$$\lambda(T) = \lambda(0)/\sqrt{1 - \left(\frac{T}{T_c}\right)^4} \tag{4.1}$$

obtaining $T_c = 4.38$ K. This very subtle change in T_c can increase λ by a factor of 2. Accordingly to [102], a local pressure of about 20 kbar could drive this small change in T_c.

This variation in T_c is very difficult to observe directly. In Fig. 4.10, we show the vortex lattice as a function of temperature, taken using MFM. The images are made in the same region at 2.75 K, 3.75 K and 4.5 K applying 300 Oe. The lattice is very ordered at all temperatures with a few dislocations at 2.75 K. There is a white linear defect located at the bottom of the image at all temperatures. It is probably caused by a crosstalk between charging effects and the magnetic signal close to a large step. Crosstalk between signals should not be temperature dependent, and thus, we expect this feature not to be magnetic. Therefore, we cannot conclusively argue that this feature is due to a decrease in T_c. Still, there is a vertical white line in the center of the image only in the highest temperature, possibly indicating a decrease in T_c in some areas of the sample.

It is very difficult to be more quantitative in the determination of these changes in T_c with the three techniques used here. MFM has these charging artefacts, SOT does not allow for accurate temperature control and STM should detect a change in 50 μV which is impossible taking into account the small but finite gap distribution at 50 μV found in this compound [62].

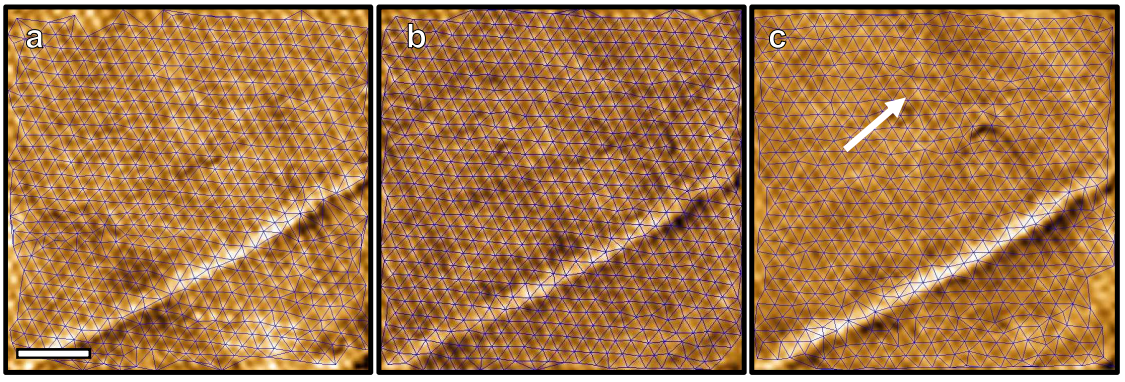

Figure 4.10: Behavior of the hexagonal vortex lattice as a function of temperature measured with MFM. (a-c) images taken at 2.75 K, 3.75 K and 4.5 K, respectively at 300 Oe. The color scale represents the observed frequency shift. Scale bar is 1 μm. The white arrow in (c) highlights the position of the vertical line.

The group of M. Milosevic has made numerical simulations of vortex behaviour close to linear defects using Ginzburg-Landau theory. The simulations are parametrized according to the values of λ, measured that are translated into small changes of T_c close to the defects and weak disorder. The behaviour close to the linear defect is modelled through a parabolic recovery of T_c at a distance of 2 μm

away from the step. This simulates pinning potential of the linear defect. The obtained vortex configuration over a 10 × 20 μm^2 area is shown in Fig. 4.11 for two values of the applied magnetic field. They capture the evolution seen in the images. At first, vortices occupy the linear defects where superconductivity is suppressed and their magnetic field is weaker than that of vortices in free defects region. Thus, a vortex free band is formed between vortices of different brightness. When the field is increased the size of the vortex free band decreases.

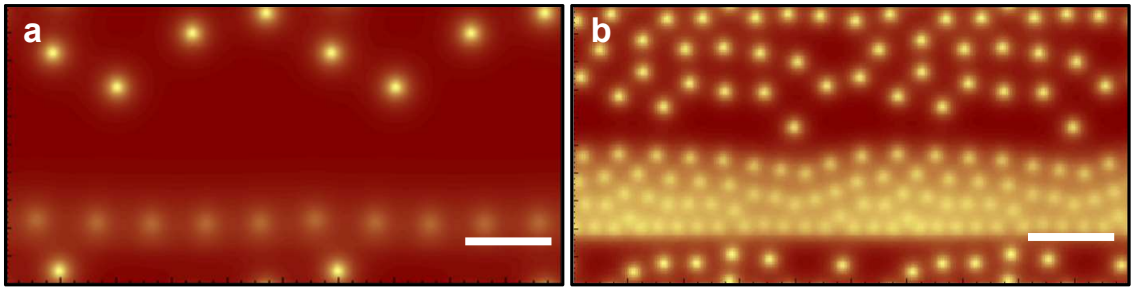

Figure 4.11: Ginzburg-Landau simulations of the behaviour of vortices close to linear defects at 2 Oe (a) and 15 Oe (b).

4.3.3 Fractographic analysis of the surface

The bonds in the tetragonal structure of β-Bi_2Pd are such that the surface is most likely formed by the square lattice of Bi atoms [98]. The cleaving plane is thus very well defined and lies perpendicular to the c-axis. There are no indications of Van der Waals like bonds as in transition metal dichalcogenides. This material has well established three-dimensional electronic properties [106]. Nevertheless, it is a fact that it can be easily cleaved using scotch tape [62, 107]. Cleavage occurs without any residues, as thick sheets of the material are removed when cleaving. The obtained surface is shown in optical and scanning electron microscope (SEM) images in Fig. 4.12. The surface is very shiny and has features which are important for the results discussed in this chapter.

Cleaving or breaking of a surface occurs through the establishment of a fracture or crack at a few places close to the edges of the sample. The fracture then propagates as a crack front through the whole sample. The action on the sample during fracture consists of tear, shear and compressive forces (called mode I, II and III fracture, respectively, see Fig. 4.12a)[108, 109, 110]. If the action would occur only along the c-axis, just tear forces that separate layers would be active. However, the competition between elastic energy and surface energy is in-plane anisotropic, leading to crack behaviour that depends on the in-plane properties of the material. This occurs irrespective of the anisotropy of the in-plane vs out-of-plane crystalline structure, and is even observed in two-dimensional Van der Waals materials [111].

In three-dimensional crystals this issue is even more important. The sample is of course not perfect and the crack front encounters defects such as small angle grain boundaries [112, 113]. In a cleaving process using scotch tape, shear forces appear

even more easily than cleaving with a knife, because scotch is highly deformable. Shear forces change the direction of crack propagation away from high symmetry crystalline lines. In addition, fracture produces a release of stress that might have been left over during crystal growth (for example by the presence of small temperature gradients). The process of releasing this load is influenced by defects and imperfections in the crystal. All of this leads to regions with alternating compressive and tensile stress and causes a twist action (combining shear and tear, modes II and III in Fig. 4.12a) that might well propagate far below the surface and influence large areas of the crystal [114].

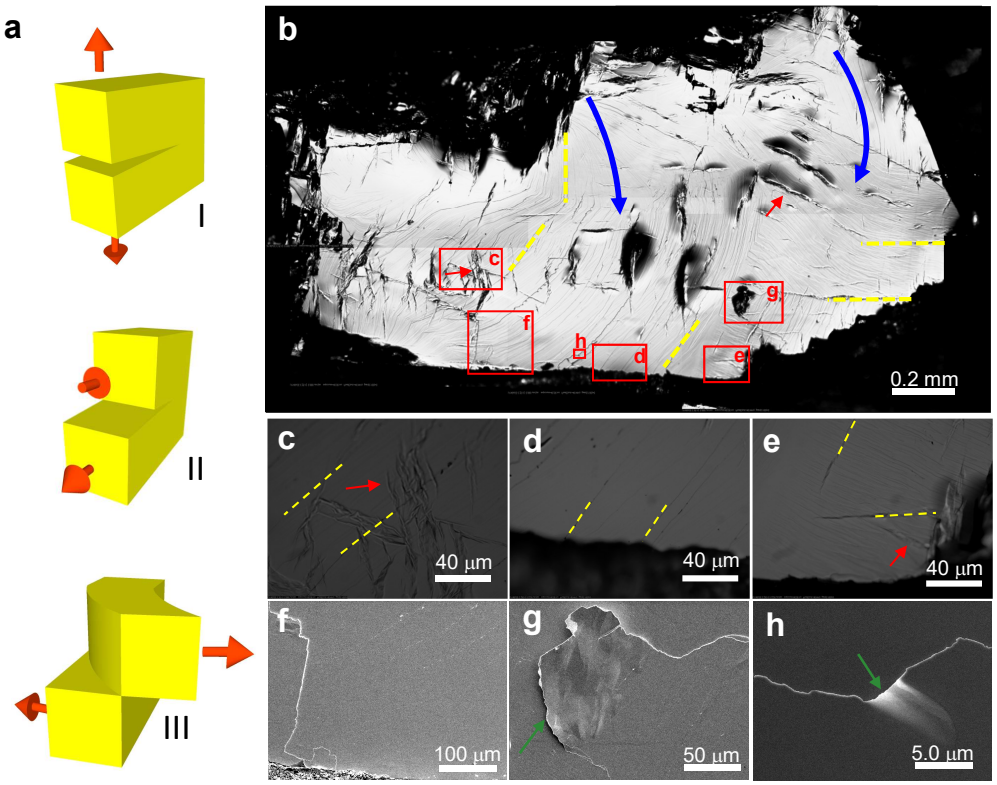

Figure 4.12: (a) Forces exerted during the cleavage process of a single crystal. In the opening mode (mode I) there is tensile stress normal to the plane of the crack. The sliding mode (mode II) describes shear stress parallel to the plane of the crack and perpendicular to the crack front. The tearing mode (mode III) a shear stress parallel to the plane of the crack and parallel to the crack front. (b) Optical picture of a sample after cleaving. We identify twist hackles (yellow dashed lines), linear features that seem step edges along crystalline directions (red dashed lines) and the debonding path, or the direction where the crack front propagated during fracture (blue lines). (c-e) Magnified areas marked by red rectangles in (b) taken using an optical camera. (f-h) SEM images. We mark places where the sample forms fully detached layers by green arrows. Images are taken at the red rectangles shown in (b) marked by the corresponding letters (f,g and h). Scale bars are of 0.2 mm in (b), 40 μm in (c), (d), (e) and (g), 50 μm in (f) and 8 μm in (h).

The features produced by this twist action are called twist hackles and must not necessarily follow a crystalline direction. They rather correspond to steps that run parallel to the crack propagation direction. In β-Bi_2Pd we observe features that can be associated to twist hackles. We mark a few of such features by yellow dashed lines in the Fig. 4.12(b-e). Close to the sample edges, twist hackles have a strong tendency to start or arrive to the end of the sample at an angle to the surface, following the crack propagation direction, as we observe in the images (blue lines in Fig. 4.12b).

However, the crack propagation direction is certainly influenced by the direction of the crystalline axis. Thus, there are also a number of linear structures at 45 or so degrees to the twist hackles that can be associated to crystalline axes (we mark a few by red dashed lines in the Fig. 4.12(b-e)). There are furthermore linear features perpendicular to all them. Thus, the surface is composed of features resulting from twisting efforts produced during fracture. The macroscopic twist is compensated by an arrangement of linear features at right angles or at 45 degrees to each other.

Let us note that we also identify large wrinkles on the surface (red arrows in Fig. 4.12b). The wrinkles appear close to very large defects (broken or open features in the Fig. 4.12a). A closer analysis using scanning electron microscopy (SEM) reveals a large number of separated layers close to wrinkles (Fig. 4.12g). Generally, step edges appear strongly marked in SEM images (Fig. 4.12(f-h)), suggesting that there is a separation of parts of the sample (green arrows in Fig. 4.12(g-h)). All this supports the presence of large twisting effort during fracture.

Our experiments are made close to the center of the sample, in locations showing no large wrinkles and the tip was carefully positioned away from optically visible defects. So that we are far from wrinkles produced during cleaving (red arrows, Fig. 4.12 b). However, the linear structures we observe in the images are certainly due to twist hackles that are all over the sample. Close to twist hackles, there is enough strain to modify the local superconducting properties, as observed in the SOT experiments.

4.3.4 Analysis of vortex positions. Calculation of average deviation

We have Delaunay triangulated the images in order to calculate intervortex distance. In Fig. 4.13a we show the intervortex distance histograms of all first nearest neighbours. Histograms show only a single peak with a very broad distribution. The peak is located exactly at $a_0 = (\frac{4}{3})^{1/4}(\frac{\Phi_0}{B})^{1/2}$ for all magnetic fields. This shows that the average intervortex distance follows the Abrikosov distance in the whole range of the magnetic field (see inset in Fig. 4.13b).

The shape of the histograms is parametrized using the standard deviation (SD) and it is shown in Fig. 4.13b. Blue points are from SOT and MFM experimental images, and orange points, from the simulations. We compared these data with results in $Bi_2Sr_2CaCuO_8$ in a similar magnetic field range for a vortex glass in pristine samples (black points) [115] and in a Bose glass in samples with columnar defects (violet points) [116].

While in the pristine and irradiated samples SD/a_0 remains mostly constant along magnetic field, in β-Bi_2Pd, it diverges at small fields. The blue line is a fit of $1/\sqrt{\mu_o H}$.

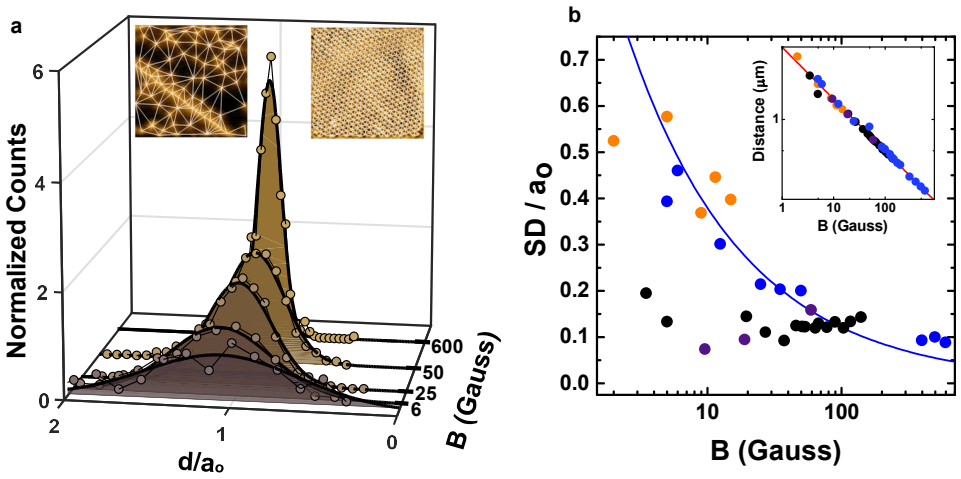

Figure 4.13: In (a), we show the histograms over the intervortex nearest neighbour distances for different magnetic fields. Histograms are normalized to give the same area. The insets show representative SOT (left panel) and MFM (right panel) images, together with the Delaunay triangulation (lines). In (b) we show the standard deviation obtained from the histograms, normalized to the intervortex distance a_0. Blue points represent the images taken with MFM and SOT. Orange points are the simulations. Black and violets points are from images of a vortex glass and Bose glass respectively [115, 116] . The blue line is $1/\sqrt{\mu_0 H}$. Inset shows intervortex distance vs magnetic field.

4.3.5 Calculation of multifractal properties

To understand the vortex distribution in the images shown previously, it is useful to first introduce fractal and multifractal analysis.

To describe this, it is useful to introduce dimensionality in a different way as we are used to. We thus introduce the topological dimension, T_d. T_d is an integer number. For a dot, it is 0, for a line, it is 1, for a plane, 2, etc. In these simple examples, T_d coincides with the usual concept of dimension. Simple objects, such as a circle, do not need additional parameters. For example, calculations of the perimeter or the area of a circle in two-dimensions are straightforward. However, calculating the length of an intricate and irregular object in two dimensions, as for instance the perimeter of a coastline, is not straightforward. We can start by choosing an object defining an area in two dimensions, whose borders are such that the shape of the border repeats itself when modifying the scale. In such an object with self-repeating patterns, the perimeter might well go to infinity. In that case, it is useful to introduce the fractal dimension, T_F, which can be understood as the ratio between the length of the perimeter and the scale used to measure such a length. We show in Fig. 4.14b an example, which is a Sierpinski triangle with T_F=1.6.

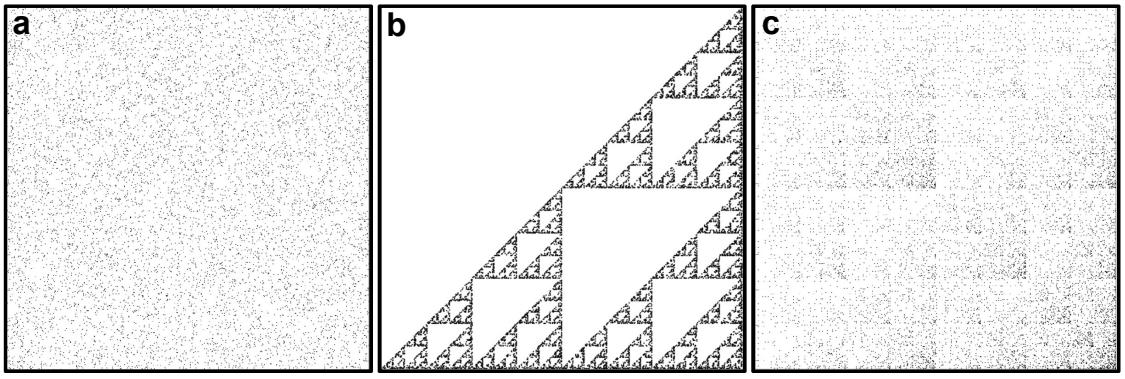

Figure 4.14: In (a) we show a random binary map. The topological and fractal dimension are the same and equals to two. In (b) a Sierpinksy triangle is shown as an example of a monofractal with a fractal dimension of 1.6. In (c) we show an example of a binary multifractal with a non standard Sierpinsky carpet.

In general, however, a self-repeating pattern might not arise exactly. A coastline is certainly not repeating itself exactly at all length scales. It has been shown that the concept of fractal dimension can be extended to systems where there are strong changes with the length scale and there is, at the same time, something that produces disorder in the pattern. For example, disordering a Sierpinski triangle leads to the figure shown in Fig. 4.14c. This figure can be described by what we call a multifractal, which is simply a set of fractal exponents that lead to the observed pattern. A fully disordered lattice (Fig. 4.14a) leads to a single exponent, 2, which coincides with the fractal and topological dimension. Deviations from this exponent, towards patterns containing strong density variations, can be characterized through a multifractal analysis.

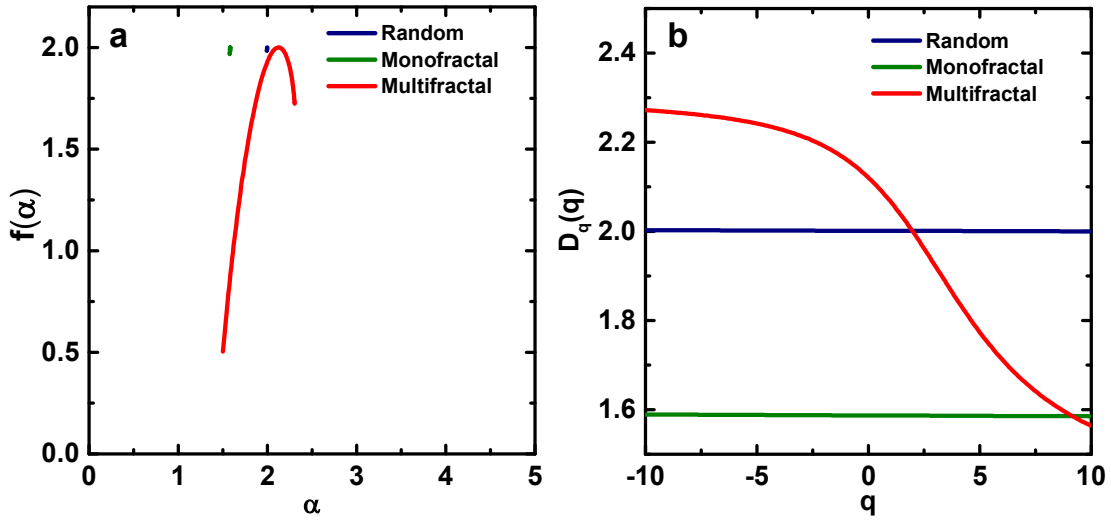

Figure 4.15: In (a) the graph $f(\alpha)$ vs α showing the difference between a multifractal (Fig. 4.14c), a non fractal (Fig. 4.14a) and a monofractal (Fig. 4.14b).In (b), we show the generalized dimension D_q for the three distributions systems

To characterize a multifractal system, we mainly use two functions $f(\alpha)$ vs α and D_q vs q. $f(\alpha)$ vs α is the multifractal singularity spectrum and typically it is a convex curve with a variable width. Fig. 4.15a shows $f(\alpha)$ vs α for a random (Fig. 4.14a), monofractal (Fig. 4.14b) and multifractal (Fig. 4.14c) distributions. $f(\alpha)$ is in random and fractal cases very narrow. For a multifractal distribution, however, $f(\alpha)$ is broad and distributed along a set of values. Also, the α value corresponding to the maximum in $f(\alpha)$ gives the fractal dimension. The nonfractal (random in Fig. 4.14a) and multifractal (non standard Sierpinski carpet in Fig. 4.14c) is more or less centred on 2, but the monofractal (Sierpinski triangle in Fig. 4.14b) is centred in 1.6. D_q vs q gives the generalized dimension for the set of scaling exponents q. These scaling exponents distort the image highlighting different areas with more or less concentration in pixels. In monofractal or nonfractal images, a flat line is expected because its dimension does not depend on q. Both of them are centred in its fractal dimension. However, for the multifractal, the dimension changes with the scaling exponent q, and a sort of sigmoidal curve is obtained. Theoretically, q varies in the range of $[\infty, -\infty]$ but for the implementation in the calculation, the limits depend on the convergence of D_q vs q. In our case a convergence in D_q was obtained in the range of $[10, -10]$. In order to calculate multifractal spectra, we used the box counting method [117]. For a given binary matrix of points, as Fig. 4.16a, we calculate the number of points, $m_i(\epsilon)$, in each box of length ϵ, and compute the probability of finding a white pixel in each box with:

$$P_i(\epsilon) = \frac{m_i(\epsilon)}{\sum_i^{N_{i(\epsilon)}} m_i(\epsilon)} \tag{4.2}$$

being $N_{i(\epsilon)}$ the number of boxes with length ϵ containing at least one point. Now we introduce the set of exponents q, which provide the dimensions in the multifractal spectra. We calculate:

$$I_{q\epsilon} = \sum_i^{N_{i(\epsilon)}} P_i(\epsilon)^q \tag{4.3}$$

$$\mu_{qi(\epsilon)} = \frac{P_i(\epsilon)^q}{I_{q\epsilon}} \tag{4.4}$$

where $I_{q\epsilon}$ represents how the pixels are distributed in space. The smaller $I_{q\epsilon}$, the larger the homogeneity in the number of pixels inside the boxes of same ϵ. $\mu_{qi(\epsilon)}$ is equivalent to $P_i(\epsilon)$ but taking into account the different behaviour of scaling exponents q. Then we calculate

$$A_{\epsilon q} = \sum_i^{N_{i(\epsilon)}} \mu_{qi(\epsilon)} P_{i(\epsilon)} \tag{4.5}$$

which gives the α_q value by calculating the slope of $log(A_{\epsilon q})$ vs $log(\epsilon)$ as shown in Fig.4.16b. When a discrete set of points is given, as in the case of vortex image, only the box with a size of ϵ bigger than minimum distance between first neighbours

is taken into account. That is why the curves of Fig.4.16(b,c) flatten at small ϵ. We also compute

$$\tau_{q\epsilon} = \frac{\sum_i^{N_{i(\epsilon)}} P_i(\epsilon)^{q-1}}{N_\epsilon} \tag{4.6}$$

shown in Fig. 4.16c. From the slope of $log(\tau_{\epsilon q})$ vs $log(\epsilon)$ we obtain τ_q. Finally we can calculate

$$f(\alpha) = \alpha_q q - \tau_q \tag{4.7}$$

$$D_q = \frac{\tau_q}{q-1} \tag{4.8}$$

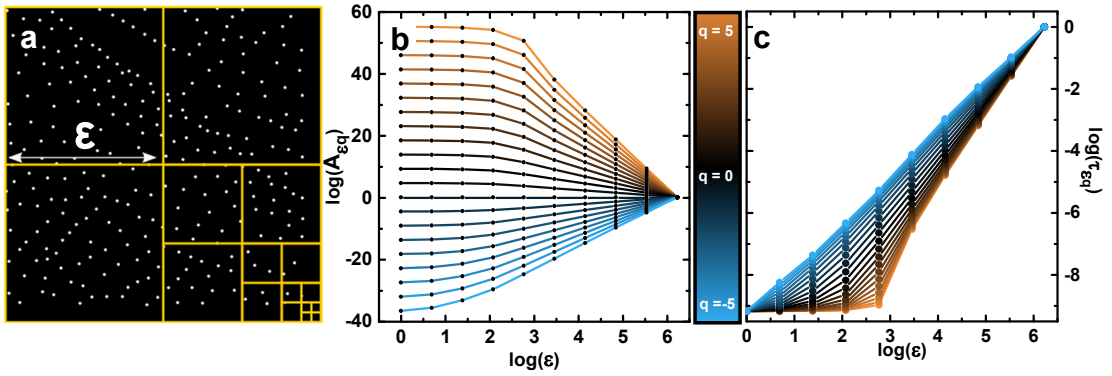

Figure 4.16: In (a) an example with vortex positions indicating how boxes decrease its size. In (b) we show $log(A_{\epsilon q})$ vs $log(\epsilon)$ curves in a set from q=-5 to q = 5. The curves have a clear slope for large $log(\epsilon)$ and become flat for low $log(\epsilon)$. The change of slope is due to the density of points. We only take in account the points before the change of slope. This gives us α_q. In (c) we show $log(\tau_{\epsilon q})$ vs $log(\epsilon)$ curves at the same set of q as in (b). The same behaviour with the size arises and we treat it similarly. The slope of this curve gives us τ_q.

We have calculated the generalized dimension D_q and the multifractal spectrum $f(\alpha)$ for the vortex lattice images (Fig. 4.7 and Fig. 4.8). First we have searched all vortex positions and calculated the images with one at a vortex and zero elsewhere (method explained in subsection 2.4.1). The results are shown in Fig. 4.17. Images showing triangular or disordered lattices provide distribution of fractal subsets centred at $\alpha = D_q = 2$. When we start observing strong variations in the vortex density, multifractality increases, which leads to $f(\alpha)$ that is much broader and whose maximum deviates from 2. D_q also increases for small values of the multi-scaling exponent q. Thus, the vortex distributions at small magnetic fields are multifractal, with a probability of fractal subsets that strongly increases when decreasing the magnetic field, leading to a widening of $f(\alpha)$. On the other hand, the maximum of $f(\alpha)$ and the value of D_q for small q is larger than two and increases when the magnetic field is decreased.

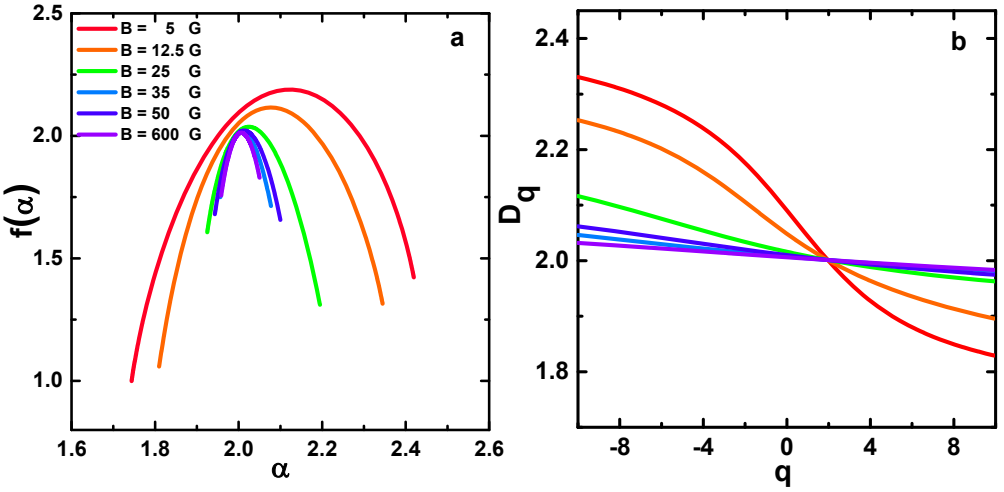

Figure 4.17: Multifractal analysis of the vortex images at very low magnetic fields. In (a), we show in a the distribution of fractal dimensions $f(\alpha)$ in β-Bi_2Pd for different magnetic fields from 5 Oe to 600 Oe. In (b), we show the generalized dimension D_q as a function of the set of exponents q. Note that the curves strongly vary for low magnetic fields.

4.4 Discussion

We have found a new arrangement in the vortex lattice of β-Bi_2Pd different to what has been previously reported in other superconductors. One of the main differences is the divergence of SD/a_0 with decreasing magnetic field. Let us discuss how this divergence can occur.

SD is defined as:

$$SD = \sqrt{\frac{1}{N}\sum_{i=1}^{N}(a_i - a_0^{2D})^2} \tag{4.9}$$

where N is the total number of vortex pairs, a_0^{2D} is the intervortex density associated to the magnetic field density ($\propto B/a_0^{2D}$ and thus $a_0^{2D} \propto 1/\sqrt{B}$) and a_i is the particular intervortex distance for each vortex pair. Thus, a_i can be redefined as a variation of the intervortex distance as:

$$a_i = a_0^{2D}(1 + rand) \tag{4.10}$$

where rand is a random number. Using Equation 4.10 in Equation 4.9, we have:

$$SD = \sqrt{\frac{1}{N}\sum_{i=1}^{N}(a_0^{2D}(1 + rand) - a_0^{2D})^2} \propto a_0^{2D} \tag{4.11}$$

Therefore, in a pure 2D system we can calculate SD/a_0 as:

$$\frac{SD}{a_0^{2D}} \propto \frac{a_0^{2D}}{a_0^{2D}} = const \tag{4.12}$$

as both of them have the same dependence in field. This explains why in most systems SD/a_0 is constant. However, in our samples at low fields, vortices form 1D chains pinned in the linear defects but with the magnetic field density distributed over a 2D area. In the 1D vortex chains the magnetic field density is proportional to B/a_0^{1D}, and thus, $a_0^{1D} \propto 1/B$. Therefore:

$$\frac{SD}{a_0^{2D}} \propto \frac{a_0^{1D}}{a_0^{2D}} \propto \frac{\sqrt{B}}{B} \propto \frac{1}{\sqrt{B}} \tag{4.13}$$

This result agrees with our observations. This is an important result because it shows how vortex positions are influenced by the linear pinning potential.

Now, let us discuss the differences between the vortex arrangement observed in β-Bi_2Pd and the spatially inhomogeneous vortex phases introduced in section 4.1. It also shows that the origin of the fractal distribution is in the presence of vortices forming rows and distributed randomly along the rows in a 2D plane.

In MgB_2 there are two characteristic distances in the vortex pattern with two peaks in the histogram of nearest neighbour vortex distributions [88]. It has been argued that the vortex stripes are independent of the crystal lattice and therefore cannot be related to strong pinning. Instead, the peculiar vortex distribution is a consequence of the two-gap superconductivity of MgB_2 [88]. The vortex patterns we report here for β-Bi_2Pd are different. At very low fields, the patterns do contain vortex stripes, clusters and vortex free regions. However, the intervortex distances do not cluster around two values as seen in MgB_2. Additionally, as it was shown in [62, 100, 118], β-Bi_2Pd is a not a multi-gap superconductor.

Also, we showed the example of the intermediate state (IMS) in a single crystal of Nb. Here, the histogram of nearest neighbour vortex distances presents two clear peaks. On the contrary, we observe only one very broad peak in β-Bi_2Pd. Furthermore, there is no evidence of multifractality in the IMS as Fig. 4.18 shows (blue curve). This can be expected because the vortex lattice remains locked to the crystal lattice, so that it remains ordered within each vortex cluster and all clusters have vortex lattices with the same orientation. Furthermore, there are no density fluctuations. There are just regions sharing all the same vortex density (coinciding here with H_{c1}) and regions with no vortices [34].

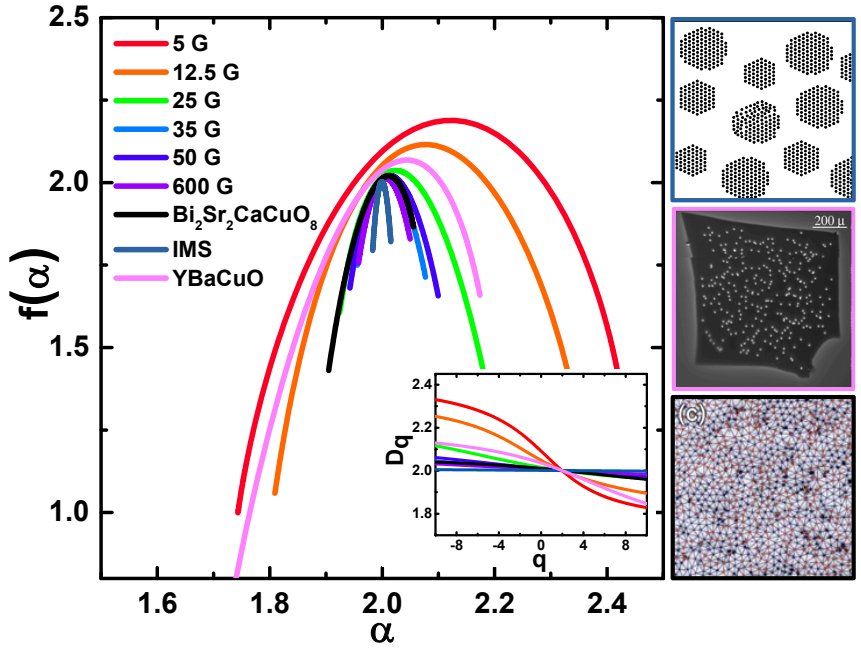

Figure 4.18: Multifractal behavior of the vortex lattice in β-Bi_2Pd , compared to the intermediate mixed state (IMS) , YBaCuO at very low magnetic fields and $Bi_2Sr_2CaCuO_6$ in the Bose glass phase. At the right, from top to bottom images of IMS [34], YBaCuO [119] and $Bi_2Sr_2CaCuO_6$ [116] respectively with the same border color as the curves.

In addition, we can also compare our results with an image taken in YBaCuO (Fig. 4.18 in pink) at a magnetic field three orders of magnitude below the magnetic fields we discuss here [119]. The standard deviation SD/a_0 is of 0.4, and thus, of the same order as the values found in the vortex lattice of β-Bi_2Pd. Additionally, an image in Co-doped $BaFe_2As_2$ also shows a similar behaviour [120]. Furthermore, when strongly anisotropic pinning centres are introduced in YBaCuO, vortex lattices showing voids and linear structures have been reported. These images show multifractal properties (Fig. 4.18 in pink) and relatively large values of SD/a_0. These systems are orthorhombic. Thus, they have twin boundaries or can show under extreme conditions strain induced domains [119, 121]. Therefore, they can provide patterns that are repeatable and situations with large strained domains.

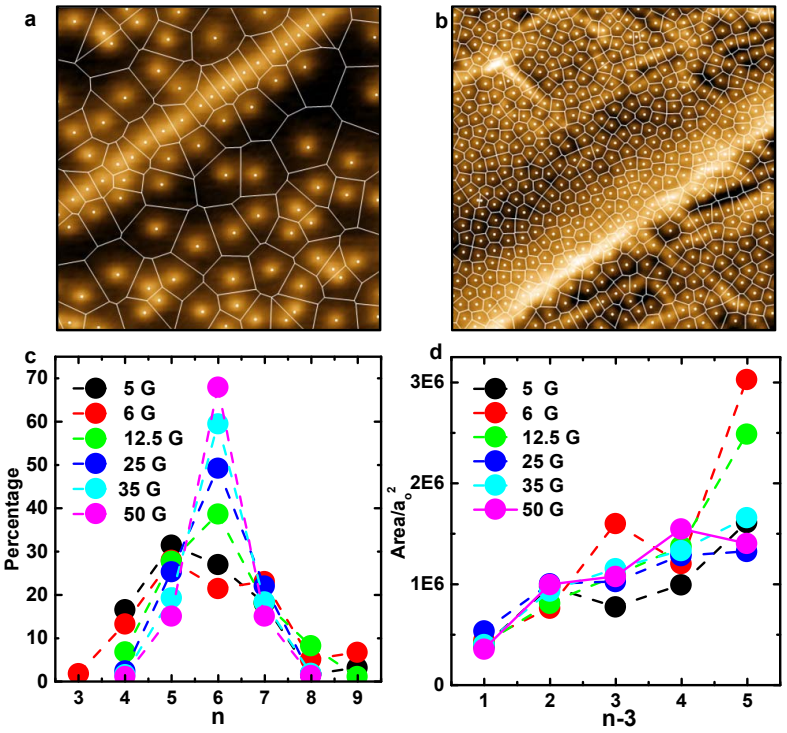

Figure 4.19: In (a) and (b) we show the Voronoi tessellation of images at 6 G (a) and at 25 G (b). In (c) we show the percentage of cells versus the number of sides of each Voronoi cell n. In the hexagonal lattice, n = 6. In (d) we show the average of the area of all cells in each image with a certain n versus n.

We can also compare our system with the suprafroth system discussed in the introduction of the chapter [93]. Both systems are radically different because in the intermediate mixed state there are no vortices but instead we find cells of normal material surrounded by superconducting material. The situation observed in the suprafroth might also show multifractal features in the distribution of the superconducting phase, but is fundamentally different. To gain further insight by comparing distributions and analysis, we have calculated the Voronoi pattern of vortices in our sample. In Fig. 4.19 we show two images at low magnetic fields and the area occupied by polygons as a function of the number of sides of the polygon. As in froths, we observe that the area increases with the number of sides of the polygon (Fig. 4.19d). However, the increase scales with the magnetic field, or the area occupied by each single vortex. In the Abrikosov phase, at higher fields, there will be an equilibrium with all cells with six sides. Nevertheless, at very low fields, in β-Bi_2Pd, we mostly observe two different phenomena. In areas where vortices are pinned, Voronoi cells have mainly four or five sides (Fig. 4.19c) and they occupy a small area. On the other hand, vortices areas free of defects have mainly polygons with 6 or more sides in bigger areas. The difference with the intermediate mixed state is in particular the organization in a scaffold-like structure of pinning centres, providing the new multifractal behaviour. The superconducting to normal area ratio just evolves with the magnetic field in the intermediate state, and the pinning

properties are not well defined and they are highly magnetic field dependent. Apart from the comparison to the suprafroth, the Voronoi tessellation in Fig. 4.19 provides a different perspective of the results shown. For example, the number of sides of the polygons clearly peaks at 6 at high magnetic fields, but goes over to 4 at very low magnetic fields. This shows that the density of vortices along the linear pinning centres is very large. The increase in the area occupied by each vortex is noisier at low magnetic fields (Fig. 4.19d), suggesting that vortices with six or more sides are located randomly in between linear pinning centres.

The differences found with other systems make us propose that one could coin a new term for the observed behaviour in β-Bi_2Pd, which would be a vortex gel phase. The vortex gel has large voids distributed very inhomogeneously in space and we name it as the gel phase because of the similarities with gels and froth systems.

4.4.1 Conclusions

In this chapter we present an analysis of vortex images in terms of multifractal properties, that shows an interplay between the geometry of defects and the vortex lattice that we deem to be new. We showed the arrangement of vortices in a wide region of magnetic field. Our analysis unveils the structural properties of this new vortex arrangement, governed by organizing principles that combine pinning centres as scaffolds and ever present Meissner screening that promotes large voids in the vortex lattice.

We show a divergence in SD/a_0 along with a multifractal spectra. Through a detailed comparison with other vortex systems, we have shown that the properties observed in β-Bi_2Pd are different from previous observations in the same field range, particularly at the smallest applied magnetic fields.

5 | Is vortex lattice hyperuniform?

5.1 Hyperuniform vs amorphous

Hyperuniformity is defined by the total suppression of density fluctuations at long distances [122]. With this definition, the first system we can think of as a hyperuniform is a crystal. A crystal has a trivial hyperuniform configuration because density is exactly the same at every length scale. However, there are other systems that could be disordered hyperuniform. Some authors propose that disordered hyperuniform systems might have interesting applications, from the behaviours that can be deduced for a system with no density fluctuations, as a crystal, but without anisotropy, as a gas or a liquid [123].

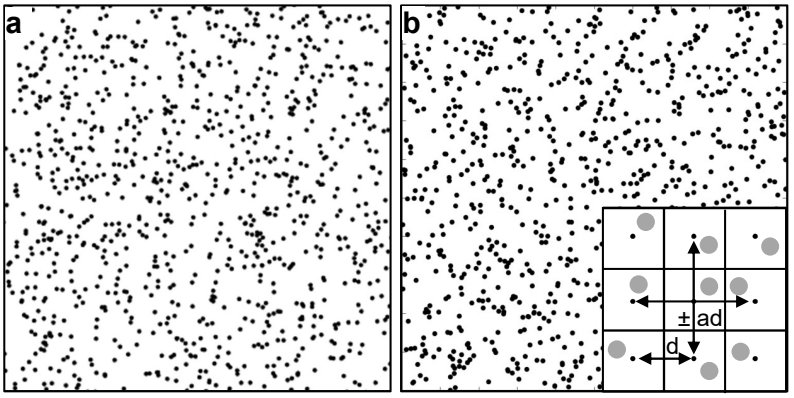

Figure 5.1: In (a) we show a random distribution of points (black dots) in a 2D square. With N points in a square of size A, the average distance is d=$\sqrt{A/N}$. The positions (x,y) of the dots have been generated randomly. In (b) we show a hyperuniform distribution of points (black dots). The number of points and the area are the same as in (a). The positions of the dots have been generated by starting with a square lattice of interparticle distance d (black dots in the lower right inset) and adding to each square lattice point a random vector (x,y). The coordinates of the vector x,y ≤ ± ad, where a=1 here.

An interesting and probably the first proposal for a disordered hyperuniform distribution came with an analysis of the distribution of photocells in the eyes of some birds. In that case, cell structure of the eyes is made in such a way as to seek to

close-pack photocells. A fundamental aspect of vision is that photoreceptors must be distributed regularly to achieve a uniform sampling of the field of view [124]. In 2D, the arrangement best filling the available space of spherically symmetric objects is a hexagonal lattice. But birds have several kinds of photoreceptors and the arrangements is complicated. How photoreceptors self-organize to build a regular distribution is under debate. A hyperuniform configuration is one possible solution when the photoreceptors build complex multicomponent objects [125]. One can then ask the question whether laws in physics, and not only evolutionary laws in biology, can produce a hyperuniform distribution or not. This is still debated and there are numerous works addressing this issue [126, 127, 128].

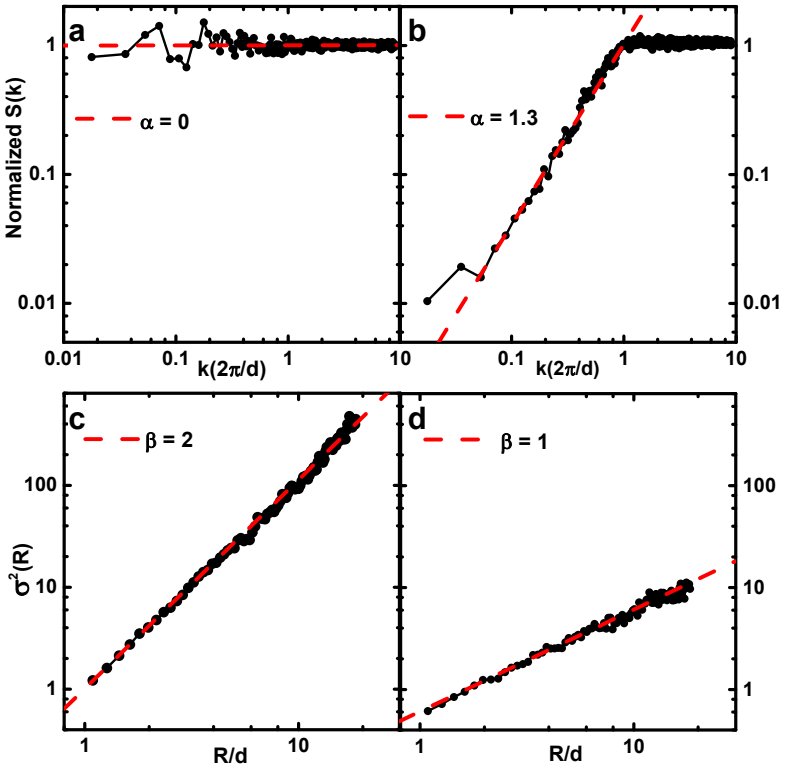

Figure 5.2: In (a) and (b), we show the structure factor (S(k)) for random and hyperuniform distribution respectively. We observe how S(k) in the hyperuniform image tends to zero at small k while for the random distribution it is totally flat. (c) and (d), show the number variance for respectively random and hyperuniform distributions in real space. The number variance σ^2 grows with R/d with an exponent β=2 (c). β is the same as the dimension (here 2) in a random distribution. In a hyperuniform distribution, however (d), β is the dimension minus one and rather grows with the perimeter instead of the area.

In Fig. 5.1a we show an example of a random configuration calculated by a point-coordinate random generator and in Fig. 5.1b we show an example of a hyperuniform arrangement. We have obtained the hyperuniform arrangement by creating a square grid with a lattice constant d and placing a point at the center of each square (black dots in the inset of Fig. 5.1b). As we show in Fig. 5.1,

we then add a vector (x,y) with random coordinates $x, y \leq \pm ad$, and $a = 1$ using periodic boundary conditions [129]. As we can see in Fig. 5.1, both distributions look randomly and their Fourier transforms, as we show below, are mostly flat. However, the hyperuniform distribution has no density fluctuations for length scales above d.

Indeed, the structure factor, which is the radial average of the Fourier transform, is flat in a random distribution but drops to zero for wavelengths k<1/d in a hyperuniform distribution as the one shown in Fig. 5.1. S(k) for k<1/d can be written as

$$S(k) \propto k^{\alpha} \tag{5.1}$$

where α is a number, often of order of 1. In Fig. 5.1b we find α=1.3 (Fig. 5.2b).

It is useful to write the number variance, in real space, as :

$$\sigma^2(R) = < N^2(R) > - < N(R) >^2 \propto R^{\beta} \tag{5.2}$$

where $N(R)$, in a 2D system, is the number of points inside a circumference of radius R. In the random system the number variance grows with the area and therefore, $\sigma^2(R) \propto R^2$ (Fig. 5.2c). In a hyperuniform system (Fig. 5.2d), instead, we can say that the noise or fluctuations in the particle density do not increase with the area, but with the perimeter. In Fig. 5.1b, each random number is distributed over a single cell and we will have $\sigma^2(R) \propto R$. Generally the number variance in a hyperuniform system grows slower than its dimension, D, as $\sigma^2(R) \propto R^{D-1}$ but in a random system, number variance grows as a power law of its dimension $\sigma^2(R) \propto R^D$. The relation between α and β is shown in Table 5.1. The details on the methods we used to calculate S(k) and number variance in images of the vortex lattice will be explained in the next section.

$S(k)$ exponent (α)	$\sigma^2(R)$ exponent (β)
α>1	$\beta = D - 1$
1<α< 0	$\beta = D - \alpha$

Table 5.1: Relation between exponents α and β for the structure factor and number variance in hyperuniform systems [122].

Superconducting vortices may be a good candidate to find a disordered hyperuniform system. Vortices repeal each other usually forming hexagonal (or square) lattices and interact with locations with depressed superconducting properties. The latter act as pinning centres and attract vortices. Pinning centres are usually distributed randomly. However, the intervortex interaction favours a triangular lattice with regular spacing a_0. In three dimensional samples, flux lines bend at pinning centres and in two dimensional systems flux lines are displaced [130, 131]. The competition of pinning potential and intervortex interaction can affect strongly the ideal hexagonal lattice.

In most part of the phase diagram the vortex lattice is ordered although pinning interaction produces the quasi long range translational order, (the so-called Bragg glass phase, see subsection 1.2.2). At small magnetic fields vortices are very far from each other and their interaction is small [31]. Furthermore, at higher temperature, close to T_c, vortex lattice melts leading to the vortex liquid which is a dynamic tangle of vortices [132] (see subsection 1.2.2). Often, experiments at low magnetic fields are made by cooling from the liquid phase, which results in quenched vortex arrangements that can be highly disordered induced by the pinning potential (see subsection 1.2.2). In field cooled conditions at intermediate magnetic fields, the lattice is often ordered. However, interaction with a disorder potential can lead to the appearance of disorder with an order-disorder transition [133, 134] observed in a two-dimensional superconductor with a very weak random disorder potential [29]. Furthermore, disordered vortex lattices appear in systems with strong pinning [22, 42, 135]. Within the vortex lattice phase diagram, it is interesting to look into whether there can be a disordered hyperuniform vortex lattice or not.

Efforts in this direction were done by Reichhardt et al. [136]. They did not address the question of to what extend the vortex lattice can be hyperuniform. Instead, they investigated if a hyperuniform arrangement of pinning centres, as opposed to a random arrangement, can lead to improved pinning properties. They find an increase in the critical current for a hyperuniform vortex distribution. The question about a hyperuniform vortex lattice has been also addressed in pristine, electron irradiated and heavy ion irradiated with columnar defects $Bi_2Sr_2CaCu_2O_{8+\delta}$ [137]. In pristine and electron irradiated samples, the lattice is very ordered, and therefore, the same hyperuniform properties as in an ordered crystal are found. But the vortex lattice in samples with columnar defects may be consistent with disordered hyperuniformity. However, the error in the determination of the exponent α is above 50% and thus, whether hyperuniformity with $\alpha \geq 1$ is present or not remains unclear. All these experiments were performed with Bitter decoration at very low magnetic fields (<100 G) where vortex interaction is small.

Here we analyse vortex lattice images at high magnetic fields, where intervortex interactions dominate, and in lattices that have not crossed the liquid phase. We chose vortex lattices with some degree of disorder obtained in zero field cooled conditions in Refs.[29, 22, 42, 135]. Our choice is determined by the availability of experiments showing large amounts of vortices and because these include cases with uncorrelated disorder, correlated disorder and symmetry breaking disorder. These lead to hexagonal lattices in the Bragg glass regime, polycrystalline lattices as well as fully disordered lattices. We also add new data obtained in a W-based thin film with a correlated arrangement of pinning centres and analyse the situation of a thin film with a highly out of equilibrium vortex configuration consisting of anti-hyperuniform behaviour, with strong density fluctuations [138, 31]. The latter shows a behaviour very similar to the gel found at low fields in β-Bi_2Pd (chapter 4).

5.2 Structure factor and number variance

As mentioned before, there are two ways for studying hyperuniformity in a system. We can do it in the reciprocal space by computing the structure factor S(k) or in the real space using the number variance, $\sigma^2(R)$. We have implemented a program in MATLAB for obtaining the structure factor and number variance using as input the vortex coordinates. Vortex coordinates are obtained using the method described in subsection 2.4.1.

Calculation of Structure factor

First, let us discuss how we can calculate the structure factor. The structure factor in a system with identical points is defined as [139]:

$$S(\boldsymbol{k}) = \frac{1}{N}\sum_{i=1}^{N}\sum_{j=1}^{N} e^{i2\pi\boldsymbol{k}(\boldsymbol{r_i}-\boldsymbol{r_j})} \tag{5.3}$$

We can also write the coordinates of vortices in a lattice as

$$I(\boldsymbol{r}) = \sum_{i=1}^{N}\delta(\boldsymbol{r}-\boldsymbol{r_i}) \tag{5.4}$$

where N is the number of points in the $\boldsymbol{r_i}$ positions. In order to compare with Equation 5.3 we transform I($\boldsymbol{r}$) to reciprocal lattice as:

$$I(\boldsymbol{k}) = \sum_{i=1}^{N}\int_{-\infty}^{\infty}\delta(\boldsymbol{r}-\boldsymbol{r_i})e^{i2\pi\boldsymbol{k}\boldsymbol{r}}d\boldsymbol{r} = \sum_{i=1}^{N} e^{i2\pi\boldsymbol{k}\boldsymbol{r}} \tag{5.5}$$

Thus, we can combine Equation 5.5 and Equation 5.3 and rewrite S($\boldsymbol{k}$) as:

$$S(\boldsymbol{k}) = \frac{1}{N}I(\boldsymbol{k})I(\boldsymbol{k})^* = \frac{1}{N}|I(\boldsymbol{k})|^2 \tag{5.6}$$

Equation 5.6 shows that we can compute S($\boldsymbol{k}$) with the Fourier transform of a binary image. Furthermore, as we are only interested in the isotropic decay of $S(\boldsymbol{k})$, we can reduce the problem to 1-D taking the radial average of $S(\boldsymbol{k})$ versus k

$$S(k) = \frac{1}{N}|I(k)|^2 \tag{5.7}$$

where $|(I(k))|^2$ is de radial average of $|(I(\boldsymbol{k})|^2$. In order to follow the steps above we have implemented a program in MATLAB to calculate S(k). As our input parameter are the vortex coordinates, first, we have to transform the coordinates to a square matrix of size $N_{pixels} \times N_{pixels}$ and length L.

Then, we compute a binary matrix, $I(\boldsymbol{r})$, where $I(\boldsymbol{r})$=1 for $\boldsymbol{r} = \boldsymbol{r}_i$ and $I(\boldsymbol{r})$=0 for other positions. We obtain $I(\boldsymbol{k})$ by using a 2D-Fast Fourier Transform (2D-FFT)

of the matrix $I(\boldsymbol{r})$. Finally we calculate $S(\boldsymbol{k})$ with Equation 5.6.

Again, we use Equation 5.7 to calculate S(k). Finally, we can plot S(k) as a function of k in a logarithmic plot and normalize k to the Bragg peak of the lattice, in order to compare data obtained at different magnetic fields.

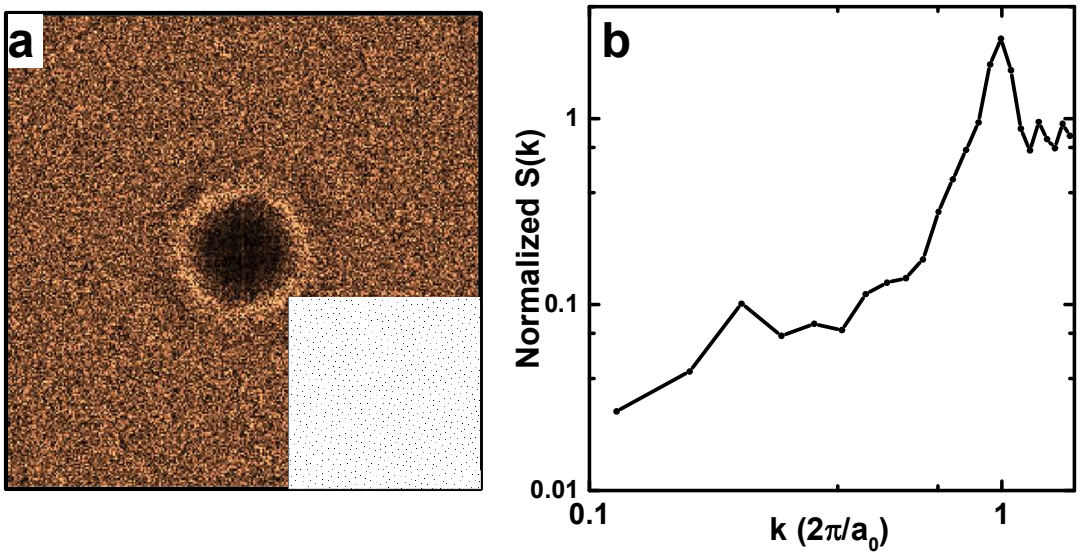

Figure 5.3: In (a), we show $S(\boldsymbol{k})$ as the square of the Fourier transform of the binary matrix in the inset. Lattice is disordered without a triangular arrangement. We obtain a radial average as shown in (b).

Calculation of the number variance

With the definition of $\sigma^2(R)$ given in Equation 5.2 we have also implemented a Matlab code to calculate $\sigma^2(R)$. In order to obtain $N(R)$ we calculate a set of random circles of different radius as shown in Fig. 5.4. We impose two conditions. First, circles must be complete, so the centre of the circle of radius R is inside a square of size [L-R, L-R] centred on the image, being L the lateral side of the image. Secondly, circles cannot overlap. Thus, the number of circles we can establish decreases rapidly with the radius. In Fig. 5.4b, we show an example of the number of circles as a function of radius normalized by the length of the image, L. For small values of R, we cut the number of circles to 1000 because otherwise it would be computationally costly too. When the radius is about 30% of the lateral size of the image, the number of circles is only 1. In Fig. 5.4c we show in black the result obtained using this method.

We generate all circles randomly and work in such a way as to take into account the same number of circles for each radius R. We can see this in more detail in Fig. 5.4c. First, for distances below the average interparticle distance, a_0, the calculation does not provide us useful information, as we are interested in fluctuations at large distances. Second, when we are at very large distances, of order of the image size, and we draw a random assignment of positions to place circles to do the calculations,

we can only find a few circles. This implies that the calculations are noisy (black line in Fig. 5.4c). To reduce the noise, we repeat this assignment a certain amount of times and then make the average. We aim at making at least a hundred circles for each R. This is achieved either by just taking one random assignment for small R, or by increasing the times we randomly assign circles and making the average for large R. This allows us to obtain $\sigma(R)$ with the same noise level for all R (red line in Fig. 5.4c).

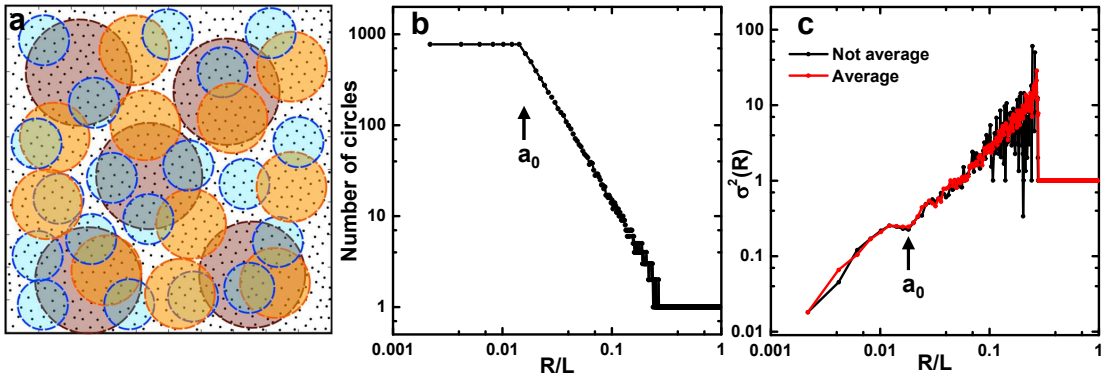

Figure 5.4: In (a) we show a random distribution of points (black dots) in a 2D field of view. We also show circles around randomly chosen positions. Circles of the same radius have the same color (blue, orange and brown for increasing radius). In (b) we show the number of circles (black points, joined by a line for clarity) we can draw by randomly generating their centres as a function of the radius of the circle R normalized to the lateral size of the image L. We mark with an arrow the average interparticle distance a_0. Below this distance, we can place a nearly arbitrary number of circles, so that we fix the value to the one found at a_0, slightly below 1000. When we increase R, the number of circles we can place in the field of view decreases, until we can just place one circle when R is about a third of L. In (c) we show (points joined by a line to help the eye) the number variance calculated in two situations. In black we show the variance calculated for a single set of random numbers giving the centres of the circles generated for each R. In red we show the variance calculated as the average of the results corresponding to a set of random numbers that increases progressively when increasing R, in such a way as to have the same number of circles at each R. The number variance has no meaning in the frame of our discussion for R/L>3 and R<a_0.

5.3 Results

Here, we present the results obtained in different materials. They are ordered by the degree of hiperuniformity. The graphs in the left show $S(k)$ and have a dashed line indicating a fixed exponent of α=1 to compare the decay of $S(k)$ when k $\to$ 0. As shown in table Table 5.1 , if α<1, then the growth of $\sigma^2(R)$ has an exponent of $\beta = 2 - \alpha$, however, if α>1, the exponent in $\sigma(R)^2$ is $\beta = 1$. In our data we fit the exponent β of $\sigma^2(R)$ and compare the result with the decay in $S(k)$.

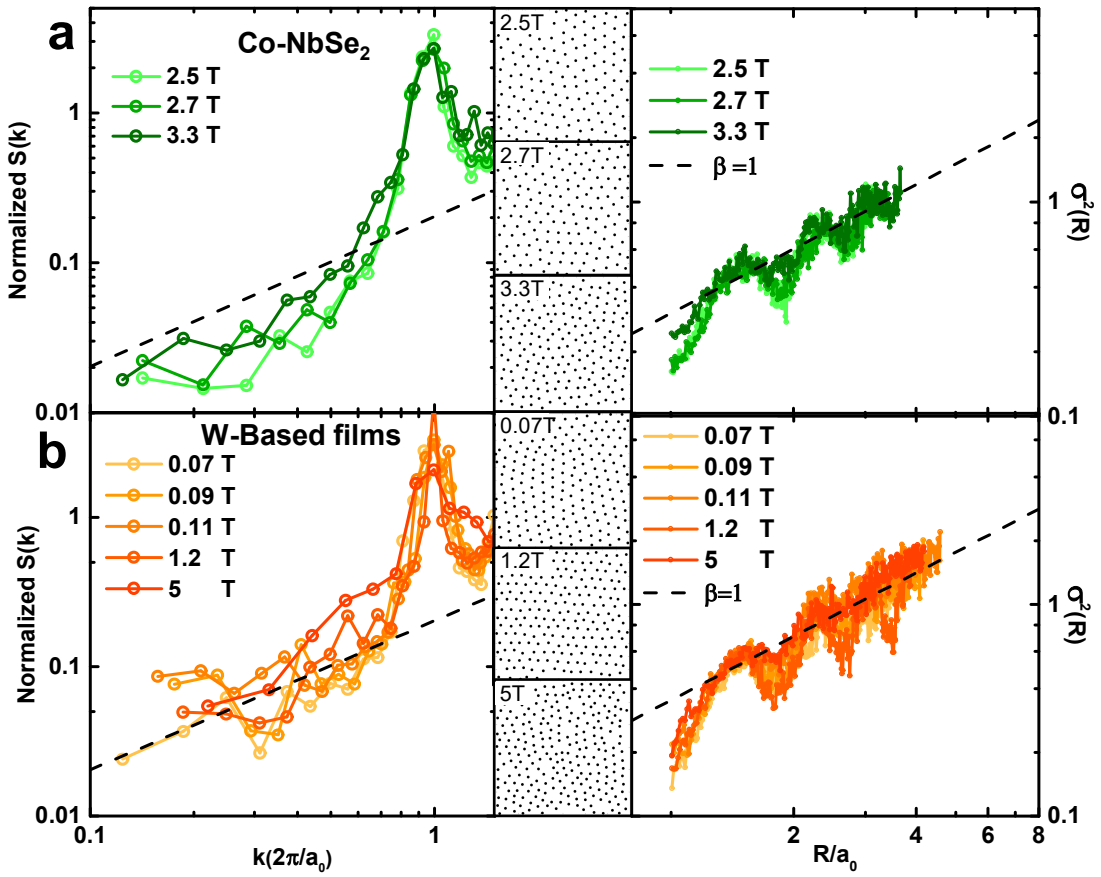

Figure 5.5: In the left and right panels we show, respectively, S(k) and $\sigma^2(R)$ as points. Lines join points to help the visualization. In the middle panels we show the binary images used in the calculation of the left and right panels. Black dashed lines are power laws, with fixed exponent α = 1 in S(k) (left panel) and the best fit for exponent β in $\sigma^2(R)$. Data in (a) are for the vortex lattice in Co-doped 2H-$NbSe_2$ [135] and in (b) for a W-based superconducting thin film with strong thickness variations. In both cases, the vortex lattice behaves as a polycrystal, with hexagonal bundles observed at all magnetic fields. As we show in the images of vortex positions (central panels), in these cases, there is short range hexagonal order, which leads to the hyperuniform properties.

We present in Fig. 5.5a the results obtained in Co-$NbSe_2$ [135] at three different fields. In pure 2H-$NbSe_2$ it would make little sense to study disordered hyperuniformity as the lattice is triangular [84, 140]. According with [135] Co-doping leads to magnetic scattering and vortex pinning in 2H-$NbSe_2$. Authors measure reduced values of T_c and of H_{c2} (T_c = 5.7 K and H_c=3.4 T), so that there is a strong effect of the Co-doping. At the three magnetic fields, we find an ordered lattice, but with different domains. We fit $\sigma^2(R)$ of Fig. 5.5a (right panel). The exponent β=1 and therefore α >1. $S(k)$ is decaying faster than the dashed line. We have to take into account that FFT at extremely low k can have some noise, and therefore, we have to observe the behaviour in the change of slope after the Bragg peak. In this material we find that $S(k)$ and $\sigma^2(R)$ are consistent with a trivial

hyperuniformity as the vortex lattice is formed by ordered domains.

In Fig. 5.5b we present results for a W-based thin film with strong and disordered thickness modulations. At low magnetic fields, these lead to the formation of hexagonal vortex bundles, as in Co-doped 2H-$NbSe_2$, and we obtain similar results. The vortex lattice is hyperuniform, but not fully disordered. The hyperuniform properties are due to the local hexagonal order.

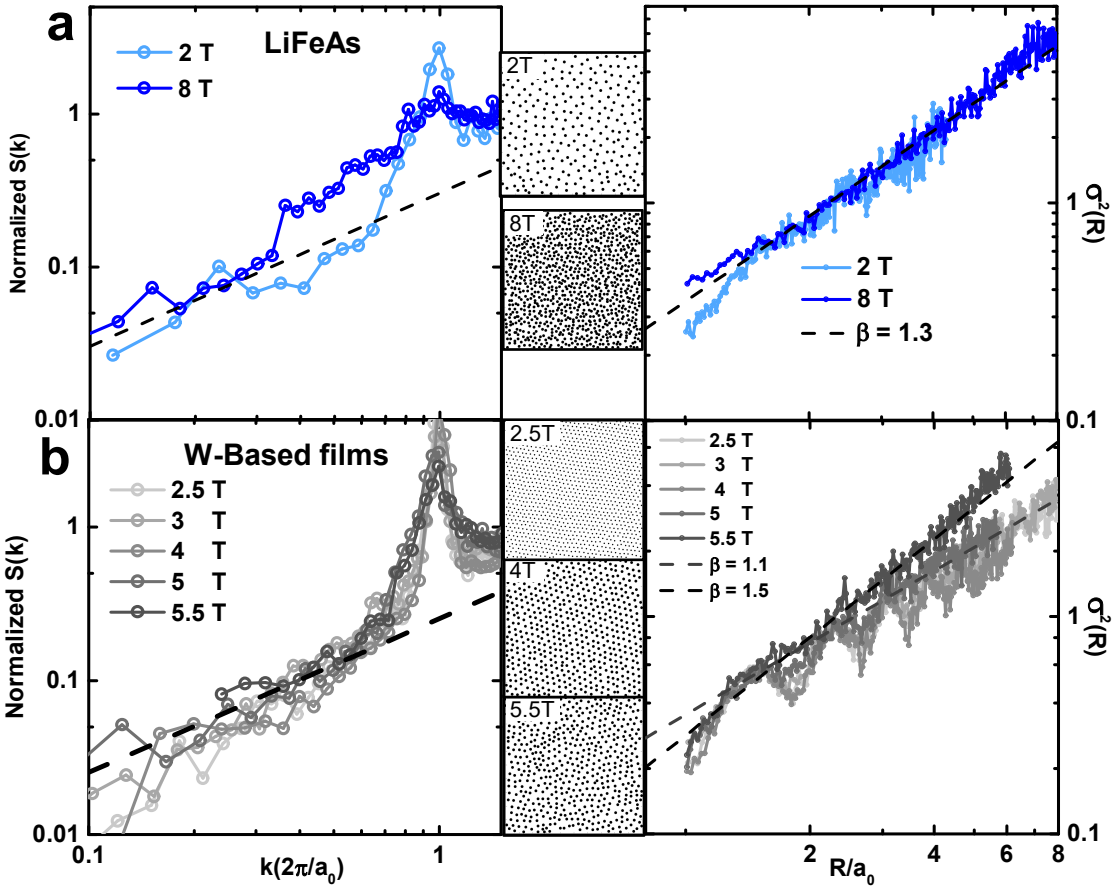

Figure 5.6: The figure follows the same representation as the previous figure. Left panel, S(k), middle panels a few images of vortex positions and right panels $\sigma^2(R)$. Dashed lines are fits in right panels and α=1 in left panels. Data (points) are now in LiFeAs from [42] (a) and in a W-based thin film which is perfectly uniform from [29] (b). The latter implies that there is practically no pinning. Note that, whereas the lattice is mostly ordered in the W-based system (b), it is highly disordered in LiFeAs (a).

In Fig. 5.6a we present the results of the pnictide LiFeAs with T_c=17.5 K and H_{c2}=15 T for magnetic fields at 2 T and 8 T [42]. In this work, an image of H=0.5 T is also presented but an ordered lattice is found. Here we chose images of disordered vortex lattices, from 2 T onwards. We see that there are no hints for local hexagonal arrangements, the lattice is fully disordered. Nevertheless, we find a value for β that is low and close to 1, namely 1.2 and 1.3 for 2 T and 8 T, respectively. Thus, this

vortex lattice is close to the disordered hyperuniform behaviour.

In the W-based thin film, which shows now practically no thickness changes as a function of the position, we find that the vortex lattice is strongly ordered until about 5 T. There, the lattice rapidly disorders, as described in [29]. Accordingly, the exponent β corresponds to the (trivial) hyperuniform behaviour of a nearly hexagonal vortex lattice until about 5 T. For the highest magnetic field, when the lattice loses all kind of order (translational and orientational, see [29]), the exponent β strongly increases, deviating from hyperuniformity. Therefore, vortex positions are randomized. Note that at this magnetic field, the lattice is close to H_{c2}, so that it is very soft.

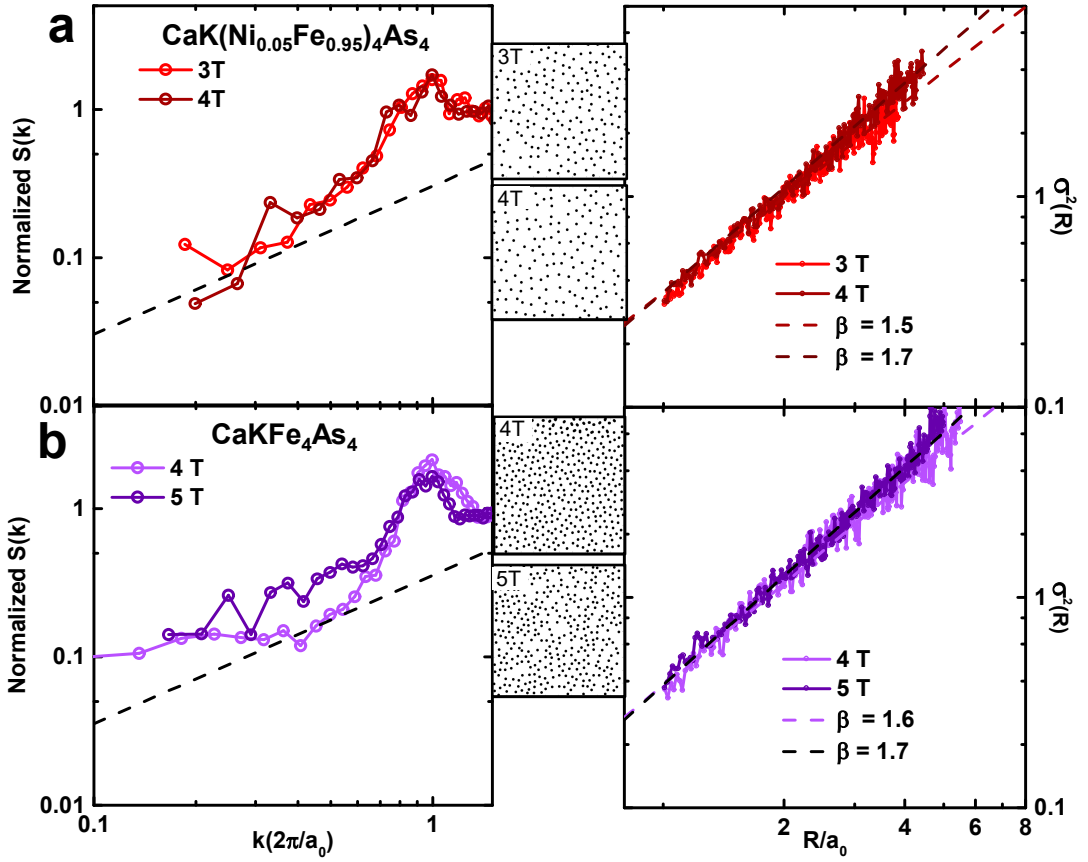

Figure 5.7: We follow the same presentation as in the previous two figures. Here we use data of very disordered vortex lattices in Ni-doped $CaKFe_4As_4$ (a) and in pure $CaKFe_4As_4$ (b) taken from [22]. We see strong deviations from hyperuniform behaviour, towards random distributions. As in previous figures, dashed lines in right panels provide the fits to the β shown and in the left panel we show α=1.

Thus, we have two opposing examples of disordered arrangements without any clear sign of a tendency to form local ordered triangular arrangements. In LiFeAs, the disorder appears at magnetic fields far from H_{c2} and the vortex lattice is still stiff. This favours absence of long range density fluctuations and thus hyperuniform-like behaviour. The opposite occurs in the W-based thin film, where the lattice is much

softer and has a tendency to lose hyperuniformity and become random.

The results of the pnictide $CaKFe_4As_4$ with and without Ni-doping ($T_c \approx 10$ K and $H_{c2} \approx 20$ T and $T_c \approx$=35 K and $H_{c2} \approx 92$ T respectively) [22] are shown in Fig. 5.7(a,b) respectively. As we explained in chapter 4, the vortex lattice is very disordered. Here we find $\beta > 1.5$. At 3 T in Fig. 5.7a the exponent is the lowest with $\beta = 1.5$, but at 4 T in Fig. 5.7a and 5 T in Fig. 5.7b $\beta = 1.7$. We also observe a decay of $S(k)$ slower than α=1.

In Fig. 5.8 we show completely different results than those shown before. In a, the material studied is a W-based thin film with a nanofabricated array of dots [141] and in b, we show the results in $\beta - Bi_2Pd$ discussed in chapter 4. In both of them $\sigma^2(R)$ grows with $\beta = 3$. This exponent is much larger than in a random system and implies antihyperuniformity [122]. This term was coined within the development of hyperuniform formalisms to describe systems in which the density fluctuations increase with distance. It includes fractal distributions and distributions with large empty spaces.

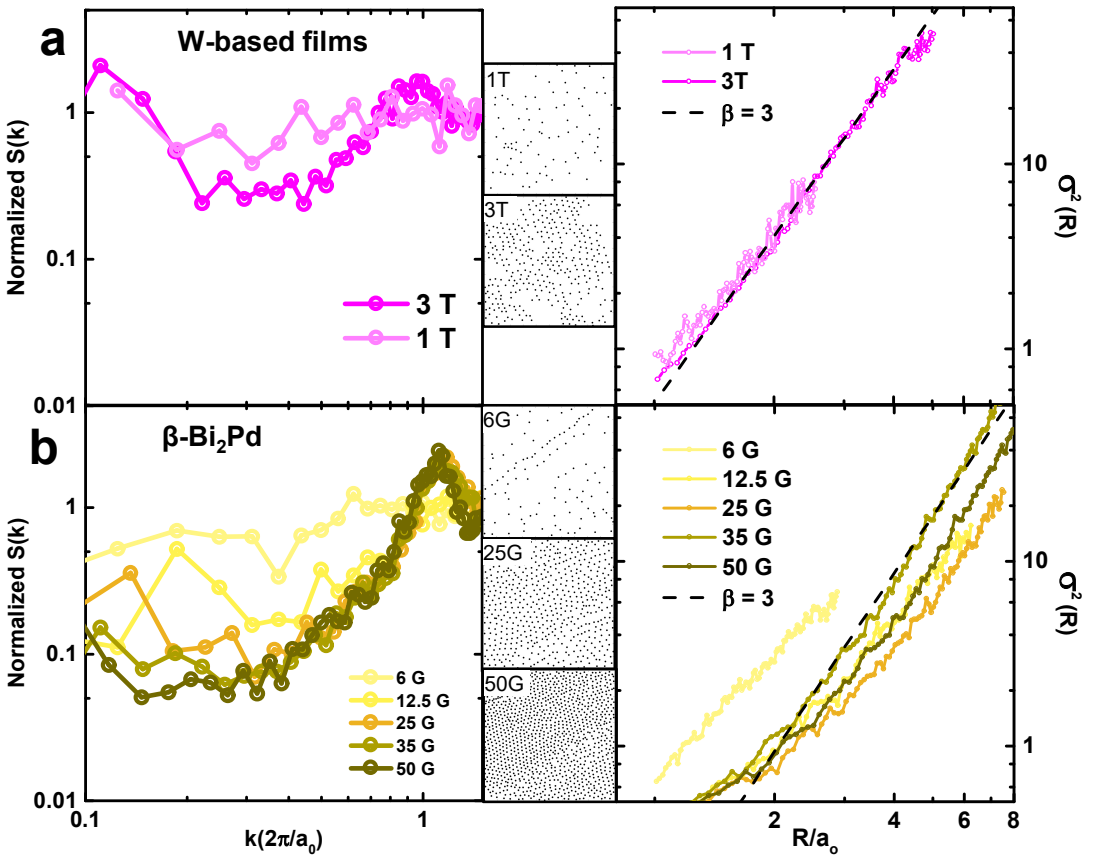

Figure 5.8: Using the same representation as in the three previous figures, we show here results in a nanostructured W-based thin film (a) [141], and at very low magnetic fields in β-Bi_2Pd [31] (b). Notice the presence of voids in the distribution of vortices (middle panels). This provides large values of β. The distribution is thus random with in addition strong density fluctuations.

5.4 Discussion

We have calculated the parameters that characterize hyperuniformity in a variety of materials with different properties and pinning potentials obtaining different values of the exponents α and β. We are interested in the possibility to have disordered hyperuniformity in the vortex lattice.

Let us discuss the origin of pinning in all of the examples we show here. 2H-$NbSe_2$ samples doped with Co are measured very close to H_{c2} in the so-called peak effect [42]. Pinning is due to the Co impurities, distributed randomly in 2H-$NbSe_2$.

The Co distribution in 2H-$NbSe_2$ leads to the formation of a polycrystalline vortex lattice, at least in the magnetic field range presented here. In the W-based thin film with strong pinning, the situation is very similar, the vortex lattice is also polycrystalline. In both systems, we find hyperuniform behavior. However, the presence of a strong tendency to form a triangular arrangement is visible in both cases, and we cannot speak about disordered hyperuniform arrangements.

In the W-based thin film with no pinning centers, the vortex lattice is hexagonal and thus trivially hyperuniform at low magnetic fields. When the lattice disorders (mainly due to strong lattice softening), a strong tendency to show a random distribution appears. Thus, the tendency here is away from hyperuniform behavior. In the LiFeAs system, the vortex lattice is disordered in a wide range of magnetic fields. In particular, in a range of fields where the lattice is stiff (it is far from H_{c2}). There, we find the closest behaviour to disordered hyperuniformity.

Finally, the results in the $CaKFe_4As_4$ family of systems show strongly disordered lattices at all magnetic fields. The vortex lattice is at magnetic fields much below H_{c2} there, even more than in LiFeAs. However, pinning seems to be too strong for hyperuniform behaviour to prevail and vortices show random behaviour.

To further analyse our results, we have calculated the first neighbour distance and the corresponding standard deviation SD from the average distance, as well as the number of defects. In Fig. 5.9a we plot the exponent β vs SD and in Fig. 5.9b β vs the defect density. From these plots, we can gain further insight.

β=1 implies hyperuniform behaviour and β=2 random behaviour. If we take the distribution of Fig. 5.1a, we see that when β=2, the SD is large, on the order of the average interparticle distance, and the density of defects is equal to one. In a perfectly ordered lattice, β=1, the SD is zero and the defect density is zero too. In a disordered hyperuniform lattice, as the one shown in Fig. 5.1b, β=1 but SD is large, on the order of the average interparticle distance, and the density of defects equals one.

Thus, if we start from an ordered lattice, we are close to β=1 and SD and defect density close to zero. From Fig. 5.9 we see that this occurs when there is a perfect hexagonal order (W-based thin film without pinning). When there is a polycrystalline arrangement (Co-$NbSe_2$ and W-based thin film with strong pinning), the SD is small but the defect density can be quite large. When we have a disordered vortex lattice, which is mostly random, we expect β to be close to 2 (or tending

towards 2) and large values for SD and for the defect density. This indeed occurs for the fully disordered lattices of the $CaKFe_4As_4$ compounds and in the W-based thin film without pinning close to H_{c2}.

For disorder hyperuniform, or close to hyperuniform behaviour, we expect β close to 1 and large values for SD and for the defect density. In LiFeAs we observe β close to 1 and a very large defect density.

Furthermore, our results (Fig. 5.9) show that there might exist a relationship between β, SD and the defect density that we did not anticipate.

First, there are no data with β=1 and SD larger than about 20% of the intervortex distance. This corresponds to a Lindemann criterion. Above a certain fluctuation amplitude, the ordered lattice is unstable. Clearly, we could not find any hyperuniform distribution that overcomes Lindemann criterion. Instead, the close to hyperuniform behaviour of LiFeAs occurs with SD being very small. Second, there is a minimal defect density associated with the presence of disorder of about 30%. Qualitatively, this means that a lattice can have a large amount of defects but remain ordered to some degree (in the form of polycrystalline arrangements). When the defect density increases above about 30%, we can no longer speak about a polycrystalline arrangement. Interestingly, at this point, β deviates from one and it increases continuously with the defect density. If all observed vortex lattices would be perfectly disordered hyperuniform, β would remain close to one when increasing the defect density. Thus, again we see that close to hyperuniform behaviour is found in LiFeAs where the defect density remains large but close to 30%

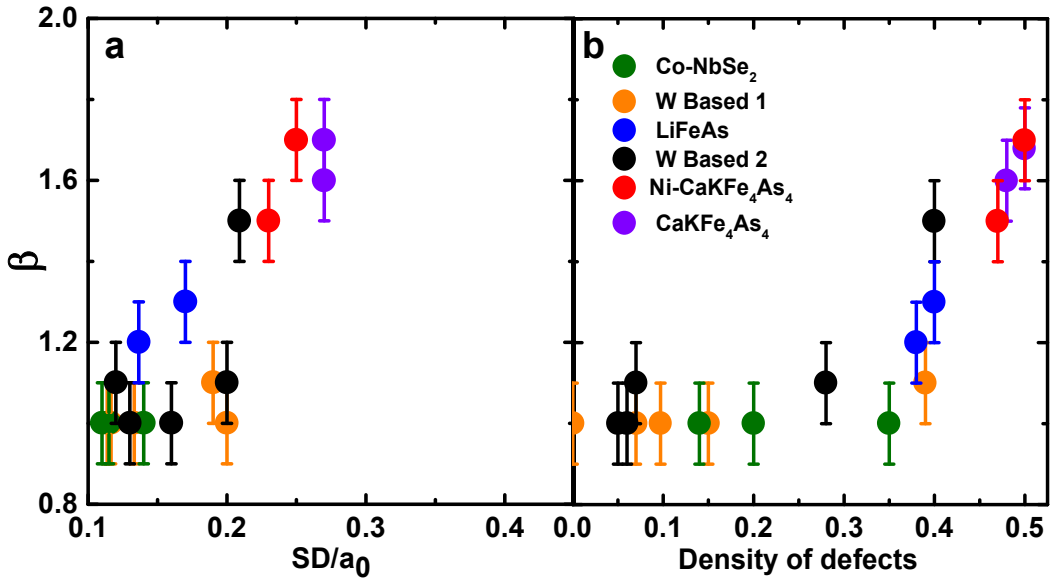

Figure 5.9: In (a) we plot a the β exponent of $\sigma^2(R)$ as a function of the standard deviation normalized by the intervortex distance SD/a_0. In (b), we plot the same β exponents with respect to the defect density in the lattice calculated by the percentage of the number of vortices with a number of first nearest neighbour different than 6.

The relation between β and SD as well as the defect density shows that the increase in density fluctuations is established by the local variations in the vortex positions (SD) and by the number of defects appearing in the lattice (defect density). The tendency of these in a vortex lattice is clearly towards random behavior. Only in particular cases, with stiff and disordered vortex lattices, hyperuniform behaviour might pop up. The latter can have strong defect densities, but small values of the SD and is thus fundamentally distinct from the mathematical construction of Fig. 5.1b.

We can also wonder which kind of pinning centres provide long range correlations and a tendency to form hyperuniform arrangements. One trivial answer is those that produce breaking of the lattice into hexagonal crystallites. If the density of defects is large enough or the lattice soft enough, this leads to random disorder, instead of hyperuniformity. A relatively hard lattice, strongly interacting with pinning centres at the level of individual vortices, as seems to be the case in LiFeAs, could be the best situation to maintain long range correlations in highly disordered vortex lattices. In other words, the elastic properties of the vortex lattice need to favour a very homogeneous field distribution, while allowing for a sufficient degree of disorder.

5.5 Conclusions

In summary, we have analysed the possible presence of disordered hyperuniform vortex lattices in superconductors in high magnetic fields. The vortex lattice shows a strong tendency away from random behaviour in soft vortex lattices with point like random pinning centres. The combination of long range correlations and disorder comes together to favour situations with a homogeneous magnetic field at large length scales and pinned vortices. This was anticipated in calculations in Ref. [142] and might be used to establish a collective response to vortex motion in a disordered vortex lattice and contribute to improve the pinning properties with applied currents

6 | Vortex creep in tilted lattices: temperature induced vortex arrest

6.1 Vortex creep

In this chapter we analyse vortex creep in tilted magnetic fields. We explain a rather peculiar phenomenon, which was found previously in the laboratory. My contribution in this chapter is to identify vortex positions from consecutive images, show how we can obtain their velocities and directions and discuss how this can be related to a model that describes creep in vortex lattices in tilted magnetic fields.

One of the greatest challenges in type II superconductivity is the ability to increase critical current. This requires to control the position of vortices by fixing them at pinning centres. However, the characteristics of vortices and pinning centres are very dependent on the structural and superconducting properties of each sample. Still, there are some important common aspects.

When varying the applied magnetic field, its strength or direction, vortices either enter or exit the sample. They are driven towards the interior or exterior by the Lorentz force due to the Meissner shielding currents. In an ideal superconductor, vortices arrange in a triangular lattice, distributing all over the sample. However, in real superconductors, there are defects that act as pinning centres. As proposed by Bean [35], vortices will create the so-called critical state (subsection 1.2.4). In the Bean critical state the magnetic field distribution in a superconductor is not homogeneous. When the field is increased, the surface barrier (Bean Livingston barrier) and the pinning hamper the motion of vortices towards the interior of the sample, and therefore the interior stays field free. This occurs until the field reaches a large enough value, and intervortex forces overcome pinning barriers making the field homogeneous. The opposite happens when the external field is decreased. Vortices at the edges first exit the sample and thus the magnetic field is larger at the center than at the border of the sample. This is a metastable state and a very small change is enough to depin vortices and move them to the interior of the sample where vortex density is smaller. Vortices that are pinned receive a drive that helps them to leave the pinning center. Vortices are caught in a potential well, defined by the pinning center, and the drive is given, within Bean's picture, by a change in the magnetic field. The jump over the potential well is mostly a thermally activated phenomenon.

When vortices jump from one pinning site to the other, they accelerate continuously, since there is no pinning force counteracting that motion. However, there is a drag force which counteracts vortex motion creating dissipation and heat [130]. The jump of vortices from one pinning center to the other, crossing a path where their motion dissipates heat, is what we call creep. For this reason it is important for applications to immobilize vortices and eliminate creep.

Usually, pinning barriers are very different in a macroscopic sample and nearly at all temperatures, the thermal energy is sufficient to create creep. [143]. In STM, vortex creep has been observed in Ref. [28, 144, 145]. This phenomenon also has been seen in several systems of interacting particles, such as colloids, polymers, solid consisting of mixtures or in lattices of entities formed by electronic interactions (domain walls or skyrmions)[146, 147, 148, 149, 150]. A useful parameter to evaluate the importance of thermal fluctuations is the Ginzburg-Levanyuk number, G_i (subsection 1.2.2).

2H-$NbSe_2$ is a dichalcogenide compound whose crystal structure is formed by blocks of Nb-Se-Nb. Nb and Se are arranged forming a triangular lattice. The interaction between Nb or Se atoms within each layer is covalent while blocks of Nb-Se-Nb layers are joined between them through Van der Waals forces. 2H-$NbSe_2$ is thus very easy to mechanically exfoliate by removing the Nb-Se-Nb blocks. This allows to find atomically flat and large areas made of Se atoms, ideal for scanning tunnelling measurements.

Critical temperature is relatively high with $T_c = 7.2$K, and superconductivity coexists with a charge density wave ($T_{CDW} = 33.5$ K) at low temperatures. Furthermore, 2H-$NbSe_2$ has a strong anisotropy of $\epsilon \approx 1/3$. As the anisotropy is presented between out-of-plane and in-plane directions, we say that 2H-$NbSe_2$ is an uniaxial superconductor. Vortex lattices under perpendicular magnetic fields have been widely studied using STM. Vortices arrange in a triangular lattice, but each vortex has a 6-fold star shape.

The behaviour of the vortex lattice in 2H-$NbSe_2$ at tilted magnetic fields has been discussed before [151, 152, 153, 154, 155, 53, 156]. The vortex lattice of anisotropic superconductors is considerably modified at magnetic fields tilted from the anisotropy axis. An in-plane vs out-of-plane anisotropy is defined as $\epsilon = \frac{H_{c2,ab}}{H_{c2,c}}$. As I mentioned above, in 2H-$NbSe_2$, $\epsilon \approx 1/3$ and one finds lattices that are no longer hexagonal in tilted magnetic fields. Instead, the lattice in the plane perpendicular to the field presents an elliptical distortion.

Furthermore, the vortices are not exactly aligned with the applied magnetic field H. We say that the B-field created by vortices is not exactly equal to the applied H-field. The angular difference is written as [130]

$$\sin(\theta_B - \theta_H) = \frac{H_{c1}}{H} \frac{(1-\epsilon^2)\sin\theta_B cos\theta_B}{\sqrt{\epsilon^2 \sin^2\theta_B + \cos^2\theta_B}} \tag{6.1}$$

where θ_B and θ_H are the angles of B and H with respect to the crystalline c-axis. The temperature dependence of the equilibrium angle θ_B is encoded in $H_{c1}(T)$. If we expand Equation 6.1 in a small change of $H_{c1}(T) = H_{c1}(T_0)+\delta H_{c1}$ the angle changes

to $\theta_B(T)$=$\theta_B(T_0)$ - $\delta\theta_B$.

$$\theta_B = -\frac{\delta H_{c1}}{H_{c1}} \sin\theta_B \cos\theta_B \left[\frac{\epsilon^2 sin^4\theta_B - \cos^4\theta_B}{\epsilon^2 \sin^2\theta_B + \cos^2\theta_B} + \frac{H}{H_{c1}} \frac{\cos(\theta_B - \theta_H)\sqrt{\epsilon^2 \sin^2\theta_B + \cos^2\theta_B}}{1-\epsilon^2} \right]^{-1} \tag{6.2}$$

We can simplify the expression by three approximations. i) H>> H_{c1}; ii) θ_B is far from 0 or $\pi/2$ and iii) θ_B-θ_H << 1. Thus

$$\delta\theta_B \approx \frac{\delta H_{c1}}{H_{c1}}(\theta_B - \theta_H) \tag{6.3}$$

We can calculate the deviation for the case of 2H-$NbSe_2$. With an angle of the magnetic field of $\theta_H = 70°$, we obtain using Equation 6.1 a mismatch of θ_H - $\theta_B \simeq 0.8°$ at base temperature (0.15K). At higher temperatures (2 K) we calculate a deviation with Equation 6.3 of θ_H - θ_B(T) $\simeq 0.5°$. Therefore, at lower temperatures the mismatch between the applied magnetic field is larger than at higher temperatures.

In Fig. 6.1 we show an sketch indicating the angle of the applied magnetic field θ_H in black, θ_B(T) in red using Equation 6.3 and in blue $\theta_B(T_0)$ using Equation 6.1.

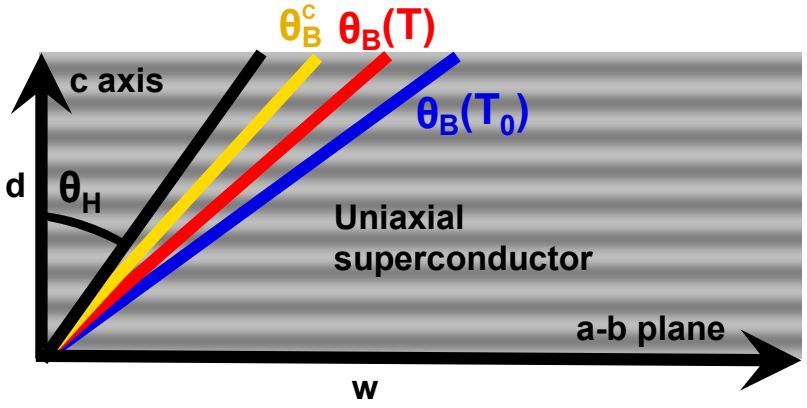

Figure 6.1: Schematic vortex alignment for an anisotropic superconductor in tilted magnetic field. In black the angle of the applied magnetic field H, in yellow, the critical angle, calculated with Bean model and in red and blue, the equilibrium angles at temperatures, T_0= 0.15 K and T=2 K respectively. Figure from [157].

If we instead consider weak pinning, a critical state occurs (as explained in subsection 1.2.4 for perpendicular high magnetic fields). Critical state changes the ideal tilted angle between the applied magnetic field and vortices to the so called critical angle, θ_B^c, written as:

$$\theta_B^c = \theta_B - sin\theta_B \frac{4\pi j_c}{cB}\frac{w}{2} = \theta_B - \frac{w}{2l_b} sin\theta_B \tag{6.4}$$

For 2H-$NbSe_2$ we can calculate a θ_B^c - $\theta_H \simeq 0.3°$. Therefore, vortices are tilted out of the equilibrium position θ_B. In Fig. 6.1 we observe that at 2 K vortex line direction

is closer to the equilibrium angle θ_B than at lower temperatures.

6.2 Results

The images shown here were taken by J.A Galvis. The set of images are measured with a scanning tunnelling microscope at a base temperature of T=150 mK. Sample was cleaved *in situ* and a gold tip used was sharpened also *in situ*. First, a parallel to c-axis magnetic field was applied of H = 0.85 T (θ_H=0°). At this stage there was no observation of vortex movement within days. Then the magnetic field was rotated up to θ_H=70°. Several consecutive images of 23 minutes each were taken at different constant temperatures. First in a warming ramp with intermediate temperatures of T=[0.2, 0.6, 1, 1.6, 2] K, and then cooled again at temperatures of T=[1.8, 1, 0.6] K.

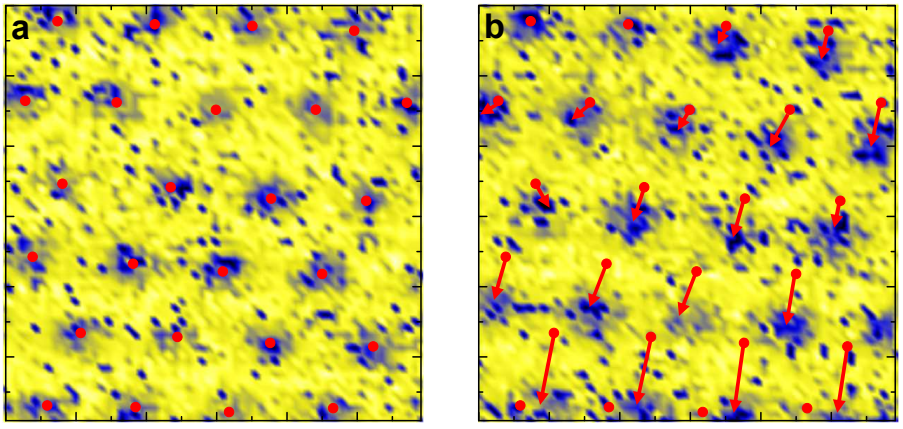

Figure 6.2: (a) and (b) represent two consecutive frames. In order to identify the motion of vortices, we plot in (b), the coordinates of the vortices in (a), using red circles. Red arrows mark the displacements of each vortex between consecutive images.

In order to analyse the images, it is important to detect vortices and follow them in consecutive images. To this end, I have developed a methodology described in the following. First, we detect the vortex centres with the method explained in subsection 2.4.1. Second, we plot the following images, comparing the positions of vortices in each consecutive set of two images. Third, we identify the general trend of vortex movement and click and drag the position of each vortex in the previous image, to the corresponding one in the present image. If a vortex appears or disappears, we create a new point or erase it. The process is iterated until the last image. At the end we have a matrix of size $N_v \times N_I$, being N_I, the number of images in the film and N_v the total number of vortices in all images. Following this procedure, we obtain the trajectories of all vortices. We follow the trajectories of vortices appearing in the images, including these from those vortices that only appear in part of the sequence. This helps us to increase the statistics in the calculation.

In Fig. 6.3, we show the first image at each temperature with the trajectories followed by each vortex in the whole sequence of images. At low temperatures, vortices move along the direction of the magnetic field within the layers. During the time of measurements at constant temperatures, ($\backsim$ 5 h) no decay on vortex velocity is observed. However, at higher temperatures vortices also move, but without a privileged direction.

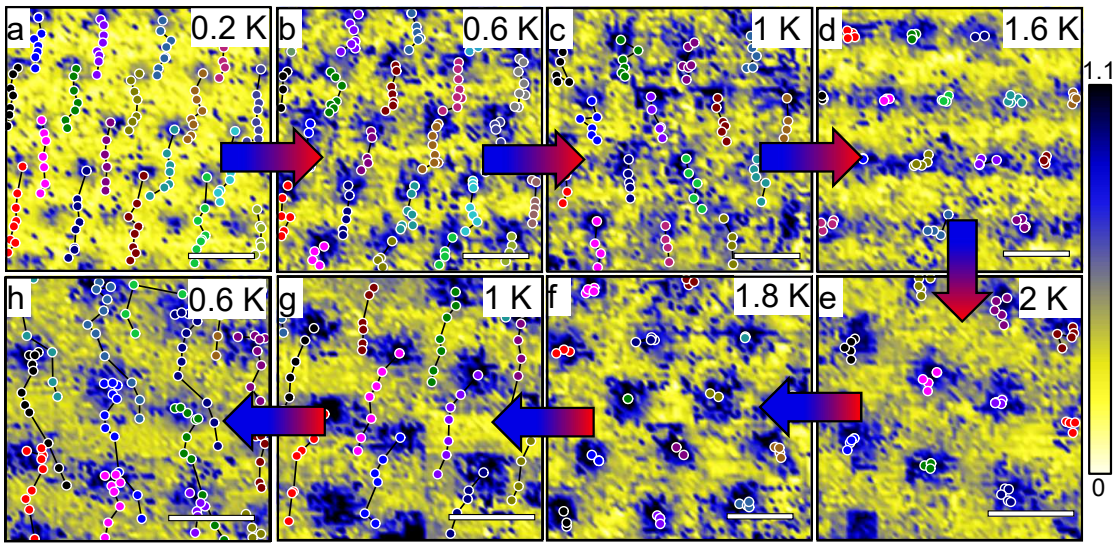

Figure 6.3: Vortex positions extracted for each image at constant temperature. The image represents the first frame of the set of images. At first, at T=0.2 K (a) there is a significant creep motion, it starts to disappear with temperature at T=0.6 K (b) and T = 1 K (c) until motion stops at a higher temperature at T= 1.6 K (d), T=2 K (e) and T=1.8 K (f). When temperature is decreased again at lower temperatures T=1 K (g) and T=0.6 K (h) creep starts again. White scalebar represents 60 nm.

Another important thing to note is that vortex motion shows a weak modulation at distances which correspond to multiples of the intervortex distance. In Fig. 6.4 we show a plot with the accumulated distance for 6 different vortices along the whole film. This self-matching has already been observed before in 2H-$NbSe_2$ and in disordered films [158, 159] and evidences that the lattice moves as a whole in the creep regime.

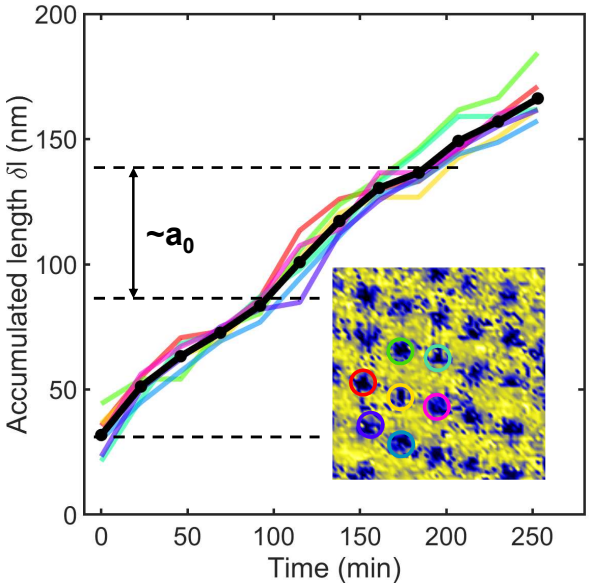

Figure 6.4: Average accumulated length vs time for 6 vortices represented in the inset at T=0.2 K. There is a weak modulation at distances multiples to the intervortex distance indicated by dashed lines.

In order to be more quantitative with the observations in Fig. 6.3, we considered it appropriate to define some quantities. The creep velocity of the vortex, $v(T)$, using the position $\mathbf{r}_j$ of vortex j in frame i, and the average displacement δr_j, for each vortex per frame defined as:

$$\delta r_j = \frac{|\mathbf{r}_j^{n_j} - \mathbf{r}_j^1|}{n_j - 1} \tag{6.5}$$

where n_j denotes the number of frames where the jth vortex appears. Averaging over all N_v vortices for a given temperature, we arrive at the average creep velocity

$$v(T) = \frac{1}{t_f N_v} \sum_{j=1}^{N_v} \delta r_j \tag{6.6}$$

Being t_f the time taken per image, t_f=23 min. We also want to define the vortex motion at higher temperature due to fluctuations around a fixed position as the jitter velocity, δs_j, with

$$\delta s_j = (\frac{1}{n_j - 1} \sum_{i=2}^{n_j} |\delta \mathbf{r}_j^i|) - \delta r_j \tag{6.7}$$

with $|\delta \mathbf{r}_j^i|$ the vortex displacement between two subsequent frames i-1 and i. The average of all frames at a fixed temperature provides the jitter motion, $\Delta x(T)$, is

given by

$$\Delta x(T) = \frac{1}{N_v}\sum_{j=1}^{N_v}\delta s_j \tag{6.8}$$

Inset of Fig. 6.5b, shows an sketch of the quantities δr_j, $\sum_{i=2}^{n_j}|\delta \mathbf{r}_j^i|$and δs_j .

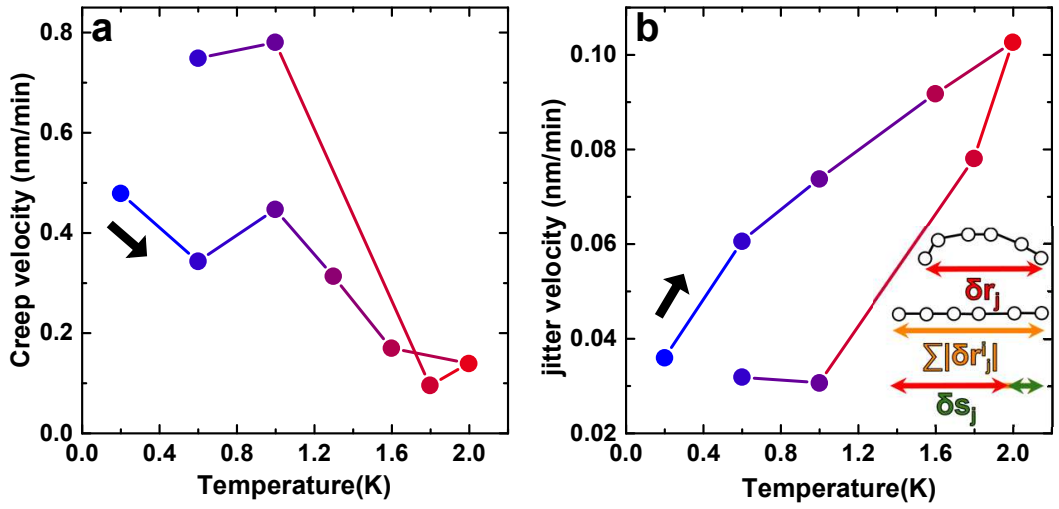

Figure 6.5: (a), Average velocity of vortices in 2H-$NbSe_2$ at titled field and fixed temperature, in a cycle starting in the black arrow. (b), Jitter motion during the same cycle of a. The inset of b, is a representation of δr_j, $\sum_{i=2}^{n_j}|\delta \mathbf{r}_j^i|$and δs_j.

In Fig. 6.5a we show the average creep velocity. The arrow indicates the beginning of the cycle. Creep velocity decreases upon warming and vanishes above 2 K. However, when system is cooled again, it reappears. Jitter velocity does the opposite, at low temperatures it is very low, and when heating, it increases (Fig. 6.5b). If vortices were to reach a temperature independent minimum, when the system is heated and cooled again, the creep motion would not reappear.

6.3 Discussion

6.3.1 Model for creep in presence of temperature

In the following we present a model developed by Roland Willa to describe vortex creep in tilted magnetic fields [157]. The main idea of the model as shown in the sketch of Fig. 6.6. Here, x is a parameter, as for example the angle formed between vortices and the applied magnetic field. As we discussed in section 6.1, vortices are in a critical state at an angle, θ_B^c (points out of the equilibrium in Fig. 6.6), different from the equilibrium angle θ_B (points at the minima Fig. 6.6). The energy landscape for the vortex with minimum at θ_B is modelled as a one dimensional parabolic trap. As θ_B depends on temperature (see Equation 6.1), low (blue) and high (red)

temperatures parabolas are different. In order to move towards the equilibrium position vortices must overcome the pinning barriers.

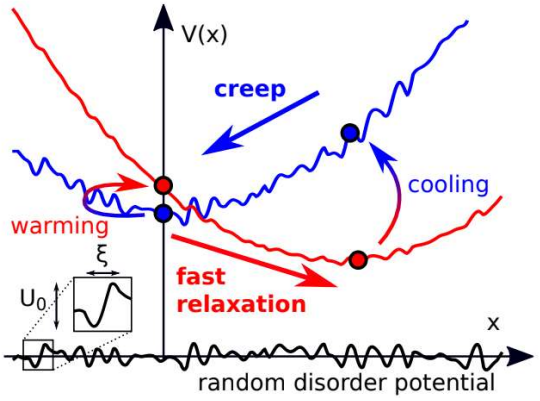

Figure 6.6: Schematic response of a particle in a confined potential and subject to random disorder. The disorder potential is characterized by local maxima of size U_0 and over a length scale ξ which is the superconducting coherence length in the case of vortices in superconductors. Upon warming, the particle moves rather quickly to a newly defined minimum as the disorder is thermally smeared out (indicated by effectively smaller wells, red). When cooling, the potential landscape U_b changes and the particle increases its energy relative to the new minimum in U_b. As the motion is impeded by pinning barriers (blue), the particle creeps by thermal relaxation towards the new minimum. Image from [157].

This model assumed that motion is driven by thermal fluctuations, through an Arrhenius-type activation process across the pinning barriers. In such a case, the timescale $t \sim \tau \exp(U_0/k_BT)$ for thermal activation is determined by (i) the temperature T, (ii) the energy barrier U_0, and (iii) a microscopic time scale $\tau = \omega^{-1}$ (ω is an attempt frequency to overcome the barrier).

In order to compare between experiment and theory, creep velocity and jitter motion have been calculated as:

$$v \approx \frac{2\xi}{t}\Big\{1 - \exp\Big[-\frac{4U_0}{k_BT}\Big(1 - \sqrt{\frac{k_BT\ln(\omega t)}{U_0}}\Big)\Big]\Big\}, \tag{6.9}$$

$$\Delta x \sim \xi\sqrt{\omega t}\exp\Big[-\frac{2U_0}{k_BT}\Big(1 - \sqrt{\frac{k_BT\ln(\omega t)}{U_0}}\Big)\Big]. \tag{6.10}$$

Note that x is not the angle but the displacement of the vortices in the surface.

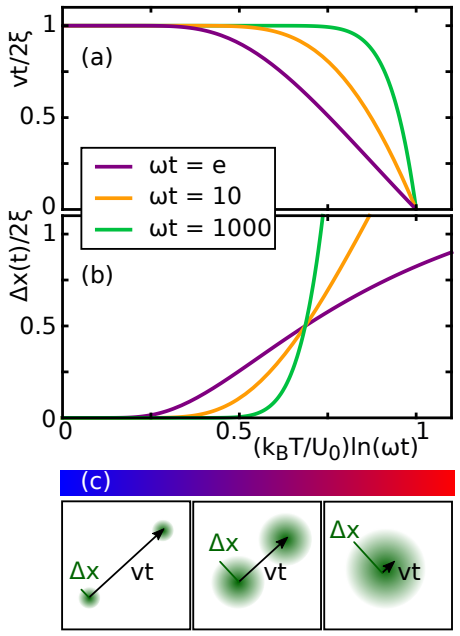

Figure 6.7: (a), Average creep velocity v (in units of $2\xi/t$) as a function of temperature, see Eq. (6.9), for different timescales ωt. When temperature affects both the activation dynamics and the global potential minimum, see Fig. 6.6, the velocity profile is traced reversibly upon warming and cooling. (b), Standard deviation Δx of the mean particle displacement, quantifying the isotropic thermal motion, or jitter, see Eq. (6.10). (c), Schematic of decreasing creep velocity (black arrow) and increasing jitter motion (green cloud) upon warming. From [157]

Equation 6.9 and Equation 6.10 are equivalent to creep (Equation 6.6) and jitter (Equation 6.8) respectively. We can observe in Fig. 6.7(a,b) the curves of the creep velocity (Equation 6.9) and jitter (Equation 6.10) for different timescales, wt. While creep velocity decreases with temperature, jitter motion is enhanced. In Fig. 6.7c an sketch of the predicted behaviour is shown. At low temperatures, vortices have less energy to overcome all the pinning barriers and therefore, they move slowly enough to be able to observe it in our timescale. However, at higher temperatures, vortices have more energy to overcome pinning barriers and they reach equilibrium position faster. Still, as they have a thermal energy they jump randomly along local minima potential increasing the jitter motion.

6.3.2 Comparison with our results

We can now compare our observations in 2H-$NbSe_2$ with the model. The typical barrier to overcome during pinning by thermal fluctuations is given by Arrhenius' law $U_0 = k_B T \ln(\omega t)$. To observe both the equilibrium phase at high temperature and reentrant creep at low temperature, it is important that the temperature of the experiment is of order of $(U_0/k_B)/\ln(\omega t)$. In contrast to the pinning energy of one defect site, here U_0 denotes the energy barrier for vortex creep [160, 161]. The theory of weak collective pinning [162, 163, 130] provides the

estimate $U_0 \sim k_B T_c[(j_c/j_{\rm dp})/Gi]^{1/2}(B/H_{c1})^{3/2}\nu$, with $j_{\rm dp} = c\Phi_0/12\sqrt{3}\pi^2\lambda^2\xi$ the depairing current, $Gi \sim [T_c/H_c(0)^2\xi^3]^2$ the Ginzburg-Levanyuk number [164, 165], $H_c(0)^2\xi^3 = \Phi_0^2\xi/8\pi^2\lambda^2$ the superconducting condensation energy and $\nu \sim 10^{-3}$. For 2H-$NbSe_2$ we find $j_c/j_{\rm dp} \sim 10^{-6}$ and $Gi \sim 8\times10^{-7}$, from Refs. [166, 167, 168, 169, 170] and obtain $U_0 \sim 5k_BT_c$, which is compatible with $U_0 \lesssim k_BT_c\ln(\omega t)$, provided $\omega t \approx 10^3 - 10^4$. This is somewhat larger than the values considered above Fig. 6.7). Given the simplicity of the one-dimensional model, the agreement is still remarkable. All important features predicted by the model (Fig. 6.7)—the disappearance and reappearance of the directed motion, together with the temperature-evolution of the jitter motion [behaviours of $v(T)$ and $\Delta x(T)$, shown in Fig. 6.5(a,b) and in Fig. 6.7(a,b)]—are found in the experiment.

Given that the experimental time scale spans several minutes, our observation $\omega t \sim 10^4$ suggest a value for ω of order of one Hz. While a route for accurate determination of this attempt frequency is still lacking, the estimate $\omega = \alpha_L/\eta$ for a single vortex depends on the vortex viscosity η and on the Labusch parameter [171] α_L (which in turn relates to the averaged potential curvature[172]). While values in the range 10^6-10^{10} Hz have been reported [173], the analysis assumes vibrations with large k-vectors. In our case, vortices are not isolated, but rather interact non-locally with many vortices [174, 130, 175, 176, 177, 178]. Low k-vectors, or wave-lengths comparable to the sample size, leads to highly dispersive elastic moduli which modify the attempt frequency by orders of magnitude [179, 176, 180]. Similar to our observation, previous measurements of slow vortex dynamics have reported very low frequency values for thermal motion and creep [177, 181]. Creep rates observed in layered cuprate superconductors involve extremely large time scales, indicating the relevance of collective creep [180, 130, 175, 179]. Thus, even if the attempt rate of individual vortices is large, the dynamics as a lattice involves rates that are many orders of magnitude smaller. The temperature is far from melting, thus favoring collective rather than a single-vortex dynamics [182, 183]. This near-equilibrium configuration with ultra-small collective dynamics is what allow for the observed cooling imposed creep in our experiments.

The creep discussed here is very slow and no decay in the vortex velocity is observed within our experimental time. However, the creep rate $S = d\ln(j)/d\ln(t)$ can assume a seizeable value compatible with the suggested lower bound[184] $S > (T/T_c)Gi^{1/2}$. Actually, 2H-$NbSe_2$ is among the materials with lowest creep rates, close to MgB_2[184]. Creep between metastable vortex states that occur near the order-disorder transition of the vortex lattice in 2H-$NbSe_2$ or related to domain formation of lattices with different orientations in MgB_2 has been reported[185, 186, 187]. Motion then appears when modifying the relative strength of competing interactions, and it might well occur that the equilibrium configuration at some particular locations is influenced by temperature. Collective motion is also found in stochastic behaviour of particle arrangements [146]. Depending on particle interactions, the dynamics transits from individual random motion to flocking. The time scale related to flocking motion shows a divergent behaviour with increasing interaction. Other long term dynamical behaviour should appear in thermal effects and might lead to creep on cooling whenever there are two or more parameters

influencing the behaviour of the system. Mixtures, such as alloys, concrete or rocks [188], liquids re-solidifying under stress [147], steel under stress [148], colloidal systems, magnetic domain walls or skyrmions [150] might all be cases of complex systems where creep combines with the temperature variations of the interaction and provide new temperature dependent effects, such as creep onset on cooling.

The model of self-imposed creep explains the critical state dynamics in 2H-$NbSe_2$ at tilted magnetic fields; in particular the commonly unexpected appearance of vortex motion when cooling. Likely, the balanced thermal activation dynamics and the temperature-dependent equilibrium could be matched in many other uniaxial superconductors with weak pinning and in complex systems.

6.3.3 Comparison with other systems showing creep

One of the first creep visualizations was realised by Kes in irradiated samples of 2H-$NbSe_2$ irradiated with columnar defects (CD) [158]. Vortex plastic flow begins when the number of vortices is twice the number of defects. Some vortices remain pinned but others flow along the high symmetry direction of the vortex lattice. This was the first observation of matching of vortex motion with a washboard potential made by the whole lattice and pinning.

Another interesting experiment was performed by Nishida in YNi_2B_2C [189]. This creep was not observed in equilibrium conditions but during a constant magnetic field ramp of 0.2T/h in high magnetic fields. Vortices flows in the same directions as glide dislocation in the vortex lattice.

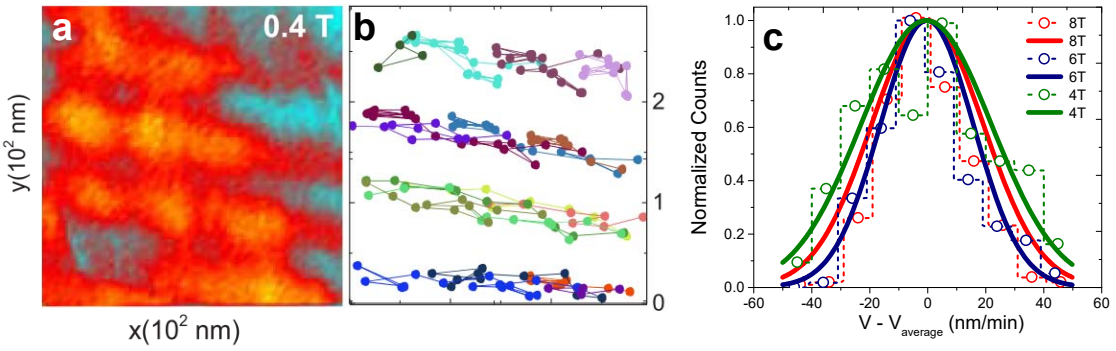

Figure 6.8: Results of low temperature creep in $Rh_9In_4S_4$ [190]. (a), average image of all the images taken at 0.4 T. (b) Trajectories of vortices (points) in consecutive images of H=0.4 T. (c), Histogram of the velocities found for the images set at H= 0.4 T, 0.6 T and 0.8 T. We represent counts for a given velocity (x axis) measured with respect to the average velocity. The counts (y axis) are normalised to one at the center. To calculate the velocity, we use the distance travelled between two subsequent images. The histograms are shown by the dashed lines and points, and the lines are Gaussian fits, giving approximately a half width of 23, 16, and 20 nm/h for 0.4, 0.6, and 0.8 T, respectively.

We also observed low temperatures creep in the system of $Rh_9In_4S_4$ [190]. For

this work we also analysed the vortex creep images taken by E. Herrera. This compound is characterised by a large Ginzburg-Landau parameter of $\kappa \approx 61$. STM images were taken at 150 mK at magnetic fields of 0.4 T, 0.6 T and 0.8 T. We observed creep a motion at common direction but also jitter-like movement. This jitter motion was comparable at all magnetic fields. In this compound, the Ginzburg Levanyuk parameter, G_i, is very large, of order of 10^{-5}. Therefore, the thermal contributions are still important even at low temperatures and vortex creep is thermally activated to reach an equilibrium position. The key difference with the observations in 2H-$NbSe_2$ is that in $Rh_9In_4S_4$ is an isotropic superconductor and therefore, the equilibrium position does not change with temperature. This means that if temperature is raised, vortex lattice will move faster to the equilibrium position, and when the temperature is cooled again, vortex lattice will be steady.

6.3.4 Conclusions

In summary, we have analysed vortex lattice images in tilted magnetic fields in 2H-$NbSe_2$. We find that vortices start creeping when cooling and provide a careful calculation of the velocities and vortex positions. This calculation has allowed us to compare to a theoretical model that brings understanding into the observation. The equilibrium position to which the vortex lattice creeps changes with temperature. This phenomenon might as well appear in other complex systems showing creep.

Summary

Since 1911 when Kamerling Onnes discovered superconductivity, a huge interest on this phenomenon arose due to its potential ability to change the way we distribute and store energy. However, the presence of superconductors in our daily lives is probably much smaller than expected 100 years ago. One important reason for this, is that the motion of vortices under the presence of a current produces non-zero resistance. Hence, vortices need to be pinned in any practical application of superconductors. Nevertheless, new and exciting discoveries in the past years, such as the iron-based superconductors or innovative methods to make superconductors operational at higher temperatures and fields, show that we are in front of a significant improvement of their properties for applications.

Throughout this thesis, we have measured and analysed vortex lattices using local probe microscopies in various superconducting materials under different external conditions. One of the main advantages of locally observing vortex lattices is that we have simultaneous information on vortex positions and disorder producing pinning in the sample, and that we we can make statistical studies of the lattice and relate these to the behaviour of individual vortices.

A disordered hyperuniform lattice is one of the vortex arrangements that have been proposed in order to increase critical current. Hyperuniformity means no long-distance density fluctuations. As this concept includes crystals and polycrystals, we have looked specifically for strongly disordered vortex lattices. We have analysed a number of vortex lattice images with different disorder levels, and find that a vortex lattice might show hyperuniform behaviour if the lattice is stiff enough and individual vortex pinning strong enough to distort the lattice at short length scales and leave a homogeneous distribution at large scales.

We have also analysed *squid-on-tip* measurements of the vortex lattice at low fields (<100 G), in the superconductor β-Bi_2Pd. The presence of linear defects produces a very inhomogeneous vortex arrangement, where the standard deviation of distances between first neighbours diverges as the magnetic field decreases. Furthermore, we have found that these arrangements are multifractal. We have compared our results with other vortex phases reported at low magnetic fields. We have found that the multifractal properties and diverging standard deviation with decreasing field are rather unique properties of this phase, that we called vortex gel using the analogy with the characteristics of gels and foams. As we have discussed, this system can be considered to be anti-hyperuniform.

Additionally, we studied the effect of a tilted magnetic field over the vortex lattice in the uniaxial superconductor 2H-$NbSe_2$. Creep is created by jumps of vortices

over small potential barriers and is on the very origin of the onset of dissipation in a superconductor. Usually, creep requires thermal energy and appears when heating. But experiments show here the opposite. By carefully following the change in the positions of the vortices as a function of time and temperature, and determining the creep speed and fluctuations with respect to their equilibrium position due to thermal jitter, we have found the origin of this peculiar effect. The anisotropic properties of 2H-$NbSe_2$ make that the equilibrium position of the vortex lattice is changed when cooling. This explains the appearance of creep upon cooling. In this work, we have collaborated with R. Willa from Karlsruhe to develop a theoretical model that explains the experimental data.

Another system that has been studied and analysed is the Ni-doped $CaK(Fe_{0.95}Ni_{0.05})_4As_4$ pnictide. In this material a non-collinear antiferromagnetic order, known as hedgehog, coexists with superconductivity at low temperatures. We have observed that the vortex lattice in the Ni-doped compound is more disordered than in the stoichiometric compound. Our quasiparticle interference (qpi) measurements show that the Fermi surface is reconstructed giving compelling evidence for the microscopic coexistence of superconductivity and hedgehog AFM order. We find that this coexistence produces a very anisotropic superconducting gap with a four-fold in-plane symmetry. These results are reproduced by band-structure calculations performed by the group of R. Valenti in Frankfurt. Finally, we have reported $\sqrt{2}\times\sqrt{2}$ charge modulation induced by atomic displacement under magnetic field in the hedgehog AFM crystalline structure.

In this thesis, I performed the first measurements of the superconducting properties and the vortex lattice of a system where superconductivity coexists with non-collinear magnetic order. I found a significant influence of the magnetic order in superconductivity. I also built a STM and developed methods to analyse vortex images. Using those methods, I pointed out the presence of a new vortex phase in β-Bi_2Pd, discussed the possibility to have hyperuniform vortex lattices in the mentioned $CaKFe_4As_4$ and in other systems, and analysed vortex creep.

Conclusiones generales

Desde 1911, cuando Kamerling Onnes descubrió la superconductividad, el interés en este fenómeno despertó un enorme interés debido a su potencial para cambiar la forma en que distribuimos y almacenamos la energía. Sin embargo, el impacto de la superconductividad en la actualidad, es probablemente mucho menor de lo que se esperaba hace 100 años. Uno de los principales motivos, es el hecho de que el movimiento de vórtices en presencia de una corriente eléctrica, produzca una resistencia. Por tanto, para lograr cualquier aplicación práctica de los superconductores, es necesario que los vórtices estén anclados. No obstante, en los últimos años se han realizado nuevos e interesantes descubrimientos, como los superconductores basados en hierro y métodos innovadores para conseguir que los superconductores sean eficientes a mayores temperaturas y campos, demostrando que estamos ante una mejora significativa de sus propiedades de cara a las aplicaciones.

A lo largo de esta tesis, hemos medido y analizado redes de vórtices usando microscopia con resolución espacial en varios materiales superconductores y bajo diferentes condiciones externas. Una de las principales ventajas de la observación local de redes de vórtices, es que simultáneamente tenemos información sobre las posiciones de los vórtices y el desorden que produce anclajes en la muestra. También, podemos realizar estudios estadísticos a la vez que mantenemos la información de vórtices individuales.

Una de las distribuciones propuestas para aumentar la corriente crítica es una red hiperuniforme desordenada. La hiperuniformidad describe un sistema en el que no existen fluctuaciones de densidad de larga distancia. Dado que este concepto podría incluir cristales y policristales, se ha buscado específicamente un sistema desordenado. Hemos analizado muchas imágenes de redes de vórtices con diferentes niveles de desorden, y hemos visto que es casi imposible desordenar una red de vórtices de manera hiperuniforme. A pesar de esto, encontramos que la red de vórtices en LiFeAs se acerca bastante a esta definición.

También hemos analizado medidas *squid-on-tip* en redes de vórtices a bajos campos (<100 G), en el superconductor β-Bi_2Pd. La presencia de defectos lineales produce una distribución de vórtices muy inhomogénea, donde la desviación estándar de las distancias entre primeros vecinos diverge a medida que el campo magnético disminuye. Además, hemos observado que estas distribuciones son multifractales. Hemos comparado nuestros resultados con la fase de vórtices de otros materiales a campos magnéticos bajos. Encontramos que tanto las propiedades multifractales, como la divergencia de la desviación estándar al disminuir el campo magnético, son

propiedades únicas de esta fase, a la que hemos denominado gel de vórtices, usando la analogía con las características de los geles y las espumas. Tal y como hemos discutido, este sistema puede considerarse anti-hiperuniforme.

Además, hemos estudiado el efecto del campo magnético inclinado sobre la red de vórtices en el superconductor uniaxial 2H-$NbSe_2$. Hemos observado, de manera inesperada, que el movimiento de arrastre de los vórtices comienza cuando la muestra se enfría. Dicho movimiento comienza cuando los vórtices sobrepasan pequeñas barreras de potencial y es el origen de la disipación del superconductor. Habitualmente, el creep requiere energía térmica y aparece cuando se calienta el material. Sin embargo, hemos observado lo contrario. Estudiando cuidadosamente los cambios en las posiciones de los vórtices en función del tiempo y de la temperatura, y, determinando la velocidad del movimiento de arrastre y sus fluctuaciones con respecto a la posición de equilibrio dada la agitación térmica, hemos localizado el origen de este peculiar efecto. Las propiedades anisótropas del 2H-$NbSe_2$ causan que el punto de equilibrio de la posición del vórtice varíe al enfriarse. Esto explica la aparición del movimiento de arrastre al bajar la temperatura. En este trabajo, hemos colaborado con R. Willa de Karlsruhe para desarrollar un modelo teórico que explique los datos experimentales.

También se ha estudiado y analizado el pnicturo $CaK(Fe_{0.95}Ni_{0.05})_4As_4$ dopado con Ni. En este material, coexiste un orden antiferromagnético no colineal, conocido como hedgehog o erizo, junto con la superconductividad a bajas temperaturas. Se ha observado que la red de vórtices del compuesto dopado con Ni está más desordenada que la del compuesto estequiométrico. Nuestras medidas de interferencias de cuasipartículas (qpi), concuerdan con una superficie de Fermi reconstruida, teniendo así indicios de la coexistencia microscópica entre la superconductividad y el orden AFM de hedgehog. Esta coexistencia, produce un gap superconductor muy anisotrópico con una simetría de orden cuatro. Estos resultados han sido reproducidos por cálculos de estructura de bandas realizados por el grupo de R. Valenti en Frankfurt. Finalmente, hemos mostrado una modulación de carga $\sqrt{2} \times \sqrt{2}$, inducida por los desplazamientos atómicos en la estructura cristalina bajo campo magnético asociados al AFM de hedgehog. En esta tesis he realizado las primeras medidas de las propiedades superconductoras y la red de vórtices en un sistema que coexiste con un orden magnético no colineal. También construí un STM y he desarrollado métodos para analizar imágenes de vórtices. Con ellos, hemos comprobado la nueva fase de vórtices en el β-Bi_2Pd, discutido la posibilidad de tener redes de vórtices hiperuniformes tanto en el material $CaKFe_4As_4$ como en otros sistemas y finalmente analizar el creep de vortices.

Publications

- E. Herrera-Vasco, **J. Benito-Llorens** , Udhara S. Kaluarachchi, S.L. Bud'ko, P. C. Canfield, I. Guillamón, H. Suderow , "Vortex creep at very low temperatures in single crystals of the extreme type-II superconductor $Rh_9In_4S_4$", *Phys. Rev. B 95, 134505 (2017).*

- R. Willa and J.A. Galvis, **J. Benito-Llorens** and E. Herrera, I. Guillamon and H. Suderow , "Thermal creep induced by cooling a superconducting vortex lattice", *accepted in PR Research (2019).*

- **J. Benito-Llorens**, Lior Embon, Alexandre Correa, Jesés David González, Edwin Herrera, Isabel Guillamón, Roberto F. Luccas, Jon Azpeitia, Federico J. Mompeán, Mar García-Hernández, Carmen Munuera, Jazmín Aragón Sánchez, Yanina Fasano, Milorad V. Milosevic, Hermann Suderow, Yonathan Anahory, "Observation of a gel of quantum vortices in a superconductor at very low magnetic fields", *submitted to PR Research (2019).*

- **J. Benito-Llorens**, E.Herrera, V.Barrena, H.Suderow, I.Guillamón, W.R. Meier, S. Bud'ko, P.C. Canfield, V Borisov and R.Valentí, "Superconducting density of states and vortex lattice in the spin-vortex state of Ni-doped", *in preparation.*

- **J. Benito-Llorens**, R. Córdoba, J.M. De Teresa, R. Ibarra, S. Vieira, I. Guillamón, M. Ortuño, and H. Suderow. , "Repulsive interactions between superconducting vortices arrested by disorder", *in preparation.*

Bibliography

[1] H. K. Onnes, "Further experiments with liquid helium. g. on the change of electrical resistance of pure metals at very low temperatures, etc. vi. on the sudden change in the rate at which the resistance of mercury disappears," *Comm. Phys. Lab. Univ. Leiden*, vol. Supp. 29, 1911.

[2] W. Meissner and B. Voigt, "Messungen mit hilfe von flüssigem helium xi widerstand der reinen metalle in tiefen temperaturen," *Annalen der Physik*, vol. 399, no. 7, pp. 761–797, 1930.

[3] H. London, ed., *Proceedings of the 2nd International Conference on Low Temperature Physics*, (Oxford, UK), Oxford Univ. Press, 1951.

[4] L. Landau, "On the theory of phase transitions," *Zh. Eksp. Teor. Fiz*, vol. 7, pp. 19–32, 1969.

[5] L. L. V.L. Ginzburg, "On the theory of superconductivity," *Zh. Eksp. Teor. Fiz.*, vol. 20, pp. 1064–1082, 1950.

[6] J. Bardeen, L. N. Cooper, and J. R. Schrieffer, "Microscopic theory of superconductivity," *Phys. Rev.*, vol. 106, pp. 162–164, Apr 1957.

[7] J. Bardeen, L. N. Cooper, and J. R. Schrieffer, "Theory of superconductivity," *Phys. Rev.*, vol. 108, pp. 1175–1204, Dec 1957.

[8] K. F. Herzfeld, E. Maxwell, and R. B. Scott, "Isotope effect and lattice properties in superconductivity," *Phys. Rev.*, vol. 79, pp. 911–911, 1950.

[9] H. Fröhlich, "Theory of the superconducting state. i. the ground state at the absolute zero of temperature," *Phys. Rev.*, vol. 79, pp. 845–856, 1950.

[10] L. N. Cooper, "Bound electron pairs in a degenerate fermi gas," *Phys. Rev.*, vol. 104, pp. 1189–1190, Nov 1956.

[11] Y. Fasano and M. Menghini, "Magnetic-decoration imaging of structural transitions induced in vortex matter," *Superconductor Science and Technology*, vol. 21, no. 2, p. 023001, 2008.

[12] D. Vasyukov, Y. Anahory, L. Embon, D. Halbertal, J. Cuppens, L. Ne'eman, A. Finkler, Y. Segev, Y. Myasoedov, M. L. Rappaport, M. Huber, and E. Zeldov, "Scanning nano-SQUID with single electron spin sensitivity," *Nature Nanotechnology*, vol. 8, no. 9, pp. 639–644, 2013.

[13] J. R. Kirtley, "Fundamental studies of superconductors using scanning magnetic imaging," *Reports on Progress in Physics*, vol. 73, no. 12, p. 126501, 2010.

[14] H. Suderow, I. Guillamón, J. G. Rodrigo, and S. Vieira, "Imaging superconducting vortex cores and lattices with a scanning tunneling microscope," *Superconductor Science and Technology*, vol. 27, no. 6, p. 063001, 2014.

[15] O. Fischer, M. Kugler, I. Maggio-Aprile, C. Berthod, and C. Renner, "Scanning tunneling spectroscopy of high-temperature superconductors," *Rev. Mod. Phys.*, vol. 79, pp. 353–419, Mar 2007.

[16] M. Tinkham, *Introduction to Superconductivity*. McGraw-Hill International Editions, 1996.

[17] V. V. Schmidt, *The physics of superconductors: introduction to fundamentals and applications*. Berlin-Heidelberg-New York: Springer - Verlag, 1 ed., 1997. Original russian edition published by Nauka Publishers, Moscow, (1982).

[18] E. H. Brandt, "The flux-line lattice in superconductors," *Rep. Prog. Phys.*, vol. 58, p. 1465, 1995.

[19] G. Blatter, M. Feigel'man, V. Geshkenbein, A. Larkin, and V. Vinokur, "Vortices in high temperature superconductors," *Rev. Mod. Phys.*, vol. 66, p. 1125, 1994.

[20] V. G. Kogan and N. V. Zhelezina, "Field dependence of the vortex core size," *Phys. Rev. B*, vol. 71, p. 134505, Apr 2005.

[21] A. Fente, E. Herrera, I. Guillamón, H. Suderow, S. Mañas Valero, M. Galbiati, E. Coronado, and V. G. Kogan, "Field dependence of the vortex core size probed by scanning tunneling microscopy," *Phys. Rev. B*, vol. 94, p. 014517, Jul 2016.

[22] A. Fente, W. R. Meier, T. Kong, V. G. Kogan, S. L. Bud'ko, P. C. Canfield, I. Guillamón, and H. Suderow, "Influence of multiband sign-changing superconductivity on vortex cores and vortex pinning in stoichiometric high-T_c $CaKFe_4As_4$," *Phys. Rev. B*, vol. 97, p. 134501, Apr 2018.

[23] A. Vargunin and M. A. Silaev, "Field dependence of the vortex-core size in dirty two-band superconductors," *Phys. Rev. B*, vol. 100, p. 014516, Jul 2019.

[24] E. H. Brandt, "Thermal fluctuation and melting of the vortex lattice in oxide superconductors," *Phys. Rev. Lett.*, vol. 63, pp. 1106–1109, Sep 1989.

[25] T. Giamarchi and P. Le Doussal, "Moving glass phase of driven lattices," *Phys. Rev. Lett.*, vol. 76, pp. 3408–3411, Apr 1996.

[26] P. Berghuis, A. L. F. van der Slot, and P. H. Kes, "Dislocation-mediated vortex-lattice melting in thin films of a-Nb_3Ge," *Phys. Rev. Lett.*, vol. 65, pp. 2583–2586, Nov 1990.

[27] A. Yazdani, W. R. White, M. R. Hahn, M. Gabay, M. R. Beasley, and A. Kapitulnik, "Observation of Kosterlitz-Thouless-type melting of the disordered vortex lattice in thin films of a-MoGe," *Phys. Rev. Lett.*, vol. 70, pp. 505–508, Jan 1993.

[28] I. Guillamón, H. Suderow, S. Vieira, R. Córdoba, J. Sesé, J. De Teresa, and M. Ibarra, "Direct observation of melting in a 2d superconducting vortex lattice through very low temperature scanning tunneling spectroscopy," in *Abstracts of the 18th International of Vacuum Congress*, 2010.

[29] I. Guillamón, R. Córdoba, J. Sesé, J. M. De Teresa, M. R. Ibarra, S. Vieira, and H. Suderow, "Enhancement of long-range correlations in a 2D vortex lattice by an incommensurate 1D disorder potential," *Nature Physics*, vol. 10, no. 11, p. 851, 2014.

[30] I. Guillamon, *Orden y desorden en superconductividad.* PhD thesis, Universidad Autonoma de Madrid, 2009.

[31] J. B. Llorens, L. Embon, A. Correa, J. D. González, E. Herrera, I. Guillamón, R. F. Luccas, J. Azpeitia, F. J. Mompeán, M. García-Hernández, C. Munuera, J. A. Sánchez, Y. Fasano, M. V. Milosevic, H. Suderow, and Y. Anahory, "Observation of a gel of quantum vortices in a superconductor at very low magnetic fields," 2019.

[32] A. L. Schawlow, "Structure of the intermediate state in superconductors," *Phys. Rev.*, vol. 101, pp. 573–579, Jan 1956.

[33] E. H. Brandt and M. P. Das, "Attractive vortex interaction and the intermediate-mixed state of superconductors," *Journal of Superconductivity and Novel Magnetism*, vol. 24, no. 1, pp. 57–67, 2011.

[34] T. Reimann, S. Mühlbauer, M. Schulz, B. Betz, A. Kaestner, V. Pipich, P. Böni, and C. Grünzweig, "Visualizing the morphology of vortex lattice domains in a bulk type-ii superconductor," *Nature Communications*, vol. 6, pp. 8813 EP –, Nov 2015. Article.

[35] C. P. Bean, "Magnetization of hard superconductors," *Physical Review Letters*, vol. 8, p. 250, 1962.

[36] J. G. Bednorz and K. A. Muller, "Possible High T_c superconductivity in the Ba-La-Cu-O system," *Zeitschrift fur Physik B Condensed Matter*, vol. 64, pp. 189–193, June 1986.

[37] Y. Kamihara, H. Hiramatsu, M. Hirano, R. Kawamura, H. Yanagi, T. Kamiya, and H. Hosono, "Iron-based layered superconductor: LaOFeP," *Journal of the American Chemical Society*, vol. 128, no. 31, pp. 10012–10013, 2006. PMID: 16881620.

[38] Y. Kamihara, T. Watanabe, M. Hirano, and H. Hosono, "Iron-based layered superconductor $LaO_{1-x}F_xFeAs$ (x= 0.05-0.12) with T_c= 26 K," *Journal of the American Chemical Society*, vol. 130, pp. 3296–3297, Mar. 2008.

[39] J. Paglione and R. L. Greene, "High-temperature superconductivity in iron-based materials," *Nature Physics*, vol. 6, pp. 645–658, Aug. 2010.

[40] A. Chubukov and P. J. Hirschfeld, "Iron-based superconductors, seven years later," *Physics Today*, vol. 68, pp. 46–52, June 2015.

[41] X. Wang, Q. Liu, Y. Lv, W. Gao, L. Yang, R. Yu, F. Li, and C. Jin, "The superconductivity at 18 k in LiFeAs system," *Solid State Communications*, vol. 148, pp. 538–540, Dec. 2008.

[42] T. Hanaguri, K. Kitagawa, K. Matsubayashi, Y. Mazaki, Y. Uwatoko, and H. Takagi, "Scanning tunneling microscopy/spectroscopy of vortices in LiFeAs," *Phys. Rev. B*, vol. 85, p. 214505, Jun 2012.

[43] J.-F. Ge, Z.-L. Liu, C. Liu, C.-L. Gao, D. Qian, Q.-K. Xue, Y. Liu, and J.-F. Jia, "Superconductivity above 100 k in single-layer FeSe films on doped $SrTiO_3$," *Nature Materials*, vol. 14, pp. 285–289, Nov. 2014.

[44] N. Ni, S. L. Bud'ko, A. Kreyssig, S. Nandi, G. E. Rustan, A. I. Goldman, S. Gupta, J. D. Corbett, A. Kracher, and P. C. Canfield, "Anisotropic thermodynamic and transport properties of single-crystalline $Ba_{1-x}K_xFe_2As_2$ (x = 0 and 0.45)," *Phys. Rev. B*, vol. 78, p. 014507, Jul 2008.

[45] A. Kordyuk, "Iron-based superconductors: Magnetism, superconductivity, and electronic structure (review article)," *Low Temperature Physics*, vol. 38, pp. 888–899, 09 2012.

[46] A. Carrington, "Quantum oscillation studies of the Fermi surface of iron-pnictide superconductors," *Reports on Progress in Physics*, vol. 74, p. 124507, oct 2011.

[47] P. J. Hirschfeld, M. M. Korshunov, and I. I. Mazin, "Gap symmetry and structure of Fe-based superconductors," *Reports on Progress in Physics*, vol. 74, p. 124508, oct 2011.

[48] A. Iyo, K. Kawashima, T. Kinjo, T. Nishio, S. Ishida, H. Fujihisa, Y. Gotoh, K. Kihou, H. Eisaki, and Y. Yoshida, "New-Structure-Type Fe-Based Superconductors: $CaAFe_4As_4$ (A = K, Rb, Cs) and $SrAFe_4As_4$ (A = Rb, Cs)," *Journal of the American Chemical Society*, vol. 138, no. 10, pp. 3410–3415, 2016. PMID: 26943024.

[49] A. Fente, *Visualizing the influence of defects and impurities on pnictide and chalcogenide superconductors*. PhD thesis, Universidad Autonoma de Madrid, 2017.

[50] E. Herrera Vasco, *Visualizing the influence of the Fermi surface on Superconductivity*. PhD thesis, Universidad Autonoma de Madrid, 2017.

[51] L. S. C. Inc., "www.lakeshore.com," 2016.

[52] "Scientific instruments." Scientific Intruments web.

[53] J. A. Galvis, E. Herrera, I. Guillamón, J. Azpeitia, R. F. Luccas, C. Munuera, M. Cuenca, J. A. Higuera, N. Díaz, M. Pazos, M. García-Hernandez, A. Buendía, S. Vieira, and H. Suderow, "Three axis vector magnet set-up for cryogenic scanning probe microscopy," *Review of Scientific Instruments*, vol. 86, no. 1, pp. –, 2015.

[54] "Segainvex uam." Segainvex web.

[55] G. Binnig, H. Rohrer, C. Gerber, and E. Weibel, "Tunneling through a controllable vacuum gap," *Applied Physics Letters*, vol. 40, pp. 178–180, Jan. 1982.

[56] H. Suderow, I. Guillamon, and S. Vieira, "Compact very low temperature scanning tunneling microscope with mechanically driven horizontal linear positioning stage," *Review of Scientific Instruments*, vol. 82, no. 3, p. 033711, 2011.

[57] J. G. Rodrigo, H. Suderow, S. Vieira, E. Bascones, and F. Guinea, "Superconducting nanostructures fabricated with the scanning tunnelling microscope," *J. Phys.: Condens. Matter*, vol. 16, p. R1151, 2004.

[58] J. Bardeen, "Tunnelling from a many-particle point of view," *Phys. Rev. Lett.*, vol. 6, pp. 57–59, Jan 1961.

[59] J. Tersoff and D. R. Hamann, "Theory and application for the scanning tunneling microscope," *Phys. Rev. Lett.*, vol. 50, pp. 1998–2001, Jun 1983.

[60] J. Tersoff and D. R. Hamann, "Theory of the scanning tunneling microscope," *Phys. Rev. B*, vol. 31, pp. 805–813, Jan 1985.

[61] H. Suderow, I. Guillamón, J. G. Rodrigo, and S. Vieira, "Imaging superconducting vortex cores and lattices with a scanning tunneling microscope," *Superconductor Science and Technology*, vol. 27, p. 063001, may 2014.

[62] E. Herrera, I. Guillamón, J. A. Galvis, A. Correa, A. Fente, R. F. Luccas, F. J. Mompean, M. García-Hernández, S. Vieira, J. P. Brison, and H. Suderow, "Magnetic field dependence of the density of states in the multiband superconductor $\beta - Bi_2Pd$," *Phys. Rev. B*, vol. 92, p. 054507, Aug 2015.

[63] M. Tinkham, *Introduction to superconductivity*. New York: McGraw-Hill, 1975.

[64] L. Petersen, P. T. Sprunger, P. Hofmann, E. Lægsgaard, B. G. Briner, M. Doering, H.-P. Rust, A. M. Bradshaw, F. Besenbacher, and E. W. Plummer, "Direct imaging of the two-dimensional Fermi contour: Fourier-transform STM," *Phys. Rev. B*, vol. 57, pp. R6858–R6861, Mar 1998.

[65] J. E. Hoffman, *A search for alternative electronic order in the high temperature superconductor $Bi_2Sr_2CaCu_2O_{8+\delta}$ by scanning tunneling microscopy*. PhD thesis, University of California, Berkeley, Ca, USA, 2003. http://users.physics.harvard.edu/~jhoffman/thesis/HoffmanThesis.pdf.

[66] P. J. Hirschfeld, D. Altenfeld, I. Eremin, and I. I. Mazin, "Robust determination of the superconducting gap sign structure via quasiparticle interference," *Phys. Rev. B*, vol. 92, p. 184513, Nov 2015.

[67] "Available at https://github.com/lowtemperaturesuam/fractal-analysis."

[68] M. Rotter, M. Pangerl, M. Tegel, and D. Johrendt, "Superconductivity and Crystal Structures of $Ba_{1-x}KxFe_2As_2$ (x = 0-1)," *Angewandte Chemie International Edition*, vol. 47, no. 41, pp. 7949–7952, 2008.

[69] X. Lai, H. Zhang, Y. Wang, X. Wang, X. Zhang, J. Lin, and F. Huang, "Observation of Superconductivity in Tetragonal FeS," *Journal of the American Chemical Society*, vol. 137, no. 32, pp. 10148–10151, 2015. PMID: 26244711.

[70] Z. Deng, X. C. Wang, Q. Q. Liu, S. J. Zhang, Y. X. Lv, J. L. Zhu, R. C. Yu, and C. Q. Jin, "A new "111" type iron pnictide superconductor LiFeP," *EPL (Europhysics Letters)*, vol. 87, p. 37004, aug 2009.

[71] J. J. Hamlin, R. E. Baumbach, D. A. Zocco, T. A. Sayles, and M. B. Maple, "Superconductivity in single crystals of LaFePO," *Journal of Physics: Condensed Matter*, vol. 20, p. 365220, aug 2008.

[72] W. R. Meier, T. Kong, U. S. Kaluarachchi, V. Taufour, N. H. Jo, G. Drachuck, A. E. Böhmer, S. M. Saunders, A. Sapkota, A. Kreyssig, M. A. Tanatar, R. Prozorov, A. I. Goldman, F. F. Balakirev, A. Gurevich, S. L. Bud'ko, and P. C. Canfield, "Anisotropic thermodynamic and transport properties of single-crystalline $CaKFe_4As_4$," *Phys. Rev. B*, vol. 94, p. 064501, Aug 2016.

[73] W. R. Meier, *Growth, properties and magnetism of $CaKFe_4As_4$*. PhD thesis, Iowa State University, 2018.

[74] S. Pyon, D. Miyawaki, I. Veshchunov, T. Tamegai, K. Takano, H. Kajitani, N. Koizumi, and S. Awaji, "Fabrication and characterization of $CaKFe_4As_4$ round wires sintered at high pressure," *Applied Physics Express*, vol. 11, p. 123101, nov 2018.

[75] K. Cho, A. Fente, S. Teknowijoyo, M. A. Tanatar, K. R. Joshi, N. M. Nusran, T. Kong, W. R. Meier, U. Kaluarachchi, I. Guillamón, H. Suderow, S. L. Bud'ko, P. C. Canfield, and R. Prozorov, "Nodeless multiband superconductivity in stoichiometric single-crystalline $CaKFe_4As_4$," *Phys. Rev. B*, vol. 95, p. 100502, Mar 2017.

[76] J. Cui, Q.-P. Ding, W. R. Meier, A. E. Böhmer, T. Kong, V. Borisov, Y. Lee, S. L. Bud'ko, R. Valentí, P. C. Canfield, and Y. Furukawa, "Magnetic fluctuations and superconducting properties of $CaKFe_4As_4$ studied by ^{75}As NMR," *Phys. Rev. B*, vol. 96, p. 104512, Sep 2017.

[77] D. Mou, T. Kong, W. R. Meier, F. Lochner, L.-L. Wang, Q. Lin, Y. Wu, S. L. Bud'ko, I. Eremin, D. D. Johnson, P. C. Canfield, and A. Kaminski, "Enhancement of the Superconducting Gap by Nesting in $CaKFe_4As_4$: A New High Temperature Superconductor," *Phys. Rev. Lett.*, vol. 117, p. 277001, Dec 2016.

[78] W. R. Meier, Q.-P. Ding, A. Kreyssig, S. L. Bud'ko, A. Sapkota, K. Kothapalli, V. Borisov, R. Valentí, C. D. Batista, P. P. Orth, R. M. Fernandes, A. I. Goldman, Y. Furukawa, A. E. Böhmer, and P. C. Canfield, "Hedgehog spin-vortex crystal stabilized in a hole-doped iron-based superconductor," *npj Quantum Materials*, vol. 3, Feb. 2018.

[79] S. L. Bud'ko, V. G. Kogan, R. Prozorov, W. R. Meier, M. Xu, and P. C. Canfield, "Coexistence of superconductivity and magnetism in $CaK(Fe_{1-x}Ni_x)_4As_4$ as probed by ^{57}Fe mössbauer spectroscopy," *Phys. Rev. B*, vol. 98, p. 144520, Oct 2018.

[80] A. Kreyssig, J. M. Wilde, A. E. Böhmer, W. Tian, W. R. Meier, B. Li, B. G. Ueland, M. Xu, S. L. Bud'ko, P. C. Canfield, R. J. McQueeney, and A. I. Goldman, "Antiferromagnetic order in $CaK(Fe_{1-x}Ni_x)_4As_4$ and its interplay with superconductivity," *Phys. Rev. B*, vol. 97, p. 224521, Jun 2018.

[81] J. E. Hoffman, "Spectroscopic scanning tunneling microscopy insights into Fe-based superconductors," *Reports on Progress in Physics*, vol. 74, p. 124513, nov 2011.

[82] H. J. Choi, D. Roundy, H. Sun, M. L. Cohen, and S. G. Louie, "The origin of the anomalous superconducting properties of MgB_2," *Nature*, vol. 418, pp. 758–760, Aug. 2002.

[83] A. Fente, E. Herrera, I. Guillamón, H. Suderow, S. Mañas Valero, M. Galbiati, E. Coronado, and V. G. Kogan, "Field dependence of the vortex core size probed by scanning tunneling microscopy," *Phys. Rev. B*, vol. 94, p. 014517, Jul 2016.

[84] I. Guillamón, H. Suderow, S. Vieira, L. Cario, P. Diener, and P. Rodière, "Superconducting Density of States and Vortex Cores of 2H-NbS_2," *Phys. Rev. Lett.*, vol. 101, p. 166407, Oct 2008.

[85] S. Teknowijoyo, K. Cho, M. Kończykowski, E. I. Timmons, M. A. Tanatar, W. R. Meier, M. Xu, S. L. Bud'ko, P. C. Canfield, and R. Prozorov, "Robust $s_\pm$ pairing in $CaK(Fe_{1-x}Ni_x)_4as_4$ (x = 0 and 0.05) from the response to electron irradiation," *Phys. Rev. B*, vol. 97, p. 140508, Apr 2018.

[86] D. Torsello, K. Cho, K. R. Joshi, S. Ghimire, G. A. Ummarino, N. M. Nusran, M. A. Tanatar, W. R. Meier, M. Xu, S. L. Bud'ko, P. C. Canfield, G. Ghigo, and R. Prozorov, "Analysis of the London penetration depth in Ni-doped $CaKFe_4As_4$," *Phys. Rev. B*, vol. 100, p. 094513, Sep 2019.

[87] Y. Fasano, M. Menghini, F. de la Cruz, Y. Paltiel, Y. Myasoedov, E. Zeldov, M. J. Higgins, and S. Bhattacharya, "Order-disorder phase transition in $NbSe_2$: Absence of amorphous vortex matter," *Phys. Rev. B*, vol. 66, p. 020512, Jul 2002.

[88] V. Moshchalkov, M. Menghini, T. Nishio, Q. H. Chen, A. V. Silhanek, V. H. Dao, L. F. Chibotaru, N. D. Zhigadlo, and J. Karpinski, "Type-1.5 superconductivity," *Phys. Rev. Lett.*, vol. 102, p. 117001, Mar 2009.

[89] T. Nishio, V. H. Dao, Q. Chen, L. F. Chibotaru, K. Kadowaki, and V. V. Moshchalkov, "Scanning squid microscopy of vortex clusters in multiband superconductors," *Phys. Rev. B*, vol. 81, p. 020506, Jan 2010.

[90] J. Gutierrez, B. Raes, A. V. Silhanek, L. J. Li, N. D. Zhigadlo, J. Karpinski, J. Tempere, and V. V. Moshchalkov, "Scanning hall probe microscopy of unconventional vortex patterns in the two-gap MgB_2 superconductor," *Phys. Rev. B*, vol. 85, p. 094511, Mar 2012.

[91] M. Ichioka, V. G. Kogan, and J. Schmalian, "Locking of length scales in two-band superconductors," *Phys. Rev. B*, vol. 95, p. 064512, Feb 2017.

[92] S. Muhlbaue, C. Peiderer, P. Boni, M. Layer, E. Forgan, D. Fort, U. Keiderling, and G. Beh, "Morphology of the superconducting vortex lattice in ultrapure niobium," *Phys. Rev. Lett.*, vol. 102, p. 136408, 2009.

[93] R. Prozorov, A. F. Fidler, J. R. Hoberg, and P. C. Canfield, "Suprafroth in type-I superconductors," *Nature Physics*, vol. 4, pp. 327–332, Apr 2008.

[94] F. Morgan, "Colloquium: Soap bubble clusters," *Rev. Mod. Phys.*, vol. 79, pp. 821–827, Jul 2007.

[95] D. L. Weaire and S. Hutzler, *The physics of foams*. Oxford University Press, 2001.

[96] F. Graner, Y. Jiang, E. Janiaud, and C. Flament, "Equilibrium states and ground state of two-dimensional fluid foams," *Phys. Rev. E*, vol. 63, p. 011402, Dec 2000.

[97] N. Zhuravlev, "Structure of superconductors. x. thermal microscopic and x-ray investigation of the bismuth-palladium system," *Journal of Experimental and Theoretical Physics*, vol. 32, pp. 1305–1312, 1957.

[98] I. Shein and A. Ivanovskii, "Electronic band structure and Fermi surface of tetragonal low-temperature superconductor Bi_2Pd as predicted from first principles," *Journal of Superconductivity and Novel Magnetism*, vol. 26, no. 1, pp. 1–4, 2013.

[99] M. Sakano, M. Kanou, H. Sanjo, T. Okuda, T. Sasagawa, and K. Ishizaka, "Topologically protected surface states in a centrosymmetric superconductor $\beta - PdBi_2$," *Nature Communications*, vol. 6, p. 8595, 2015.

[100] J. Kačmarčík, Z. Pribulová, T. Samuely, P. Szabó, V. Cambel, J. Šoltýs, E. Herrera, H. Suderow, A. Correa-Orellana, D. Prabhakaran, and P. Samuely, "Single-gap superconductivity in $\beta - Bi_2Pd$," *Phys. Rev. B*, vol. 93, p. 144502, Apr 2016.

[101] K. Zhao, B. Lv, Y.-Y. Xue, X.-Y. Zhu, L. Z. Deng, Z. Wu, and C. W. Chu, "Chemical doping and high-pressure studies of layered $\beta - \mathrm{PdBi_2}$ single crystals," *Phys. Rev. B*, vol. 92, p. 174404, Nov 2015.

[102] G. Pristáš, M. Orendáč, S. Gabáni, J. Kačmarčík, E. Gažo, Z. Pribulová, A. Correa-Orellana, E. Herrera, H. Suderow, and P. Samuely, "Pressure effect on the superconducting and the normal state of $\beta - \mathrm{Bi_2Pd}$," *Phys. Rev. B*, vol. 97, p. 134505, Apr 2018.

[103] X. Zhang, M. Zhao, and F. Liu, "Enhancing superconductivity in bulk β–$\mathrm{Bi_2Pd}$ by negative pressure induced by quantum electronic stress," *Phys. Rev. B*, vol. 100, p. 104527, Sep 2019.

[104] A. Correa, F. Mompeán, I. Guillamón, E. Herrera, M. García-Hernández, T. Yamamoto, T. Kashiwagi, K. Kadowaki, A. I. Buzdin, H. Suderow, *et al.*, "Attractive interaction between superconducting vortices in tilted magnetic fields," *Communications Physics*, vol. 2, no. 1, p. 31, 2019.

[105] Y. Li, X. Xu, M.-H. Lee, M.-W. Chu, and C. L. Chien, "Observation of half-quantum flux in the unconventional superconductor β-$\mathrm{Bi_2Pd}$," *Science*, vol. 366, pp. 238–241, Oct. 2019.

[106] K. S. Novoselov, D. Jiang, F. Schedin, T. J. Booth, V. V. Khotkevich, S. V. Morozov, and A. K. Geim, "Two-dimensional atomic crystals," *Proceedings of the National Academy of Sciences*, vol. 102, no. 30, pp. 10451–10453, 2005.

[107] K. Iwaya, Y. Kohsaka, K. Okawa, T. Machida, M. S. Bahramy, T. Hanaguri, and T. Sasagawa, "Full-gap superconductivity in spin-polarised surface states of topological semimetal β-$\mathrm{PdBi_2}$," *Nature Communications*, vol. 8, no. 1, p. 976, 2017.

[108] A. T. Zehnder, "Fracture mechanics," *Lecture notes in applied and computational mechanics*, vol. 62, 2012.

[109] J. J. Mecholsky, "Fractography: Determining the sites of fracture initiation," *Dental Materials*, vol. 11, no. 2, pp. 113 – 116, 1995.

[110] J. A. Hauch, D. Holland, M. P. Marder, and H. L. Swinney, "Dynamic fracture in single crystal silicon," *Phys. Rev. Lett.*, vol. 82, pp. 3823–3826, May 1999.

[111] Y. Guo, C. Liu, Q. Yin, C. Wei, S. Lin, T. B. Hoffman, Y. Zhao, J. H. Edgar, Q. Chen, S. P. Lau, J. Dai, H. Yao, H.-S. P. Wong, and Y. Chai, "Distinctive in-plane cleavage behaviors of two-dimensional layered materials," *ACS Nano*, vol. 10, no. 9, pp. 8980–8988, 2016. PMID: 27564525.

[112] J. R. Kermode, L. Ben-Bashat, F. Atrash, J. J. Cilliers, D. Sherman, and A. De Vita, "Macroscopic scattering of cracks initiated at single impurity atoms," *Nature Communications*, vol. 4, pp. 2441 EP –, Sep 2013. Article.

[113] M. Marx, W. Schaef, and H. Vehoff, "Interaction of short cracks with the local microstructure," *Procedia Engineering*, vol. 2, no. 1, pp. 163 – 171, 2010. Fatigue 2010.

[114] H. F. Hess, R. B. Robinson, and J. V. Waszczak, "Vortex-core structure observed with a scanning tunneling microscope," *Phys. Rev. Lett.*, vol. 64, pp. 2711–2714, May 1990.

[115] Y. Fasano, M. D. Seta, M. Menghini, H. Pastoriza, and F. de la Cruz, "Commensurability and stability in nonperiodic systems," *Proceedings of the National Academy of Sciences*, vol. 102, pp. 3898–3902, Jan. 2005.

[116] N. R. C. Bolecek, A. B. Kolton, M. Konczykowski, H. Pastoriza, D. Domínguez, and Y. Fasano, "Vortex matter freezing in $Bi_2Sr_2CaCu_2O_8$ samples with a very dense distribution of columnar defects," *Phys. Rev. B*, vol. 93, p. 054505, Feb 2016.

[117] A. Chhabra and R. V. Jensen, "Direct determination of the f(α) singularity spectrum," *Physical Review Letters*, vol. 62, pp. 1327–1330, Mar. 1989.

[118] J. Zheng and E. Margine, "Electron-phonon coupling and pairing mechanism in β-Bi_2Pd centrosymmetric superconductor," *Phys. Rev. B*, vol. 95, p. 014512, 2017.

[119] K. A. Moler, J. R. Kirtley, R. Liang, D. Bonn, and W. N. Hardy, "Scanning SQUID microscopy of sparsely twinned $YBa_2Cu_3O_{7-}\delta$," *Phys. Rev. B*, vol. 55, pp. 12753–12758, May 1997.

[120] R. Luccas, X. Granados, X. Obradors, and T. Puig, "Vortex energy landscape from real space imaging analysis of $YBa_2Cu_3O_7$ with different defect structures," *Physica C: Superconductivity and its Applications*, vol. 505, pp. 47–54, Oct. 2014.

[121] A. Fente, A. Correa-Orellana, A. E. Böhmer, A. Kreyssig, S. Ran, S. L. Bud'ko, P. C. Canfield, F. J. Mompean, M. García-Hernández, C. Munuera, I. Guillamón, and H. Suderow, "Direct visualization of phase separation between superconducting and nematic domains in Co-doped $CaFe_2As_2$ close to a first-order phase transition," *Phys. Rev. B*, vol. 97, p. 014505, Jan 2018.

[122] S. Torquato and F. H. Stillinger, "Publisher's note: Local density fluctuations, hyperuniformity, and order metrics [phys. rev. e 68, 041113 (2003)]," *Phys. Rev. E*, vol. 68, p. 069901, Dec 2003.

[123] "Comments on: Hyperuniformity in jammed packings."

[124] Y. A. Kram, S. Mantey, and J. C. Corbo, "Avian cone photoreceptors tile the retina as five independent, self-organizing mosaics," *PLoS ONE*, vol. 5, p. e8992, Feb. 2010.

[125] Y. Jiao, T. Lau, H. Hatzikirou, M. Meyer-Hermann, J. C. Corbo, and S. Torquato, "Avian photoreceptor patterns represent a disordered hyperuniform solution to a multiscale packing problem," *Phys. Rev. E*, vol. 89, p. 022721, Feb 2014.

[126] S. Torquato, A. Scardicchio, and C. E. Zachary, "Point processes in arbitrary dimension from fermionic gases, random matrix theory, and number theory," *Journal of Statistical Mechanics: Theory and Experiment*, vol. 2008, p. P11019, nov 2008.

[127] C. E. Zachary, Y. Jiao, and S. Torquato, "Hyperuniform long-range correlations are a signature of disordered jammed hard-particle packings," *Phys. Rev. Lett.*, vol. 106, p. 178001, Apr 2011.

[128] J. H. Weijs, R. Jeanneret, R. Dreyfus, and D. Bartolo, "Emergent hyperuniformity in periodically driven emulsions," *Phys. Rev. Lett.*, vol. 115, p. 108301, Sep 2015.

[129] S. Torquato, G. Zhang, and F. H. Stillinger, "Ensemble theory for stealthy hyperuniform disordered ground states," *Phys. Rev. X*, vol. 5, p. 021020, May 2015.

[130] G. Blatter, M. V. Feigel'man, V. B. Geshkenbein, A. I. Larkin, and V. M. Vinokur, "Vortices in high-temperature superconductors," *Review of Modern Physics*, vol. 66, p. 1125, 1994.

[131] E. H. Brandt and U. Essmann, "The flux line lattice in type-II superconductors," *Phys. Stat. Sol.(b)*, vol. 13, p. 144, 1987.

[132] E. Zeldov, D. Majer, M. Konczykowski, V. B. Geshkenbein, V. M. Vinokur, and H. Shtrikman, "Thermodynamic observation of first-order vortex-lattice melting transition in $Bi_2Sr_2CaCu_2O_8$," *Nature*, vol. 375, pp. 373–376, June 1995.

[133] S. Bhattacharya and M. J. Higgins, "Dynamics of a disordered flux line lattice," *Phys. Rev. Lett.*, vol. 70, pp. 2617–2620, Apr 1993.

[134] R. Wördenweber, P. H. Kes, and C. C. Tsuei, "Peak and history effects in two-dimensional collective flux pinning," *Phys. Rev. B*, vol. 33, pp. 3172–3180, Mar 1986.

[135] M. Iavarone, R. Di Capua, G. Karapetrov, A. E. Koshelev, D. Rosenmann, H. Claus, C. D. Malliakas, M. G. Kanatzidis, T. Nishizaki, and N. Kobayashi, "Effect of magnetic impurities on the vortex lattice properties in $NbSe_2$ single crystals," *Phys. Rev. B*, vol. 78, p. 174518, Nov 2008.

[136] Q. Le Thien, D. McDermott, C. J. O. Reichhardt, and C. Reichhardt, "Enhanced pinning for vortices in hyperuniform pinning arrays and emergent hyperuniform vortex configurations with quenched disorder," *Phys. Rev. B*, vol. 96, p. 094516, Sep 2017.

[137] G. Rumi, J. A. Sanchez, F. Elias, R. C. Maldonado, J. Puig, N. R. C. Bolecek, G. Nieva, M. Konczykowski, Y. Fasano, and A. B. Kolton, "Hyperuniform vortex patterns at the surface of type-II superconductors," 2019.

[138] I. Guillamón, H. Suderow, P. Kulkarni, S. Vieira, R. Córdoba, J. Sesé, J. D. Teresa, M. Ibarra, G. Shaw, and S. Bannerjee, "Nanostructuring superconducting vortex matter with focused ion beams," *Physica C: Superconductivity and its Applications*, vol. 503, pp. 70–74, Aug. 2014.

[139] C. Kittel, *Introduction to Solid State Physics*. Wiley, 8 ed., 2004.

[140] I. Guillamón, R. Córdoba, J. Sesé, J. M. De Teresa, M. R. Ibarra, S. Vieira, and H. Suderow, "Enhancement of long-range correlations in a 2d?vortex lattice by an incommensurate 1d disorder?potential," *Nature Physics*, vol. 10, pp. 851 EP –, Oct 2014.

[141] I. Guillamón, R. Córdoba, J. Sesé, J. M. De Teresa, M. R. Ibarra, S. Vieira, and H. Suderow, "Enhancement of long-range correlations in a 2d?vortex lattice by an incommensurate 1d disorder?potential," *Nature Physics*, vol. 10, pp. 851 EP –, Oct 2014.

[142] Q. Le Thien, D. McDermott, C. J. O. Reichhardt, and C. Reichhardt, "Enhanced pinning for vortices in hyperuniform pinning arrays and emergent hyperuniform vortex configurations with quenched disorder," *Phys. Rev. B*, vol. 96, p. 094516, Sep 2017.

[143] P. H. Kes, J. Aarts, J. van den Berg, C. J. van der Beek, and J. A. Mydosh, "Thermally assisted flux flow at small driving forces," *Superconductor Science and Technology*, vol. 1, pp. 242–248, feb 1989.

[144] E. Herrera, J. Benito-Llorens, U. S. Kaluarachchi, S. L. Bud'ko, P. C. Canfield, I. Guillamón, and H. Suderow, "Vortex creep at very low temperatures in single crystals of the extreme type-II superconductor $Rh_9In_4S_4$," *Physical Review B*, vol. 95, p. 134505, 2017.

[145] I. Guillamón, H. Suderow, S. Vieira, J. Sesé, R. Córdoba, J. M. De Teresa, and M. R. Ibarra, "Direct observation of stress accumulation and relaxation in small bundles of superconducting vortices in tungsten thin films," *Phys. Rev. Lett.*, vol. 106, p. 077001, Feb 2011.

[146] N. W. Bode, D. W. Franks, and A. J. Wood, "Making noise: Emergent stochasticity in collective motion," *Journal of Theoretical Biology*, vol. 267, p. 292, 2010.

[147] B. J. Landrum, W. B. Russel, and R. N. Zia, "Delayed yield in colloidal gels: Creep, flow, and re-entrant solid regimes," *Journal of Rheology*, vol. 60, no. 4, p. 783, 2016.

[148] D. E. Newland, "On the Time-Dependent Spin Creep of a Railway Wheel," *Journal of Mechanical Engineering Science*, vol. 24, no. 2, p. 55, 1982.

[149] S. DuttaGupta, S. Fukami, C. Zhang, H. Sato, M. Yamanouchi, F. Matsukura, and H. Ohno, "Adiabatic spin-transfer-torque-induced domain wall creep in a magnetic metal," *Nature Physics*, vol. 12, pp. 333 EP –, Dec 2015.

[150] C. Zhou, C. Reichhardt, C. J. Olson Reichhardt, and I. J. Beyerlein, "Dynamic Phases, Pinning, and Pattern Formation for Driven Dislocation Assemblies," *Scientific Reports*, vol. 5, p. 8000 EP, 2015.

[151] H. F. Hess, C. A. Murray, and J. V. Waszczak, "Scanning-tunneling-microscopy study of distortion and instability of inclined flux-line-lattice structures in the anisotropic superconductor 2H-$NbSe_2$," *Physical Review Letters*, vol. 69, p. 2138, 1992.

[152] H. F. Hess, C. A. Murray, and J. V. Waszczak, "Flux lattice and vortex structure in 2H-$NbSe_2$ in inclined fields," *Physical Review B*, vol. 50, p. 16528, 1994.

[153] P. L. Gammel, D. A. Huse, R. N. Kleiman, B. Batlogg, C. S. Oglesby, E. Bucher, D. J. Bishop, T. E. Mason, and K. Mortensen, "Small angle neutron scattering study of the magnetic flux-line lattice in single crystal 2H-$NbSe_2$," *Physical Review Letters*, vol. 72, p. 278, 1994.

[154] L. J. Campbell, M. M. Doria, and V. G. Kogan, "Vortex lattice structures in uniaxial superconductors," *Physical Review B*, vol. 38, p. 2439, 1988.

[155] I. Fridman, C. Kloc, C. Petrovic, and J. Y. T. Wei, "Lateral imaging of the superconducting vortex lattice using Doppler-modulated scanning tunneling microscopy," *Appl. Phys. Lett.*, vol. 99, p. 192505, 2011.

[156] V. G. Kogan, L. N. Bulaevskii, P. Miranović, and L. Dobrosavljević-Grujić, "Vortex-induced strain and flux lattices in anisotropic superconductors," *Phys. Rev. B*, vol. 51, pp. 15344–15350, Jun 1995.

[157] R. Willa, J. A. Galvis, J. Benito-Llorens, E. Herrera, I. Guillamon, and H. Suderow, "Thermal creep emerging from cooling a tilted vortex lattice in uniaxial superconductor," 2019.

[158] A. M. Troyanovski, J. Aarts, and P. H. Kes, "Collective and plastic vortex motion in superconductors at high flux densities," *Nature*, vol. 399, p. 665, 1999.

[159] I. Guillamón, H. Suderow, S. Vieira, J. Sesé, R. Córdoba, J. M. De Teresa, and M. R. Ibarra, "Direct Observation of Stress Accumulation and Relaxation in Small Bundles of Superconducting Vortices in Tungsten Thin Films," *Physical Review Letters*, vol. 106, p. 077001, 2011.

[160] M. Buchacek, R. Willa, V. B. Geshkenbein, and G. Blatter, "Persistence of pinning and creep beyond critical drive within the strong pinning paradigm," *Physical Review B*, vol. 98, p. 094510, 2018.

[161] M. Buchacek, R. Willa, V. B. Geshkenbein, and G. Blatter, "Strong pinning theory of thermal vortex creep in type II superconductors," *arXiv:1903.09083 [cond-mat.supr-con]*, 2019.

[162] A. I. Larkin and Y. N. Ovchinnikov, "Pinning in type-II superconductors," *Journal of Low Temperature Physics*, vol. 34, p. 409, 1979.

[163] M. V. Feigel'man, V. B. Geshkenbein, A. I. Larkin, and V. M. Vinokur, "Theory of collective flux creep," *Physical Review Letters*, vol. 63, p. 2303, 1989.

[164] A. P. Levanyuk, "Contribution to the Theory of Light Scattering near the Second-Order Phase-Transition Points," *[Zh. Eksp. Teor. Fiz. **36**, 810 (1959)] JETP*, vol. 9, p. 571, 1959.

[165] V. L. Ginzburg, "Some remarks on phase transitions of second kind and the microscopic theory of ferroelectric materials," *[Fiz. Tverd. Tela (Leningrad) 2, 2031 (1960)] Sov. Phys. Solid State*, vol. 2, p. 1824, 1961.

[166] S. S. Banerjee, N. G. Patil, S. Saha, S. Ramakrishnan, A. K. Grover, S. Bhattacharya, G. Ravikumar, P. K. Mishra, T. V. Chandrasekhar Rao, V. C. Sahni, M. J. Higgins, E. Yamamoto, Y. Haga, M. Hedo, Y. Inada, and Y. Onuki, "Anomalous peak effect in $CeRu_2$ and 2H-$NbSe_2$: Fracturing of a flux line lattice," *Physical Review B*, vol. 58, p. 995, 1998.

[167] M. Menghini, Y. Fasano, and F. de la Cruz, "Critical current and topology of the supercooled vortex state in $NbSe_2$," *Physical Review B*, vol. 65, p. 064510, 2002.

[168] G. Pasquini, D. P. Daroca, C. Chiliotte, G. S. Lozano, and V. Bekeris, "Ordered, disordered, and coexistent stable vortex lattices in $NbSe_2$ single crystals," *Physical Review Letters*, vol. 100, p. 247003, 2008.

[169] S. Mohan, J. Sinha, S. S. Banerjee, A. K. Sood, S. Ramakrishnan, and A. K. Grover, "Large Low-Frequency Fluctuations in the Velocity of a Driven Vortex Lattice in a Single Crystal of 2H-$NbSe_2$ Superconductor," *Physical Review Letters*, vol. 103, p. 167001, 2009.

[170] A. Maldonado, S. Vieira, and H. Suderow, "Supercurrent on a vortex core in $2H$-$NbSe_2$: Current-driven scanning tunneling spectroscopy measurements," *Physical Review B*, vol. 88, p. 064518, 2013.

[171] R. Labusch, "Calculation of the critical field gradient in type-II superconductors," *Crystal Lattice Defects*, vol. 1, p. 1, 1969.

[172] R. Willa, V. B. Geshkenbein, and G. Blatter, "Probing the pinning landscape in type-II superconductors via Campbell penetration depth," *Physical Review B*, vol. 93, p. 064515, 2016.

[173] E. Brandt, "Thermal fluctuation of the vortex positions in high-Tc superconductors," *Physica C: Superconductivity and its Applications*, vol. 162, p. 1167, 1989.

[174] E. H. Brandt, "Penetration of magnetic ac fields into type-II superconductors," *Physical Review Letters*, vol. 67, p. 2219, 1991.

[175] E. H. Brandt, "The flux-line lattice in superconductors," *Reports on Progress in Physics*, vol. 58, p. 1465, 1995.

[176] E. H. Brandt, "Statics and Dynamics of the Vortex Lattice in High-Tc Superconductors," *Journal of Low Temperature Physics*, vol. 139, p. 21, 2005.

[177] B. Raes, C. C. de Souza Silva, A. V. Silhanek, L. R. E. Cabral, V. V. Moshchalkov, and J. Van de Vondel, "Closer look at the low-frequency dynamics of vortex matter using scanning susceptibility microscopy," *Physical Review B*, vol. 90, p. 134508, 2014.

[178] S. Eley, K. Khilstrom, R. Fotovat, Z. L. Xiao, A. Chen, D. Chen, M. Leroux, U. Welp, W. K. Kwok, and L. Civale, "Glassy dynamics in a heavy ion irradiated $NbSe_2$ crystal," *Scientific Reports*, vol. 8, Sept. 2018.

[179] Y. Yeshurun, A. P. Malozemoff, and A. Shaulov, "Magnetic relaxation in high-temperature superconductors," *Review of Modern Physics*, vol. 68, p. 911, 1996.

[180] M. V. Feigel'man and V. M. Vinokur, "Thermal fluctuations of vortex lines, pinning, and creep in high-T_c superconductors," *Physical Review B*, vol. 41, p. 8986, 1990.

[181] C. C. d. S. Silva, B. Raes, J. Brisbois, L. R. E. Cabral, A. V. Silhanek, J. Van de Vondel, and V. V. Moshchalkov, "Probing the low-frequency vortex dynamics in a nanostructured superconducting strip," *Physical Review B*, vol. 94, p. 024516, 2016.

[182] O. M. Auslaender, L. Luan, E. W. J. Straver, J. E. Hoffman, N. C. Koshnick, E. Zeldov, D. A. Bonn, R. Liang, W. N. Hardy, and K. A. Moler, "Mechanics of individual isolated vortices in a cuprate superconductor," *Nature Physics*, vol. 5, no. 1, p. 35, 2009.

[183] L. Embon, Y. Anahory, A. Suhov, D. Halbertal, J. Cuppens, A. Yakovenko, A. Uri, Y. Myasoedov, M. L. Rappaport, M. E. Huber, A. Gurevich, and E. Zeldov, "Probing dynamics and pinning of single vortices in superconductors at nanometer scales," *Scientific Reports*, vol. 5, p. 7598, 2015.

[184] S. Eley, M. Miura, B. Maiorov, and L. Civale, "Universal lower limit on vortex creep in superconductors," *Nature Materials*, vol. 16, p. 409 EP, 2017.

[185] C. Rastovski, K. J. Schlesinger, W. J. Gannon, C. D. Dewhurst, L. DeBeer-Schmitt, N. D. Zhigadlo, J. Karpinski, and M. R. Eskildsen, "Persistence of Metastable Vortex Lattice Domains in MgB_2 in the Presence of Vortex Motion," *Physical Review Letters*, vol. 111, p. 107002, 2013.

[186] M. Marziali Bermúdez, M. R. Eskildsen, M. Bartkowiak, G. Nagy, V. Bekeris, and G. Pasquini, "Dynamic Reorganization of Vortex Matter into Partially Disordered Lattices," *Physical Review Letters*, vol. 115, p. 067001, 2015.

[187] M. Marziali Bermúdez, E. R. Louden, M. R. Eskildsen, C. D. Dewhurst, V. Bekeris, and G. Pasquini, "Metastability and hysteretic vortex pinning near the order-disorder transition in $NbSe_2$: Interplay between plastic and elastic energy barriers," *Physical Review B*, vol. 95, p. 104505, 2017.

[188] Y. Zhang, D. C. Richardson, O. S. Barnouin, C. Maurel, P. Michel, S. R. Schwartz, R.-L. Ballouz, L. A. Benner, S. P. Naidu, and J. Li, "Creep stability of the proposed AIDA mission target 65803 Didymos: I. Discrete cohesionless granular physics model," *Icarus*, vol. 294, p. 98, 2017.

[189] K. Uchiyama, S. Suzuki, A. Kuwahara, K. Yamasaki, S. ichi Kaneko, H. Takeya, K. Hirata, and N. Nishida, "Importance of dislocations in vortex creep revealed in yni$_2$b$_2$c by observations in real time and space stm," *Physica C: Superconductivity and its Applications*, vol. 470, pp. S795–S796, Dec. 2010.

[190] E. Herrera, J. Benito-Llorens, U. S. Kaluarachchi, S. L. Bud'ko, P. C. Canfield, I. Guillamón, and H. Suderow, "Vortex creep at very low temperatures in single crystals of the extreme type-II superconductor $Rh_9In_4S_4$," *Physical Review B*, vol. 95, p. 134505, 2017.